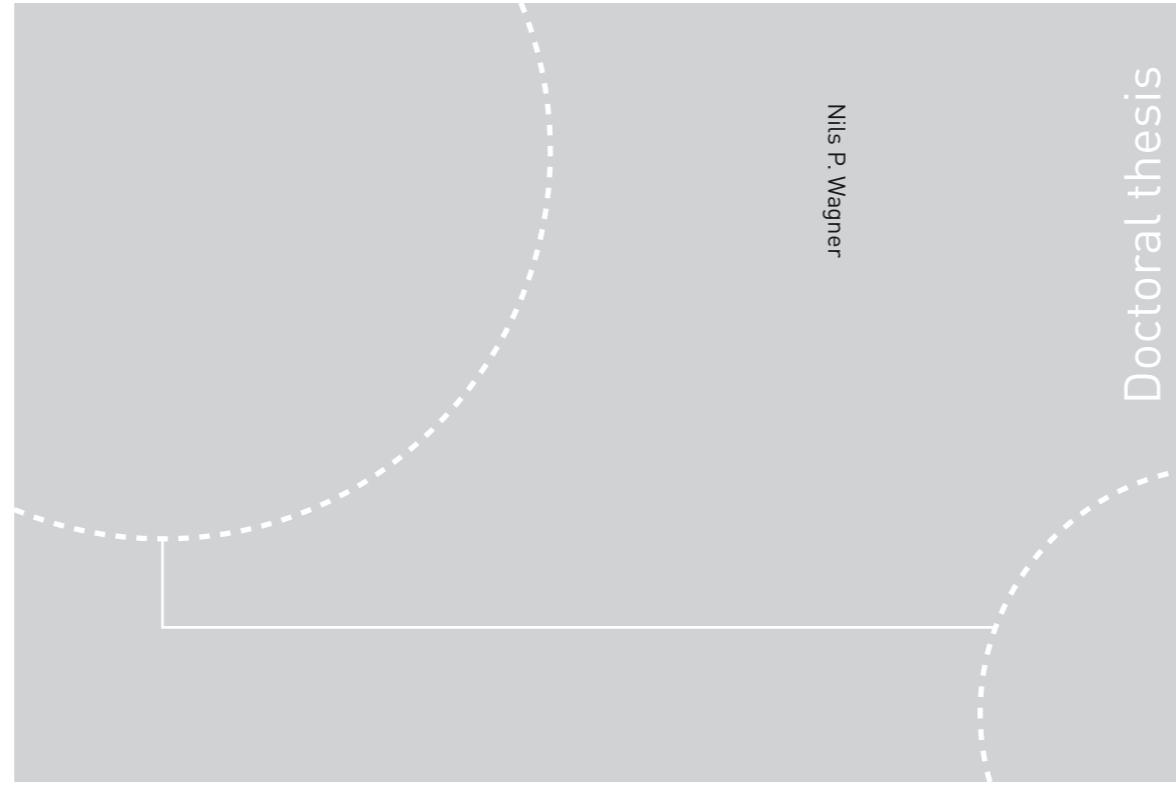


ISBN 978-82-326-1452-3 (printed ver.)  
ISBN 978-82-326-1453-0 (electronic ver.)  
ISSN 1503-8181



Doctoral theses at NTNU, 2016:57

Nils P. Wagner

# Alternative Li-ion Cathodes based on Transition Metal Orthosilicates

Doctoral theses at NTNU, 2016:57

**NTNU**  
Norwegian University of  
Science and Technology  
Thesis for the Degree of  
Philosophiae Doctor  
Faculty of Natural Sciences and Technology  
Department of Materials Science and  
Engineering

 **NTNU**  
Norwegian University of  
Science and Technology

 NTNU

 **NTNU**  
Norwegian University of  
Science and Technology

Nils P. Wagner

# Alternative Li-ion Cathodes based on Transition Metal Orthosilicates

Thesis for the Degree of Philosophiae Doctor

Trondheim, March 2016

Norwegian University of Science and Technology  
Faculty of Natural Sciences and Technology  
Department of Materials Science and Engineering



Norwegian University of  
Science and Technology

**NTNU**

Norwegian University of Science and Technology

Thesis for the Degree of Philosophiae Doctor

Faculty of Natural Sciences and Technology  
Department of Materials Science and Engineering

© Nils P. Wagner

ISBN 978-82-326-1452-3 (printed ver.)  
ISBN 978-82-326-1453-0 (electronic ver.)  
ISSN 1503-8181

IMT-report 2016:222

Doctoral theses at NTNU, 2016:57

Printed by NTNU Grafisk senter

# Preface

This dissertation has been submitted to the Norwegian University of Science and Technology (NTNU) in partial fulfilment of the requirements for the academic degree Philosophiae Doctor.

The doctoral studies were performed at the Inorganic Materials and Ceramics Research Group, Department of Materials Science and Engineering, NTNU, Trondheim, under supervision of Associate Professor Fride Vullum-Bruer and Professor Ann Mari Svensson. The project has been funded by the research council of Norway (SilicatBatt project (grant number: 216469/E20)).

Nils P. Wagner

Trondheim, 11<sup>th</sup> of January 2016



# Acknowledgements

Several people deserve acknowledgement for supporting and encouraging me during the last three years, and I would like to take this opportunity to express my sincere gratitude to all who have in one way or another supported me during the time of my PhD studies.

First and foremost I would like to thank my supervisor Fride Vullum-Bruer, for the excellent support, guidance and input during my PhD studies. I would also like to thank my co-supervisor Ann Mari Svensson for her guidance and contribution, especially concerning electrochemical characterisation methods. Also deserving of mention here are Per Erik Vullum and Magnus Nord for TEM/EELS analysis and their invaluable contribution to the discussion of the results. Thank you very much!

The Research Council of Norway is acknowledged for financing the “SilicatBatt” project.

Furthermore, I would like to express appreciation to the SINTEF colleagues involved in the “SilicatBatt” project, namely: Tommy Mokkelbost, Anita Fossdal, Kaushik-Jayasayee, Sidsel Meli Hanetho and Edel Sheridan. To the same effect, I would like to thank the other members of the IMT battery group: Xinzhi Chen, Muhammad Hasanuzzaman, Lu Wang, Pei Na Kui and Magnus Bentzen Følstad. It was a pleasure to work with you!

It also was, and still is, very inspiring to supervise the master/exchange students Antoine Dalod, Julien Claquesin and Vyacheslav Lobintsev. Thank you very much for your contribution to this work and to the battery research at NTNU.

The academic, technical and administrative staff of IMT are acknowledged for help whenever needed. A special thanks goes to Julian Tolchard and Kristin Høydalsvik for assistance with *in situ* XRD measurements and Rietveld analysis.

At this point I want to thank all my friends and office mates here in Trondheim and my friends back home in Germany. You made this PhD experience and my stay in Trondheim enjoyable and delightful.

Last but not least, I have to express my deepest gratitude and appreciation to my mother and my entire family back home and to my lovely and caring girlfriend Katie for all the good times we had and will have as well as her patience and support during the stressful times of finalising this work.

## Summary

Rechargeable batteries can store energy in the form of chemical energy and facilitate it with a high conversion rate when needed. Moreover, rechargeable batteries are used in almost all kinds of portable consumer electronics, hybrid and pure electric vehicles. Thus, the development of advanced battery technologies is a major field of scientific focus. Li-ion technology has been shown to be superior to other battery concepts with respect to energy density, cycling stability, self-discharge and expected lifetime. Alternative cathode materials based on polyanionic compounds have attracted interest since the discovery of  $\text{LiFePO}_4$  as a safer cathode material in 1997 and  $\text{Li}_2\text{FeSiO}_4$  as a new Li-battery cathode material in 2005. Lithium transition metal orthosilicates, where the transition metal is iron or manganese, are promising candidates as cathode materials since they consist of cheap, environmentally benign and abundant elements. The  $\text{SiO}_4$  backbone not only stabilises the structure but also raises the transition metal 2+/3+ redox couple to higher voltages by an inductive effect. This class of materials could further allow Li extraction/insertion beyond one Li-ion per formula unit, if the transition metal possesses two available redox couples within the stability limit of the electrolyte. This study concerns the improvement of the electrochemical properties of lithium transition metal orthosilicates.

The first part is devoted to the development of a controllable synthesis method for nanoscaled and carbon coated  $\text{Li}_2\text{MnSiO}_4$  and the characterisation of the electrochemical properties. A PVA assisted sol-gel route was explored and optimised, and the importance of the carbon coating and the porous nanostructure to the electrochemical properties was highlighted.

$\text{Li}_2\text{MnSiO}_4$  is a rather poor electronic and ionic conductor and suffers from severe capacity fading upon electrochemical cycling. The second part of this work investigates if these shortcomings can be manipulated by the incorporation of foreign species, via substitution studies based on the synthesis method developed in part one. The investigated substituents were iron and vanadium. V substitution was shown to be especially interesting and, since it has not been well understood, efforts have been made to explore the feasibility and limitations of V substitution and the impact on the electrochemical properties of  $\text{Li}_2\text{MnSiO}_4$ . It was shown that the solid solubility of V on Mn-sites is very limited and the intended substitution causes phase separation into V containing spinel phases.. On the other hand, when intended to replace Si, V entered the structure without such phase separation. The structure was highly defec-



tive but had improved charge transfer resistance and Li diffusion. Furthermore, additional redox activity attributable to V was recorded. The downside was that V rather replaces Si and hence showed no influence on the poor stability upon cycling which is caused by tetrahedrally coordinated Mn.

The last part of this project was dedicated to exploring the possibility of a scalable and time efficient route, allowing the synthesis of nanoscaled lithium transition metal orthosilicates. As a first novel approach  $\text{Li}_2\text{MSiO}_4$  compounds were synthesised by liquid-feed flame spray pyrolysis combined with a reducing heat treatment and carbon coating. The importance of a highly combustible solution and the influence of the precursor concentration are discussed. Synthesised  $\text{Li}_2\text{MnSiO}_4$  and  $\text{Li}_2\text{FeSiO}_4$  were highly electrochemical active. The former showed capacities exceeding the value of a one electron reaction while the latter offered a superior rate performance and retained over 50% of its initial capacity when the current density was increased by a factor of  $10^2$ .

# Contents

Preface.....	iii
Acknowledgements .....	v
Summary .....	vii
Contents .....	ix
Scientific Papers.....	xi
Appendix.....	xi
The author's contribution.....	xiii
1. Introduction.....	1
1.1 Motivation.....	1
1.2 Aim of work.....	3
2. Li-ion batteries .....	5
2.1 General .....	5
2.2 Working principle of a Li-ion battery .....	5
2.3 Cathode Materials .....	8
2.4 Anode Materials .....	12
2.5 Electrode additives.....	14
2.6 Current collectors .....	15
2.7 Electrolytes.....	16
2.8 Electrode interphases .....	18
2.9 Separator .....	21
3. Lithium Transition Metal Orthosilicates ( $\text{Li}_2\text{MSiO}_4$ ) .....	23
3.1 General .....	23
3.2 Crystal structure and polymorphism .....	23

3.3	Lithium diffusion pathways.....	27
3.4	Delithiation potentials.....	31
3.5	Electronic behaviour.....	32
3.6	Cationic substitutions on the M or Si-site .....	33
3.7	Synthesis methods and electrochemical properties of nanostructured carbon coated $\text{Li}_2\text{MSiO}_4$ compounds.....	35
4.	Brief description of the applied Synthesis methods.....	39
4.1	Overview.....	39
4.2	Sol-gel synthesis .....	39
4.2.1	Silicate based sol-gel process.....	39
4.2.2	Multi component sol-gel processes.....	41
4.2.3	Gel ageing .....	42
4.2.4	Gel drying .....	43
4.3	Liquid Feed Flame Spray Pyrolysis .....	44
4.4	Phase formation and carbon coating.....	45
5.	Summary of the main results .....	49
5.1	Foreword .....	49
5.2	Synthesis of $\text{Li}_2\text{MnSiO}_4$ by an acidic PVA assisted sol-gel method.....	49
5.3	Feasibility of cationic substitutions in $\text{Li}_2\text{MnSiO}_4$ .....	58
5.4	Investigations on V substitution in $\text{Li}_2\text{MnSiO}_4$ .....	61
5.5	Liquid-feed flame spray pyrolysis as scalable $\text{Li}_2\text{MnSiO}_4$ synthesis approach ...	77
5.6	$\text{Li}_2\text{FeSiO}_4$ and $\text{Li}_2\text{Fe}_{0.5}\text{Mn}_{0.5}\text{SiO}_4$ by liquid-feed flame spray pyrolysis .....	82
6.	Conclusions.....	87
7.	Outlook.....	91
8.	References .....	93

## Scientific Papers

<b>I</b>	Effect of carbon content and annealing atmosphere on phase purity and morphology of $\text{Li}_2\text{MnSiO}_4$ synthesized by a PVA assisted sol-gel method	117
<b>II</b>	Fe and V Substituted $\text{Li}_2\text{MnSiO}_4/\text{C}$ as Potential Cathode Material for Li-ion Batteries	127
<b>III</b>	On Vanadium Substitution in $\text{Li}_2\text{MnSiO}_4/\text{C}$ as Positive Electrode for Li-ion Batteries	143
<b>IV</b>	Liquid-Feed Flame Spray Pyrolysis as Alternative Synthesis for Electrochemically Active Nanosized $\text{Li}_2\text{MnSiO}_4$	179
<b>V</b>	Flame-made Lithium Transition Metal Orthosilicates	203

## Appendix

<b>A</b>	Supporting Material Paper I	229
<b>B</b>	Supporting Material Paper IV	233



## The author's contribution

The author wrote and performed all experimental work presented in Paper I-V and this dissertation, except for the following parts: The synthesis and physical characterisation of  $\text{Li}_2\text{Mn}_{1-x}\text{Fe}_x\text{SiO}_4$  ( $0 \leq x \leq 0.2$ ) was performed by Antoine R. M. Dalod during his master project under supervision of the author; TEM and EDS/EELS analysis presented in Paper I, III and IV was performed by Dr. Per Erik Vullum, SINTEF Materials and chemistry; EELS spectra were corrected by Magnus Kristofer Nord, Department of Physics, NTNU. Characterisation and interpretation of the EELS results presented in Paper III was a joint effort of the author, Dr Per Erik Vullum and Magnus Kristofer Nord.

The following scientific papers are included in this dissertation.

- Paper I: N. Wagner, A. M. Svensson, F. Vullum-Bruer, "*Effect of carbon content and annealing atmosphere on phase purity and morphology of  $\text{Li}_2\text{MnSiO}_4$  synthesized by a PVA assisted sol-gel method*", Solid State Ionics, 276 (2015) 26-32.
- Paper II: N. Wagner, A. Dalod, A. M. Svensson, F. Vullum-Bruer, "*Fe and V Substituted  $\text{Li}_2\text{MnSiO}_4/\text{C}$  as Potential Cathode Material for Li-ion Batteries*", ECS Transactions, 64 (22) (2015) 33-45.
- Paper III: N. P. Wagner, P. E. Vullum, M. K. Nord, A. M. Svensson, F. Vullum-Bruer, "*On Vanadium Substitution in  $\text{Li}_2\text{MnSiO}_4/\text{C}$  as Positive Electrode for Li-ion Batteries*"
- Paper IV: N. P. Wagner, A. M. Svensson, F. Vullum-Bruer, "*Liquid Feed Flame Spray Pyrolysis as Alternative Synthesis for Electrochemically Active Nanosized  $\text{Li}_2\text{MnSiO}_4$* "
- Paper V: N. P. Wagner, A. M. Svensson, F. Vullum-Bruer, "*Flame-made Lithium Transition Metal Orthosilicates*"



# 1. Introduction

## 1.1 Motivation

The world's energy needs and energy consumption are constantly increasing. At the same time modern society is more aware of the vast increase in CO<sub>2</sub> emissions and environmental pollution caused by classical energy production. To minimise the resulting greenhouse effect, future energy supplies must be environmentally friendly and cause a minimum carbon footprint. Hence, energy production must become independent from crude oil and Nuclear Power. Environmentally friendly renewable energy can be produced in several ways, for example wind energy, tidal energy or by photovoltaic devices. Since all these forms of energy production are discontinuous, they need to be linked to energy storage devices. Rechargeable batteries can store this energy in the form of chemical energy and facilitate it with a high conversion rate when needed. Further, the markets for electronic vehicles (EV's) and portable consumer electronics are constantly growing and these demand rechargeable battery technologies with ever higher efficiencies.

It takes just a quick glance into a chemical data book to understand that lithium is one of the lightest elements and offers a high electrode potential of -3.04 V versus the standard hydrogen electrode.<sup>1</sup> This combination of low weight and a high potential gives rise for elevated power and specific energy. In fact, research concerning Li based batteries started in the 1970s, and at present rechargeable batteries based on Li ions outperform all other commercially available battery concepts with respect to specific energy, energy density per volume, cycling stability, self-discharge and expected lifetime.<sup>2</sup>

Early Li batteries were restricted to primary (non-rechargeable) concepts since dendritic growth of plated Li on the anode side caused severe safety issues. The discovery of reversible intercalation of Li in carbonaceous materials at low potentials solved this problem and in 1991 Sony Corporation commercialised the petroleum coke/LiCoO<sub>2</sub> Li-ion cell.<sup>2-5</sup> As the name implies, the Li-ion battery concept omits Li in its metallic form. In modern Li-ion batteries petroleum coke is substituted by graphite which offers an increased capacity ranging from 300-400 mAhg<sup>-1</sup>. However,



most Li-ion batteries are still equipped with  $\text{LiCoO}_2$  cathodes,<sup>2,6-10</sup> first reported by J. B. Goodenough and co-workers in 1980, which deliver a modest specific capacity of about  $140 \text{ mAhg}^{-1}$  and have some major safety and pricing issues.<sup>4,7,11,12</sup>

It was also J. B. Goodenough, now leading a different research group, who first reported the phospho-ovline  $\text{LiFePO}_4$  as a potential new cathode material, solving safety and cost issues, in 1997.<sup>13</sup> The phospho-olivine is based on a much more abundant and nontoxic transition metal, iron, delivering an increased specific capacity of about  $170 \text{ mAhg}^{-1}$  and is used as cathode for Li-ion batteries in EVs.<sup>14</sup> The discovery also offered interesting possibilities in the search for new alternative cathode materials, by tuning the transition metal redox couple by the inductive effect of the polyanion group. In 2005, Nytén *et al.* introduced  $\text{Li}_2\text{FeSiO}_4$  as a potential cathode material and only a year later Dominko *et al.* reported the Mn analogue.<sup>15,16</sup> The di-lithium transition metal orthosilicates where the transition metal is Fe or Mn, gained attention because they consist of cheap and nontoxic elements and could thus be a serious alternative as low cost electrode, as seen in the element abundance diagram shown in Figure 1.1.

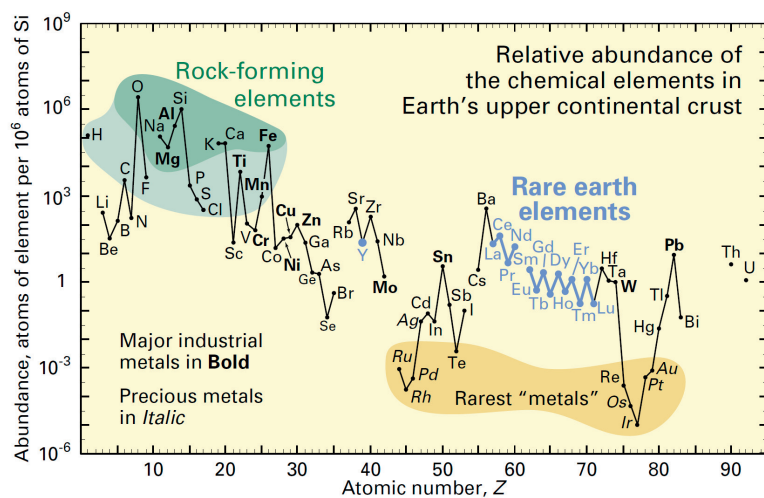


Figure 1.1: The chemical elements' relative abundance in the upper earth crust.

17

Additionally, this class of materials comes with a lithium to transition metal ratio of 2:1, and they could potentially provide two Li ions per formula unit if the transition metal possesses two available redox couples within the potential window of the applied electrolyte. This leads to a theoretical capacity of about  $330 \text{ mAhg}^{-1}$ , which

would drastically decrease the existing gap in capacity between the cathode and anode side of a Li-ion battery. Unfortunately,  $\text{Li}_2\text{MSiO}_4$  ( $\text{M} = \text{Mn}$  or  $\text{Fe}$ ) are insulators and also poor ionic conductors, making the bulk material unsuitable as an electrode.<sup>18–22</sup> A further challenge is the structural instability upon oxidation of  $\text{Li}_2\text{MnSiO}_4$  which is believed to be triggered by the Jahn-Teller active ion  $\text{Mn}^{3+}$ .<sup>19,22,23</sup>

Nonetheless, advances in nano science over the last few decades have made it possible to tailor particle morphologies to allow fast exchange of Li ions from the material to the electrolyte. The increased performance of these structures is accomplished by drastically shortening the mean diffusion lengths and increasing the surface to bulk ratio.<sup>24</sup> Further, tremendous amounts of knowledge have been gathered on conductive coatings and the beneficial effects of cation substitutions.<sup>4,25</sup> Combing this gathered knowledge, makes the lithium transition metal orthosilicate family an interesting system both as alternative low cost and high capacity cathode material for the next generation of Li-ion batteries.

## 1.2 Aim of work

The purpose of this study was to investigate and improve the electrochemically properties of lithium transition metal orthosilicates as positive electrode for Li-ion batteries. Since a previous project at the same department was focused on advances in  $\text{Li}_2\text{FeSiO}_4$ , the main focus in this study is dedicated to the Mn analogue. The work presented here can be divided into three main parts.

In the first part a wet chemical route was developed, which allows a controlled synthesis of highly phase pure and nanostructured  $\text{Li}_2\text{MnSiO}_4/\text{C}$ . A PVA assisted sol-gel method was chosen and optimised. Further, the effect of carbon content on the phase purity, morphology and electrochemical properties was analysed. Consequently, samples with different carbon contents were characterised in terms of phase composition and purity, morphology and the electrochemical properties. The results are published in Paper I.

One basis of the synthesis method developed in part one, cationic substitutions in  $\text{Li}_2\text{MnSiO}_4$  were studied. The results are published in Paper II and III. The chosen cations were Fe and V.  $\text{Li}_2\text{FeSiO}_4$  is known to exist in the same structural polymorphs as  $\text{Li}_2\text{MnSiO}_4$ , and both cations have a similar ionic radius and electronegativity. Hence, the Hume-Rothery rules should apply and Fe should populate empty Mn-sites. For V, which is known to exist in multiple oxidation states, the feasibility of substituting it on either the Mn-site or the Si-site was considered. The aim was to investigate if substitutions alter the physical properties like the

stability of the delithiated phase, the electronic conductivity and the Li diffusion coefficient, and explore the possibility to incorporate an additional redox couple into the structure. The phase formation was studied by X-ray diffraction. For V substituted samples additional *in situ* X-ray diffraction studies were conducted, to analyse the behaviour upon delithiation, and electron energy loss spectroscopy characterisations (EELS) were performed to provide information about local derivations of the overall structure and determine the oxidation state of V. Origins of the improved cycling performance and the redox activity of V in  $\text{Li}_2\text{MnSiO}_4$  were further investigated by cyclic voltammetry and AC impedance.

The last part of this study concerns the feasibility of a scalable synthesis method for highly electrochemically active lithium transition metal orthosilicates as cathode materials for Li-ion batteries. The feasibility by liquid-feed flame spray pyrolysis with subsequent annealing is shown in Paper IV and V. Focus here was given to produce nanostructures in the range of 20-30 nm.

## 2. Li-ion batteries

### 2.1 General

The following chapter summarises the working principle of a Li-ion battery. Furthermore, the individual components of a Li-ion battery are described and the research progress is briefly reviewed. Since this study focuses on the properties of cathode materials, the so called half-cell concept versus a Li metal counter electrode was applied throughout the study. Nonetheless, whenever applicable, examples of the author's materials of choice are included in the specific section of this chapter.

### 2.2 Working principle of a Li-ion battery

As in any conventional battery concept, the Li-ion battery consists of two electrodes connected by an ionic conducting media called the electrolyte. Secondary Li-ion batteries convert chemical energy into electrical energy during the discharge and vice versa during the charge. Since the terminology of the specific parts of a battery originates from primary concepts of pure galvanic cells, they are strictly speaking only valid during the discharge of a secondary Li-ion battery. Figure 2.1 shows a schematic of a Li-ion battery during discharge.

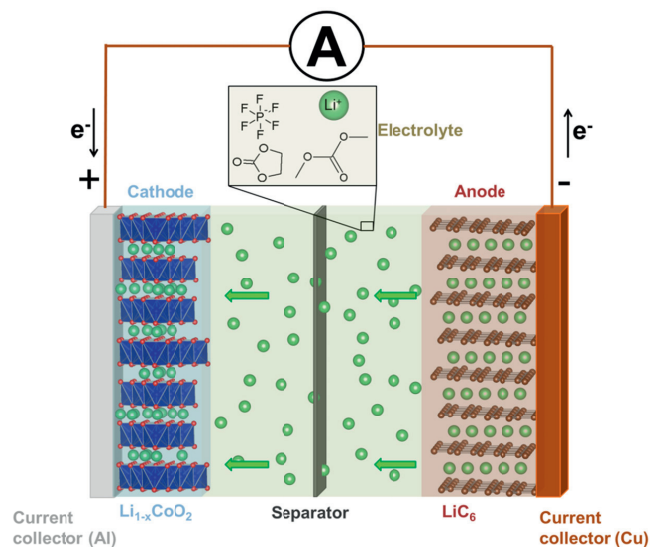
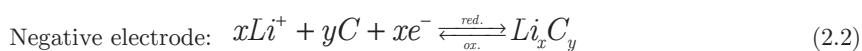


**Figure 2.1:** Scheme of a Li-ion battery during discharge, motion of Li ions is indicated by green arrows while the motion of electrons through the external circuit is indicated by black arrows. The crystal structures are visualised using VESTA, with schematic Li positions in the graphite layers and vacant Li positions in the  $\text{Li}_{1-x}\text{CoO}_2$  layers.

The cell consists of a Li transition metal oxide positive pole, termed cathode during discharge, connected to an aluminium current collector, an organic electrolyte containing a dissociated Li salt and a graphite negative pole, termed anode during discharge, connected to a copper current collector. The two electrodes are separated by a permeable separator and connected by an external circuit.

During discharge, Li is driven to oxidation by the potential difference at the anode and Li ions migrate towards the cathode, where they intercalate into the Li layers. At the same time, electrons generated at the anode are transported through an external circuit and subsequently reduce the transition metal ions to a lower valence to maintain electroneutrality. The generated current can be utilised by a device.

The charge of a secondary Li-ion battery is the reverse of this step and requires reversibility of the reaction. During charge the cell works in electrolytic mode. The positive pole is now the anode and the transition metal ions get oxidised to a higher valence while Li ions deintercalate out of the structure and migrate towards the negative pole (now cathode) where they intercalate into the graphite layers and get reduced by the electrons moving through the external circuit. The electrochemical reactions of a  $\text{LiCoO}_2/\text{C}$  cell are summarised in the following equations:



As noticeable from the scheme in Figure 2.1 and from the electrochemical equations, a Li-ion cell does not contain metallic Li but two host materials from where Li is inserted and extracted (intercalation). Metallic Li offers a high capacity, but must be omitted in this set up due to safety issues. Li ions tend to plate inhomogeneously on a negative Li electrode and cause the formation of dendrites. These dendrites can short circuit the two electrodes causing exothermic reactions which could lead to an explosion of the cell. Accordingly, Li was replaced by materials that can reversibly intercalate Li. To keep a high operation voltage, materials for the negative electrode should exhibit a redox potential for Li close to metallic Li, while for materials for the positive electrode the redox potential of the transition metal should be high against  $\text{Li}/\text{Li}^+$ . An overview of electrode materials for Li-ion batteries known by the year 2001 is shown in Figure 2.2.

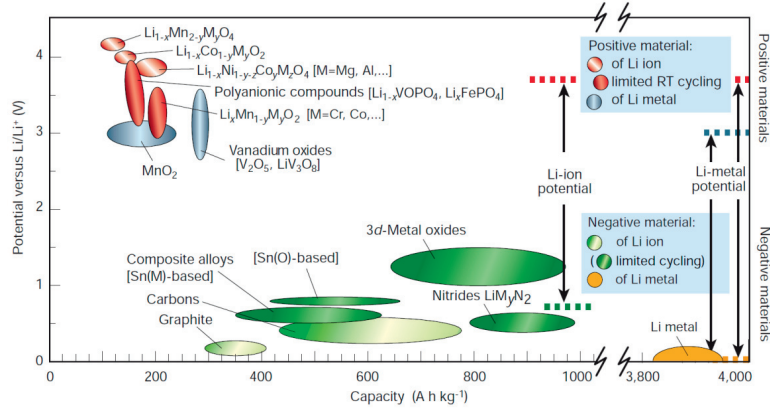


Figure 2.2: Specific capacities and potentials of electrode materials for Li-ion batteries. <sup>2</sup>

Figure 2.2 shows a prominent mismatch in specific capacity  $Q$  between cathode materials (positive materials) and anode materials (negative materials). The specific capacity is often expressed in  $\text{Ahkg}^{-1}$  or  $\text{mAhg}^{-1}$ . The theoretical specific capacity ( $Q^{\text{th}}$ ) can be calculated from Faraday's first law using the following equation <sup>10</sup>:

$$Q^{\text{th}} = \frac{nF}{M} \quad (2.4)$$

where  $n$  is the number of the exchanged electrons,  $F$  is the Faraday constant ( $96,485 \text{ Cmol}^{-1} = 26.8 \text{ Ahmol}^{-1}$ ) and  $M$  is the molar mass. When  $Q^{\text{th}}$  is multiplied with the open circuit potential (OCP) we obtain the theoretical specific energy of the battery in terms of  $\text{Whkg}^{-1}$ . Since Figure 2.2 is already older than a decade, it lacks the most recent innovations and a more detailed overview of electrode materials for Li-ion batteries is given in the following chapters.

## 2.3 Cathode Materials

As previously mentioned, the positive electrode in a Li-ion battery is termed the cathode, although this is strictly speaking just valid during the discharge. According to M. S. Whittingham there are eight major criteria that a cathode material must fulfil. The cathode material must contain a transition metal ion, which is readily re-





The stacking of transition metal and Li layers results in a two dimensional Li diffusion network. It offers a theoretical capacity of  $274 \text{ mAhg}^{-1}$  but only about  $140 \text{ mAhg}^{-1}$  can practically be utilised, so the delithiation is cut-off at about 4.2 V.<sup>4</sup> On further delithiation structural changes occur and at full delithiation the cubic close-packed (ccp) oxygen sub lattice changes to the hexagonal close-packed (hcp) structure of  $\text{CoO}_2$ .<sup>25</sup> The reduced stability of the heavily delithiated phase causes dissolution of Co and the loss of oxygen from the lattice, which results in an irreversible capacity fade upon cycling.<sup>28,29</sup> The iso-structural nickel compound would be of interest since Ni is more abundant than Co. Unfortunately,  $\text{LiNiO}_2$  is reported to exist in  $\text{Li}_{1-y}\text{Ni}_{1+y}\text{O}_2$  stoichiometry, where Ni is partly reduced to the divalent state and occupies the Li layer, and thus has a negative influence on the Li diffusion and power capability of the material.<sup>4,25</sup> Later, it was shown that trivalent Co substitution hinders the Ni reduction, and thus reduces anti-site defects, leading to a reduced capacity fade of the  $\text{LiNi}_{1-x}\text{Co}_x\text{O}_2$  solid solution compared to the pure Ni compound.<sup>30</sup> Further, the incorporation of divalent or trivalent inert diluents like  $\text{Mg}^{2+}$  and  $\text{Al}^{3+}$  or the partial substitution of  $\text{O}^{2-}$  by  $\text{F}^-$  or  $\text{S}^{2-}$  were shown to improve the stability and cyclability of  $\text{LiNiO}_2$  and  $\text{LiNi}_{1-x}\text{Co}_x\text{O}_2$ .<sup>31-34</sup> The Mn analogous  $\text{LiMnO}_2$  is thermodynamically unstable at elevated synthesis temperatures, and even when prepared at low temperatures it forms the thermodynamically stable spinel structure  $\text{LiMn}_2\text{O}_4$  upon cycling. This spinel structure can be described as an exceptional case where the transition-metals are ordered in all layers.  $\text{LiMn}_2\text{O}_4$  displays an interesting high voltage and is thus a high power cathode material, although its capacity is lower than the capacity of  $\text{LiCoO}_2$ .<sup>25,35,36</sup> 50% Ni substitution in  $\text{LiMnO}_2$  yields the layered structure and finally resulted in the discovery of the solid solution of all three cations in  $\text{LiNi}_{1-x-y}\text{Mn}_x\text{Co}_y\text{O}_2$  (NMC).<sup>37-40</sup> NMC compounds show almost no Li transition metal anti-site defects. The most studied composition is the symmetric 1/3 composition. In NMC, Ni is divalent, Co trivalent and Mn tetravalent and 2/3 Li can be exchanged by the  $\text{Ni}^{2+}/\text{Ni}^{4+}$  redox pair.<sup>41,42</sup> Higher reversible capacities ( $\sim 200 \text{ mAhg}^{-1}$ ), low volume changes and an increased stability of the delithiated state compared to  $\text{LiCoO}_2$  and  $\text{LiNi}_{1-x}\text{Co}_x\text{O}_2$  make NMC compounds extremely interesting as cathode material for Li-ion batteries.<sup>4,25</sup>

In addition to the layered structures, a second category of materials comprises more open structures like vanadium oxides, manganese dioxide and polyanionic compounds. Although, one has to keep in mind that in a Li-ion battery the cathode is the source of Li ions which excludes materials like  $\text{V}_2\text{O}_5$  and  $\text{MnO}_2$  for a conventional Li-ion battery. This category offers safer and potentially cheaper materials. The polyanion group stabilises the structure and gives rise to tuning the redox potential of the transition metal by an inductive effect altering the ionic-covalent character of the transition metal oxygen bond.<sup>2,25,43</sup> To the group of polyanionic compounds we count

for example the olivine structured materials  $\text{LiMPO}_4$  ( $M = \text{Fe}, \text{Mn}$ ), the vanadium phosphate compounds  $\text{Li}_3\text{V}_2(\text{PO}_4)_3$  and  $\text{LiVOPO}_4$ , the fluoro-phosphates and sulphates  $\text{Li}_2\text{MPO}_4\text{F}$  ( $M = \text{Fe}, \text{V}$ ) and  $\text{LiMSO}_4\text{F}$  ( $M = \text{Fe}, \text{Mn}$ ) and the orthosilicates  $\text{Li}_2\text{MSiO}_4$  ( $M = \text{Fe}, \text{Mn}, \text{Co}$ ).<sup>13,15,16,44-47</sup>

Since its first description as potential cathode in 1997,  $\text{LiFePO}_4$  (LFP) in particular has gained a lot of attention.<sup>13</sup> It consists of abundant elements and occurs as the mineral triphylite, which makes it environmentally benign. The crystal structure of LFP is shown in Figure 2.4. It adopts the olivine structure consisting of a distorted hexagonal close-packed (hcp) oxygen lattice where 1/8 of the tetrahedral voids are occupied by P and 1/2 of the octahedral voids are occupied by Fe. The second half of the octahedral voids are occupied by Li, resulting in a channel like structure in the b-direction.<sup>13</sup>

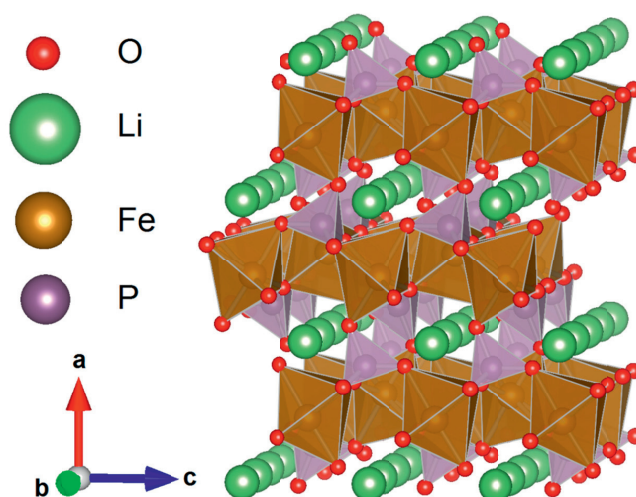


Figure 2.4: Crystal structure of LFP showing the one dimensional Li diffusion channels along the b-axis<sup>48</sup> illustrated with VESTA.

LFP has a theoretical capacity of  $170 \text{ mAhg}^{-1}$  and a flat intercalation/deintercalation profile at 3.5 V. The flat profile indicates that the reaction proceeds by the motion of a two phase interface according to a shrinking core model. The two end members,  $\text{FePO}_4$  and  $\text{LiFePO}_4$ , both crystallise in the orthorhombic space group  $Pnma$  and offer a difference in unit cell volume of 6.8%.<sup>13,49</sup> Studies revealed the existence of two solid solutions,  $\text{Li}_\alpha\text{FePO}_4$  and  $\text{Li}_{1-\beta}\text{FePO}_4$ , outside the miscibility gap at room temperature. Furthermore, the values for  $\alpha$  and  $\beta$  at the mono-phase/bi-phase boundary show an inversely proportional dependence on particle size.<sup>49,50</sup> The flat voltage profile makes it difficult to monitor the state of charge of a LFP Li-ion battery. In comparison, the layered oxides all offer a slightly sloping voltage profile allowing direct monitoring of the state of charge.<sup>5,51</sup>

LFP is compatible with common electrolyte systems and stable against over-charge. However, the disadvantages compared to the layered oxides are the low electronic and ionic conductivity values. The latter can be overcome by nanosizing and the former by the application of a conductive coating. This coating usually consists of a thin layer of carbon or the combination of carbon and conducting phosphides as a result of a carbothermal reduction.<sup>4,52,53</sup>

More recently, the orthosilicates with the general formula  $\text{Li}_2\text{MSiO}_4$  gained attention since they also consist of cheap and environmentally benign elements and could, due to a Li to transition metal ratio of 2:1, allow the reversible exchange of 2 Li ions per formula unit and thus in theory offer high capacities exceeding  $300 \text{ mAhg}^{-1}$ .<sup>15,16</sup> Additionally, the strong Si-O bonds in the orthosilicate framework ensure an increased thermal stability and give rise to potentially low cost, safe and environmentally benign cathode materials. The reported transition metals are Fe, Mn and Co where the former two have gained more attention since they are non-toxic and abundant. A more detailed description of the crystal structure, delithiation mechanism and research progress of the orthosilicate family is given in chapter 3.

## 2.4 Anode Materials

The negative electrode of a Li-ion battery is the anode during discharge. Requirements for anode materials are quite similar to those for cathode materials, but on the anode side the reversible reaction should preferably occur at low potentials vs.  $\text{Li}/\text{Li}^+$  to maintain a high potential against the cathode and thus enable high energy output. On the other hand the potential should not be too low, to not risk Li plating on the anode which could cause dendritic Li growth resulting in failure of the cell.<sup>2</sup> Since most anodes operate well outside the stability limit of commercial electrolytes, the

formation of a stable solid electrolyte interphase (SEI) to prevent further electrolyte decomposition is yet another majorly important requirement.<sup>5,8,54,55</sup> Since the first commercialisation of the Li-ion battery concept, carbonaceous materials have been exclusively used as the anode. In the first Li-ion batteries, petroleum coke was used as carbon anode, while later generations have been equipped with graphite materials exploiting the theoretical capacity of  $372 \text{ mAhg}^{-1}(\text{LiC}_6)$ .<sup>2,3,9</sup> The main problem with carbonaceous materials is the large irreversible capacity loss during the first cycle caused by formation of the SEI. A lot of research is on-going in order to replace graphite as the anode material.

Alternative anode materials can be divided into three main groups with respect to the reaction mechanism. The first group is intercalation host materials. This group contains carbonaceous materials like porous carbons, carbon nanotubes and graphene, where the latter two exceed the capacity of graphite by far with theoretical capacities over  $1000 \text{ mAhg}^{-1}$ , allowing a Li/C ratio of 1:2 instead of 1:6 in graphite.<sup>56,57</sup> Unfortunately, these materials suffer from high voltage hysteresis and high irreversible losses during cycling.<sup>54</sup> Anatase  $\text{TiO}_2$  and  $\text{Li}_4\text{Ti}_5\text{O}_{12}$  also belong to the group of intercalation host materials. The latter especially gained interest due to a stable intercalation/deintercalation profile at 1.55 V vs.  $\text{Li}/\text{Li}^+$ , eliminating the danger of Li plating and SEI problems.<sup>58</sup> The theoretical capacity of this spinel structure is  $175 \text{ mAhg}^{-1}$ , which is rather low compared to other anode materials, and the high potential would reduce the energy output of a Li-ion battery.<sup>8,54</sup>

The second group contains alloy forming compounds, for example Si, Ge, Sn, Bi and  $\text{SnO}_2$ , which react with Li in an alloying/dealloying manner. Group IV elements are especially interesting since they form high Li content alloy phases with Li/M ratios exceeding 4:1, thus delivering very high specific capacities dependent on the molar mass of the specific alloy.<sup>59</sup> Since Si is the lightest element in this series it offers the highest theoretical capacity of about  $4200 \text{ mAh g}^{-1}$ .<sup>60</sup> The major problem with alloy anodes is the immense volume change of up to 400% during cycling. This causes fracturing of the anode and loss of contact to the conducting additives and the current collector, which yields severe capacity fading and irreversible losses.<sup>54,61–63</sup> Additionally, the extremely reactive lithiated alloy tends to self-discharge.<sup>64</sup> However, Si/C nanocomposites have shown progress and potential as anode materials, since the nanoarchitectures can withstand the volume expansion better than larger particles and the addition of carbon not only promotes electronic conductivity but also formation of a stable SEI film.<sup>6</sup> According to a statement by U. Wang, Tesla Motors incorporates small amounts of Si in their newest battery systems.<sup>65</sup>

The third group of potential anode materials consists of conversion materials based on transition metal chalcogenides and pnictogenides of the general formula  $M_xA_y$  where  $M = \text{Mn, Fe, Co, Ni, Cu}$  and  $A = \text{O, S, N, P}$ . These undergo conversion reactions with Li ions where the transition metal gets reduced and the corresponding  $\text{Li}_zA$  compound is formed. Since the number of electrons per transition metal that partakes in this reaction is high, conversion compounds can reach high specific capacities. This makes conversion materials like  $\text{Fe}_2\text{O}_3$  interesting, but issues with severe capacity fading and large polarisations must be solved before commercialisation.<sup>54</sup>

## 2.5 Electrode additives

A good contact allowing electron transfer from the electrode to the current collector and thus to the external circuit needs to be guaranteed in every battery. In Li-ion batteries, this is done by a conductive binder, which is polyvinylidene fluoride (PVDF) in most cases. Unfortunately, the choice of solvents for this polymer is limited, and carcinogenic N-methyl-2-pyrrolidone (NMP) is most often used.<sup>12,66</sup> Next to the binder material usually another carbonaceous material is added as conductivity enhancer on both electrode sides. This is especially important for polyanionic compounds which offer low intrinsic electronic conductivity values.<sup>12,67</sup> Figure 2.5 shows different approaches to the incorporation of conductive carbon to a cathode material.<sup>67</sup> Part a) illustrates the physical mixture of conductive carbon black, graphite, a binder and a cathode material. In part b) the additive-cathode blend is cast on a carbon coated current collector to optimise the contact and part c) shows a carbon coated  $\text{LiFePO}_4$  particle.

A carbon coating is the most common way to increase the conductivity of orthophosphates and orthosilicates. Dominko *et al.* found a minimum of 1.5-2 wt. % carbon residue was needed to form this coating on titania particles, but this value should be highly dependent on the particle size and the density of the material.<sup>4,19,68</sup> Nonetheless, a conductive carbon additive needs to be physically blended in to guarantee an overall conductive matrix.<sup>4,6,14,19</sup>

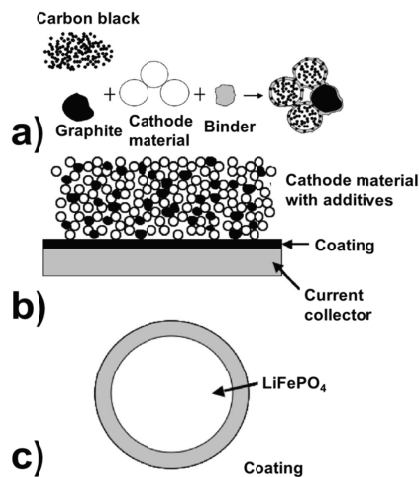


Figure 2.5: Possible incorporation means of conductive carbon additives: a) physical mixture, b) coated current collector, c) particle coating.<sup>67</sup>

## 2.6 Current collectors

Current collectors for Li-ion batteries must be good electronic conductors and collect and direct the flow of electrons towards the external circuit with minimal losses. Furthermore, the current collector must be stable under high operating voltages and in the organic electrolyte. In commercial Li-ion batteries, aluminium is the material of choice for the cathode side while copper is used on the anode side. Al is stable towards high oxidising potentials due to the formation of an  $\text{Al}_2\text{O}_3$  passivation layer. When in contact with alkyl solvents and  $\text{LiPF}_6$  an  $\text{AlF}_3$  layer also forms. Al cannot, however, be used on the anode side since a potential close to 0 V vs.  $\text{Li/Li}^+$  will cause the formation of a Li Al alloy.<sup>69,70</sup>

Cu, on the other hand, is stable at low potentials, and cyclic voltammetry experiments by Myung *et al.* showed no cathodic peaks from 1.5 to 0 V vs.  $\text{Li/Li}^+$ . If the potential is increased, a large anodic peak occurs at 3.3 V vs.  $\text{Li/Li}^+$ , caused by oxidation and dissolution of Cu ions.<sup>69</sup> This makes Cu the material of choice for the anode side but prohibits its use as cathode current collector. Other possible current collectors that have been investigated are e.g. Fe, Cr, Ti, Ni and stainless steel.<sup>69,70</sup>

## 2.7 Electrolytes

Research on different types of electrolytes for Li-ion batteries is a broad scientific field and includes research areas within solid inorganic electrolytes, polymeric solid electrolytes, ionic liquids and organic electrolytes. To give a detailed description of all these different systems is beyond the scope of this chapter, thus focus will be given to conventional Li salts dissolved in organic electrolytes. Thorough reviews by K. Xu are recommended for the interested reader.<sup>71,72</sup>

The high reactivity of Li and the large potential window of a Li-ion battery prohibit the use of proton based electrolytes. The electrolyte solvent has to fulfil a number of requirements. It has to readily dissolve the inorganic Li salt in satisfying concentrations, thus offering a high dielectric constant (high polarity). At the same time, the viscosity of the solvent has to be low to allow facile ion transport. It must be inert in a high potential window and should not react with the charged surfaces of the electrodes. The temperature window in which the solvent remains liquid should be high and hence the solvent should have a low melting point ( $T_m$ ) and a high boiling point ( $T_b$ ). Additionally, a high flame point ( $T_f$ ) is required for safe operation. To date, there has been no single solvent identified which fulfils all these requirements and so conventional solvents consist of a mixture of cyclic and linear aliphatic carbonates or esters.<sup>73</sup> An overview of carbonate based solvent molecules including the most important properties is given in Figure 2.6.

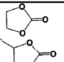
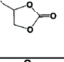
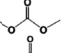
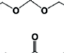
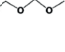
	Solvent	Structure	M. Wt	$T_m$ / °C	$T_b$ / °C	$\eta$ /cP	$\epsilon$	Dipole	$T_f$ / °C	$d$ /gm <sup>-3</sup> , 25 °C
						25 °C	25 °C	Moment/debye		
Cyclic carbonates	Ethylene (EC) carbonate		88	36.4	248	1.90, (40 °C)	89.78	4.61	150	1.321
	Propylene (PC) carbonate		102	-48.8	242	2.53	64.92	4.81	132	1.200
Linear carbonates	Dimethyl (DMC) carbonate		90	4.6	91	0.59 (20 °C)	3.107	0.76	18	1.063
	Diethyl (DEC) carbonate		118	-74.3 <sup>a</sup>	126	0.75	2.805	0.96	31	0.969
	Ethyl methyl carbonate (EMC)		104	-53	110	0.65	2.958	0.89		1.006

Figure 2.6: Overview of organic solvents for Li-ion battery electrolytes, including the parameters of importance, adapted and altered from reference.<sup>73</sup>

As seen from Figure 2.6, the polar cyclic carbonates propylene carbonate (PC) and ethylene carbonate (EC) have high viscosity values. Accordingly, they need to be mixed with a low viscosity and low melting point compound like dimethyl carbonate (DMC), ethyl methyl carbonate (EMC) or diethyl carbonate (DEC) to guarantee fluidity and hence easy ion transport. Earlier, research was focused on PC based electrolytes, since the similar compound EC has an extremely high  $T_m$ . Unfortunately, PC cannot be used in Li-ion batteries equipped with carbonaceous anode materials since PC does not form a stable SEI film on the anode but rather co-intercalates, causing exfoliation of the graphene layers and disintegration of the anode. EC, on the other hand, forms a stable SEI and is hence used as a solvent, even though the high  $T_m$  is unfavourable for low temperature applications.<sup>73,74</sup> The cyclic carbonates are also the preferred species in the first solvation sheet of Li ions, interacting with Li through the carbonyl oxygen.<sup>72,75</sup> Li salt concentrations are commonly around 1 M, with the most commonly used Li salt being  $\text{LiPF}_6$ , because of its overall compromising properties with respect to the ionic mobility and dissociation constant. Alternative Li salts are  $\text{LiClO}_4$ ,  $\text{LiBF}_4$ ,  $\text{LiAsF}_6$ ,  $\text{LiTFSI}$  (bis(trifluoromethane)sulfonimide Li) and  $\text{LiBOB}$  (Li bis(oxalato)borate).<sup>72,73</sup>

None of the known electrolyte compositions are thermodynamically stable in the operation voltage window, but the stability limit is kinetically controlled under the presumption that passivation films prevent contact with the severely reducing or oxidising electrode surfaces.<sup>8,73</sup> Figure 2.7 shows the cyclic voltammetry profile of a C/ $\text{LiCoO}_2$  Li-ion battery and of the pure EC–DMC  $\text{LiPF}_6$  electrolyte where the counter electrode is amorphous Super P carbon against Li metal. The positive electrode works within the stability window of the electrolyte, and the onset of decomposition is at about 4.5 V vs.  $\text{Li/Li}^+$ . At potential of about 5 V the slope of the anodic current density is strongly increasing, reflecting the rapid oxidative decomposition of the electrolyte at these potentials. On the other side, the negative electrode works outside the stability window, stressing the major importance of a passivation layer preventing the reductive electrolyte decomposition.



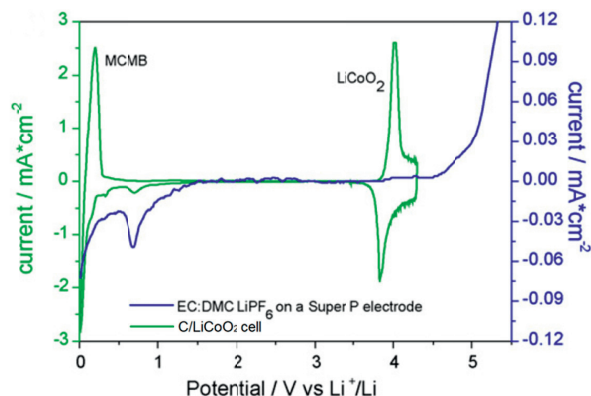


Figure 2.7: CV profile of EC–DMC,  $\text{LiPF}_6$  electrolyte (blue) and a C/ $\text{LiCoO}_2$  cell (green) from.<sup>8</sup>

As a result of the vast requirements towards the electrolyte systems, there are several additives available to enhance certain properties. For example, vinylene carbonate (VC) is often added as an interphase formation aid. Other additives enhance the stability of  $\text{LiPF}_6$  which suffers from a labile P-F bond that would otherwise form the highly reactive  $\text{PF}_5$  species and  $\text{LiF}$ . It has to be kept in mind that additives may enhance some properties but could introduce new shortcomings in such a complex system. An informative review about electrolyte additives by S. S Zhang is recommended.<sup>76</sup>

Throughout this study, the electrolytes used were 1 M  $\text{LiPF}_6$  in EC/DEC 3:7 by volume and later 1:1 by volume due to availability of ready mixed electrolytes from chemical suppliers. Optimisation studies of the electrolyte are beyond the scope of this thesis and were omitted.

## 2.8 Electrode interphases

The arise of a protective interphase on Li metal in contact with an aprotic electrolyte was first reported by Peled in 1979.<sup>77</sup> He also termed this interphase the solid electrolyte interphase (SEI) which is the common terminology today for the anode interphase. Contrary to Li metal where the interphase forms instantaneously when the metal is in contact with the electrolyte, the SEI forms on carbonaceous material during the first cathodic polarisation. The discovery by Fong *et al.* that EC based electrolytes form a stable film on graphite was the breakthrough both for EC based elec-

trolites and graphitic carbon anodes, since formerly used PC based electrolytes caused PC co-intercalation, exfoliation of the van der Waals bound graphene layers and thus disintegration of the graphite material.<sup>73,74</sup> While the exact mechanism of SEI formation on carbonaceous materials is controversially discussed e.g. by Besenhard *et al.* and Peled *et al.*, the chemical nature of the SEI is well known.<sup>78–80</sup> Recent insights have shown that the cathodic reduction reactions of the electrolyte lead to a multi-layered film. Figure 2.8 sketches the SEI on a graphite particle.

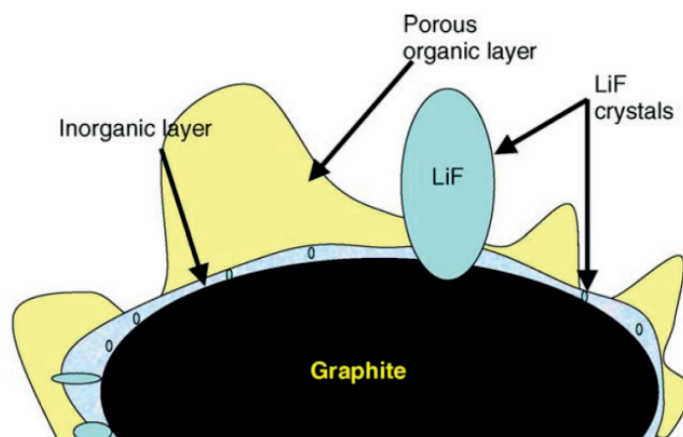


Figure 2.8: Multi-layered SEI on a graphite particle.<sup>81</sup>

The dense innermost inorganic layer mainly consists of  $\text{Li}_2\text{CO}_3$  and  $\text{LiF}$ .  $\text{Li}_2\text{CO}_3$  is primarily formed by the reductive decomposition EC, while  $\text{LiF}$  is a product of the degradation of fluorine containing polyanions. Furthermore, reactions with contaminants can cause formation of both compounds.<sup>76,81–84</sup>

The porous organic layer mainly consists of lithium alkyl carbonates and lithium semi carbonates. These compounds are formed by a two electron reduction or by a one electron reduction with subsequent radical termination of the cyclic and linear carbonates of the electrolyte solution.<sup>85–87</sup>

The formation of these layers consumes Li ions and leads to an irreversible capacity loss during the first cycle. The SEI must be an ionic conductor but at the same time an electronic insulator, in order to act as barrier for further electrolyte decomposition while allowing Li ion migration into the electrode.<sup>73</sup> Furthermore, it was shown that

the SEI shows dynamic behaviour, meaning that its composition is altered in the delithiated and lithiated state and that the amount of LiF grows during cycling of a Li-ion battery.<sup>88</sup> SEI growth and an increased resistance caused by increased amounts of inorganic compounds like LiF limit the lifetime of a Li-ion battery.

The positive electrode exhibits an interphase or surface layer which should, analogous to the SEI, allow Li migration while building a barrier for further electrolyte decomposition.<sup>73</sup> Many oxide materials tend to build a carbonate surface film, making it hard to prevent  $\text{Li}_2\text{CO}_3$  formation. Usually this layer erodes in contact with acidic electrolyte salts.<sup>73</sup> Andersson *et al.* reported LiF surface layers on pristine  $\text{LiNi}_{0.8}\text{Co}_{0.2}\text{O}_2$  electrode laminates originating from dehydrofluorination reactions, which are catalysed by alkali impurities in the solvent (1-methyl-2-pyrrolidone).<sup>89</sup> They further found polycarbonates, LiF,  $\text{Li}_x\text{PF}_y$  and  $\text{Li}_x\text{PF}_y\text{O}_z$  on the cathode surface of calendar-life tested batteries, originating from  $\text{LiPF}_6$  decomposition and hydrolysis reactions.<sup>89</sup> Thomas and co-workers reported similar interphase components for  $\text{LiFePO}_4$  and  $\text{Li}_2\text{FeSiO}_4$  cathodes using  $\text{LiPF}_6$  as the electrolyte salt. However, they did not find any evidence for polycarbonates on either material. The same group further investigated the surface layer of  $\text{Li}_2\text{FeSiO}_4$  using a LiTFSI electrolyte, showing a completely different interphase. Polyethylene oxide polymer, resultant from decomposition reactions of the cyclic carbonate, with embedded LiTFSI particles and minor traces of  $\text{Li}_2\text{CO}_3$  are the main components. The authors also found that the thickness of this interphase is highly dependent on the state of charge while the interphase from the  $\text{LiPF}_6$  electrolyte stayed unchanged at different states of charge.<sup>90-92</sup> These thorough studies clarify the dependence of the interphase not only on the nature of the electrode material but also on the electrolyte used.

## 2.9 Separator

The separator in a Li-ion battery must provide a physical barrier to prevent a short circuit between the electrodes. It has to be inert towards the electrolyte and dimensionally stable within the operating temperature range of the battery and beyond. At the same time it must be highly permeable to the solvent and solvated electrolyte ions to offer a low electrochemical resistance. The most common separators for liquid electrolyte Li-ion batteries are porous polyolefines like PE and PP or sandwich structures of both.<sup>93</sup> Figure 2.9 shows an SEM micrograph of a Celgard 2400 monolayer PP separator, used in this study, with a thickness of 25  $\mu\text{m}$  and a porosity of 40%.

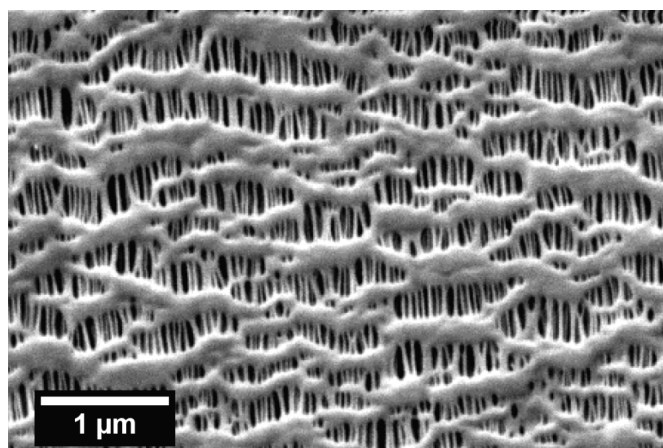


Figure 2.9: Celgard 2400 monolayer PP separator.<sup>93</sup>



## 3. Lithium Transition Metal Orthosilicates ( $\text{Li}_2\text{MSiO}_4$ )

### 3.1 General

This chapter describes the lithium transition metal orthosilicates. In the first part of this chapter, an overview of physical, chemical and electrochemical properties is given. The second part discusses the effects of cationic substitutions and summarises synthesis methods and morphological aspects of nanostructured lithium transition metal orthosilicates.

### 3.2 Crystal structure and polymorphism

The  $\text{Li}_2\text{MSiO}_4$  ( $M = \text{Mn, Fe, Co}$ ) compounds belong to the tetrahedral structures and exhibit rich polymorphism. In all cases the structure consists of a distorted hexagonal array of oxygen atoms (tetragonal packing) with half the tetrahedral sites occupied by cations. Different ordering of the cations and a variety of structural distortions give rise to many polymorphs. The polymorphs can be divided into two groups. In the first group all tetrahedra point in the same direction, adopting  $\beta$   $\text{Li}_3\text{PO}_4$  structures where the connectivity of all tetrahedra is accomplished solely by corner-sharing. The second group adopts  $\gamma$   $\text{Li}_3\text{PO}_4$  structures where tetrahedra are arranged in groups of three, with the central tetrahedra pointing in the opposite direction causing distortion and edge-sharing between tetrahedra. If both  $\beta$  and  $\gamma$  polymorphs exist for a given transition metal, the latter is the high temperature form.<sup>19</sup> Figure 3.1 shows the three known  $\beta$  polymorphs, namely  $\beta_{\text{I}}$ , and  $\beta_{\text{II}}$  and inverse  $\beta_{\text{II}}$ . All three crystallise in an orthorhombic system. The space group of  $\beta_{\text{I}}$   $\text{Li}_2\text{MSiO}_4$  is  $Pbn2_1$  while the  $\beta_{\text{II}}$  polymorphs have  $Pmn2_1$  symmetry.

The difference between the  $\beta$  polymorphs is the connectivity of the tetrahedra. In the  $\beta_{\text{I}}$  structure,  $\text{LiO}_4\text{-MO}_4$  and  $\text{LiO}_4\text{-SiO}_4$  build parallel alternating chains in the  $a$ -direction and the structure can be seen as a framework. The  $\beta_{\text{II}}$  polymorph, however,

is a layered structure with chains of  $\text{LiO}_4$  tetrahedra and chains of alternating  $\text{MO}_4$ - $\text{SiO}_4$  tetrahedra along the a-axis. A special case is  $\text{Li}_2\text{CoSiO}_4$ , which can be synthesised in the inverse form of the  $\beta_{\text{II}}$  polymorph.<sup>94</sup> In this case, half of the Li occupies the transition metal-site, and Co and the remaining Li ions occupy the Li-site.  $\text{Li}_2\text{FeSiO}_4$  shows a similar behaviour upon cycling which will be discussed in the next section. The high temperature  $\gamma$  polymorphs are shown in Figure 3.2.

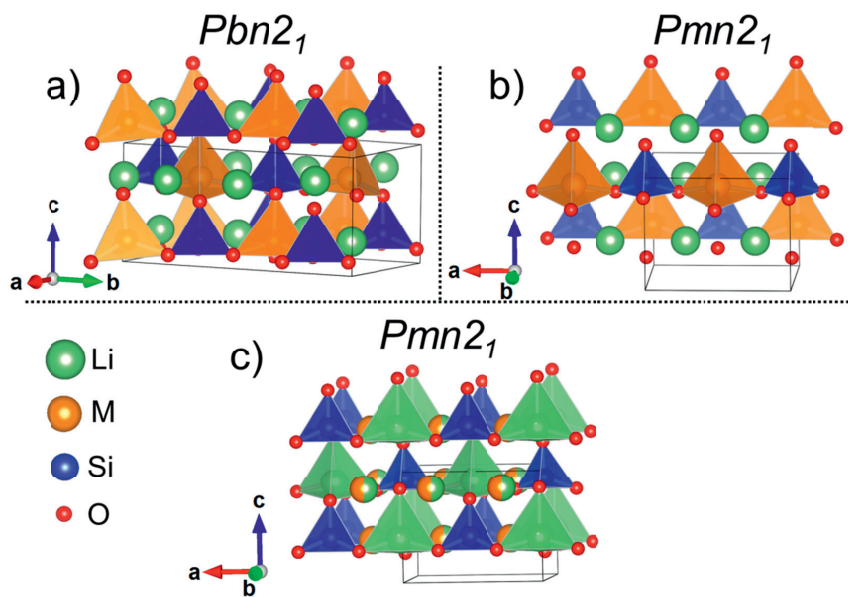


Figure 3.1: Crystal structures of  $\beta$   $\text{Li}_2\text{MSiO}_4$  a)  $\beta_{\text{I}}$   $\text{Li}_2\text{MSiO}_4$  ( $Pbn2_1$ )<sup>95</sup>, b)  $\beta_{\text{II}}$   $\text{Li}_2\text{MSiO}_4$  ( $Pmn2_1$ )<sup>96</sup> - this work and c) inverse  $\beta_{\text{II}}$   $\text{Li}_2\text{MSiO}_4$  ( $Pmn2_1$ )<sup>94</sup> illustrated with VESTA.

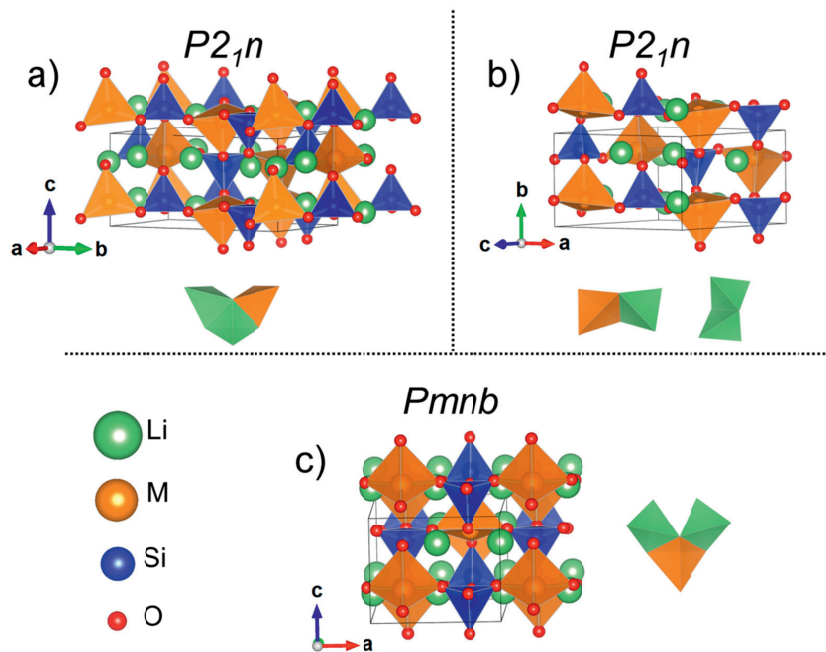


Figure 3.2: Crystal structures and edge-sharing tetrahedra of  $\gamma$   $\text{Li}_2\text{MSiO}_4$  a)  $\gamma_0$   $\text{Li}_2\text{MSiO}_4$  ( $P2_1n$ )<sup>94</sup>, b)  $\gamma_s$   $\text{Li}_2\text{MSiO}_4$  ( $P2_1n$ )<sup>20 - this work</sup> and c)  $\gamma_{II}$   $\text{Li}_2\text{MSiO}_4$  ( $Pmnb$ )<sup>97</sup> illustrated with VESTA.

The  $\gamma_0$  polymorph is a framework structure which is characterised by an arrangement of three tetrahedra, of which the central one points in the opposite direction resulting in edge-sharing in a sequence  $\text{LiO}_4\text{-LiO}_4\text{-MO}_4$ . The  $\gamma_s$  polymorph is a layered structure, similar to the  $\beta_{II}$  in connectivity of the tetrahedra but half of the tetrahedra point in the opposite direction in a 2-2 sequence, resulting in edge sharing between two  $\text{LiO}_4$  and  $\text{MO}_4\text{-LiO}_4$  units. In the  $\gamma_{II}$  polymorph, tetrahedra also point in opposite directions but in a sequence of 1-1, resulting in a layered structure where edge-sharing between a central  $\text{MO}_4$  unit with two  $\text{LiO}_4$  units occurs. In the case of  $\text{Li}_2\text{MnSiO}_4$ , another metastable polymorph was recently discovered by ion exchange starting from  $\text{Na}_2\text{MnSiO}_4$ . This framework structure has  $P_n$  symmetry and is illustrated in Figure 3.3.<sup>98</sup>



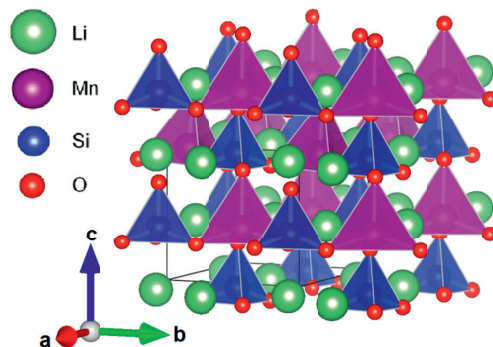


Figure 3.3: Crystal structures of metastable  $P_n \text{Li}_2\text{MnSiO}_4$ <sup>98</sup> illustrated with VESTA.

An overview of which polymorphs have been synthesised with a given transition metal (Mn, Fe and Co) is given in Table 3.1. Included is the synthesis method, heat treatment temperature and dwell time. Purely theoretical reports, which are available for  $\text{Li}_2\text{NiSiO}_4$  are not included in this table.<sup>99–101</sup> To the author's knowledge there is only one experimental study which claims the successful preparation of  $\text{Li}_2\text{NiSiO}_4$ , but the XRD data does not show any similarity with any other  $\text{Li}_2\text{MSiO}_4$  compound, nor was any refinement performed and the results are omitted from the table.<sup>102</sup>

Table 3.1: Overview of synthesised  $\text{Li}_2\text{MSiO}_4$  polymorphs.

Polymorph	Compound	Synthesis method	Annealing temperature [°C] and dwell time in brackets [h]	Reference
$\beta_{\text{I}}$ $Pbn2_1$	$\text{Li}_2\text{CoSiO}_4$	Crystal growth	not given	Yamaguchi <i>et al.</i> <sup>95</sup>
		Hydrothermal	700 (2)	Lyness <i>et al.</i> <sup>103</sup>
$\beta_{\text{II}}$ $Pmn2_1$	$\text{Li}_2\text{MnSiO}_4$	Modified Pechini sol-gel	700 (1-96)	Dominko <i>et al.</i> <sup>16,104</sup>
	$\text{Li}_2\text{FeSiO}_4$	Hydrothermal	150 (72)	Dominko <i>et al.</i> <sup>16</sup>
Inverse- $\beta_{\text{II}}$ $Pmn2_1$	$\text{Li}_2\text{CoSiO}_4$	Hydrothermal	150 (72)	Lyness <i>et al.</i> <sup>103</sup>
	$\text{Li}_2\text{MnSiO}_4$	Ion exchange		Duncan <i>et al.</i> <sup>98</sup>
$\beta$ $P_n$				
$\gamma_0$ $P2_1n$	$\text{Li}_2\text{MnSiO}_4$	Solid State	1150	Politaev <i>et al.</i> <sup>105</sup>
	$\text{Li}_2\text{CoSiO}_4$	Hydrothermal	1100 (2) quenched	Lyness <i>et al.</i> <sup>103</sup>
$\gamma_s$ $P2_1n$	* $\text{Li}_2\text{FeSiO}_4$	Solid-state	750 (24)	Nytén <i>et al.</i> <sup>15</sup>
	$\text{Li}_2\text{FeSiO}_4$	Solid-state	800 (not given)	Nishimura <i>et al.</i> <sup>106</sup>
	$\text{Li}_2\text{FeSiO}_4$	Hydrothermal	700 (not given)	Boulineau <i>et al.</i> <sup>107</sup>
$\gamma_{\text{II}}$ $Pmnb$	$\text{Li}_2\text{FeSiO}_4$	Solid-state	900 (168) quenched	Sirisopanaporn <i>et al.</i> <sup>97</sup>
	$\text{Li}_2\text{MnSiO}_4$	Solid-state	900 (10)	Gummow <i>et al.</i> <sup>108</sup>

\*The first group who synthesised and characterised  $\text{Li}_2\text{FeSiO}_4$  suggested the symmetry to be  $Pmn2_1$

### 3.3 Lithium diffusion pathways

In the following section the diffusion pathways of Li ions in  $\text{Li}_2\text{MSiO}_4$  ( $M = \text{Mn}, \text{Fe}$ ) are summarised. The Co compound is disregarded since it is of less importance as an alternative cathode material due to cost issues and toxicity of Co.

Table 3.2 comprises measured Li diffusion coefficients of  $\text{Li}_2\text{MSiO}_4$  ( $M = \text{Mn}, \text{Fe}$ ) electrodes, including the polymorph and the method of determination. For  $\text{Li}_2\text{FeSiO}_4$ , data suggests the diffusion coefficient to be in the range of  $10^{-13} \text{ cm}^2 \text{ s}^{-1}$ . The data for  $\text{Li}_2\text{MnSiO}_4$  shows quite some discrepancy but suggests even lower values for Li diffusion. In general, the values of  $\text{Li}_2\text{FeSiO}_4$  are in the same range as the Li diffusion coefficient of  $\text{LiFePO}_4$ .<sup>109,110</sup> The Li diffusion pathways and calculated activation energies are discussed below.

Table 3.2: Li diffusion coefficients of  $\text{Li}_2\text{MSiO}_4$  (M = Mn, Fe) electrodes.

Compound	Polymorph	Method	$D_{\text{Li}}$ [ $\text{cm}^2 \text{s}^{-1}$ ]	Reference
$\text{Li}_2\text{MnSiO}_4$	$\beta_{\text{II}}$ $Pmn2_1$	AC Impedance	$3.4 \cdot 10^{-18}$	Swietoslawski <i>et al.</i> <sup>111</sup>
$\text{Li}_2\text{MnSiO}_4$	$\beta_{\text{II}}$ $Pmn2_1$	AC Impedance	$1.47 \cdot 10^{-14}$	Hwang <i>et al.</i> <sup>112</sup>
$\text{Li}_2\text{FeSiO}_4$	$\gamma_{\text{s}}$ $P2_1n$	AC Impedance	$1.38 \cdot 10^{-12}$	Li <i>et al.</i> <sup>113</sup>
$\text{Li}_2\text{FeSiO}_4$	$\gamma_{\text{s}}$ $P2_1n$	Cyclic voltammetry	$7.52 \cdot 10^{-13}$ - $1.46 \cdot 10^{-12}$	Zheng <i>et al.</i> <sup>114</sup>
$\text{Li}_2\text{FeSiO}_4$	$\gamma_{\text{s}}$ $P2_1n$	AC Impedance	$4.5 \cdot 10^{-14}$ - $5.37 \cdot 10^{-13}$	Zhang <i>et al.</i> <sup>115,116</sup>

 $\text{Li}_2\text{FeSiO}_4$ 

Most conventional synthesis methods lead to the layered  $\gamma_{\text{s}}$  polymorph. However,  $\text{Li}_2\text{FeSiO}_4$  undergoes structural changes during electrochemical cycling. After removal of half of the Li atoms from the structure, and thus complete oxidation of  $\text{Fe}^{2+}$  to  $\text{Fe}^{3+}$ , the system relaxes through a reorganisation of the tetrahedral orientation and Li/Fe site reversal with Fe occupying the empty half of the Li-sites. The delithiated reversed structure was calculated by DFT to offer a stabilisation of  $\sim 0.25$  eV per formula unit against the delithiated non-reversed structure. After relithiation the reversed structure remains, with the inserted Li ions in the empty former Fe-sites. The former Li-sites are now occupied by Li ions alternating with Fe ions. <sup>117,118</sup> A long-range order between the alternating  $\text{LiO}_4$ - $\text{FeO}_4$  units has not been detected, but calculations suggest a high degree of correlation. <sup>20,117</sup> The result is two crystallographically distinct Li-sites, Li1 and Li2. The former Fe-sites are exclusively occupied by Li1. Li2 and Fe share the former Li-site. The structure is now a 3D-framework with inverse  $\beta_{\text{II}}$  structure, similar to  $\text{Li}_2\text{CoSiO}_4$ . The structure and Li pathways are shown in Figure 3.4.

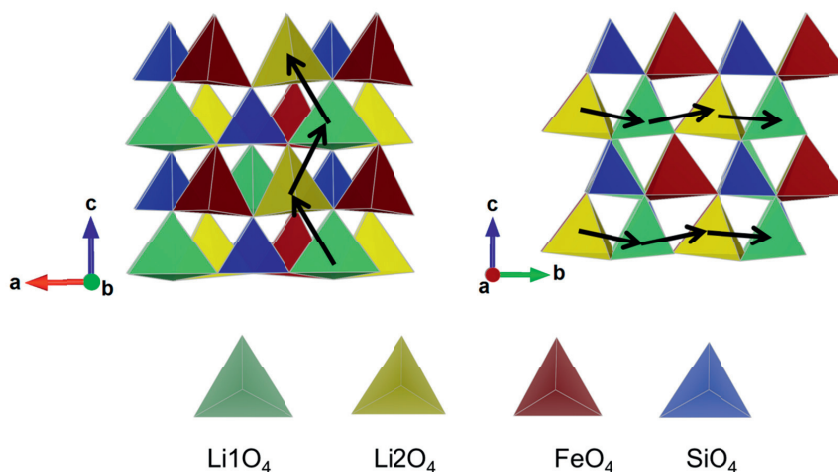


Figure 3.4: Inverse  $\beta_{II}$  cyclized structure of  $\text{Li}_2\text{FeSiO}_4$  with the two possible Li diffusion pathways in c and b-directions. Redrawn from <sup>20</sup> using VESTA.

There are two possible pathways for Li diffusion. Armstrong *et al.* calculated the energy barriers for Li diffusion in the cyclized structure and found the lowest activation energy for Li diffusion to be 0.91 eV in the c-direction. This involves a zigzag like path as shown in Figure 3.4. The second path is along the b-axis and has an activation energy of 1.55 eV. <sup>20</sup> The reported energy barrier is higher than for other Li-ion cathode compounds ( $\text{LiFePO}_4 \sim 0.6$  eV), implying a low rate capability for the system.

#### $\text{Li}_2\text{MnSiO}_4$

The most commonly reported polymorph of  $\text{Li}_2\text{MnSiO}_4$  is orthorhombic  $\beta_{II}$ . This structure has layers occupied solely by Li, which gives rise to two dimensional Li diffusion. Figure 3.5 shows the two possible pathways for Li diffusion in the two dimensional layer.

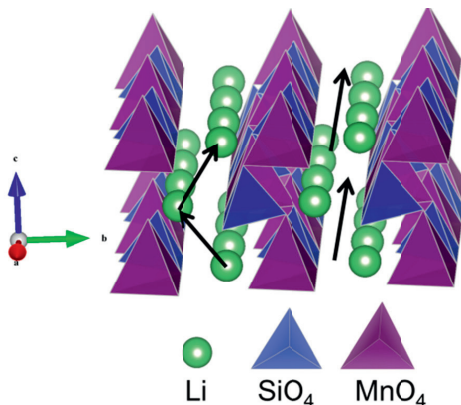


Figure 3.5: Possible Li diffusion pathways in  $\beta_{II}$   $\text{Li}_2\text{MnSiO}_4$  ( $Pmn2_1$ ).

The zigzag trajectory path along the  $c$ -direction was calculated to have the lowest activation energy in the range of 0.95-1.03 eV whilst the straight path along the  $a$ -direction has an activation energy of 1.13-1.29 eV.<sup>21,119</sup>

However, upon delithiation  $\text{Mn}^{2+}$  is oxidised to the highly Jahn-Teller active  $\text{Mn}^{3+}$ .<sup>120,121</sup> Both  $\text{Mn}^{3+}$  (Ar  $3d^4$ ) and, at severe delithiation,  $\text{Mn}^{4+}$  (Ar  $3d^3$ ) have electrons in the high energy  $t_2$  orbitals in the tetrahedral environment. Accordingly, distortions and finally a change in coordination stabilise the system.  $\text{Mn}^{3+}$  has the highest crystal field stabilisation energy in square pyramidal geometry and  $\text{Mn}^{4+}$  in octahedral geometry. A recent computational study by Saracibar *et al.* determined that the system distorts upon delithiation by changes in the Mn coordination accompanied with a loss of the orthogonal shape.<sup>122</sup> Larsson *et al.*<sup>23</sup> also reported severe distortions of the Mn units and both computational studies are supported by experimental studies reporting capacity fade and loss of crystallinity upon cycling.<sup>18,123</sup>

### 3.4 Delithiation potentials

The potential at which delithiation occurs is dependent on the transition metal and its environment. As previously mentioned, the inductive effect of the  $\text{SiO}_4$  groups shifts the redox potential to higher voltages and thus makes the  $\text{M}^{2+}/\text{M}^{3+}$  redox couples of Mn and Fe interesting.

Furthermore, the different polymorphs of  $\text{Li}_2\text{MSiO}_4$  generate different environments for the  $\text{MO}_4$  tetrahedra. While in  $\beta$  polymorphs only corner-sharing occurs,  $\text{MO}_4$  tetrahedra share edges in the  $\gamma$  polymorphs. This causes a reduced M-O bond length and thereby a higher covalency. This results in higher energy differences of the bonding and anti-bonding states, compared to the corner-sharing polymorph, and thus a lowered redox potential.<sup>124</sup> In the case of  $\text{Li}_2\text{FeSiO}_4$  the effect is only visible during the first few cycles since all polymorphs relax to the inverse  $\beta_{\text{II}}$  form. It is even more complicated for  $\text{Li}_2\text{MnSiO}_4$  due to the structural collapse. Additionally, overpotentials during the measurements caused by low conductivity, and hence a significant charge transfer resistance, make it hard to compare different studies. Figure 3.6 compares the deinsertion (delithiation) potentials of Mn and Fe from computational studies ( $\beta_{\text{II}}$  polymorphs)<sup>99,101</sup> and experiments.<sup>104,125,126</sup>

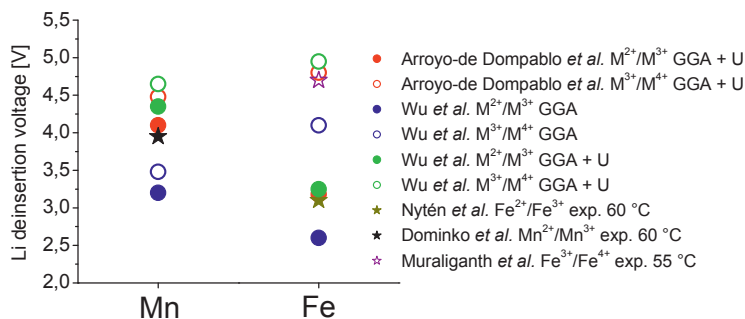


Figure 3.6: Comparison of delithiation potentials of  $\beta_{\text{II}}$   $\text{Li}_2\text{MSiO}_4$  from computational and experimental studies. DFT data from Arroyo-de Dompablo *et al.*<sup>99</sup> and Wu *et al.*<sup>101</sup> Experimental data from Nytén *et al.*<sup>125</sup> ( $\text{Li}_2\text{FeSiO}_4$ ), Muraliganth<sup>126</sup> ( $\text{Li}_2\text{FeSiO}_4$ ) and Dominko *et al.*<sup>104</sup> ( $\text{Li}_2\text{MnSiO}_4$ ) (All experiments carried out at elevated temperature).

In both cases the data modelled by the generalised gradient approximation + Dudarev method (GGA+U) approach is similar to the experimental data. Further, it is noteworthy that the experiments were carried out at elevated temperatures. The increased kinetics at higher temperatures reduces the overpotential and thus the deintercalation potentials are shifted to slightly lower voltages. The deinsertion and the insertion potentials are influenced by different factors, such as the conductivity of the material and the diffusion of Li ions which can lead to significant overpotentials both in the anodic direction upon delithiation and in the cathodic direction upon lithiation. The difference between the delithiation and lithiation potential is termed the polarisation and should preferably be small to obtain a high energy efficiency. As mentioned in the previous chapter, the stability of the electrolytes is limited to approximately 4.4-4.5 V, thus making it challenging to exploit the full potential of the  $\text{Li}_2\text{MSiO}_4$  compounds.

### 3.5 Electronic behaviour

Electronic conductivity is of major importance for an electrode material, to allow the redox processes to take place and to transport electrons to the current collectors. In  $\text{Li}_2\text{MSiO}_4$ , the connectivity of  $\text{MO}_4$  units is interrupted by  $\text{SiO}_4$  and  $\text{LiO}_4$  units. The calculated band gaps for  $\text{Li}_2\text{MnSiO}_4$  and  $\text{Li}_2\text{FeSiO}_4$  range from 3.4-4.2 and 3-3.3 eV, respectively.<sup>99,101,127</sup> Accordingly, the expected behaviour is semi-conducting to insulating. Dominko measured the electronic conductivity for both compounds and found values of  $3 \cdot 10^{-14} \text{ S cm}^{-1}$  for  $\text{Li}_2\text{MnSiO}_4$  and  $2 \cdot 10^{-12} \text{ S cm}^{-1}$  for  $\text{Li}_2\text{FeSiO}_4$  at 60 °C. At room temperature these values are expected to be two orders of magnitude lower, which led him to the conclusion that a conductive coating and a nanosized material is key to making both compounds work as an electrode material.<sup>18</sup> The same author also showed a conductivity increase from  $10^{-9} \text{ S cm}^{-1}$  to  $10^{-1} \text{ S cm}^{-1}$  for titania particles by introducing a thin carbon coating. Also highlighted was the importance of this carbon coating for low conductivity electrodes like phosphates and silicates.<sup>68</sup>

### 3.6 Cationic substitutions on the M or Si-site

As previously mentioned, properties like stability, conductivity and redox potential of  $\text{Li}_2\text{MSiO}_4$  are strongly dependent on the transition metal cation.  $\text{Li}_2\text{FeSiO}_4$  can deliver one Li per formula unit while sustaining a stable structure, while  $\text{Li}_2\text{MnSiO}_4$  gives rise to the possibility of a two-electron reaction at more moderate potentials than Fe. Accordingly, it is not surprising that researchers have tried to combine these properties by synthesising solid solutions of the general formula  $\text{Li}_2\text{Fe}_{1-x}\text{Mn}_x\text{SiO}_4$ . The resulting polymorph of such a solid solution is dependent on the synthesis conditions, such as temperature and the amount of each cation. Under conventional synthesis conditions ( $T = 600\text{-}700\text{ }^\circ\text{C}$ )  $\text{Li}_2\text{FeSiO}_4$  is present in  $\gamma_s$  and  $\text{Li}_2\text{MnSiO}_4$  in  $\beta_{\text{II}}$  polymorphs. Solid solutions thus often contain a mixture of these polymorphs.<sup>128</sup> An early computational study concluded that Fe substitution in  $\text{Li}_2\text{MnSiO}_4$  could stabilise the structure and that a composition of  $\text{Li}_2\text{Fe}_{0.5}\text{Mn}_{0.5}\text{SiO}_4$  should be capable of delivering more than one Li per formula unit whilst maintaining structural integrity.<sup>129</sup> On the contrary, a more recent study concluded that just 12.5 mol % Mn substitution into the structure would have a destabilising effect.<sup>23</sup> Additionally, experimental studies come to the conclusion that Mn substitution in  $\text{Li}_2\text{FeSiO}_4$  causes irreversible capacity fading, with clear trends visible in the slope of the capacity decay against the Mn concentration.<sup>18,130-132</sup>

Another strategy to stabilise the structure of  $\text{Li}_2\text{MnSiO}_4$  has been the introduction of inert diluents like  $\text{Mg}^{2+}$ . Gummow *et al.* synthesised a  $\gamma_0$  Mg substituted  $\text{Li}_2\text{MnSiO}_4$  but electrochemical cycling still resulted in a capacity fade.<sup>133</sup> Zhang *et al.* reported Cr substituted  $\text{Li}_2\text{MnSiO}_4$  nanofibres with enhanced capacity and capacity retention compared to a non-substituted sample and argue that increased unit cell dimensions stabilise the structure.<sup>134</sup> A recent computational study by Saracibar *et al.* concluded that Ni substitution could stabilise  $\text{Li}_2\text{MnSiO}_4$ , but their experiments with low Ni concentrations did not show any stabilising effect and they failed to synthesise  $\text{Li}_2\text{MnSiO}_4$  with Ni concentration higher than 20 mol %.<sup>122</sup> Another computational study suggested a mixed metal orthosilicate of the general formula  $\text{Li}_2\text{Fe}_{1-x-y}\text{Mn}_x\text{Ni}_y\text{SiO}_4$ , analogous to the mixed metal layered oxides, to have superior properties with respect to a stable reaction with more than one Li per formula unit.<sup>127,135</sup> Kuganathan *et al.* suggest Al substitution on the Si-site with excess Li on interstitial positions for charge compensation to increase the capacity of  $\text{Li}_2\text{MnSiO}_4$ .<sup>21</sup>

Another interesting approach is the incorporation of V into the structure of  $\text{Li}_2\text{MSiO}_4$ . V is known as a cathode material in the form of  $\text{V}_2\text{O}_5$ ,<sup>2,136</sup> and a recent computational study has shown up to 50 mol % V substitution in  $\text{Li}_2\text{FeSiO}_4$  to be



stable and to give rise to three additional redox couples.<sup>137</sup> V can be present in a divalent-to-pentavalent state with an accordingly decreasing ionic radius, which would also give rise to the possibility of substituting Si by V.<sup>138</sup> A computational study by Liivat and Thomas supports the possibility of low level ( $\leq 30$  mol %) substitution of V on the Si-site being beneficial in terms of conductivity and capacity by the  $\text{V}^{4+}/\text{V}^{5+}$  redox couple at potentials  $< 3$  V.<sup>139</sup> As the redox couple of the transition metal in polyanionic compounds is influenced by the polyanion group, the redox potential of V should show significant differences when it populates either the polyanionic or the cationic site. However, experimental studies of V doping in  $\text{Li}_2\text{FeSiO}_4$  show inconsistencies. A study by Hong *et al.* shows the appearance of V containing spinel phases at higher doping levels and a general decay of the electrochemical properties.<sup>140</sup> Zhang *et al.* substituted up to 7 mol % V on the Fe-site of  $\text{Li}_2\text{FeSiO}_4$  and found a strong increase of electrochemical properties for 5 mol % V substitution. They further show that almost all major  $\text{Li}_2\text{FeSiO}_4$  diffraction peaks disappear at higher V concentrations.<sup>141</sup> Hao *et al.* reported an increase in electrochemical performance when 10 mol % V is substituted on the Si-site of  $\text{Li}_2\text{FeSiO}_4$ .<sup>142</sup> No computational studies concerning V substitution in  $\text{Li}_2\text{MnSiO}_4$  are yet available. A broader experimental substitution study including up to 10 mol % V on either the Mn or Si-site of  $\text{Li}_2\text{MnSiO}_4$  by Deng *et al.* demonstrated an increased discharge capacity for 5 mol % V on both sites, but deterioration for 10 mol % V.<sup>143</sup> A recent study by Hwang *et al.* reports an increased Li diffusion coefficient for 5 and 10 mol % V incorporation on the Mn-site of  $\text{Li}_2\text{MnSiO}_4$  but no redox activity of V was detected, nor did it influence the stability.<sup>112</sup>

Other authors report positive effects of Co and Cr substitution in  $\text{Li}_2\text{FeSiO}_4$ .<sup>115,116</sup> The incorporation of Ni seems to be challenging. A study by Jaén *et al.* revealed an increase in  $\text{Li}_2\text{SiO}_3$  and a Fe-Ni alloy with increasing substitution level of Ni in  $\text{Li}_2\text{FeSiO}_4$ , suggesting a difficulty in keeping Ni in a divalent state under the synthesis conditions applied.<sup>144</sup>

An important point is often disregarded when substitution/doping effects are discussed, namely the interrelation of substitution and the resulting morphology and microstructure. Especially for compounds with low ionic and electronic conductivity like the orthosilicates, changes in microstructure drastically change the electrochemical properties. The incorporation of a foreign species to the synthesis can alter the microstructure, and thus the electrochemical performance, and should not be ignored when discussing cationic substitution.<sup>7</sup>

### 3.7 Synthesis methods and electrochemical properties of nanostructured carbon coated $\text{Li}_2\text{MSiO}_4$ compounds

There are various methods reported to synthesise nanostructured  $\text{Li}_2\text{MSiO}_4$  compounds and this section will briefly summarise selected examples. In principle, top-down methods like solid-state reaction combined with high-energy ball milling and wet chemical bottom-up methods are distinguished. But various wet chemical means are also combined with high energy milling for de-agglomeration. Common approaches are solution gelation methods where different complexing or chelating agents like citric acid or a combination of citric acid and ethylene glycol (Pechini) can be added.<sup>16,18,96,104,111,114,128,130,134,140-143,145-156</sup> Solution combustion methods have also been applied. Here, a fuel like sucrose or PVA reacts spontaneously with an oxidiser resulting in the combustion of the material.<sup>157,158</sup> Further advanced methods include solvothermal methods, which often work at supercritical conditions,<sup>16,126,159-162</sup> and polyol methods.<sup>163</sup> Not only wet chemical approaches have been reported. Some authors report aerosol processes like spray pyrolysis or spray drying.<sup>131,164-166</sup> Table 3.3 summarises some synthesis methods including secondary phases, particle size, surface area, carbon content, discharge capacity, rate and temperature, when given.

**Table 3.3: Nanosized  $\text{Li}_2\text{MSiO}_4$  compounds**

Synthesis method	Compound	Synthesis description	Sec. phases	Particle size and surface area	C content	Potential window and temperature if not measured at room temp.	Capacity in C or current density	Ref.
Solution gelation	$\text{Li}_2\text{MnSiO}_4$	Modified Pechini + ball milling	MnO	20-50 nm	5%	2-4.2 V 60 °C	140 mAhg <sup>-1</sup> C/20	104
	$\text{Li}_2\text{MnSiO}_4$	Citric acid sol-gel	MnO	50 nm	~*	1.5-4.8 V	145 mAhg <sup>-1</sup> C/16	148
	$\text{Li}_2\text{FeSiO}_4$	Citric acid sol-gel	Fe	42 nm	-	1.5-4.8 V	152 mAhg <sup>-1</sup> C/16	148
	$\text{Li}_2\text{MnSiO}_4$	Sol-gel	-	21 nm 70 m <sup>2</sup> g <sup>-1</sup>	8.9%	1.5-4.8 V	204 mAhg <sup>-1</sup> 30 mA g <sup>-1</sup>	155
	$\text{Li}_2\text{MnSiO}_4$	Modified Pechini	Mn <sub>2</sub> SiO <sub>4</sub> MnO	50-80 nm	7%	1.5-4.6 V	144 mAhg <sup>-1</sup> 10 mA g <sup>-1</sup>	146
	$\text{Li}_2\text{FeSiO}_4$	Solution polymerisation	-	30-50 nm	16%	1.5-4.8 V	225 mAhg <sup>-1</sup> C/16	154
	$\text{Li}_2\text{FeSiO}_4$	Tartaric acid assisted sol-gel	-	30 nm 62.1 m <sup>2</sup> g <sup>-1</sup>	8%	1.5-4.8 V	177 mAhg <sup>-1</sup> 0.5C	114

**Chapter 3 Lithium Transition Metal Orthosilicates ( $\text{Li}_2\text{MSiO}_4$ )**

	$\text{Li}_2\text{FeSiO}_4$	PVA assisted sol-gel	$\text{Li}_2\text{SiO}_3$ $\text{LiFeO}_{2-x}$	$\sim 20$ nm $21 \text{ m}^2\text{g}^{-1}$	5.5%	1.5-4.2 V	$165 \text{ mAhg}^{-1}$ C/16	150
<b>Solvo-thermal</b>	$\text{Li}_2\text{FeSiO}_4$	Microwave assisted solvo-thermal	-	20 nm	12%	1.5-4.8 V 55 °C	$200 \text{ mAhg}^{-1}$ C/20	126
	$\text{Li}_2\text{MnSiO}_4$	Microwave assisted solvo-thermal	-	20 nm	12%	1.5-4.8 V 55 °C	$250 \text{ mAhg}^{-1}$ C/20	126
	$\text{Li}_2\text{FeSiO}_4$	Ascorbic acid mediated hydrothermal	-	60 nm $36.6 \text{ m}^2\text{g}^{-1}$	-	1.5-4.6 V	$167 \text{ mAhg}^{-1}$ C/10	167
	$\text{Li}_2\text{FeSiO}_4$	Solvothermal	no XRD	Ultra-thin nanosheet	-	1.5-4.8 V 45 °C	$340 \text{ mAhg}^{-1}$ C/50	160
	$\text{Li}_2\text{MnSiO}_4$	Solvothermal	no XRD	Ultra-thin nanosheet	-	1.5-4.8 V 45 °C	$350 \text{ mAhg}^{-1}$ C/50	160
<b>Com-bustion</b>	$\text{Li}_2\text{FeSiO}_4$	PVA assisted combustion	$\text{Li}_2\text{SiO}_3$	$37.7 \text{ m}^2\text{g}^{-1}$	-	1.5-4.5 V	$135 \text{ mAhg}^{-1}$ C/16	158
	$\text{Li}_2\text{FeSiO}_4$	Sucrose assisted combustion	Phase pure	29 nm $60 \text{ m}^2\text{g}^{-1}$	11.4%	1.8-4 V 60 °C	$130 \text{ mAhg}^{-1}$ C/20	157
<b>Aerosol pro-cesses</b>	$\text{Li}_2\text{MnSiO}_4$	Spray pyrolysis and ball milling	MnO	50 nm	6.8%	1.5-4.8 V 60 °C	$230 \text{ mAhg}^{-1}$ C/20	164
	$\text{Li}_2\text{FeSiO}_4$	Spray pyrolysis and ball milling	$\text{Li}_2\text{SiO}_3$	65 nm	20%	1.5-4.8 V	$155 \text{ mAhg}^{-1}$ C/20	165 168
	$\text{Li}_2\text{FeSiO}_4$	Solution spray drying	-	20-40 nm $84.1 \text{ m}^2\text{g}^{-1}$	16.7%	1.5-4.8 V	$165 \text{ mAhg}^{-1}$ C/5	169
<b>Solid state</b>	$\text{Li}_2\text{FeSiO}_4$	Solid state and high energy milling	FeO	50-150 nm	-	2-3.7 V 60 °C	$102 \text{ mAhg}^{-1}$ $4 \text{ mA}g^{-1}$	170
	$\text{Li}_2\text{MnSiO}_4$	Solid state embedded in graphene nanosheets	MnO	50 nm	-	2-4.6 V	$215 \text{ mAhg}^{-1}$ C/20	

\* - = not mentioned

It is clearly seen from Table 3.3 that a variety of results is achieved by different means. Direct comparisons can be problematic since many parameters have to be considered. Many reports use C rates without defining C. Also, potential windows of the electrochemical tests are different and the temperature at which the test was performed varies. Additionally, not all the information is given in every report. For example, some authors report extremely high carbon contents but the report does not clarify if the amount of C is subtracted from the sample weight when calculating the specific capacity.

Also, the table shows that synthesis of  $\text{Li}_2\text{MSiO}_4$  compounds rarely leads to phase pure materials. Often reported secondary phases are binary oxides like MnO or FeO, and meta- and orthosilicates like  $\text{Li}_2\text{SiO}_3$ ,  $\text{Mn}_2\text{SiO}_4$  or  $\text{Fe}_2\text{SiO}_4$ . In the case of  $\text{Li}_2\text{FeSiO}_4$ , the reduction to elementary Fe is also observed.<sup>158</sup>

Additional to a small particle size, the porosity of the synthesised material is of importance since a high porosity in the meso and macro ranges enable a high contact area of the electrolyte and hence high reaction rates.<sup>7,72,114,150,167,171,172</sup> However, the tapping density has to be considered. Some authors report high capacity with nanoparticles or nanocoatings on carbon nanotubes, nanoparticles in a graphene network, or ultrathin nanosheets<sup>155,160,170,173,174</sup>. These structures might create high specific gravimetric capacities but will deliver extremely low tapping densities, and hence volumetric capacities, so these structures are of scientific value only.

Generally, a carbon coating is meant as conductivity enhancer and should uniformly surround the particles and be thin enough to allow easy Li diffusion.<sup>68</sup> Most commonly, the coatings are generated during reducing or inert heat treatment by the pyrolysis of carbon containing compounds. Further, the Boudouard reaction generates CO, which acts as a reducing agent for the transition metal, which is not necessary in the divalent state before the heat treatment.

For the carbon coating, we distinguish between two different routes. In the first route, an organic molecule or macromolecule is added during a wet chemical synthesis. This could form complexes or be evenly distributed in the resulting solid precursor. The second route is the mechanic introduction and homogenisation of an organic molecule, macro-molecule or amorphous carbon by mortaring or milling. A homogeneous, thin layer of carbon is important to guarantee an overall conducting matrix. Furthermore, the amount of  $\text{sp}^2$  hybridised carbon should be high since it has been shown to have a major impact on the conductivity of the coating.<sup>175</sup> Commonly applied carbon formers are mono-, di- and poly-saccharides like glucose,<sup>170</sup> sucrose,

<sup>126,155,157,164,176</sup> corn-starch <sup>150,156,158</sup> this study and cellulose or cellulose acetate. <sup>153,177</sup>  
Also common are carboxylic acids, which are often already added during the synthesis. Examples here are adipic acid, <sup>34,156,178</sup> ascorbic acid, <sup>123</sup> citric acid, <sup>104,142,173</sup> pyromellitic acid <sup>147</sup> and tartaric acid. <sup>114</sup> Some authors use polymeric substances like polyacrylonitrile, <sup>134</sup> poly-N-vinylformamide, <sup>147</sup> polyethylene-polyethyleneglycol copolymer <sup>125</sup> or phenolic resin. <sup>155,172</sup> Further, carbonaceous materials like pitch <sup>168</sup> or acetylene black are used in some studies. <sup>131,169</sup>

## 4. Brief description of the applied Synthesis methods

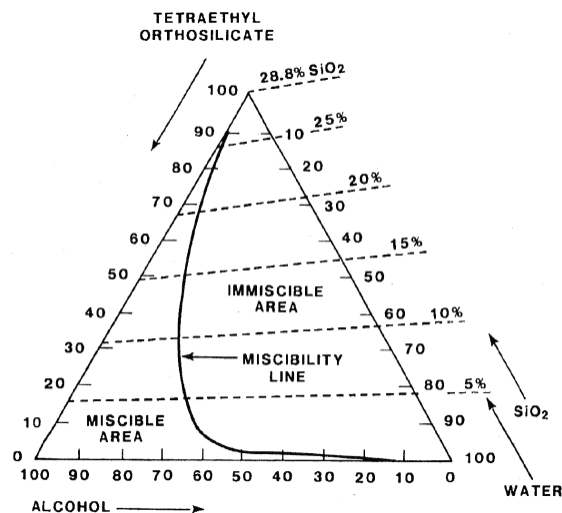
### 4.1 Overview

There are numerous sophisticated synthesis means available for exploration of complex phases. All samples prepared in this thesis were either synthesised by a sol-gel route or by liquid-feed flame spray pyrolysis. Subsequently, the samples were annealed under reducing conditions to obtain the desired phase. The following chapters summarise the principles of the synthesis techniques applied.

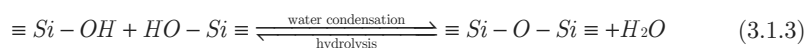
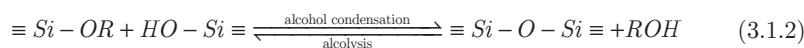
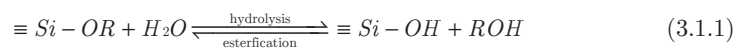
### 4.2 Sol-gel synthesis

#### 4.2.1 Silicate based sol-gel process

The sol-gel process is a wet chemical precursor process used to synthesise ceramic powders. It includes the synthesis of either a stable suspension of colloids, called a colloid sol, or a polymeric solution without dense particles, called a polymeric sol. The process continues with gelation of the sol and removal of the solvent by a drying step.<sup>179</sup> Sol-gel processes were first discovered with silicon. Silicon alkoxides are less reactive than metal alkoxides since silicon offers only one stable oxidation state and is less electropositive. Thus, a change in the coordination number during reactions does not occur. The kinetics of hydrolysis and condensation are relatively slow and silicon sol-gel chemistry can be done in water based systems.<sup>179,180</sup> A typical silicon sol-gel precursor is tetraethyl orthosilicate (TEOS). As shown in Figure 4.1, TEOS is insoluble in water, hence a common solvent for TEOS and water is often added. This is in many cases ethanol.<sup>181</sup>

Figure 4.1: Ternary phase diagram for TEOS, ethanol and H<sub>2</sub>O <sup>181</sup>

Alcohols are not only solvents but also take part in the reactions. The formation of a sol includes the steps of hydrolysis and condensation. The according reactions are given in the following equations: <sup>180</sup>



The reaction rates are strongly pH dependent and they affect the resulting sol. As shown in Figure 4.2 a) the hydrolysis rate is minimal at pH 7. The hydrolysis is generally acid or base driven and at pH 7 the concentration of oxonium and hydroxide ions is at its lowest. <sup>180,182</sup> Basic conditions also promote condensation, thus, base catalysed processes end in a colloidal sol while acid catalysis ends in polymeric sols, as shown in Figure 4.2 b). Furthermore, the reaction rates are dependent on the nature of the alcoholate ligands, the water content and the reaction temperature. <sup>183</sup>

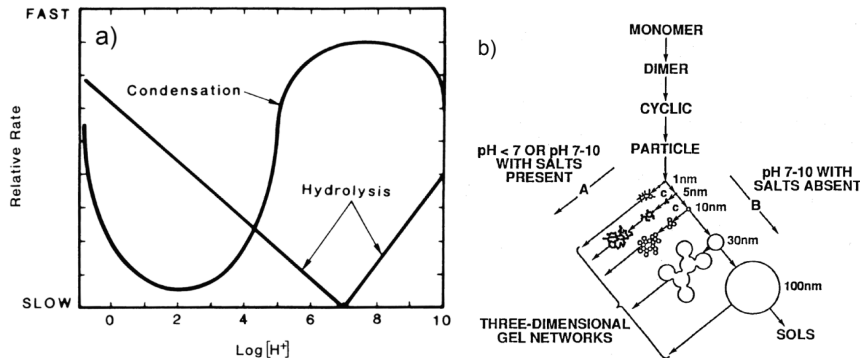


Figure 4.2: a) pH dependence of the reaction rates for hydrolysis and condensation<sup>182,184</sup> b) pH dependence of the polymerisation of aqueous silica<sup>183</sup>

The evaporation of solvent molecules and further growth of the clusters by either polycondensation in an acidic environment or cluster aggregation in a basic environment leads to a point where clusters collide. At this point the clusters percolate, i.e. they build a giant cluster that spreads through the whole reaction container. This point is termed the gel point<sup>180</sup>. Since the viscosity of a sol is dependent on the shear rate applied, the viscosity is not an optimal parameter to determine the gel point. More precise information can be extracted by the loss tangent ( $\tan \delta$ ), which goes through a maximum as the gel point approaches and then declines. The maximum in a  $\tan \delta$  plot is caused by a more rapid increase of elastic behaviour of the network than the increase in viscosity.<sup>185</sup>

#### 4.2.2 Multi component sol-gel processes

There are many sol-gel related processes known to form multi-component oxides or silicates. Metal alkoxides can be used as sol-gel precursors, but their reactivity is much higher since metal alkoxides are more electropositive than silicon alkoxides. In addition, many metal cations can undergo redox reactions and change their coordination number during nucleophilic attacks. These characteristics force metal alkoxide sol-gel syntheses to be water-free.<sup>179,182</sup>



Another sol-gel related process is the Pechini method, where metal cations are dissolved in water, and citric acid and ethylene glycol are added. Citric acid acts as a chelating agent for the metal cations and at elevated temperatures the ethylene glycol undergoes polyesterification reactions with the carboxyl groups of citric acid, causing a gel network to form.<sup>182</sup> Many different complexing (chelating) agents and di-alcohols can be combined in Pechini-like sol-gel syntheses.

In this study, the desired structure is  $\text{Li}_2\text{MSiO}_4$  so the silicon alkoxide based sol-gel route is applicable. Lithium and transition metal salts are mixed with the silicon alkoxide. Polyvinyl alcohol (PVA) was chosen as the complexing agent in this study. The hydroxyl groups of PVA can complex metal cations and they can also undergo condensation reactions with the hydroxyl or alkoxy group of the condensed silanol chains or build up hydrogen bonding and thus enable a homogeneous distribution of cations throughout the network.<sup>186,187</sup> The precursors used were metal nitrates and tetraethyl orthosilicate. The synthesis conditions were kept acidic to form a polymeric gel and to avoid Mn oxidation and or precipitation in the form of hydroxides.<sup>188</sup> The vanadium precursor used for the synthesis of samples in paper II and III was ammonium metavanadate ( $\text{NH}_4\text{VO}_3$ ) since simple vanadium nitrates are not available. Working in an acidic environment is also beneficial for vanadium chemistry since monomeric vanadium oxo-ions are formed rather than poly-ions.<sup>189</sup> During the first syntheses of vanadium substituted LMS (paper II) the vanadium precursor was added to the nitric acidic Mn precursor. Later, a more sophisticated route was explored and is described in paper III. The vanadium precursor was dissolved in a 1.5 · molar amount of oxalic acid prior to mixing with the other precursors. Dissociated oxalate ions did partly reduce vanadium from +5 to +4, accompanied with a change in solution colour from yellow to a deep greenish blue. Furthermore, oxalate ions can complex vanadium oxo-ions,<sup>190,191</sup> which can be beneficial for the formation of a homogeneous gel.

### 4.2.3 Gel ageing

During ageing of a gel the structure undergoes further processes that lead to a strengthened network. Further polymerisation occurs by condensation reactions. These increase the connectivity of the network and may cause syneresis, shrinkage of the gel caused by expelling liquids from the pores of the network. There are two different syneresis processes, namely macro and micro syneresis. In the former process shrinkage occurs over the whole network, while in the latter case a phase separation occurs. This process is driven by a greater affinity of the polymer for itself, leading to formation of polymer clusters and areas of free liquid.<sup>179</sup>

The network can also undergo coarsening or ripening processes. These processes are driven by dissolution and re-precipitation reactions. In particulate gels different radii of curvatures of the particle surface result in different solubility and neck growth. This process does not lead to shrinkage of the network since there is no bulk mass transport.<sup>179</sup> Crystallisation may also take place during gel ageing. All ageing phenomena mentioned above have a strong influence on the drying process. A strengthened network can withstand the high capillary forces which are active during drying and can yield in a highly porous powder.<sup>179</sup> This is beneficial for a  $\text{Li}_2\text{MSiO}_4$  cathode since the high surface area of a nanosized porous powder can overcome the low ionic conductivity of the orthosilicates by minimising the mean diffusion length.

#### 4.2.4 Gel drying

Prior to any annealing a gel needs to be desiccated. The desiccated gel is termed xerogel when desiccation is performed at subcritical conditions which allow shrinkage of the network. The drying process can be divided into two main stages, namely the constant rate period (CRP) and the falling rate period (FRP).

During the CRP the gel surface is always wet, so the meniscus of the liquid-vapour interface is fixed to the gel surface. The shrinkage of the gel is equal to the volume of liquid evaporated. Liquid flows from the inside to the surface of the gel to keep the surface wetted since capillary forces and adsorption work against an exposure of the solid surface. This results in the formation of concave menisci. As a result the liquid is in tension counterbalanced by the gel in compression. The soft structure of the gel causes it to contract into the liquid filled pores. In the CRP the radii of the menisci are larger than pore radii but decreasing in size while the gel network becomes stiffer due to the reduced porosity as drying proceeds.<sup>179</sup>

The forces on the gel network are maximised at the end of the CRP when the radii of the menisci become equal to the pore radii. This stage is called the critical point. A highly porous structure might collapse due to the enormous capillary forces at the critical point. Therefore, if a porous structure is requested, gel ageing prior to drying is required to strengthen the network.<sup>179,182</sup>

After the critical point the liquid menisci move into the pores of the network during the FRP. Further drying mechanisms during the FRP are fluid flow and vapour phase diffusion.<sup>179</sup>

### 4.3 Liquid Feed Flame Spray Pyrolysis

Liquid-feed flame spray pyrolysis (LF-FSP) is a relatively new procedure for the preparation of nanoparticles. It is, so to speak, the logical advance of well-known flame processes like flame hydrolysis, which is used for the commercial production of soot (carbon black), pyrogenic silica, titania and other oxides.<sup>192,193</sup> The main issue with flame hydrolysis production of oxide materials is the need for a volatile metal halogenide ( $\text{SiCl}_4$ ,  $\text{TiCl}_4$ ) and the release of gaseous HCl. LF-FSP bypasses these issues by using liquid precursors. During the LF-FSP process a liquid precursor is pumped through a nozzle, where it gets nebulised by a dispersion gas stream and forms an aerosol. The dispersion gas (often  $\text{O}_2$ ) also acts as an oxidiser. Alongside the nozzle is the burner, where a flame is fed by a constant flow of fuel ( $\text{CH}_4$ ,  $\text{C}_2\text{H}_4$ ,  $\text{H}_2$ ) and oxidiser ( $\text{O}_2$ , air). The aerosol droplets evaporate and combust and form a self-sustaining flame.<sup>194</sup> After leaving the flame the powder is guided to a filter by an air stream.

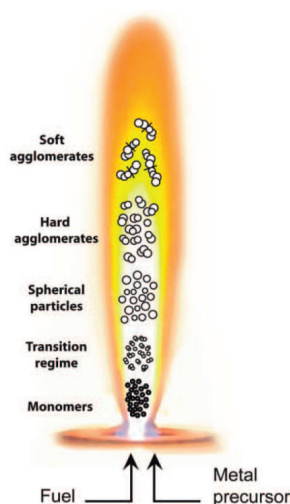


Figure 4.3: Particle formation and growth during liquid feed flame spray pyrolysis<sup>193</sup>

Usually in LF-FSP processes, organometallic compounds such as metal alkoxides, carboxylates, acetylacetonates and acetates are dissolved in organic, combustible liquids like ethanol, toluene, xylene and acetyl acetone. Simple metal nitrates can also be applied as long they are soluble in a combustible media for example an ethanol

water mixture.<sup>193-197</sup> During LF-FSP not only do the fuel, oxidiser and burner geometry control the flame temperature but also the combustion of the precursor liquid itself. The temperature, which can be well above 2000 °C for particle loaded CH<sub>4</sub>/O<sub>2</sub> flames, and the residence time are the most important factors controlling the resulting particle morphology.<sup>193,194</sup> Figure 4.3 illustrates the particle formation and growth mechanisms during LF-FSP.

The elevated temperatures during combustion ideally lead to the formation of a homogeneous gas phase monomer which forms the first nuclei. These nuclei grow by collisions with additional monomers and finally coalesce and form nearly spherical primary particles. The primary particles further develop by surface growth and coagulation and coalescence by Brownian motion, forming fractal structures. These too merge and finally build fractal aggregates which can be held together by either van der Waals forces (soft) or sinter necks (hard).<sup>193,198</sup> Finally, particle growth becomes sluggish and halts when the temperature becomes much lower further away from the flame, comparable to a quenching mechanism.<sup>193</sup>

In this study, for the flame driven synthesis of Li<sub>2</sub>MSiO<sub>4</sub> compounds, metal nitrates and tetraethyl orthosilicate were dissolved in ethanol/water and ethanol/p-xylene with ratios of 5:1. The solutions were sprayed into a CH<sub>4</sub>/O<sub>2</sub> (flow rate 1.5/3 Lmin<sup>-1</sup>) flame at a constant solution and dispersion gas (O<sub>2</sub>) flow rate of 5 mLmin<sup>-1</sup>. The pressure drop (dispersion gas at the nozzle tip) was set to ~2.0 bar. The extremely short residence time and the extremely high temperature hinder the formation of the orthosilicate phase, which usually occurs at temperatures of 600-800 °C and prolonged dwell times. Even though, reducing flames or inert shielding gases are applicable during LF-FSP, no such experiments were carried out due to the risk of fully reducing the transition metal.<sup>22,193,199</sup>

#### 4.4 Phase formation and carbon coating

The resulting dried xerogels from the PVA assisted sol-gel route were amorphous multi-phase compounds with high contents of organic residues and unreacted nitrates. In some cases minor precipitation of LiNO<sub>3</sub> was also observed. A calcination step is hence necessary to eliminate these residues and nitrates. This step gives a better control for the mass ratio of active material to the carbon former. Knowledge obtained previously in the research group showed that decomposition is finalised at temperatures  $\geq 400$  °C.<sup>158</sup> Accordingly, the xerogels were calcined at 450 °C for 1 h in air or 5% H<sub>2</sub> 95% Ar. The reducing atmosphere during calcination was chosen to hinder Mn oxidation upon nitrate decomposition and to preserve the carbon of the

organic residue. The LF-FSP powder on the other hand, does not require any calcination since it consists of mixed oxides and minor amounts of carbonates.

Prior to the final heat treatment, the samples were mixed with the carbon former. In this study the carbon former was corn-starch, which was chosen based on previous experience,<sup>158</sup> low price and ease of handling. The carbon former was mixed with the orthosilicate precursor using two different methods. All sol-gel powders were intensively wet mortared with corn-starch using ethanol as dispersant. The LF-FSP powders on the other hand were extremely voluminous and fluffy which made homogenisation by mortaring problematic. The LF-FSP powders were instead mixed by wet ball milling on a roller bench. The powder and corn-starch were mixed with an equivalent volume of YSZ grinding balls ( $\varnothing$  5 mm), ethanol as dispersant and ball milled for approximately 10 h to ensure homogenisation. Afterwards, the powders were dried and heat treated in a tubular furnace at temperatures between 600-700 °C for a period of 10 hours under a constant flow of 5% H<sub>2</sub> 95% Ar, 2% H<sub>2</sub> 98% Ar, or 100% Ar.

In addition to the temperature, the gas composition and flow have a major impact on phase formation and purity. Fe especially, is very sensitive to the level of p<sub>O2</sub>. Fe is commercially produced by carbothermal reduction of Fe-containing ores in blast furnaces and the thermodynamic stability region of divalent Fe at elevated temperatures is extremely limited, as shown in the oxygen partial pressure / temperature phase diagram of the Fe-O system in Figure 4.4.

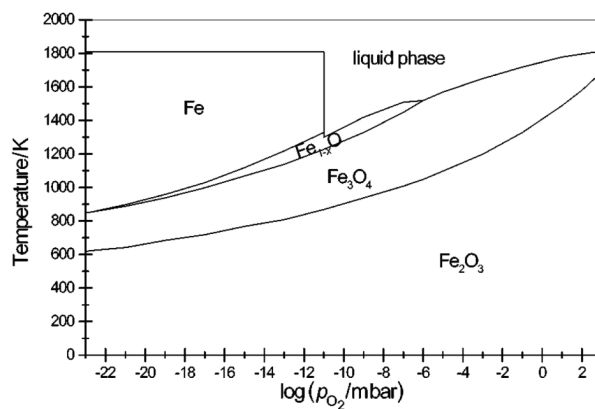


Figure 4.4: Temperature pressure phase diagram calculated for the Fe-O system

200

The silicate structure might stabilise the divalent Fe but the  $p_{O_2}$  needs to be controlled by the gas flow and amount of carbon former to hinder Fe reduction. Reduction of Mn, on the other hand, does not occur since elementary Mn is not thermodynamically stable under the given boundary conditions.<sup>201</sup> In contrast to Fe, a more reducing atmosphere resulted in higher phase purities of the  $Li_2MnSiO_4$  samples synthesised in this study.



## 5. Summary of the main results

### 5.1 Foreword

The following chapter summarises and discusses the main findings of the 5 papers the dissertation is composed of. The chapter is divided into 5 sections, where 1 section is dedicated to the main findings of each paper. All results achieved in this study, and a more thorough discussion can be found in the corresponding papers.

### 5.2 Synthesis of $\text{Li}_2\text{MnSiO}_4$ by an acidic PVA assisted sol-gel method

The first objective of this study was to elaborate a wet chemical process, which allows the synthesis of highly phase pure  $\text{Li}_2\text{MnSiO}_4$  with a desired porous nanostructure. A sol-gel method based on metal nitrates and tetraethyl orthosilicate was chosen as an adequate and controllable synthesis method. In chapter 4 the importance of the pH value on the resulting gel was described, and for Mn chemistry a low pH value is crucial to hinder oxidation and precipitation of Mn hydroxides. Polyvinyl alcohol was chosen as a complexing agent to promote a homogeneous network. It was found that the amount of PVA has to be limited to suppress a spontaneous combustion of the gel upon drying. The gelled solutions were aged for 72 h to increase the strength of the network in order to withstand the forces upon drying and hence result in highly porous nanostructures. The dried gels were calcined to decompose the organic PVA matrix and the nitrates. During the first calcination, the  $p_{\text{O}_2}$  showed a strong impact on the phase purity of the final powders, since a high  $p_{\text{O}_2}$  would promote the oxidation of Mn to higher valences and the complete removal of the carbon containing matrix by carbon oxidation to CO and  $\text{CO}_2$ .



In addition to the carbon residues from the thermal pyrolysis, varying amounts of corn-starch were added to form a carbon coating. This mixture was finally heated under inert and reducing atmospheres to obtain highly porous, nanosized and carbon coated  $\text{Li}_2\text{MnSiO}_4$  compounds. Also here a high impact of the  $p_{\text{O}_2}$  towards the phase formation was detected. The  $p_{\text{O}_2}$  is in this case governed by the applied atmosphere and flow rate, as well as by the Boudouard reaction and hence the amount of the carbon source employed. Highest phase purities were achieved using 5%  $\text{H}_2$  in Ar and corn-starch amounts  $\geq 25$  wt. %. The structural model of  $\text{Li}_2\text{MnSiO}_4$ , adopting a  $\beta_{\text{II}}$   $\text{Li}_3\text{PO}_4$  structure, suggested by Dominko *et al.*<sup>16</sup> was confirmed by a full pattern refinement. A slightly simplified description suggested by Li *et al.*<sup>96</sup> and later by Sato *et al.*<sup>161</sup> was used as the starting point for the refinement. The refined powder X-ray diffraction pattern and the structural parameters are given in Figure 5.1 and Table 5.1 respectively.

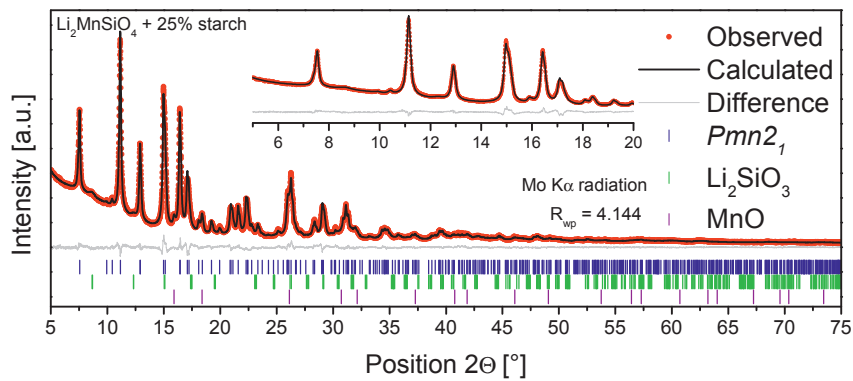


Figure 5.1: Full pattern refinement of a  $\text{Li}_2\text{MnSiO}_4$  sample containing 25 wt. % corn-starch.  $hkl$  values of  $Pmn2_1$   $\text{Li}_2\text{MnSiO}_4$ ,  $\text{Li}_2\text{SiO}_3$  and  $\text{MnO}$  are included.

Table 5.1: Structural parameters obtained from Rietveld refinement of  $\text{Li}_2\text{MnSiO}_4$ 

Space group: $Pmn2_1$							
a = 6.30570(31) Å							
b = 5.38379(28) Å							
c = 4.96512(24) Å							
Atom	Wyckoff	x	y	z	Atom	Occ.	B (Å <sup>2</sup> )
Li	4b	0.2424	0.3313	0.8647	Li <sup>+</sup>	0.9972	0.30(16)
Mn on	4b	0.2424	0.3313	0.8647	Mn <sup>2+</sup>	0.0028 <sup>1</sup>	0.30(16)
Li							
Mn	2a	0.5000	0.8327	0.8327	Mn <sup>2+</sup>	0.7930 <sup>2</sup>	0.58(12)
Si	2a	0.0000	0.8196	-0.0792	Si <sup>4+</sup>	1	0.92(14)
O1	4b	0.2136	0.6717	0.8059	O <sup>2-</sup>	1	0.45(15)
O2	2a	0.0000	0.1229	0.8484	O <sup>2-</sup>	1	1.19(16)
O3	2a	0.5000	0.1707	0.7533	O <sup>2-</sup>	1	0.48(16)

<sup>1</sup> Almost no Li Mn anti-site defects detectable <sup>2</sup> Underestimation of the 2a Mn<sup>2+</sup> occupancy

The refined data fits well with data from the literature confirming the  $Pmn2_1$   $\beta_{\text{II}}$  structure.<sup>16,96,161</sup> Noteworthy is that the 2a occupancy of Mn<sup>2+</sup> is slightly underestimated without showing high amounts of Li/Mn anti-site defect. But it has to be kept in mind that the powder sample was prepared as active cathode material and not for structural refinements. The nanostructure and the amorphous carbon content hence limit the ability of structural refinements. Powder X-ray diffraction patterns of  $\text{Li}_2\text{MnSiO}_4$  samples using varying amounts of corn-starch as carbon source, and the calculated phase fractions are given in Figure 5.2. The samples with a low amount of corn-starch showed traces of  $\text{Mn}_2\text{SiO}_4$  and  $\text{Li}_2\text{SiO}_3$ . Diffraction lines which can be attributed to a  $\gamma_{\text{II}}$  ( $Pmnb$ ) polymorph of  $\text{Li}_2\text{MnSiO}_4$  were also present. Higher corn-starch amounts resulted in high phase purities of  $\beta_{\text{II}}$   $\text{Li}_2\text{MnSiO}_4$  and minor traces of MnO.

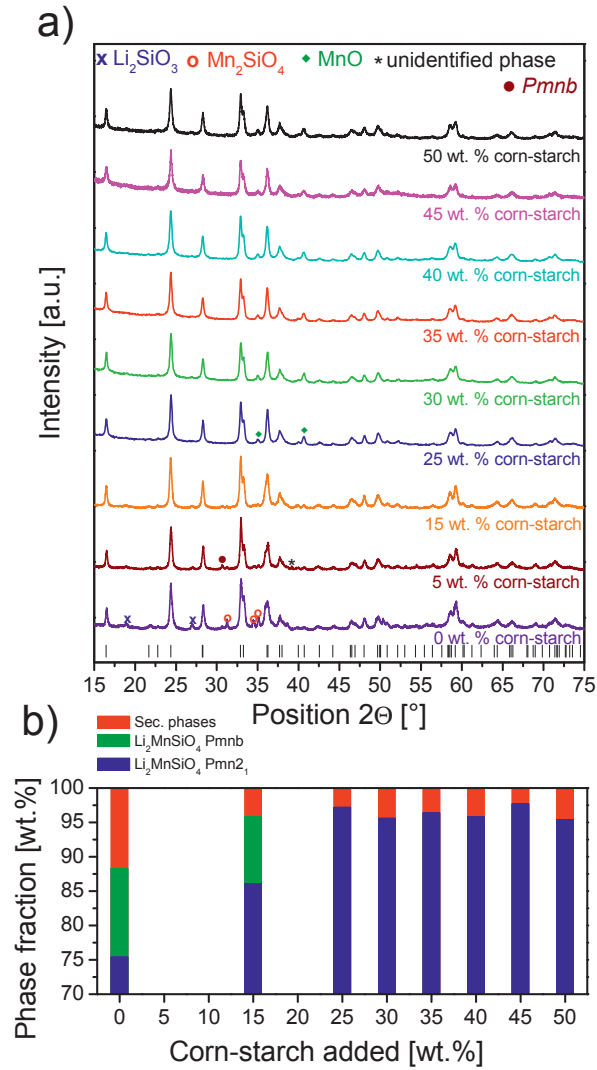


Figure 5.2: Powder XRD patterns a) and calculated phase fractions b) of  $\text{Li}_2\text{MnSiO}_4$  samples with varying corn-starch amounts. Markers show the visible peaks of the secondary phases and the  $\gamma$ II polymorph of  $\text{Li}_2\text{MnSiO}_4$  ( $Pmnb$ ) (PDF 01-080-8499),  $\text{MnO}$  (PDF 04-015-5273),  $\text{Li}_2\text{SiO}_3$  (PDF 00-015-0519),  $\text{Mn}_2\text{SiO}_4$  (PDF 00-009-0485).

The addition of the carbon source also influenced the morphology of the resulting powders. To characterise the active surface area (external surface area) of the materials, the amount of surface area attributed to microporosity ( $< 2\text{nm}$ ) has to be subtracted from the BET surface area according to T-plot theory. The surface area of the samples and the carbon content including the correlation of carbon content and microporosity is shown in Figure 5.3. The carbonising additive was shown to hinder particle growth and the external surface area saturates for corn-starch amounts above 30 wt. %. The microporosity is increasing with increasing corn-starch content. Furthermore, Figure 5.3 shows the microporosity to strongly correlate with the measured carbon content after the reducing heat treatment. Hence, the microporosity in the sample is caused by the carbon coating. This is in agreement with TEM observations, pointing out the porous nature of the coating. 25 and 50 wt. % corn-starch addition resulted in 9 and 27 wt. % carbonaceous residue, respectively. While the latter value would be beneficial for the conduction of electrons, it reduces the gravimetric and especially the volumetric amount of active material in the compound.

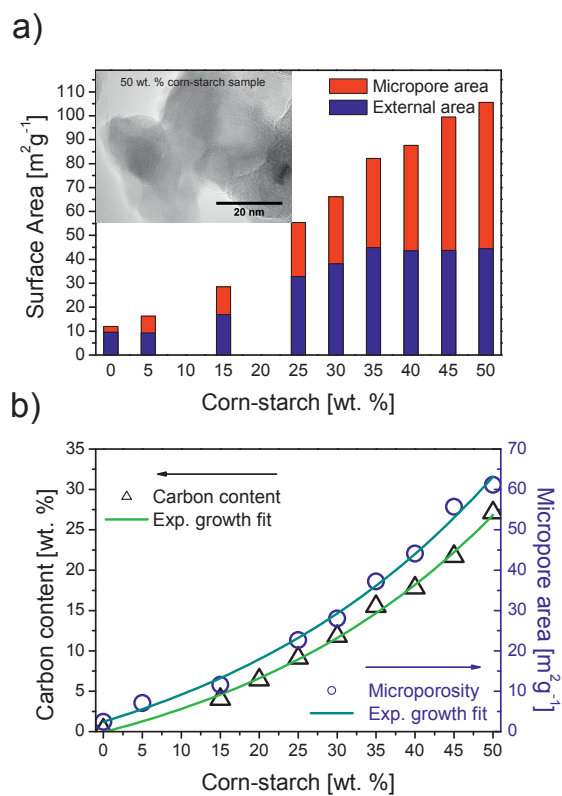


Figure 5.3: a) BET surface area divided into external area and micropore area of  $\text{Li}_2\text{MnSiO}_4$  samples with varying addition of corn-starch prior to annealing. The inset shows a TEM micrograph of a sample containing 50 wt. % corn-starch. b) Resulting carbon content (left ordinate black triangles) and the correlation to the microporosity (right ordinate blue circles) values.

The galvanostatic cycling curves of all samples are shown in Figure 5.4 a). The applied current density was  $10 \text{ mA g}^{-1}$ .  $\text{Li}_2\text{MnSiO}_4$  is a rather poor electronic conductor ( $3 \cdot 10^{-14} \text{ Scm}^{-1}$  at  $60^\circ\text{C}$ ),<sup>18</sup> hence only minor electrochemical activity was detected for samples with no or minor carbon content. The highest discharge capacity was observed for the 25 wt. % corn-starch sample. Higher corn-starch amounts caused the capacity to decrease again.

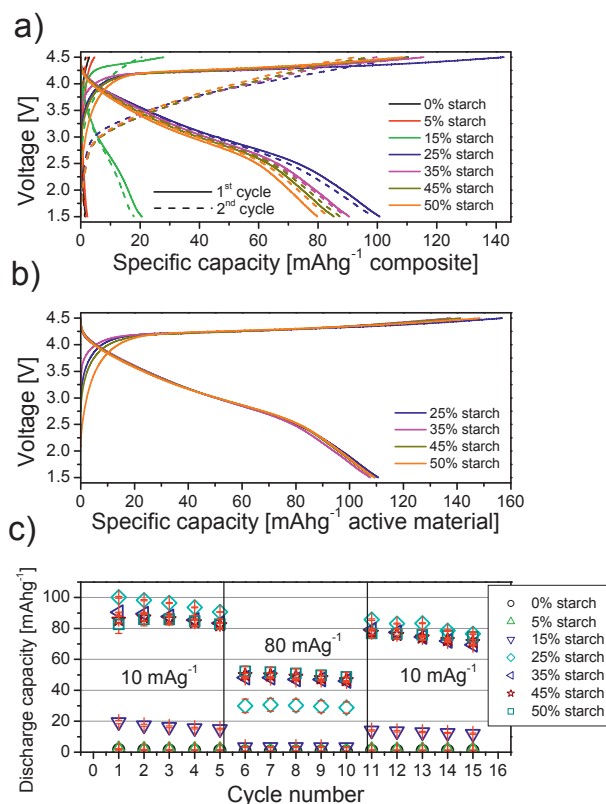


Figure 5.4: a) First and second galvanostatic cycle of the  $\text{Li}_2\text{MnSiO}_4$  samples with varying corn-starch amount. The measurement was carried out at room temperature and a current density of  $10 \text{ mAg}^{-1}$  in the potential window from 1.5 to 4.5 V. b) First galvanostatic cycle of the samples containing 25, 35, 45 and 50 wt. % corn-starch. Note: Here the carbon content presented in Figure 2 was subtracted from the sample mass! c) Discharge capacity evolution of all samples during 15 cycles. First 5 cycles at  $10 \text{ mAg}^{-1}$ , the following 5 cycles at  $80 \text{ mAg}^{-1}$  and the final 5 cycles again at  $10 \text{ mAg}^{-1}$ .

All samples showed a prominent irreversible loss during the first cycle. This loss of up to 30% cannot be solely explained by side reactions like the oxidative electrolyte decomposition. Furthermore, a significant difference in the charge and discharge curve profiles was present. The charge profile reassembles a plateau like profile at potentials  $> 4$  V. Against that, the discharge profile is strongly sloping. The domi-

nant loss in combination with a strongly sloping discharge profile indicates severe structural changes upon cycling. Dominko confirmed the amorphisation of the structure upon first oxidation by X-ray diffraction.<sup>18</sup> This amorphous structure seems to not allow full relithiation. Additionally, in the amorphous state the connectivity and orientation of the tetrahedra may be altered. The redox potential of a transition metal is strongly influenced by the ionocovalent character and hence its chemical environment. In the  $\beta_{II}$  polymorph each Mn is bound to 4  $\text{SiO}_4$  groups which raise the redox potential of Mn by an inductive effect.<sup>43</sup> A change in connectivity and chemical environment would cause variations in local redox potentials and hence would explain the strongly sloping curve. Trivalent Mn is well known to be Jahn-Teller active in an octahedral crystal field.<sup>120,121</sup> In a tetrahedral environment the triply degenerated  $t_2$  states are higher in energy than the doubly degenerated  $e_g$  states. Since the crystal field energy in a tetrahedral field is lower than the spin pairing energy, the electrons of  $\text{Ar } 3d^4$  ion  $\text{Mn}^{3+}$  would singly occupy the  $e_g$  and 2 of the  $t_2$  levels according to Hund's rules. This energetically unfavourable state would lead to strong distortions and could result in changes in the Mn coordination. This behaviour is also predicted by computational studies.<sup>23,122</sup> Upon the second oxidation the charge profile showed a steep slope as well. The decreased performance at higher corn-starch amounts is caused by the reduced amount of active material in the composite. Figure 5.4 b) shows the first cycle of the 25, 35, 45 and 50 wt. % samples with subtracted carbon content. The curves look nearly identical and reach a discharge capacity of about  $110 \text{ mAhg}^{-1}$ . This value corresponds to the exchange of 0.66 Li per transition metal cation, and further suggests that 25 wt. % corn-starch is satisfactory to build up a carbon coating with a sufficient electronic conductivity at slow charge rates.

Samples containing 25 and 50 wt. % corn-starch were also cycled at a low current density of  $3.3 \text{ mA}g^{-1}$  to a higher cut-off voltage of 4.8 V. These materials reached capacities of  $170 \text{ mAhg}^{-1}$  and  $192 \text{ mAhg}^{-1}$  on the first discharge, respectively, when the amount of carbon was subtracted from the sample mass. The corresponding first charge capacity was in both cases close to  $300 \text{ mAhg}^{-1}$ . Even though side reactions will account for a part of the charge capacity at these high potentials, the values strongly suggest that more than 1 Li per formula unit were extracted.

At a higher current density the samples with corn-starch amounts  $> 25$  wt. % showed a higher capacity, as seen in Figure 5.4 c). This suggests that the electronic conductivity to be rate limiting for the 25 wt. % corn-starch samples at higher current densities. Overall, all samples regardless of carbon content suffered from steady capacity decay. Figure 5.5 shows the long-term performance of the 25 and the 50 wt. % corn-starch samples at a current density of  $10 \text{ mA}g^{-1}$  in a potential window of 1.5-4.8 V. The cells were cycled for 100 cycles, and while the coulombic efficiency ap-

proaches values between 90 and 100%, the capacity fades rapidly. The slope of the 50 wt. % corn-starch sample is less steep, indicating that the structural amorphisation has a more prominent impact on the Li-extraction/insertion kinetics of larger particles present in the 25 wt. % corn-starch sample. Ultimately, both samples lose almost all their capacity after 100 cycles.

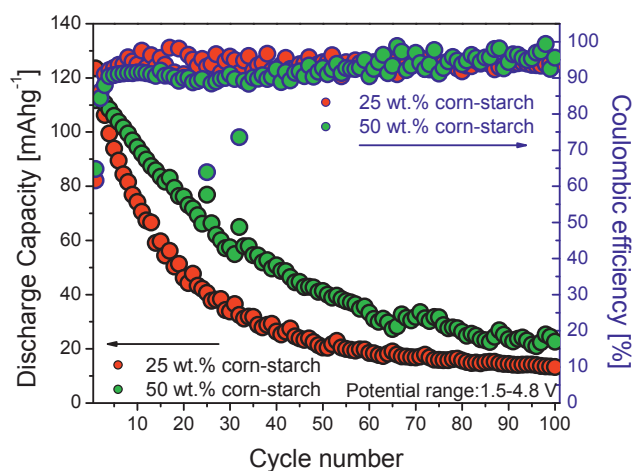


Figure 5.5: Long-term cycling of  $\text{Li}_2\text{MnSiO}_4$  samples with 25 and 50 wt. % corn-starch addition at  $10 \text{ mA g}^{-1}$  in a potential window of 1.5-4.8 V. The black outlined symbols show the discharge capacity on the left ordinate, while the blue outlined symbols show the coulombic efficiency on the right ordinate.



### 5.3 Feasibility of cationic substitutions in $\text{Li}_2\text{MnSiO}_4$

On basis of the synthesis elaborated in Paper I cation substituted samples were synthesised, with the aim to investigate changes in the electrochemical properties and the structural stability during cycling. The samples prepared in this study were heat treated in a different tubular furnace, which resulted in slightly reduced surface area values with correspondingly slightly lower capacities. Two different substitutes were investigated, namely Fe and V. The former was substituted on Mn-site, while V was substituted on either Mn- or Si-site.

It was possible to substitute up to 20 mol % Mn by Fe using the synthesis method described in Paper I. Higher concentrations of the  $\text{Fe}(\text{NO}_3)_3$  precursor caused a too acidic environment and did not show proper gelation. Instead of a gel, a resin-like viscous mass developed which did not lead to the desired nanostructure. Fe substitution led to phase purity as shown in Figure 5.6. At 20 mol % Fe substitution a very weak signal corresponding to elementary Fe could be identified in the X-ray diffraction pattern, indicating that further increase in the Fe substitution level would not only require an altered synthesis but also a less reducing atmosphere. Additionally, Fe substitution showed a slightly negative effect on the external surface area values.

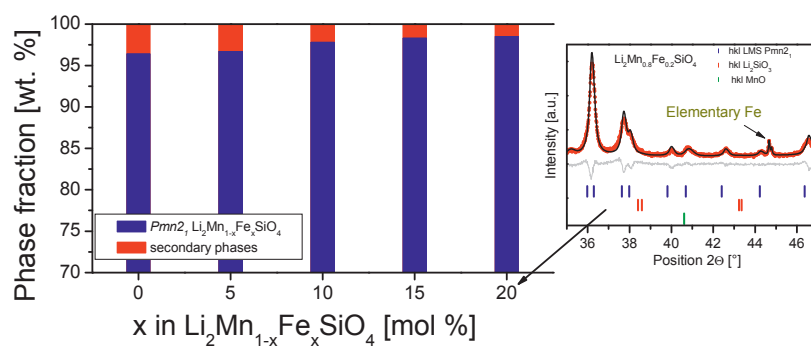


Figure 5.6: Phase fraction of the Fe substituted samples. Secondary phases present were MnO and  $\text{Li}_2\text{SiO}_3$ . The inset shows a magnified region of the full pattern fit, indicating traces of elementary Fe in the 20 mol % Fe sample.

The electrochemical properties of the Fe substituted samples were assessed by galvanostatic cycling. The first galvanostatic cycle of  $\text{Li}_2\text{Mn}_{1-x}\text{Fe}_x\text{SiO}_4$  samples where  $x = 0, 0.1, 0.15$  and  $0.2$  is shown in Figure 5.7. The cells were cycled at  $10 \text{ mA g}^{-1}$  in a potential window of 1.5-4.8 V.

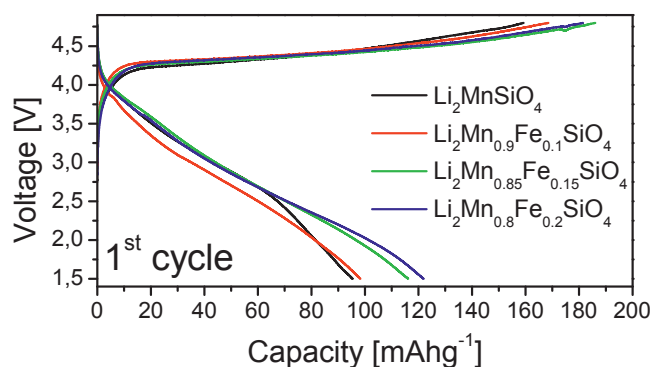


Figure 5.7: First galvanostatic cycle of  $\text{Li}_2\text{Mn}_{1-x}\text{Fe}_x\text{SiO}_4$  samples ( $x = 0, 0.1, 0.15$  and  $0.2$ ) at  $10 \text{ mA g}^{-1}$ .

The charge behaviour of the Fe substituted samples resembles the profile of the reference sample. Even at 20 mol % Fe substitution no reactions at lower potential according to the  $\text{Fe}^{2+}/\text{Fe}^{3+}$  redox couple could be detected during the first charge. Oxidation of Fe hence could have occurred already upon storage of the powders prior to battery fabrication. The discharge revealed activity that can be attributed to the  $\text{Fe}^{2+}/\text{Fe}^{3+}$  redox couple. Despite the increased polarisation of the 10 mol % Fe sample, the discharge curves of the Fe substituted samples resemble the profile of  $\text{Li}_2\text{MnSiO}_4$  down to potentials of about 2.5 V. At this point a change of slope in the discharge profile occurs for  $\text{Li}_2\text{MnSiO}_4$ . The slope of the Fe substituted samples stays almost unchanged and just shows a kink in the slope at potentials close to cut-off. The different profile of the substituted samples suggests that a different process occurs in this region. The equilibrium  $\text{Fe}^{2+}/\text{Fe}^{3+}$  redox potential in  $\beta_{\text{II}}$   $\text{Li}_2\text{FeSiO}_4$  was measured by Sirisopanaporn *et al.*, using a galvanostatic intermittent titration technique, to be 3.1 V.<sup>124</sup> Inversion of the structure upon cycling and polarisations cause a reduced lithiation potential of about 2.7-2.8 V, which resembles a relatively flat profile over a large compositional range.<sup>15,125</sup> In a Mn rich solid solution of the gen-

eral formula  $\text{Li}_2\text{Mn}_{1-x}\text{Fe}_x\text{SiO}_4$  the  $\text{FeO}_4$  units would experience distortions caused by the difference in ionic radii of Mn and Fe. These distortions could influence the bond length and hence lower the  $\text{Fe}^{2+}/\text{Fe}^{3+}$  redox potential.<sup>124</sup> More importantly, the structural instability caused by Mn described in the previous chapter will cause changes in the chemical environment of Fe and thus result in a sloping profile in the discharge curve for the Fe reduction as well. The performance of the 10 mol % Fe sample shows slightly higher polarisation and no overall gain in capacity, while the capacity of the 15 and 20 mol % sample is increased by 20 and 27  $\text{mAhg}^{-1}$  respectively. If this increase is solely caused by Fe redox activity, these values correspond to  $\sim 80\%$  of the theoretical value for the  $\text{Fe}^{2+}/\text{Fe}^{3+}$  reduction. Despite the increased capacity, Fe substitution did not influence the stability, and capacity fade was observed for all samples.

The next step was to incorporate 5 mol % V into the  $\beta_{\text{II}}$  structure of  $\text{Li}_2\text{MnSiO}_4$ , which was shown to be successful and the corresponding X-ray diffractograms are shown in Figure 5.8. To form a sufficient carbon coating on V substituted samples 40 wt. % corn-starch was necessary. Accordingly, a reference sample was synthesised containing 40 wt. % corn-starch. The increase in the necessary amount of corn-starch was later in the project found to be caused by inconsistencies in the gas flow and furnace atmosphere.

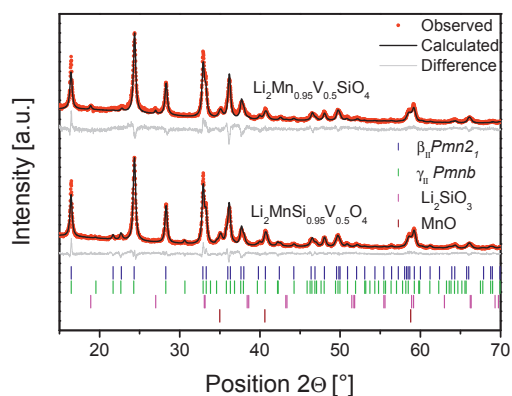


Figure 5.8: Powder XRD patterns of the nominal compositions  $\text{Li}_2\text{Mn}_{0.95}\text{V}_{0.05}\text{SiO}_4$  and  $\text{Li}_2\text{MnSi}_{0.95}\text{V}_{0.05}\text{O}_4$  including  $hkl$  markers of the calculated phase fractions, namely  $\beta_{\text{II}}$   $Pmn2_1$ ,  $\gamma_{\text{II}}$   $Pmnb$ ,  $\text{Li}_2\text{SiO}_3$  and  $\text{MnO}$ .

Both samples showed similar phase purities as the reference. In the case of  $\text{Li}_2\text{MnSi}_{0.95}\text{V}_{0.05}\text{O}_4$ , small amounts of the high temperature  $\gamma_{\text{II}}$  polymorph were present. First attempts to analyse the site occupancy of V were based on the Ellingham diagram of the V-O system.<sup>202,203</sup> According to this V should be present in a trivalent form and hence most probably occupy the Mn-site. An earlier broad substitution study by Deng *et al.* concluded V to be trivalent. The authors argued that trivalent V could occupy both sites since its ionic radius lies in between the radii of  $\text{Mn}^{2+}$  and  $\text{Si}^{4+}$  in tetrahedral coordination. While the comprehensive work by Shannon<sup>138</sup> does not include data for the ionic radius of  $\text{V}^{3+}$  in a four-fold coordination, the difference in ionic radius between  $\text{Si}^{4+}$  and  $\text{V}^{3+}$ , both in six-fold coordination, is 44%. Assuming a similar trend for both cations in a four-fold coordination makes it unlikely that large amounts of  $\text{V}^{3+}$  could occupy the tetrahedral Si-site without severe structural consequences.

The V substituted samples showed a better electrochemical response with a slightly reduced polarisation and irreversible capacity loss. The improved performance and the fact that the V substitution in  $\text{Li}_2\text{MnSiO}_4$  is yet not well understood, led to a further investigation of V substitution in these materials.

## 5.4 Investigations on V substitution in $\text{Li}_2\text{MnSiO}_4$

To further investigate the possibility of substituting V for Mn or Si, two concentration series were synthesised. The V content was progressively increased in 5 mol % steps. To allow a good control about the synthesis, slight modifications, as described in the previous chapter of this thesis, were necessary. Nominal compositions  $\text{Li}_2\text{Mn}_{1-x}\text{V}_x\text{SiO}_4$  ( $0 \leq x \leq 0.2$ ) and  $\text{Li}_2\text{MnSi}_{1-x}\text{V}_x\text{O}_4$  ( $0 \leq x \leq 0.3$ ) were synthesised with 25 wt. % corn-starch addition as carbon former. All samples were analysed by means of powder X-ray diffraction. The patterns of  $\text{Li}_2\text{Mn}_{1-x}\text{V}_x\text{SiO}_4$  ( $0 \leq x \leq 0.2$ ) are presented in Figure 5.9.

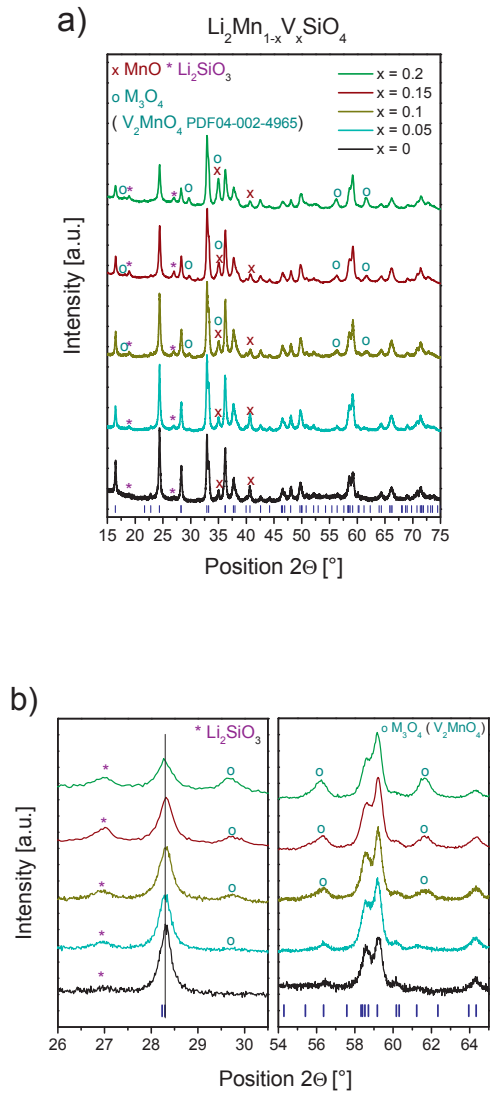


Figure 5.9: a) Powder XRD patterns of the nominal compositions  $\text{Li}_2\text{Mn}_{1-x}\text{V}_x\text{SiO}_4$  ( $0 \leq x \leq 0.2$ ), b) Magnified regions 16-30.5 and 54-65 °  $2\theta$ . Calculated  $hkl$  values of  $\beta_{\text{II}}$   $Pmn2_1$   $\text{Li}_2\text{MnSiO}_4$  included. Further included are markers to indicate the secondary phases MnO,  $\text{Li}_2\text{SiO}_3$  and the new appearing V containing spinel phase which can be indexed to  $\text{V}_2\text{MnO}_4$  (PDF 04-004-4965).

The reference sample showed minor traces of  $\text{Li}_2\text{SiO}_3$  and  $\text{MnO}$ . The same is valid for 5 mol % V substitution. If the substitution level is further increased, the  $\text{MnO}$  secondary phase disappears and instead a V rich spinel phase with its main  $311$  diffraction line at  $34.9^\circ 2\Theta$  appears. The magnified regions in Figure 5.9 b) show a progressive increase of the spinel phase. Furthermore, a vertical line as guide to the eye is included for the  $200$  diffraction line of  $\beta_{\text{II}} Pmn2_1 \text{Li}_2\text{MnSiO}_4$ . No major changes in peak positions were observed, but the intensity was progressively decreasing and the peak shapes showed broadening for higher V levels. Reduced intensities were also detected for  $010$ ,  $011$  and  $002$  diffraction lines at  $16.4$ ,  $24.4$  and  $36.2^\circ 2\Theta$ , while other peaks seemed rather unchanged in intensity. Figure 5.10 shows details of the structure of  $\beta_{\text{II}} Pmn2_1 \text{Li}_2\text{MnSiO}_4$  including the  $010$ ,  $011$  and  $002$  lattice planes. Both  $010$  and  $011$  cut Mn, which offers the highest electron density. The same is valid for  $200$ , but for clarity of the figure this was excluded. The observations that the peaks corresponding to the lattice planes with a high electron density governed by Mn are decreasing in intensity, while at the same time the amount of a V containing spinel phase is increasing leads to the conclusion that V solid solubility is very limited. Elevated concentrations of V, which is octahedrally coordinated and trivalent in the spinel phase, <sup>204</sup> do not populate the tetrahedral Mn-sites but rather causes phase separation.

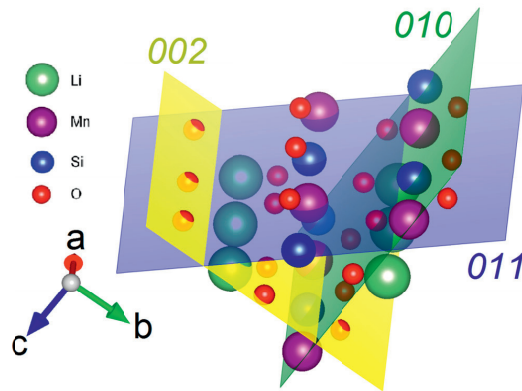


Figure 5.10: Atom arrangements in  $\beta_{\text{II}} Pmn2_1$  including the  $010$ ,  $011$  and  $002$  lattice planes. Bonds and tetrahedral isosurfaces are excluded to increase the readability of the figure.

V substitution on the Si-site did not cause the appearance of V containing spinel phases. The only secondary phase which showed an increasing amount with increasing V concentration was a rock-salt structured MnO related phase. Moreover, clear peak shape broadening and a slight shift to higher  $2\Theta$  angles of this phase was detected. The patterns were fitted to a  $\text{Li}_2\text{MnSiO}_4$  model elaborated earlier in this study, as shown in Figure 5.11. Incorporation of V into the model in order to find the site occupancy would be more than questionable, since the nanocrystalline character and low signal to noise ratio caused by the amorphous carbon would not allow a meaningful refinement. Additionally, irregular changes in peak intensities and substantially increased intensities of the  $Pmn2_1$   $110$  and  $101$  diffraction lines were observed. Interestingly, the position of the former changed within the concentration series while the latter stayed at its initial position. Increasing disorder in the crystal structure, as well as local deviations can be expected.

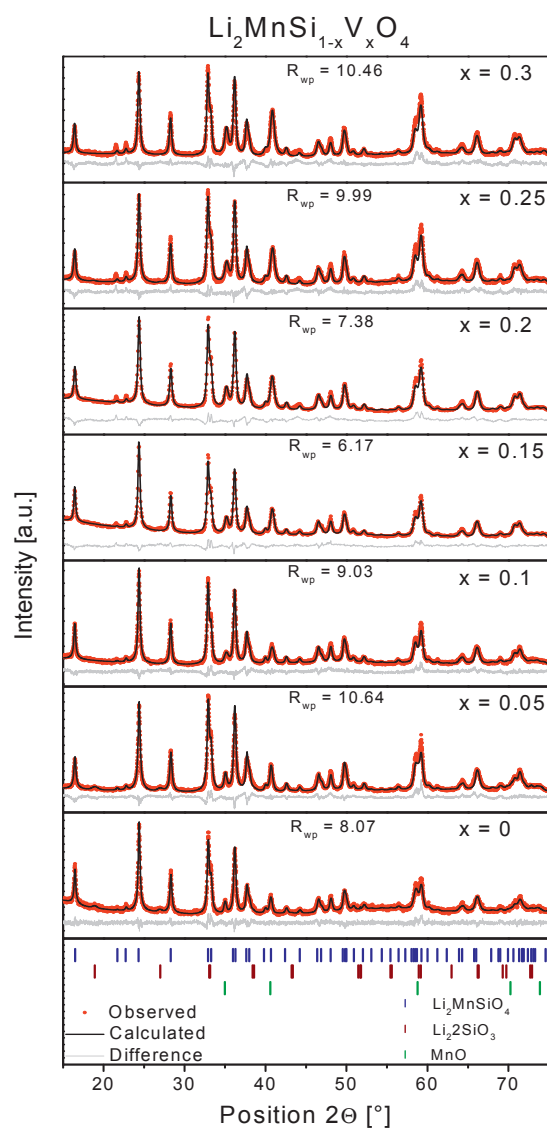


Figure 5.11: Powder XRD patterns of the  $\text{Li}_2\text{MnSi}_{1-x}\text{V}_x\text{O}_4$  ( $0 \leq x \leq 0.3$ ) concentration series fitted to the model shown in the previous section.



The increased intensity of the two peaks could indicate a partly inversed structure, where with increasing V concentration either Mn or V partly occupies Li-sites. This behaviour is well known to occur in  $\text{Li}_2\text{FeSiO}_4$  upon cycling. The material undergoes a transition to an inversed  $\beta_{\text{II}}$  structure which is similar to the structure of  $\text{Li}_2\text{MnSiO}_4$ , but Fe occupies half the Li-site. The reversal causes increased intensities of the  $110$  and  $101$  diffraction line peaks.<sup>20</sup>  $Pmn2_1$  lattice parameters, the calculated crystallite size and the carbon content from TGA analysis are given in Table 5.2. The lattice parameters in the concentration series show a minor inconsistent trend to an increased cell volume. This observation was unexpected, since even pentavalent V has a bigger ionic radius than Si, and should influence the lattice parameters more pronounced if it substitutes Si. Crystallite sizes were calculated to range between 36-56 nm from the full width at half maximum of the  $011$  peak.

**Table 5.2: Lattice constants and XRD crystallite sizes of the nominal compositions  $\text{Li}_2\text{MnSi}_{1-x}\text{V}_x\text{O}_4$  ( $0 \leq x \leq 0.3$ )**

x in $\text{Li}_2\text{MnSi}_{1-x}\text{V}_x\text{O}_4$	A[Å]	B[Å]	C[Å]	Cell vol- ume [Å <sup>3</sup> ]	Crystallite size [nm]	Carbon content [wt. %]
<b>0</b>	6.30499(85)	5.38475(78)	4.96513(66)	168.570(40)	41.1	6
<b>0.05</b>	6.3041(12)	5.38533(91)	4.96266(88)	168.481(52)	37.9	5
<b>0.1</b>	6.30693(95)	5.38441(82)	4.96386(73)	168.568(44)	38.5	5
<b>0.15</b>	6.3038(12)	5.3859(11)	4.9640(11)	168.538(61)	55.8	4
<b>0.2</b>	6.3043(14)	5.3844(14)	4.9622(13)	168.442(73)	42.5	4
<b>0.25</b>	6.30972(96)	5.38682(84)	4.96421(75)	168.730(45)	36.2	5
<b>0.3</b>	6.3094(12)	5.3889(10)	4.96461(93)	168.801(55)	36.6	5

To further investigate the incorporation of V and to support the findings made by X-ray diffraction, the nominal compositions  $\text{Li}_2\text{MnSiO}_4$ ,  $\text{Li}_2\text{MnSi}_{0.9}\text{V}_{0.1}\text{O}_4$  and  $\text{Li}_2\text{MnSi}_{0.75}\text{V}_{0.25}\text{O}_4$  were examined by scanning transmission electron microscopy coupled with energy dispersive X-ray spectroscopy and electron energy loss spectroscopy. EDS was applied to map the element distribution. The distribution of Si, O, and Mn was homogeneous in all cases and despite the carbon coating, no amorphous areas were detected. Figure 5.12 shows the elementary distribution of a 25 mol % V substituted sample.

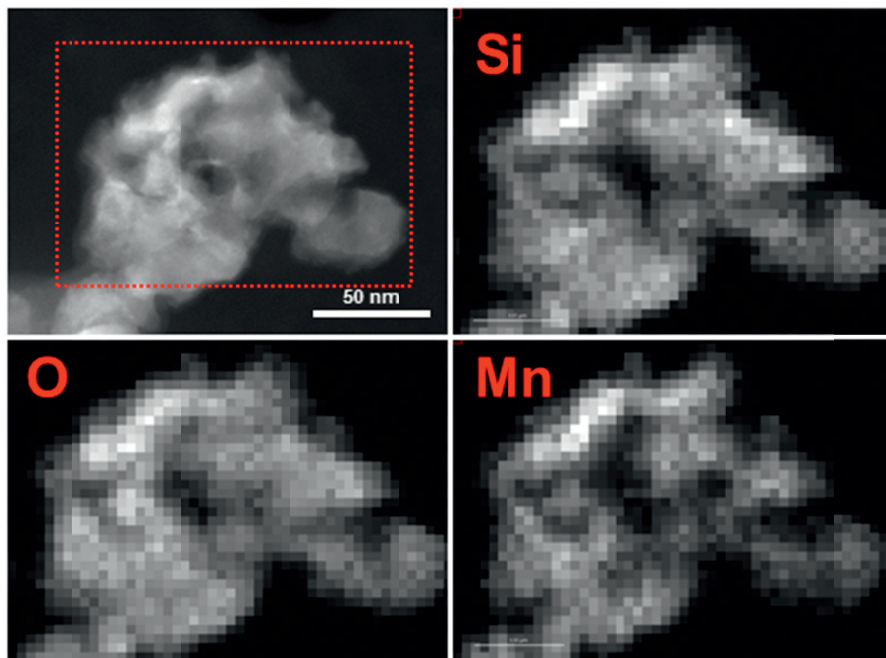


Figure 5.12: EDS map of Si, O and Mn of a  $\text{Li}_2\text{MnSi}_{0.75}\text{V}_{0.25}\text{O}_4$  sample. HAADF micrograph with indicated mapping area is included.

EELS is a powerful tool which allows not only to map the elemental distribution, but also to distinguish oxidation states of chemical elements. High resolution EELS mapping with sub-pixel alignment was performed to map the V distribution. The setup described in Paper III was carefully chosen to hinder beam damages during acquisition, since V is prone to reduction if exposed to the high energy electron beam for prolonged periods of time.<sup>205,206</sup> V distributions in  $\text{Li}_2\text{MnSi}_{0.9}\text{V}_{0.1}\text{O}_4$  and  $\text{Li}_2\text{MnSi}_{0.75}\text{V}_{0.25}\text{O}_4$  are shown in Figure 5.13. The V distribution in the structure is highly inhomogeneous, where distinct areas show a much higher V content. These V inhomogeneities will have a major influence on the local compositions of the materials and probably cause numerous defects like stacking faults and local breaches of symmetry. These results indicate that it is highly unlikely that V occupies one distinct crystallographic site in the material. The primary valence of V was the same in both samples, but the 10 mol % and the 25 mol % sample showed some different minor signal corresponding to different secondary oxidation states. The V  $L_{2,3}$  and the corresponding Mn  $L_{2,3}$  from the same location are shown in Figure 5.14. The minor secondary signal (blue dashed line) originated from a different location of the map.

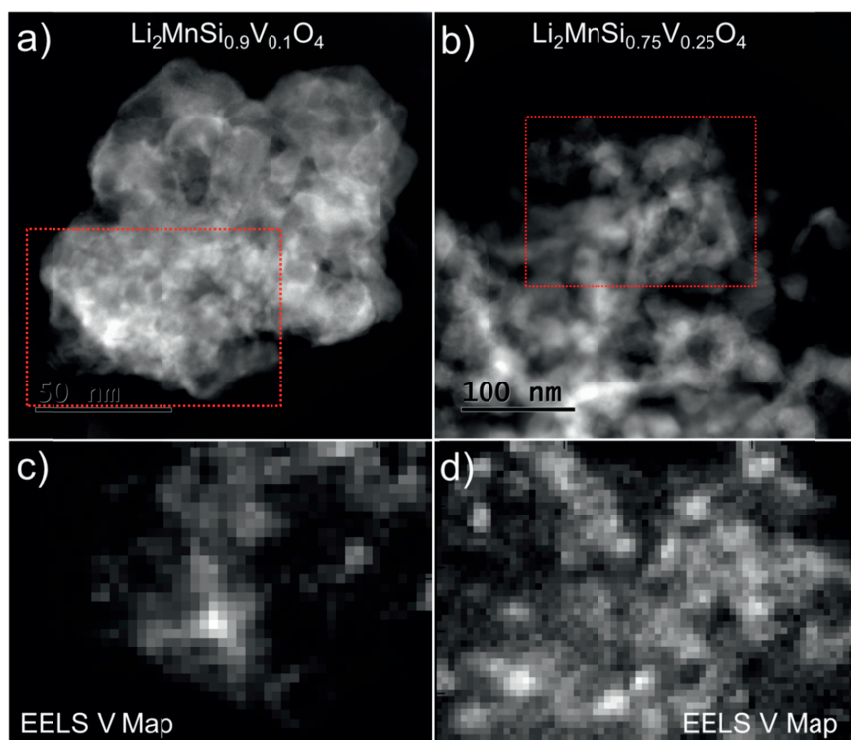


Figure 5.13: HAADF STEM micrographs of the nominal compositions a)  $\text{Li}_2\text{MnSi}_{0.9}\text{V}_{0.1}\text{O}_4$  and b)  $\text{Li}_2\text{MnSi}_{0.75}\text{V}_{0.25}\text{O}_4$ . Areas of EELS spectra acquisition are highlighted. EELS V maps of c)  $\text{Li}_2\text{MnSi}_{0.9}\text{V}_{0.1}\text{O}_4$  and d)  $\text{Li}_2\text{MnSi}_{0.75}\text{V}_{0.25}\text{O}_4$ .

The energy loss at the peak onset, the shape of the fine structure, and comparison to data from other well established microscopy research groups<sup>207,208</sup> suggest the majority of V to be present in a tetravalent state. Computational studies by Liivat and Thomas suggest the tetrahedral structure of the orthosilicate framework is offering a stabilising effect on  $\text{VO}_4^{4-}$  units.<sup>139</sup> Differences were detected in a slightly different minor V signal in both samples. In the case of  $\text{Li}_2\text{MnSi}_{0.9}\text{V}_{0.1}\text{O}_4$  the minor signal was shifted towards a lower energy loss, and the difference in onset was  $\sim 0.8$  eV. In  $\text{Li}_2\text{MnSi}_{0.75}\text{V}_{0.25}\text{O}_4$  the opposite trend was detected. A minor signal with higher energy loss, shifted about 1.2 eV in onset, was observed. These shifts in onset correlate excellently with reported values<sup>207</sup> and can be attributed to small amounts of trivalent V present in  $\text{Li}_2\text{MnSi}_{0.9}\text{V}_{0.1}\text{O}_4$  and pentavalent V in  $\text{Li}_2\text{MnSi}_{0.75}\text{V}_{0.25}\text{O}_4$ . The fine

structure of Mn, in close neighbourhood to the measured V signal can be clearly attributed to divalent Mn.<sup>207</sup> However, minor fractions of trivalent Mn were also detected in all samples, which could be a result of charge compensation.

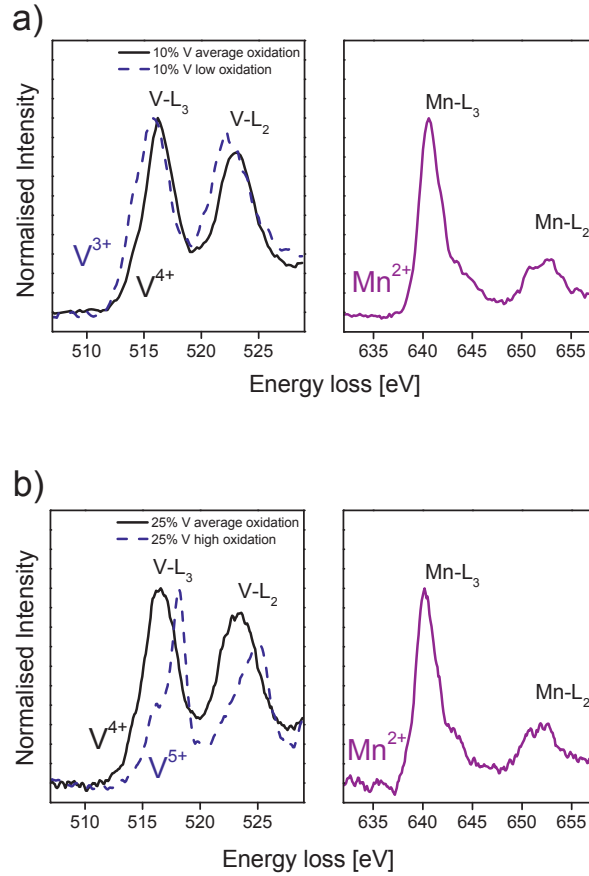


Figure 5.14: Major V L<sub>2,3</sub> and the corresponding Mn L<sub>2,3</sub> acquired from the same pixel (solid lines) and minor V L<sub>2,3</sub> signal from a different pixel of the nominal compositions a)  $\text{Li}_2\text{MnSi}_{0.9}\text{V}_{0.1}\text{O}_4$  and b)  $\text{Li}_2\text{MnSi}_{0.75}\text{V}_{0.25}\text{O}_4$ .

The V signals corresponding to a different valence require charge compensation. A lower valence could be compensated by partly oxidation of Mn to a trivalent state. Pentavalent V on the other hand, would require the formation of vacancies in the Li or Mn sub-lattice.

Furthermore, EDS mapping of Mn and O rich particles, which can be attributed to the MnO related phase, also showed considerable amounts of V. This suggests that the secondary phase detected by XRD should more correctly be addressed as rock-salt structured  $\text{Mn}_{1-x}\text{V}_y\text{O}$  ( $1-x+y < 1$ ). It cannot be concluded if the increase in this phase indicates a thermodynamically limited solid solubility or if it is due to the thermal and atmospheric history of the samples. Reduction of the initially pentavalent V to a trivalent or even divalent state could occur during the annealing step, and our findings suggest only limited solubility for the trivalent ion. A non-stoichiometric situation may occur if parts of the V is reduced and cannot be incorporated into the structure. This resulting non-stoichiometry would then cause segregation of the excess Mn and Li. The inhomogeneous character, the different oxidation states of V, and the increasing amount of the  $\text{Mn}_{1-x}\text{V}_y\text{O}$  ( $1-x+y < 1$ ) will cause significant amounts of point defects and defects of a higher order in the structure. Hence it might alter the electronic structure of the material and possibly also affect the Li diffusion.

Galvanostatic cycling revealed no improved properties of the nominal compositions  $\text{Li}_2\text{Mn}_{1-x}\text{V}_x\text{SiO}_4$  ( $0 \leq x \leq 0.2$ ) (see Paper III), while the nominal compositions  $\text{Li}_2\text{MnSi}_{1-x}\text{V}_x\text{O}_4$  ( $0 \leq x \leq 0.3$ ) showed superior properties compared to the reference sample. Figure 5.15 shows the first galvanostatic cycle of  $\text{Li}_2\text{MnSi}_{1-x}\text{V}_x\text{O}_4$  ( $0 \leq x \leq 0.3$ ) at a current density of  $10 \text{ mA g}^{-1}$ .

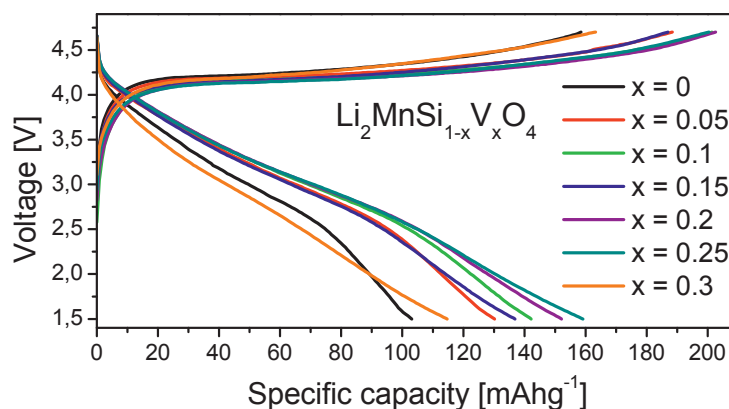


Figure 5.15: First galvanostatic cycle of the nominal compositions  $\text{Li}_2\text{MnSi}_{1-x}\text{V}_x\text{O}_4$  ( $0 \leq x \leq 0.3$ ) recorded at room temperature and a current density of  $10 \text{ mA g}^{-1}$ .

An increased discharge capacity within the concentration series which peaks at 25 mol % V is observed. The 15 mol % sample showed a slightly decreased capacity compared to the 10 mol % sample. XRD data suggested the crystallite size of this sample to be significantly larger, which could have a negative influence on the charge/discharge characteristics of this sample. The 25 mol % V substituted sample offered a 25% increase in charge capacity and 60% in discharge capacity, compared to the values of the reference sample. The irreversible capacity loss hence is decreased to a value of 20%. However, the sloping discharge profile suggests the known structural collapse of  $\text{Li}_2\text{MnSiO}_4$  to also occur in V substituted samples. The less pronounced change in slope at a potential of about 2.5 V which changes also in the concentration series indicates increased redox activity at low potentials. Additionally, a remarkable improvement in rate capability was observed. Figure 5.16 shows  $\text{Li}_2\text{MnSi}_{0.75}\text{V}_{0.25}\text{O}_4$  cycled at different current densities. At a current density of  $160 \text{ mA g}^{-1}$  the sample delivers a comparable capacity to the reference at  $10 \text{ mA g}^{-1}$ . Comparing the given values to values in Figure 5.4 shows a major improvement at elevated current densities.

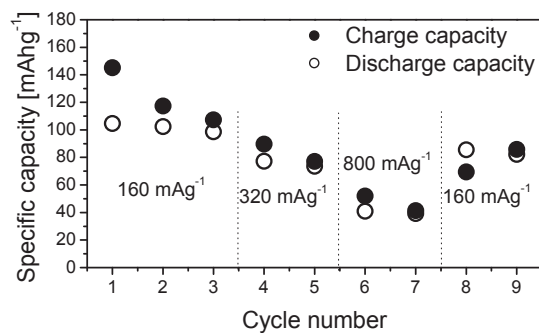
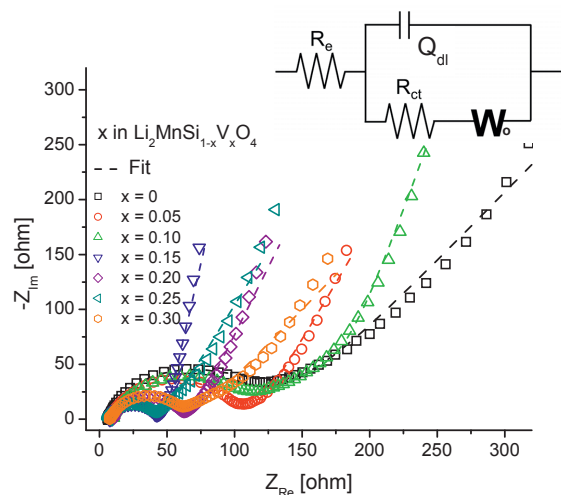


Figure 5.16: Li<sub>2</sub>MnSi<sub>0.75</sub>V<sub>0.25</sub>O<sub>4</sub> cycled at different current densities, values given in the Figure.

In order to understand the reasons for the improved electrochemical response, the samples were analysed by AC impedance at open circuit conditions. The impedance profile in Nyquist representation resembled a depressed semi-circle in the high frequency region followed by a line profile. The data was fitted to a modified Randles circuit. The first resistor accounts for the electrolyte resistance  $R_e$ . The following elements in parallel are a resistor accounting for the charge transfer resistance  $R_{ct}$  and a constant phase element (CPE) accounting for the double layer capacitance  $Q_{dl}$ . The depressed profile of the semi-circle is most probably caused by an inhomogeneous charge density distribution due to the porous structure. A CPE instead of a normal capacitor in parallel to the resistor (Cole element) was chosen to account for this depressed profile. The low frequency part of the impedance spectra was fitted by an open circuit terminus Generalised Finite Warburg element ( $W_o$ ). The Nyquist plot with the suggested equivalent circuit model in the inset is shown in Figure 5.17.



**Figure 5.17:** AC impedance data of  $\text{Li}_2\text{MnSi}_{1-x}\text{V}_x\text{O}_4$  ( $0 \leq x \leq 0.3$ ) in Nyquist representation, including the fitted line and the equivalent circuit.

The AC impedance data further allows the estimation of the Li diffusion coefficient according to a Warburg model with a linear overvoltage-current relationship.<sup>209,210</sup> Table 5.3 shows the parameters for  $R_e$ ,  $R_{ct}$ , and  $D_{\text{Li}}$ . V substitution influences the charge transfer resistance and the Li diffusion coefficient. The results are in agreement with the galvanostatic cycling experiments. A strongly decreased charge transfer resistance is observed for V substitution levels  $\geq 15$  mol %. The lowered charge transfer resistance is probably caused by  $\text{VO}_4$  units interrupting the strongly insulating  $\text{SiO}_4$  framework. The defects in the structure seem to also positively influence the diffusion coefficient for Li ions for all V substituted samples, as  $D_{\text{Li}}$  is found to be one order of magnitude higher than the reference value. The exact values have to be taken with caution since the assumptions made (Paper III) do not reflect the reality. The observed relative trends should still be valid.



**Table 5.3: Electrolyte and charge transfer resistance data, and the calculated Li diffusion coefficients from fitted AC impedance data of  $\text{Li}_2\text{MnSi}_{1-x}\text{V}_x\text{O}_4$  ( $0 \leq x \leq 0.3$ ).**

x in $\text{Li}_2\text{MnSi}_{1-x}\text{V}_x\text{O}_4$	$^1R_e$ [Ohm]	$^1R_{ct}$ [Ohm]	$^2D_{Li}$ [ $\text{cm}^2\text{s}^{-1}$ ]
0	6.312 (1.11%)	84.31 (3.42%)	9.7E-16
0.05	8.08 (0.76%)	86.43 (0.89%)	8.1E-15
0.1	8.86 (0.85%)	95.41 (1.31%)	3.6E-15
0.15	7.61 (1.20%)	31.88 (1.36%)	1.6E-14
0.2	9.51 (0.82%)	49.29 (1.16%)	3.1E-15
0.25	6.78 (0.84%)	24.76 (1.78%)	3.0E-15
0.3	7.71 (1.12%)	43.49 (1.18%)	5.2E-15

<sup>1</sup> Uncertainty given in brackets. <sup>2</sup> Assumptions are described in the main text.

Cyclic voltammetry was carried out to reveal if any additional redox activity occurs in V substituted samples. Figure 5.18 shows the voltammograms of the first and second cycle of  $\text{Li}_2\text{MnSi}_{1-x}\text{V}_x\text{O}_4$  ( $0 \leq x \leq 0.3$ ).

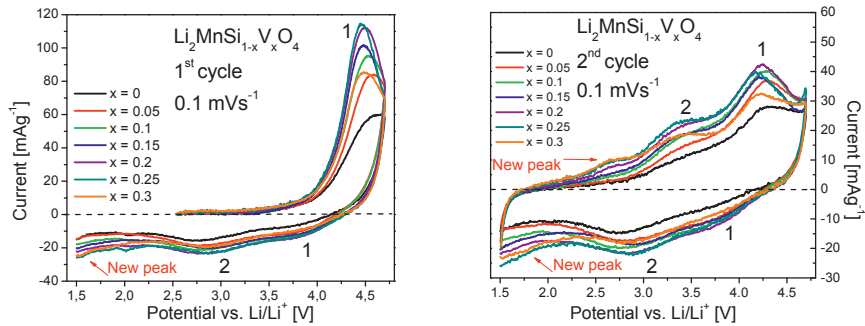


**Figure 5.18: Cyclic voltammograms of the first and second cycle of the nominal compositions  $\text{Li}_2\text{MnSi}_{1-x}\text{V}_x\text{O}_4$  ( $0 \leq x \leq 0.3$ ) at  $0.1 \text{ mVs}^{-1}$ .**

On the first anodic polarisation one peak was detected corresponding to the oxidation of divalent Mn. The onset and the centre of the anodic peak are shifted to slightly lower potentials with increasing V concentration. Furthermore, the anodic peak area is increasing in the concentration series and peaking at 25 mol % V substitution. The

signal for 30 mol % V substitution is reduced again and the data is in agreement with the galvanostatic load curves. On the subsequent cathodic polarisation two broad peaks are observable, where the first minor peak is located at about 3.8 V and the second major peak at about 2.7 V. The split into two extremely broad peaks can directly be attributed to the structural degradation, since the redox potential of a given cation is dependent on its chemical environment. Here, the first minor peak is believed to correspond to Mn still in its initial coordination, while the second major peak at lower potential can be attributed to the altered chemical environment. For V substituted samples both peaks are shifted to slightly higher potentials, which is caused by a decreased overpotential due to a lowered charge transfer resistance. An additional peak appears for V substituted samples, which is located at potentials close to the cut off. Upon the second anodic polarisation, the reference sample shows two broad anodic peaks, one obvious and the other barely visible. The same peaks are observed for the V substituted samples, with the same increasing behaviour as described for the first cycle. In addition, a new anodic peak, of increasing intensity within the concentration series, at about 2.7 V is observed. The second cathodic polarisation qualitatively resembles the first cycle where V substituted samples show an increased response, and the additional peak at relatively low potentials. Liivat and Thomas calculated the redox potential of  $V^{4+}/V^{5+}$  vs.  $Li/Li^+$  to be 2.1 V in a hypothetical  $Li_2FeVO_4$  structure.<sup>139</sup> This value would fit to the observed additional anodic peak at 2.7 V and the cathode peak below 2 V, but cannot explain why no additional anodic peak was observed upon the first oxidation. Contrary, if V would occupy Mn-sites, its redox potential should be strongly influenced by the inductive effect of the polyanion, and hence located at higher potentials.<sup>137</sup>

The structural changes that are proposed by CV and galvanostatic cycling were examined by *in situ* X-ray diffraction upon galvanostatic cycling, using Mo  $K_\alpha$  radiation in transmission mode.  $Li_2MnSiO_4$  and  $Li_2MnSi_{0.75}V_{0.25}O_4$  were chosen for investigations, and the evolution of the  $Pmn2_1$   $111$   $200$  and  $210$   $020$  double peaks was investigated. For an adequate time resolution the scan time was limited to about 22 min per scan, while the cells were cycled at a low current density of  $10 \text{ mA g}^{-1}$ . The level plots of  $Li_2MnSiO_4$  and  $Li_2MnSi_{0.75}V_{0.25}O_4$  are shown in Figure 5.19 a) and b) respectively.

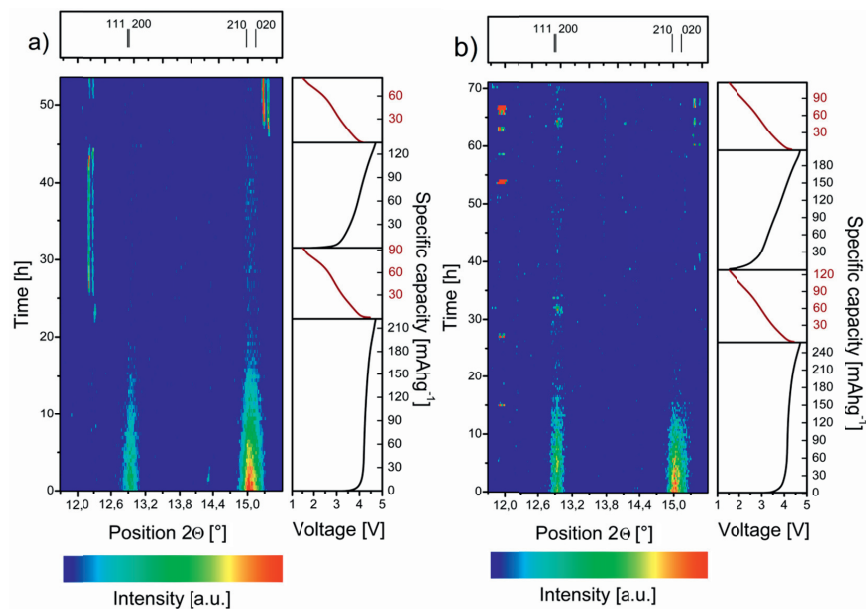


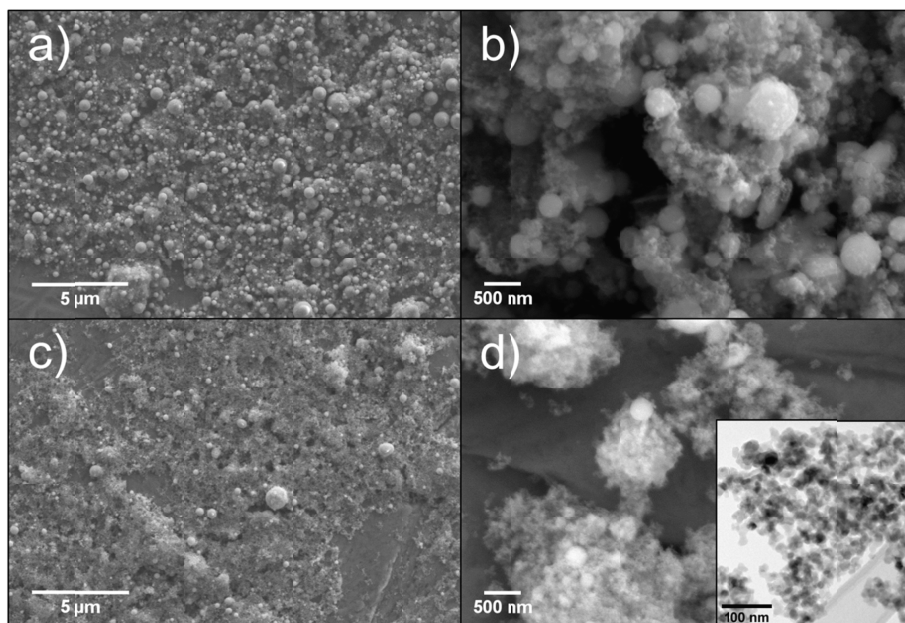
Figure 5.19: *In situ* XRD upon the first two galvanostatic cycle of a)  $\text{Li}_2\text{MnSiO}_4$  and b)  $\text{Li}_2\text{MnSi}_{0.75}\text{V}_{0.25}\text{O}_4$ .

The peak intensity of both samples is decreasing upon the first oxidation. In both cases the peaks corresponding to the  $Pmn2_1$  structure diminish into the background noise at capacities close to the value for the one electron reaction. V substitution shows no stabilising effect on the well-known structural degradation. The amorphisation was shown to be irreversible since none of the corresponding peaks reappears upon reduction or the subsequent cycle.

## 5.5 Liquid-feed flame spray pyrolysis as scalable $\text{Li}_2\text{MnSiO}_4$ synthesis approach

A scalable, not too time consuming, and inexpensive synthesis method, capable of producing large amounts of orthosilicate materials with a desired nanostructure, is crucial if these materials should ever be considered as an alternative electrode. Dahbi *et al.* addressed this issue for  $\text{Li}_2\text{FeSiO}_4$ , and invented a combustion synthesis which is rather quick and could eventually be scaled up.<sup>157</sup> Furthermore, it is well known that the industrial production of nanoparticles is feasible by aerosol flame processes. Combining such a process with a liquid precursor leads to liquid-feed flame spray pyrolysis (LFSP). This process has been explored during the last couple of decades and is used for the synthesis of ceramic nanoparticles.<sup>194</sup> However, this method was never applied to  $\text{Li}_2\text{MSiO}_4$  materials. Since the project was so far focused on  $\text{Li}_2\text{MnSiO}_4$ , it was also the material of choice for liquid-feed flame spray pyrolysis. To keep the synthesis cost low it was attempted to use an ethanol/water (5:1 by volume) based solution and waive expensive metal alkoxides as Mn and Li precursors. However, tetraethyl orthosilicate was the logical Si source due to its solubility in ethanol. Unfortunately, water has a negative influence on the enthalpy of combustion which led to inhomogeneities in the resulting morphology. To increase the enthalpy of combustion and hence the combustibility, the metal nitrates and TEOS were dissolved in pure alcohol. Additionally, 20 vol. % p-xylene was added to the solution as fuel enhancer. P-xylene has a high enthalpy of combustion ( $\Delta_c H^\circ = -4552 \text{ kJmol}^{-1}$  at 25 °C<sup>211</sup>) compared to ethanol ( $\Delta_c H^\circ = -1366 \text{ kJmol}^{-1}$  at 25 °C<sup>212</sup>) and showed a high influence on the combustibility of the solution. As previously discussed, the addition of a carbon former hinders particle growth during annealing, and hence it was possible to preserve the nanostructure during phase formation and carbon coating. A reducing heat treatment was still necessary to form the orthosilicate phase. As presented in chapter 3, the kinetics of phase formation at the moderate applied temperature are rather sluggish. The short residence time in the heat zone of the flame and the oxidising nature of the combustion itself did not allow for phase formation. The heat treatment parameters were reevaluated for this different synthesis approach, and finally powders were annealed at 650 °C for 10h in a flow of 5%  $\text{H}_2$  in Ar. 25 wt. % cornstarch acted as carbon source. Figure 5.20 points out the morphological differences of the two approaches, where a) shows the as-pyrolysed powder from the 5:1 ethanol/water solution and b) the reduced and carbon coated sample. The sample from the 5:1 ethanol/p-xylene solution are shown in the as-pyrolysed state in c) and in the reduced and coated state in d). The ethanol/water combustion resulted in an inhomogeneous powder morphology. In addition to the desired nanoparticles, the powder contained a high amount of spherical particles in the sub- $\mu\text{m}$  to  $\mu\text{m}$  range. The increased enthalpy of combustion of the ethanol/p-xylene solution resulted in much

higher homogeneity of the powder. Only a few larger particles were still present. The inset of Figure 5.20 d) shows a TEM micrograph of the loosely agglomerated nanoparticles of about 20 nm in size.

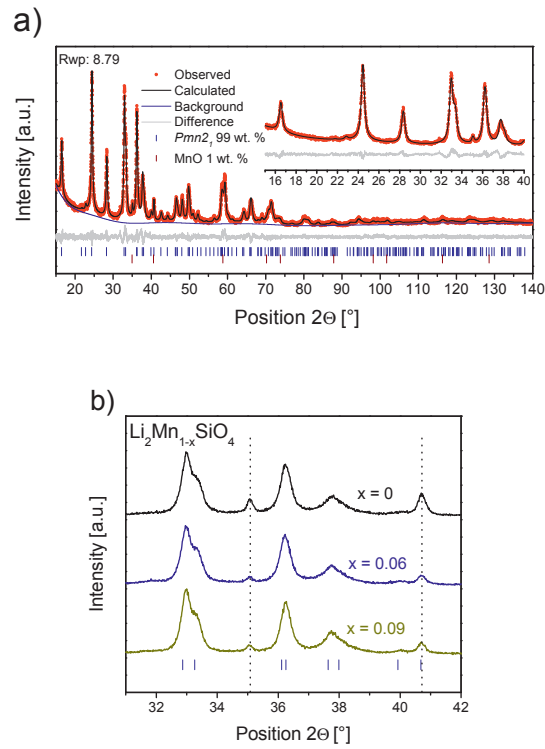


**Figure 5.20:** FE-SEM micrographs of a) the as-pyrolysed and b) the carbon coated powder from EtOH/H<sub>2</sub>O solution. c) shows the as pyrolysed powder from the EtOH/p-xylene solution, and d) the corresponding carbon coated sample. The inset shows a TEM bright-field micrograph of the same sample.

The resulting powders offered an amorphous carbon content of ~6 wt. % and exhibited high phase purity. The sample from the ethanol/p-xylene solution showed only MnO as secondary phase. Samples with 6 and 9 mol % Mn sub-stoichiometry were synthesised to analyse the possibility of eliminating the secondary phase. The phase fraction and the calculated crystallite size from the full width at half maximum are summarised in Table 5.4 Where the figure behind M indicates the nominal Mn stoichiometry. Figure 5.21 shows the full pattern refinements of the sample with 6 mol % Mn sub-stoichiometry and the evolution of the MnO secondary phase with decreasing Mn content.

Table 5.4: Phase fractions of LMS, LM0.94S and LM0.91S from EtOH/p-xylene solutions according to Rietveld refinements.

Sample Index	$\text{Li}_2\text{MnSiO}_4$ [wt. %]	MnO [wt. %]	$\text{Li}_2\text{SiO}_3$ [wt. %]	Crystallite size from XRD [nm]
LMS	97	3	-	23.5
LM0.94S	99	1	-	24
LM0.91S	96.5	1.5	2	25

Figure 5.21: a) Full pattern refinement of a nominal 6 mol % Mn sub-stoichiometric  $\text{Li}_2\text{MnSiO}_4$  sample. b) Evolution of the MnO secondary phase with increasing Mn sub-stoichiometry.

The fact that progressive Mn sub-stoichiometry did not result in the disappearance of the MnO secondary phase, but rather results in the occurrence of  $\text{Li}_2\text{SiO}_3$  suggests a tolerance towards slight non-stoichiometry in the Mn sub lattice.

The large difference in the powder morphology due to the enhanced solution combustibility suggests changes in the charge/discharge characteristics of the powders. Figure 5.22 shows the first galvanostatic cyclic of the flame spray pyrolysed powders and compares them to the sol-gel sample from paper I.

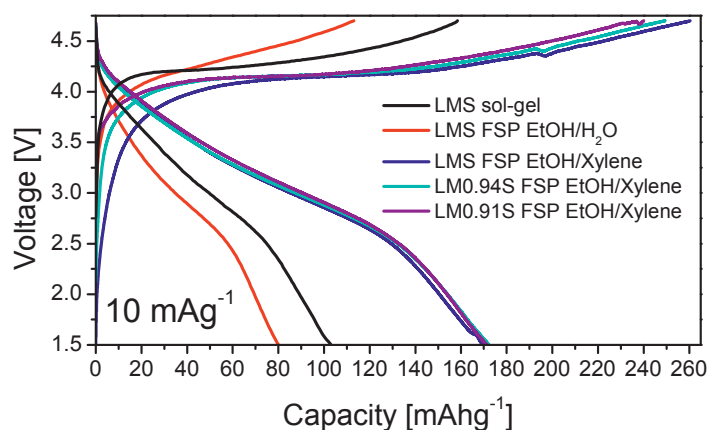


**Figure 5.22: First galvanostatic cycle of the flame pyrolysed  $\text{Li}_2\text{MnSiO}_4$  powders from different solutions. Mn sub-stoichiometry is denoted by the figure behind the M. A sol-gel sample synthesised according the description in Paper I is included.**

The sample based on the ethanol/water pyrolysis showed a low discharge capacity of  $80 \text{ mAhg}^{-1}$ , caused by a huge amount of large spherical particles, which do not allow extensive delithiation. However, substituting water against p-xylene as combustion aid showed a major impact and resulted in an over 100% increased discharge capacity. The discrepancy between charge and discharge and the resulting loss was previously discussed. Interestingly, the charge capacity showed a slight decreasing trend, reflecting the Mn stoichiometry, while the discharge capacity was not influenced.

The nanostructure also influenced the rate capability. Samples from the p-xylene aided pyrolysis reached values corresponding to the exchange of more than 1 Li per formula unit and showed a high initial discharge capacity of over  $140 \text{ mAhg}^{-1}$  even at a moderate current density of  $80 \text{ mA}g^{-1}$ . The initial discharge capacity of a 6 mol % Mn sub-stoichiometric sample is shown in Figure 5.23. The inset shows 25 cycles at different current densities. In the cycling plot it has to be considered that the initial cycles will influence the capacity of the later cycles due to the structural degradation. Comparing the values to capacities achieved in Paper I clearly illustrates the improved properties with respect to discharge capacity and rate capability.

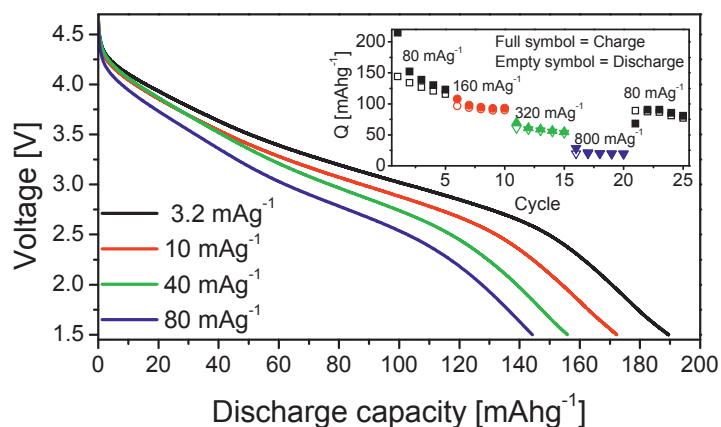


**Figure 5.23:** First discharge, of a 6 mol % Mn deficient sample from xylene aided pyrolysis at different rates. The inset shows 25 cycles at higher current densities.

*In situ* XRD revealed that also the nanostructured  $\text{Li}_2\text{MnSiO}_4$  particles made by flame spray pyrolysis become amorphous upon the first oxidation. Furthermore, it was shown that the structural degradation is directly linked to the amount of Li exchanged, hence the amount of Mn oxidised. The degradation was slowed down by limiting the potential window, but it could not be prevented.



## 5.6 $\text{Li}_2\text{FeSiO}_4$ and $\text{Li}_2\text{Fe}_{0.5}\text{Mn}_{0.5}\text{SiO}_4$ by liquid-feed flame spray pyrolysis

In the last part of this thesis the gained knowledge gained from Paper IV was used to synthesise  $\text{Li}_2\text{FeSiO}_4$  and  $\text{Li}_2\text{Fe}_{0.5}\text{Mn}_{0.5}\text{SiO}_4$  by liquid-feed flame spray pyrolysis (LF-FSP). The solution was based on the previously described 5:1 ethanol/p-xylene ratio and the same concentration of precursors were dissolved. As Fe precursor ferric nitrate was used, and the mixed metal orthosilicate was synthesised using ferric nitrate and Mn nitrate. Ferric nitrate was chosen because of the oxidation tendency and solubility limitations of available ferrous precursors. Furthermore, the applied atmosphere during annealing was changed to a slow flow of 2%  $\text{H}_2$  in Ar to hinder Fe reduction to the elementary state. FE-SEM analysis revealed differences to the previously synthesised  $\text{Li}_2\text{MnSiO}_4$  samples. The  $\text{Li}_2\text{FeSiO}_4$  sample showed bigger particles and large dense agglomerates. Since the only altered parameter compared to the synthesis described in Paper IV, was the Fe salt, concentration effects were investigated. The original concentration of the metal cation was  $0.24 \text{ molL}^{-1}$ , disregarding volume effects of the ethanol/p-xylene mixture. A new synthesis was performed with a diluted Fe concentration of  $0.12 \text{ molL}^{-1}$ . The FE-SEM micrograph of the two  $\text{Li}_2\text{FeSiO}_4$  samples and the  $\text{Li}_2\text{Fe}_{0.5}\text{Mn}_{0.5}\text{SiO}_4$  sample are shown in Figure 5.24.

Comparing the micrographs in a) and b) to the micrographs in c) and d), which correspond to the more diluted precursor solution, the desired effect is clearly visible. The powder from the less concentrated solution resulted in more loosely agglomerated nanoparticles and despite some spherical bigger particles, no exaggerated particle growth and aggregation could be observed. The morphology of  $\text{Li}_2\text{Fe}_{0.5}\text{Mn}_{0.5}\text{SiO}_4$  was also influenced by the Fe precursor, and fewer dense particles were present. The surface area measurements correlate well with the SEM observations. While  $\text{Li}_2\text{FeSiO}_4$  from a  $0.24 \text{ molL}^{-1}$  solution offered an external surface area of  $37 \text{ m}^2 \text{ g}^{-1}$ , the more diluted solution resulted in an increased external surface area of  $72 \text{ m}^2 \text{ g}^{-1}$ . The value of the mixed metal orthosilicate gave an average value in between these two with  $57 \text{ m}^2 \text{ g}^{-1}$ . The refined X-ray diffraction patterns of  $\text{Li}_2\text{FeSiO}_4$  and  $\text{Li}_2\text{Fe}_{0.5}\text{Mn}_{0.5}\text{SiO}_4$  are shown in Figure 5.25.

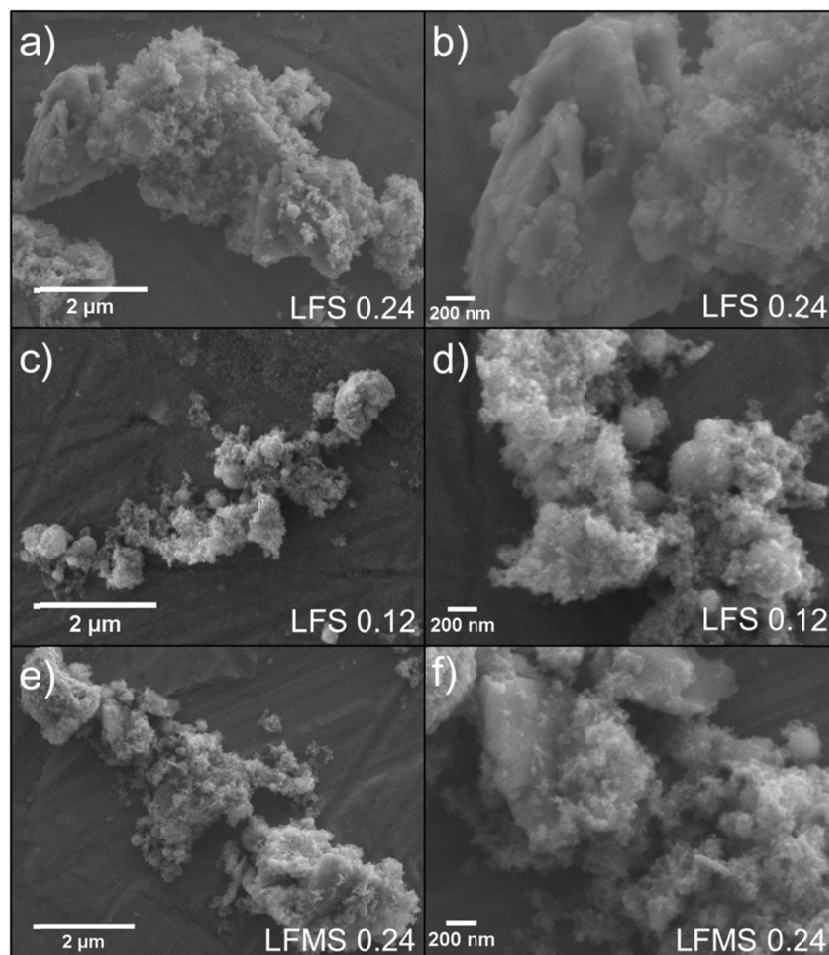


Figure 5.24: FE-SEM micrographs of a) and b)  $\text{Li}_2\text{FeSiO}_4$  from a  $0.24 \text{ molL}^{-1}$  Fe solution, c) and d)  $\text{Li}_2\text{FeSiO}_4$  from a  $0.12 \text{ molL}^{-1}$  Fe solution, e) and f)  $\text{Li}_2\text{Fe}_{0.5}\text{Mn}_{0.5}\text{SiO}_4$  from a  $0.24 \text{ molL}^{-1}$  Fe/Mn solution.

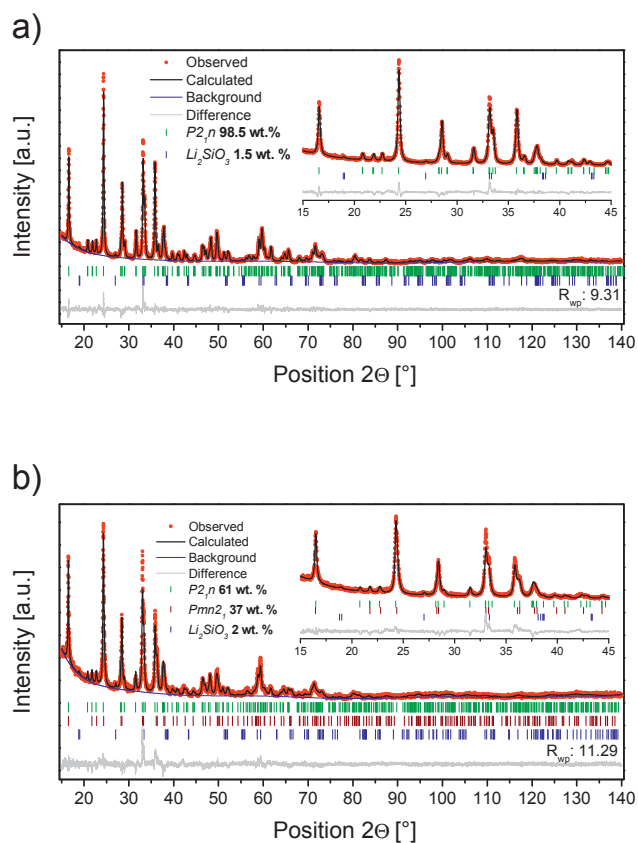


Figure 5.25: Full pattern refinements of  $\text{Li}_2\text{FeSiO}_4$  and  $\text{Li}_2\text{Fe}_{0.5}\text{Mn}_{0.5}\text{SiO}_4$  including  $hkl$  markers and phase fractions.

$\text{Li}_2\text{FeSiO}_4$  was fitted to a monoclinic  $\gamma_s$  polymorph ( $P2_1n$ ). Suggested atomic positions and lattice parameters of Dahbi *et al.*<sup>157</sup> were chosen as initial parameters.  $\text{Li}_2\text{Fe}_{0.5}\text{Mn}_{0.5}\text{SiO}_4$  on the other hand, could not be described by a single polymorph, but was shown to exist as a mixture of monoclinic  $\gamma_s$  and orthorhombic  $\beta_{\text{II}}$ . The lattice parameters, the calculated crystallite sizes and the carbon content, estimated from TGA data, are summarised in Table 5.5.

**Table 5.5: Unit cell parameters, calculated crystallite size and carbon content of  $\text{Li}_2\text{FeSiO}_4$  from  $0.24 \text{ molL}^{-1}$  and  $0.12 \text{ molL}^{-1}$  solution, and  $\text{Li}_2\text{Fe}_{0.5}\text{Mn}_{0.5}\text{SiO}_4$  from a  $0.24 \text{ molL}^{-1}$  solution.**

Sample	a [Å]	b [Å]	c [Å]	$\beta$ [°]	Unit cell volume [Å <sup>3</sup> ]	Crystallite size from <i>111</i> [nm]	Carbon content [wt. %]
<b>LFS 0.24</b> ( <i>P2<sub>1</sub>n</i> )	8.21987(37)	5.01401(15)	8.24400(37)	98.9590(21)	335.628(24)	42	12
<b>LFS 0.12</b> ( <i>P2<sub>1</sub>n</i> )	8.2164(10)	5.01225(39)	8.2424(11)	98.9363(54)	335.326(66)	28.5	10
<b>LFMS 0.24</b> ( <i>P2<sub>1</sub>n</i> )	8.2688(23)	5.00961(39)	8.2689(26)	98.8757(26)	338.43(15)	40	6-7
<b>LFMS 0.24</b> ( <i>Pmn2<sub>1</sub></i> )	6.2772(17)	5.374(14)	4.96277(80)	-	167.428(68)	34*	

\* Calculated from orthorhombic *011*

Calculated unit cell dimensions of both  $\text{Li}_2\text{FeSiO}_4$  samples are very similar to each other and in agreement with data from the literature.<sup>150,157</sup>  $\text{Li}_2\text{Fe}_{0.5}\text{Mn}_{0.5}\text{SiO}_4$  shows an increased *P2<sub>1</sub>n* cell volume. While, the volume of the *Pmn2<sub>1</sub>* unit cell is slightly smaller than for  $\text{Li}_2\text{MnSiO}_4$  reported in the previous sections. This is caused by differences in ionic radius of tetrahedrally coordinated  $\text{Mn}^{2+}$  and  $\text{Fe}^{2+}$ , where the former has an ionic radius of 0.80 Å, and the latter 0.77 Å.<sup>138</sup> Furthermore, the decreased precursor concentration led to a reduced calculated crystallite size, which is in agreement with the SEM observations and BET data.  $\text{Li}_2\text{Fe}_{0.5}\text{Mn}_{0.5}\text{SiO}_4$  shows a discrepancy of the calculated crystallite size between the two polymorphs. The crystallite size calculation could in this case be highly influenced by the overlapping peaks and strain between both polymorphs.

The morphological differences showed a significant impact on the charge/discharge behaviour. Figure 5.26 shows the first and second galvanostatic cycle of the 3 samples.

Structural changes of  $\text{Li}_2\text{FeSiO}_4$  are well understood. The structure forms an inverted  $\beta_{\text{II}}$  structure upon cycling.<sup>20,117</sup> The low initial charge capacity is due to the partial oxidation of Fe during prolonged storage in air.<sup>213</sup> Increased surface area values, by less densely aggregated and smaller particles resulted in a 60% higher discharge capacity.

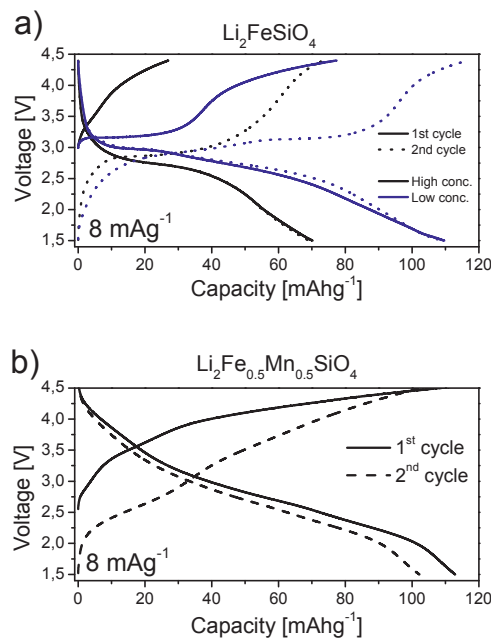


Figure 5.26: First and second galvanostatic cycles of a)  $\text{Li}_2\text{FeSiO}_4$  and b)  $\text{Li}_2\text{Fe}_{0.5}\text{Mn}_{0.5}\text{SiO}_4$

The discharge behaviour of  $\text{Li}_2\text{Fe}_{0.5}\text{Mn}_{0.5}\text{SiO}_4$  is more complicated. The strongly sloping profile and the capacity decay suggest the same structural collapse as known from  $\text{Li}_2\text{MnSiO}_4$ . Differential capacity plots (Paper V) show 2 broad Mn peaks in cathodic and anodic direction. The Fe redox peaks are also broad and situated at a lower potential of 2.3 V in cathodic and 2.6 V in anodic direction. This is probably caused by the changed chemical environment due to the structural collapse, induced by tetrahedrally coordinated trivalent Mn.  $\text{Li}_2\text{Fe}_{0.5}\text{Mn}_{0.5}\text{SiO}_4$  suffers from severe capacity decay upon cycling, but the retention after prolonged cycling is increased compared to  $\text{Li}_2\text{MnSiO}_4$ . In addition, differential capacity plots revealed that the redox activity after prolonged cycling can be attributed solely to Fe. In contrary to  $\text{Li}_2\text{MnSiO}_4$ , the structure of  $\text{Li}_2\text{Fe}_{0.5}\text{Mn}_{0.5}\text{SiO}_4$  was still partially crystalline after 40 cycles, indicating a slight stabilisation. In comparison,  $\text{Li}_2\text{FeSiO}_4$  offered a good cycling performance and showed more than 90% capacity retention after 300 cycles. Also, the rate performance was exceptional with more than 50% capacity retention when the current density was increase from 8 to 800 mA g<sup>-1</sup> at room and elevated temperatures.

## 6. Conclusions

In the first part of this project, porous, nanosized and carbon coated  $\text{Li}_2\text{MnSiO}_4$  was successfully synthesised by a PVA assisted sol-gel route. The synthesis parameters were optimised in order to achieve high phase purities and a desired porous nanostructure. The samples were indexed and refined to the orthorhombic  $\beta_{\text{II}}$  phase ( $Pmn2_1$ ), but samples synthesised with low amounts of corn-starch showed a higher amount of secondary phases, namely  $\text{Li}_2\text{SiO}_3$ ,  $\text{MnO}$  and  $\text{Mn}_2\text{SiO}_4$ . Next to the main polymorph, traces of the orthorhombic  $\gamma_{\text{II}}$  phase were present in samples with low or no corn-starch addition. The addition of corn-starch as carbon former has been further shown to have a huge impact on the particle size and surface area and is believed to hinder excessive particle growth. Hence it also greatly affected the electrochemical performance. The highest reversible capacities achieved with these materials were in the range of a reversible 1 electron reaction, but high irreversible losses in the first cycle and general capacity decay, caused by a structural collapse occurred. High amounts of residual carbon further increased the generally poor rate performance, which highlight the impact of the low conductivity of  $\text{Li}_2\text{MnSiO}_4$ .

In the second part, cationic substitutions based on the elaborated synthesis method were investigated. The incorporation of up to 20 mol % Fe was shown. Higher Fe concentration would require changes in the synthesis method since the acidic behaviour of ferric nitrate had a strong influence on the gelation. Fe substituted samples showed an increased electrochemical performance. Also here, poor rate capability and high capacity decay was observed. Furthermore, the incorporation of 5 mol % V into  $\text{Li}_2\text{MnSiO}_4$  was successfully shown. It was intended to incorporate V either on a Mn site or on a Si site in the structure. The enhanced electrochemical performance and the not well understood nature of V substitution were further investigated.

For subsequent in-depth investigations concerning the feasibility of substituting V for Mn or Si, nominal compositions  $\text{Li}_2\text{Mn}_{1-x}\text{V}_x\text{SiO}_4$  ( $0 \leq x \leq 0.2$ ) and  $\text{Li}_2\text{MnSi}_{1-x}\text{V}_x\text{O}_4$  ( $0 \leq x \leq 0.3$ ) were synthesised. Limited solid solubility of V on the Mn-site was shown to cause phase separation and V exclusion at V concentrations  $\geq 10$  mol %. The substitution onto the Si-site caused increased misfits in the patterns, suggesting disorder. However, overall the system could still be described by the space group  $Pmn2_1$ . An

inhomogeneous distribution of V, which was mainly present in a tetravalent state, was revealed by STEM EELS. Dependent on the concentration, some lower valence V at lower concentrations and higher valence V at higher concentrations were detected. A combination of the findings strongly suggests varying local compositions. XRD and STEM EELS further revealed the apparent secondary MnO phase to be more correctly addressed as  $\text{Mn}_{1-x}\text{V}_y\text{O}$  ( $1-x+y < 1$ ). This phase is believed to be caused either by a limited solid solubility of the system, or induced by the thermal history of the sample. Superior electrochemical performance was detected for  $\text{Li}_2\text{MnSi}_{1-x}\text{V}_x\text{O}_4$  ( $0 \leq x \leq 0.25$ ) structures. The highest discharge capacity was offered by the nominal composition  $\text{Li}_2\text{MnSi}_{0.75}\text{V}_{0.25}\text{O}_4$ , which reached  $160 \text{ mAhg}^{-1}$  in the initial cycle at  $10 \text{ mAg}^{-1}$ . This value corresponds roughly to the 1 Li per formula unit reaction. The value was 40% higher than the reference sample. CV measurements revealed additional redox activity which could be attributed to the  $\text{V}^{4+}/\text{V}^{5+}$  redox couple. AC impedance spectroscopy showed decreased charge transfer resistance and increased values for Li diffusion. Unfortunately, no effect on the structural instability upon cycling was detected, and *in situ* XRD analysis showed amorphisation of the substituted and reference samples.

The last part concerned the feasibility of a scalable method capable of synthesising desired nanostructures. Liquid-feed flame spray pyrolysis was shown as an alternative method which enables preparation of nanoscaled  $\text{Li}_2\text{MnSiO}_4$  in large quantities. The heat of combustion of the precursor solution had a major impact on the particle morphology and the resulting electrochemical performance. Furthermore, the likelihood of  $\text{Li}_2\text{MnSiO}_4$  tolerating slight Mn sub-stoichiometry was shown. The highest capacity achieved in this study was  $190 \text{ mAhg}^{-1}$  during the first discharge at a current density of  $3.2 \text{ mAg}^{-1}$ . At an elevated current density of  $80 \text{ mAg}^{-1}$  the first discharge capacity still exceeded  $140 \text{ mAhg}^{-1}$ , demonstrating the improved rate performance. Values over  $166 \text{ mAhg}^{-1}$  cannot solely be caused by the  $\text{Mn}^{2+/3+}$  redox couple. Also, the high charge capacities suggest activity of the second redox couple ( $\text{Mn}^{3+/4+}$ ) at low current densities, but the structural collapse does not allow full delithiation during the discharge. It was not possible to reach the theoretical capacity even at low current densities, and it can thus be concluded that the mobilisation of the second Li ion not only requires the structural instability to be overcome, but also electrolytes with a larger potential window. All samples in this study showed a prominent irreversible capacity loss between the first charge and discharge and capacity fade caused by the structural instability of  $\text{Li}_2\text{MnSiO}_4$ . *In situ* XRD experiments showed that an irreversible loss of crystallinity already occurs during the first charge. It is concluded that  $\text{Li}_2\text{MnSiO}_4$  has major shortcomings to be solved before it could potentially become interesting for battery applications, since the ability of delivering two Li per

formula unit is not possible in the given potential range without the stabilisation of the structure.

Furthermore, the synthesis method was shown to be applicable also to  $\text{Li}_2\text{FeSiO}_4$  and  $\text{Li}_2\text{Fe}_{0.5}\text{Mn}_{0.5}\text{SiO}_4$ . Both compounds were successfully synthesised with high phase purities. The concentration of ferric nitrate showed a major impact on particle growth, and  $\text{Li}_2\text{FeSiO}_4$  synthesised from a less concentrated solution showed increased surface area and electrochemical properties.  $\text{Li}_2\text{FeSiO}_4$  was indexed to the monoclinic  $\gamma_s$  polymorph and converted to the inverse  $\beta_{\text{II}}$  structure upon cycling.  $\text{Li}_2\text{Fe}_{0.5}\text{Mn}_{0.5}\text{SiO}_4$  was present in a mixture of monoclinic  $\gamma_s$  and orthorhombic  $\beta_{\text{II}}$ . It reached a discharge capacity of  $115 \text{ mAhg}^{-1}$  at a current density of  $8 \text{ mA g}^{-1}$ , suggesting that both cations undergo to a large extent the one electron redox reaction. Severe capacity fading upon cycling was observed, similar to the well-known behaviour of  $\text{Li}_2\text{MnSiO}_4$ . However, while  $\text{Li}_2\text{MnSiO}_4$  loses almost all capacity upon prolonged cycling,  $\text{Li}_2\text{Fe}_{0.5}\text{Mn}_{0.5}\text{SiO}_4$  retained 40% of the initial capacity after prolonged cycling. The solid solution  $\text{Li}_2\text{Fe}_{0.5}\text{Mn}_{0.5}\text{SiO}_4$  was shown to be at least partly crystalline after prolonged cycling, hence indicating a slightly more stable structure. Differential capacity plots suggest the redox activity in later cycles to be caused solely by  $\text{Fe}^{2+}/\text{Fe}^{3+}$ . Mn is believed to either form an electrochemically inactive amorphous phase or dissolve into the electrolyte. In comparison,  $\text{Li}_2\text{FeSiO}_4$  was shown to be stable upon prolonged cycling. In this study,  $\text{Li}_2\text{FeSiO}_4$  was cycled up to 300 times with more than 90% capacity retention. Post cycling X-ray diffraction and the evolution of the differential capacity demonstrate a stable system. At elevated temperatures and a slow rate, the reversible exchange of up to one Li per Fe was shown.





## 7. Outlook

While it was shown in the last part of this work, that nanosizing and carbon coating can overcome capacity and rate performance issues caused by the poor ionic and electronic conductivity, the structural instability upon oxidation and the need for higher potentials limit the performance of  $\text{Li}_2\text{MnSiO}_4$ . To completely exploit the 2 Li per formula unit and hence the second redox couple  $\text{Mn}^{3+}/\text{Mn}^{4+}$ , electrolytes with a stable potential window of at least 5 V are required. But even if that might be the case soon, stabilising higher valences of Mn in a tetrahedral environment seems hopeless, since even 50% cation substitution cannot hinder the severe capacity fade.

V substitution has been shown to have a major influence on the performance, by decreasing the charge transfer resistance and increasing the Li ion mobility. Additionally, the results in this study strongly suggest redox activity of V in the orthosilicate structure. Since the available literature on V substitution is unsatisfactory it would be highly interesting to see if V incorporation in  $\text{Li}_2\text{FeSiO}_4$  would show the same positive effect. Furthermore, the control of  $p_{\text{O}_2}$  and the thermal history should be improved in order to determine the limitations of V substitution, and give rise to elaborate a phase diagram.

Liquid-feed flame spray pyrolysis has shown capability of producing a nanoscale precursor, which can be converted into highly active  $\text{Li}_2\text{MSiO}_4$  compounds. The addition of carbon former and an annealing step are still required. But, in contrast to top-down approaches the mixing step is only a homogenisation step, rather than a grinding step in order to reduce the particle size. Hence, a soluble carbon former would simplify this step. Furthermore, the morphology of  $\text{Li}_2\text{FeSiO}_4$  has to be improved to the same level as observed for  $\text{Li}_2\text{MnSiO}_4$ . The substitution of ferric nitrate by more combustible Fe containing compounds would be promising. Since the solubility of most inorganic compounds in organic solutions, like the ethanol p-xylene mixture used here, is very limited, organometallic Fe compounds like ferrocene, Fe carboxylates or Fe alkoxides should be considered.

## Chapter 7 Outlook

---

Liquid-feed flame spray pyrolysis of such a highly combustible solution could result in a morphology, equal to or even improved comparable to the morphology observed for  $\text{Li}_2\text{MnSiO}_4$ . If combined with a soluble carbon former, the method could give rise to the production of battery grade  $\text{Li}_2\text{FeSiO}_4$  in a short amount of time and hence be promising as cathode material.

## 8. References

- (1) Milazzo, G.; Caroli, S.; Sharma, V. K. *Elektrodenpotentiale: Tables of Standard Electrode Potentials.*; 1978.
- (2) Tarascon, J. M.; Armand, M. Issues and Challenges Facing Rechargeable Lithium Batteries. *Nature* **2001**, *414* (6861), 359–367.
- (3) Nagaura, T.; Tozawa, K. Lithium Ion Rechargeable Battery. *Prog. Batter. Sol. Cells* **1990**, *9*, 209.
- (4) Ellis, B. L.; Lee, K. T.; Nazar, L. F. Positive Electrode Materials for Li-Ion and Li-Batteries. *Chem. Mater.* **2010**, *22* (3), 691–714.
- (5) Kurzweil, P.; Brandt, K. Secondary Batteries. *Encycl. Electrochem. Power Sources* **2009**, *13* (323), 1–26.
- (6) Ellis, B. L.; Town, K.; Nazar, L. F. New Composite Materials for Lithium-Ion Batteries. *Electrochim. Acta* **2012**, *84*, 145–154.
- (7) Fergus, J. W. Recent Developments in Cathode Materials for Lithium Ion Batteries. *J. Power Sources* **2010**, *195* (4), 939–954.
- (8) Scrosati, B.; Garche, J. Lithium Batteries: Status, Prospects and Future. *J. Power Sources* **2010**, *195* (9), 2419–2430.
- (9) Ozawa, K. Lithium-Ion Rechargeable Batteries with LiCoO<sub>2</sub> and Carbon Electrodes: The LiCoO<sub>2</sub>/C System. *Solid State Ionics* **1994**, *69* (3-4), 212–221.
- (10) Daniel, C.; Besenhard, J. O. *Handbook of Battery Materials, Second Edition*, 2nd ed.; Wiley-VCH, 2011.
- (11) Mizushima, K.; Jones, P.; Wiseman, P.; Goodenough, J. B. Li<sub>x</sub>CoO<sub>2</sub> (0 < x < 1): A New Cathode Material for Batteries of High Energy Density. *Mater. Res. Bull.* **1980**, *15*, 783–789.

- (12) Gaines, L.; Cuenca, R. *Costs of Lithium-Ion Batteries for Vehicles*; 2000; Vol. 48.
- (13) Padhi, A. K.; Nanjundaswamy, K. S.; Goodenough, J. B. Phospho-Olivines as Positive-Electrode Materials for Rechargeable Lithium Batteries. *J. Electrochem. Soc.*, **1997**, *144* (4), 1188.
- (14) Andre, D.; Kim, S.-J.; Lamp, P.; Lux, S. F.; Maglia, F.; Paschos, O.; Stiaszny, B. Future Generations of Cathode Materials: An Automotive Industry Perspective. *J. Mater. Chem. A* **2015**, *3*, 6709–6732.
- (15) Nytén, A.; Abouimrane, A.; Armand, M.; Gustafsson, T.; Thomas, J. O. Electrochemical Performance of  $\text{Li}_2\text{FeSiO}_4$  as a New Li-Battery Cathode Material. *Electrochem. commun.* **2005**, *7* (2), 156–160.
- (16) Dominko, R.; Bele, M.; Gabersček, M.; Meden, A.; Remškar, M.; Jamnik, J. Structure and Electrochemical Performance of  $\text{Li}_2\text{MnSiO}_4$  and  $\text{Li}_2\text{FeSiO}_4$  as Potential Li-Battery Cathode Materials. *Electrochem. commun.* **2006**, *8* (2), 217–222.
- (17) Haxel, G. B.; Hedrick, J. B.; Orris, G. J.; Sound, S.; Of, M.; Mineral, O. U. R. Rare Earth Elements — Critical Resources for High Technology. *United States Geol. Surv. Fact Sheet* **2002**, *087*, 4.
- (18) Dominko, R.  $\text{Li}_2\text{MSiO}_4$  (M = Fe And/or Mn) Cathode Materials. *J. Power Sources* **2008**, *184* (2), 462–468.
- (19) Islam, M. S.; Dominko, R.; Masquelier, C.; Sirisopanaporn, C.; Armstrong, A. R.; Bruce, P. G. Silicate Cathodes for Lithium Batteries: Alternatives to Phosphates? *J. Mater. Chem.* **2011**, *21*, 9811–9818.
- (20) Armstrong, A. R.; Kuganathan, N.; Islam, M. S.; Bruce, P. G. Structure and Lithium Transport Pathways in  $\text{Li}_2\text{FeSiO}_4$  Cathodes for Lithium Batteries. *J. Am. Chem. Soc.* **2011**, *133*, 13031–13035.
- (21) Kuganathan, N.; Islam, M. S.  $\text{Li}_2\text{MnSiO}_4$  Lithium Battery Material: Atomic-Scale Study of Defects, Lithium Mobility, and Trivalent Dopants. *Chem. Mater.* **2009**, *21* (21), 5196–5202.

- (22) Gummow, R. J.; He, Y. Recent Progress in the Development of  $\text{Li}_2\text{MnSiO}_4$  Cathode Materials. *J. Power Sources* **2014**, *253*, 315–331.
- (23) Larsson, P.; Ahuja, R.; Liivat, A.; Thomas, J. O. Structural and Electrochemical Aspects of Mn Substitution into  $\text{Li}_2\text{FeSiO}_4$  from DFT Calculations. *Comput. Mater. Sci.* **2010**, *47* (3), 678–684.
- (24) Aricò, A. S.; Bruce, P.; Scrosati, B.; Tarascon, J.; Schalkwijk, W. V. a N.; Picardie, U. De; Verne, J.; Umr-, C. Nanostructured Materials for Advanced Energy Conversion and Storage Devices. **2005**, *4* (May).
- (25) Whittingham, M. S. Lithium Batteries and Cathode Materials. *Chem. Rev.* **2004**, *104* (10), 4271–4301.
- (26) Whittingham, M. S. Electrical Energy Storage and Intercalation Chemistry. *Science (80-. )*. **1976**, *192* (4244), 1126–1127.
- (27) J.Orman, H.; J.Wiseman, P. Cobalt(III) Lithium Oxide,  $\text{CoLiO}_2$ : Structure Refinement by Powder Neutron Diffraction. *Acta Cryst.* **1984**, *C40*, 12–14.
- (28) Amatucci, G. Cobalt Dissolution in  $\text{LiCoO}_2$ -Based Non-Aqueous Rechargeable Batteries. *Solid State Ionics* **1996**, *83* (1-2), 167–173.
- (29) Wang, H.; Jang, Y.; Huang, B.; Sadoway, D. R.; Chiang, Y. TEM Study of Electrochemical Cycling-Induced Damage and Disorder in  $\text{LiCoO}_2$  Cathodes for Rechargeable Lithium Batteries. *J. Electrochem. Soc.* **1999**, *146* (2), 473–480.
- (30) Zhecheva, E.; Stoyanova, R. Stabilization of the Layered Crystal Structure of  $\text{LiNiO}_2$  by Co-Substitution. *Solid State Ionics* **1993**, *66* (1-2), 143–149.
- (31) Poullierie, C.; Croguennec, L.; Delmas, C.  $\text{Li}_x\text{Ni}_{1-y}\text{Mg}_y\text{O}_2$  ( $y = 0.05, 0.10$ ) System: Structural Modifications Observed upon Cycling. *Solid State Ionics* **2000**, *132* (1), 15–29.
- (32) Guilmard, M.; Poullierie, C.; Croguennec, L.; Delmas, C. Structural and Electrochemical Properties of  $\text{LiNi}_{0.70}\text{Co}_{0.15}\text{Al}_{0.15}\text{O}_2$ . *Solid State Ionics* **2003**, *160* (1-2), 39–50.
- (33) Naghash, A. R.; Lee, J. Y. Lithium Nickel Oxyfluoride ( $\text{Li}_{1-z}\text{Ni}_{1+z}\text{F}_y\text{O}_{2-y}$ ) and Lithium for Lithium Rechargeable Batteries II . Electrochemical

- Investigations. *Electrochim. Acta* **2001**, *46*, 2293–2304.
- (34) Park, S. H.; Sun, Y. K.; Park, K. S.; Nahm, K. S. Synthesis and Electrochemical Properties of Lithium Nickel Oxysulfide ( $\text{LiNi}_x\text{S}_y\text{O}_{2-y}$ ) Material for Lithium Secondary Batteries. *Electrochim. ...* **2002**, *47*, 1–6.
- (35) Thackeray, M. M.; David, W. I. F.; Bruce, P. G.; Goodenough, J. B. Lithium Insertion into Manganese Spinel. *Mater. Res. Bull.* **1983**, *18* (4), 461–472.
- (36) Tarascon, J. M.; Wang, E.; Shokoohi, F. K. The Spinel Phase of  $\text{LiMn}_2\text{O}_4$  as a Cathode in Secondary Lithium Cells. *J. Electrochem. Soc.* **1991**, *138* (10), 2859.
- (37) Liu, Z.; Yu, A.; Lee, J. Y. Synthesis and Characterization of  $\text{LiNi}_{1-x-y}\text{Co}_x\text{Mn}_y\text{O}_2$  as the Cathode Materials of Secondary Lithium Batteries. *J. Power Sources* **1999**, *81-82*, 416–419.
- (38) Rossen, E.; Jones, C. D. W.; Dahn, J. R. Structure and Electrochemistry of  $\text{Li}_x\text{Mn}_y\text{Ni}_{1-y}\text{O}_2$ . *Solid State Ionics* **1992**, *57*, 311–318.
- (39) Ohzuku, T.; Makimura, Y. Layered Lithium Insertion Material of  $\text{LiCo}_{1/3}\text{Ni}_{1/3}\text{Mn}_{1/3}\text{O}_2$  for Lithium-Ion Batteries. *Chem. Lett.* **2001**, No. 7, 642–643.
- (40) Yabuuchi, N.; Ohzuku, T. Novel Lithium Insertion Material of  $\text{LiCo}_{1/3}\text{Ni}_{1/3}\text{Mn}_{1/3}\text{O}_2$  for Advanced Lithium-Ion Batteries. *J. Power Sources* **2003**, *119-121*, 171–174.
- (41) Koyama, Y.; Tanaka, I.; Adachi, H.; Makimura, Y.; Ohzuku, T. Crystal and Electronic Structures of Superstructural  $\text{Li}_{1-x}[\text{Co}_{1/3}\text{Ni}_{1/3}\text{Mn}_{1/3}]\text{O}_2$  ( $0 < x < 1$ ). *J. Power Sources* **2003**, *119-121*, 644–648.
- (42) Hwang, B. J.; Tsai, Y. W.; Carlier, D.; Ceder, G. A Combined Computational/Experimental Study on  $\text{LiNi}_{1/3}\text{Co}_{1/3}\text{Mn}_{1/3}\text{O}_2$ . *Chem. Mater.* **2003**, *15* (19), 3676–3682.
- (43) Nanjundaswamy, K. S.; Padhi, A. K.; Goodenough, J. B.; Okada, S.; Ohtsukab, H.; Arai, H.; Yamakib, J. Synthesis, Redox Potential Evaluation and Electrochemical Characteristics of NASICON-Related-3D Framework

- Compounds. *Solid State Ionics* **1996**, *92*, 1–10.
- (44) Azmi, B. M.; Ishihara, T.; Nishiguchi, H.; Takita, Y. Vanadyl Phosphates of  $\text{VOPO}_4$  as a Cathode of Li-Ion Rechargeable Batteries. *J. Power Sources* **2003**, *119-121*, 273–277.
- (45) Ramesh, T. N.; Lee, K. T.; Ellis, B. L.; Nazar, L. F. Tavorite Lithium Iron Fluorophosphate Cathode Materials: Phase Transition and Electrochemistry of  $\text{LiFePO}_4\text{F-Li}_2\text{FePO}_4\text{F}$ . *Electrochem. Solid-State Lett.* **2010**, *13* (4), A43.
- (46) Recham, N.; Chotard, J.-N.; Dupont, L.; Delacourt, C.; Walker, W.; Armand, M.; Tarascon, J.-M. A 3.6 V Lithium-Based Fluorosulphate Insertion Positive Electrode for Lithium-Ion Batteries. *Nat. Mater.* **2010**, *9* (1), 68–74.
- (47) Tripathi, R.; Ramesh, T. N.; Ellis, B. L.; Nazar, L. F. Scalable Synthesis of Tavorite  $\text{LiFeSO}_4\text{F}$  and  $\text{NaFeSO}_4\text{F}$  Cathode Materials. *Angew. Chemie Int. Ed.* **2010**, *49* (46), 8738–8742.
- (48) Andersson, A. S.; Kalska, B.; Haggstrom, L.; Thomas, J. O. Lithium Extraction/insertion in  $\text{LiFePO}_4$ : An X-Ray Diffraction and Mössbauer Spectroscopy Study. *Solid State Ionics* **2000**, *130*, 41–52.
- (49) Yamada, A.; Koizumi, H.; Nishimura, S.-I.; Sonoyama, N.; Kanno, R.; Yonemura, M.; Nakamura, T.; Kobayashi, Y. Room-Temperature Miscibility Gap in  $\text{Li}_x\text{FePO}_4$ . *Nat. Mater.* **2006**, *5* (5), 357–360.
- (50) Kobayashi, G.; Nishimura, S. I.; Park, M.-S. S.; Kanno, R.; Yashima, M.; Ida, T.; Yamada, A. Isolation of Solid Solution Phases in Size-Controlled  $\text{Li}_x\text{FePO}_4$  at Room Temperature. *Adv. Funct. Mater.* **2009**, *19* (3), 395–403.
- (51) Chang, M. H.; Huang, H. P.; Chang, S. W. A New State of Charge Estimation Method for  $\text{LiFePO}_4$  Battery Packs Used in Robots. *Energies* **2013**, *6*, 2007–2030.
- (52) Herle, P. S.; Ellis, B.; Coombs, N.; Nazar, L. F. Nano-Network Electronic Conduction in Iron and Nickel Olivine Phosphates. *Nat. Mater.* **2004**, *3* (3), 147–152.
- (53) Lin, Y.; Gao, M. X.; Zhu, D.; Liu, Y. F.; Pan, H. G. Effects of Carbon Coating



- and Iron Phosphides on the Electrochemical Properties of  $\text{LiFePO}_4/\text{C}$ . *J. Power Sources* **2008**, *184* (2), 444–448.
- (54) Goriparti, S.; Miele, E.; De Angelis, F.; Di Fabrizio, E.; Proietti Zaccaria, R.; Capiglia, C. Review on Recent Progress of Nanostructured Anode Materials for Li-Ion Batteries. *J. Power Sources* **2014**, *257*, 421–443.
- (55) Sandí, G. Development of New Anodes for Rechargeable Lithium Batteries. *J. New Mater. Mater. Electrochem. Syst.* **2001**, *4* (October), 259–265.
- (56) Nishidate, K.; Hasegawa, M. Energetics of Lithium Ion Adsorption on Defective Carbon Nanotubes. *Phys. Rev. B - Condens. Matter Mater. Phys.* **2005**, *71* (24), 1–6.
- (57) Hou, J.; Shao, Y.; Ellis, M. W.; Moore, R. B.; Yi, B. Graphene-Based Electrochemical Energy Conversion and Storage: Fuel Cells, Supercapacitors and Lithium Ion Batteries. *Phys. Chem. Chem. Phys.* **2011**, *13* (34), 15384–15402.
- (58) Ohzuku, T.; Ueda, A.; Yamamoto, N. Zero-Strain Insertion Material of  $\text{Li}[\text{Li}_{1/3}\text{Ti}_{5/3}\text{O}_4]$  for Rechargeable Lithium Cells. *J. Electrochem. Soc.* **1995**, *142* (5), 1431.
- (59) Park, C.-M.; Kim, J.-H.; Kim, H.; Sohn, H.-J. Li-Alloy Based Anode Materials for Li Secondary Batteries. *Chem. Soc. Rev.* **2010**, *39* (8), 3115.
- (60) Teki, R.; Krishnan, R.; Parker, T. C.; Lu, T. M.; Kumta, P. N.; Koratkar, N. Nanostructured Silicon Anodes for Lithium Ion Rechargeable Batteries. *Small* **2009**, *5* (20), 2236–2242.
- (61) McDowell, M. T.; Lee, S. W.; Harris, J. T.; Korgel, B. a.; Wang, C.; Nix, W. D.; Cui, Y. In Situ TEM of Two-Phase Lithiation of Amorphous Silicon Nanospheres. *Nano Lett.* **2013**, *13* (2), 758–764.
- (62) Liu, X. H.; Zheng, H.; Zhong, L.; Huang, S.; Karki, K.; Zhang, L. Q.; Liu, Y.; Kushima, A.; Liang, W. T.; Wang, J. W.; Cho, J. H.; Epstein, E.; Dayeh, S. a.; Picaux, S. T.; Zhu, T.; Li, J.; Sullivan, J. P.; Cumings, J.; Wang, C.; Mao, S. X.; Ye, Z. Z.; Zhang, S.; Huang, J. Y. Anisotropic Swelling and Fracture of Silicon Nanowires during Lithiation. *Nano Lett.* **2011**, *11* (8), 3312–3318.

- (63) McDowell, M. T.; Ryu, I.; Lee, S. W.; Wang, C.; Nix, W. D.; Cui, Y. Studying the Kinetics of Crystalline Silicon Nanoparticle Lithiation with In Situ Transmission Electron Microscopy. *Adv. Mater.* **2012**, *24* (45), 6034–6041.
- (64) Key, B.; Bhattacharyya, R.; Morcrette, M.; Seznéc, V.; Tarascon, J.-M.; Grey, C. P.; Sezne, V.; Verne, D. P. J. Real-Time NMR Investigations of Structural Changes in Silicon Electrodes for Lithium-Ion Batteries. *J. Am. Chem. Soc.* **2009**, *131* (26), 9239–9249.
- (65) Wang, U. Why Tesla Rolls Out Better EV Batteries “Ludicrous Mode” <http://www.forbes.com/sites/uciliawang/2015/07/17/why-tesla-rolls-out-better-ev-batteries/> (accessed Dec 14, 2015).
- (66) Sanner, T. *OPINION ON N-Methyl-2-Pyrrolidone (NMP)*; 2011.
- (67) Chen, Y.-H.; Wang, C.-W.; Liu, G.; Song, X.-Y.; Battaglia, V. S.; Sastry, A. M. Selection of Conductive Additives in Li-Ion Battery Cathodes. *J. Electrochem. Soc.* **2007**, *154* (10), A978.
- (68) Moskon, J.; Dominko, R.; Cerc-Korosec, R.; Gaberscek, M.; Jamnik, J. Morphology and Electrical Properties of Conductive Carbon Coatings for Cathode Materials. *J. Power Sources* **2007**, *174* (2), 683–688.
- (69) Myung, S. T.; Sasaki, Y.; Sakurada, S.; Sun, Y. K.; Yashiro, H. Electrochemical Behavior of Current Collectors for Lithium Batteries in Non-Aqueous Alkyl Carbonate Solution and Surface Analysis by ToF-SIMS. *Electrochim. Acta* **2009**, *55* (1), 288–297.
- (70) Myung, S.-T.; Hitoshi, Y.; Sun, Y.-K. Electrochemical Behavior and Passivation of Current Collectors in Lithium-Ion Batteries. *J. Mater. Chem.* **2011**, *21* (27), 9891.
- (71) Xu, K. Nonaqueous Liquid Electrolytes for Lithium-Based Rechargeable Batteries. *Chem. Rev.* **2004**, *104* (10), 4303–4417.
- (72) Xu, K. Electrolytes and Interphases in Li-Ion Batteries and Beyond. *Chem. Rev.* **2014**, *114*, 11503–11618.
- (73) Xu, K.; About, M.; Article, T. Nonaqueous Liquid Electrolytes for Lithium-

- Based Rechargeable Batteries Nonaqueous Liquid Electrolytes for Lithium-Based Rechargeable Batteries. *Chem. Rev.* **2004**, *104* (September), 4303–4418.
- (74) Fong, R.; von Sacken, U.; Dahn, J. R. Studies of Lithium Intercalation into Carbons Using Nonaqueous Electrochemical Cells. *J. Electrochem. Soc.* **1990**, *137* (7), 2009–2013.
- (75) von Cresce, A.; Xu, K. Preferential Solvation of  $\text{Li}^+$  Directs Formation of Interphase on Graphitic Anode. *Electrochem. Solid-State Lett* **2011**, *14*, A154.
- (76) Zhang, S. S. A Review on Electrolyte Additives for Lithium-Ion Batteries. *J. Power Sources* **2006**, *162* (2 SPEC. ISS.), 1379–1394.
- (77) Peled, E. The Electrochemical Behavior of Alkali and Alkaline Earth Metals in Nonaqueous Battery Systems—The Solid Electrolyte Interphase Model. *J. Electrochem. Soc.* **1979**, *126* (12), 2047.
- (78) Besenhard, J. O.; Winter, M.; Yang, J.; Biberacher, W. Filming Mechanism of Lithium-Carbon Anodes in Organic and Inorganic Electrolytes. *J. Power Sources* **1995**, *54* (2), 228–231.
- (79) Peled, E.; Golodnitsky, D.; Ardel, G. Advanced Model for Solid Electrolyte Interphase Electrodes in Liquid and Polymer Electrolytes. *J. Electrochem. Soc.* **1997**, *144* (8), L208.
- (80) Aurbach, D.; Markovsky, B.; Levi, M. D.; Levi, E.; Schechter, A.; Moshkovich, M.; Cohen, Y. New Insights into the Interactions between Electrode Materials and Electrolyte Solutions for Advanced Nonaqueous Batteries. *J. Power Sources* **1999**, *81-82*, 95–111.
- (81) Edström, K.; Herstedt, M.; Abraham, D. P. A New Look at the Solid Electrolyte Interphase on Graphite Anodes in Li-Ion Batteries. *J. Power Sources* **2006**, *153* (2), 380–384.
- (82) Kanamura, K. X-Ray Photoelectron Spectroscopic Analysis and Scanning Electron Microscopic Observation of the Lithium Surface Immersed in Nonaqueous Solvents. *J. Electrochem. Soc.* **1994**, *141* (9), 2379.
- (83) Ein-ely, Y.; Aurbach, D.; Ein-ely, Y. The Surface Chemistry of Lithium

- Electrodes in Alkyl Carbonate Solutions. *J. Electrochem. Soc.* **1994**, *141* (1), L1.
- (84) Andersson, A. M.; Edström, K. Chemical Composition and Morphology of the Elevated Temperature SEI on Graphite. *J. Electrochem. Soc.* **2001**, *148* (10), A1100.
- (85) Aurbach, D. Identification of Surface Films Formed on Lithium in Propylene Carbonate Solutions. *J. Electrochem. Soc.* **1987**, *134* (7), 1611.
- (86) Aurbach, D.; Gofer, Y.; Ben-Zion, M.; Apeid, P. The Behaviour of Lithium Electrodes in Propylene and Ethylene Carbonate: The Major Factors That Influence Li Cycling Efficiency. *J. Electroanal. Chem.* **1992**, *339* (1-2), 451–471.
- (87) Seo, D. M.; Chalasani, D.; Parimalam, B. S.; Kadam, R.; Nie, M.; Lucht, B. L. Reduction Reactions of Carbonate Solvents for Lithium Ion Batteries. *ECS Electrochem. Lett.* **2014**, *3* (9), A91–A93.
- (88) Bryngelsson, H.; Stjerndahl, M.; Gustafsson, T.; Edström, K. How Dynamic Is the SEI? *J. Power Sources* **2007**, *174* (2), 970–975.
- (89) Andersson, A. M.; Abraham, D. P.; Haasch, R.; MacLaren, S.; Liu, J.; Amine, K. Surface Characterization of Electrodes from High Power Lithium-Ion Batteries. *J. Electrochem. Soc.* **2002**, *149* (10), A1358.
- (90) Herstedt, M.; Stjerndahl, M.; Nyttén, A.; Gustafsson, T.; Rensmo, H.; Siegbahn, H.; Ravet, N.; Armand, M.; Thomas, J. O.; Edström, K. Surface Chemistry of Carbon-Treated LiFePO<sub>4</sub> Particles for Li-Ion Battery Cathodes Studied by PES. *Electrochem. Solid-State Lett.* **2003**, *6* (9), A202–A206.
- (91) Ensling, D.; Stjerndahl, M.; Nyttén, A.; Gustafsson, T.; Thomas, J. O. A Comparative XPS Surface Study of Li<sub>2</sub>FeSiO<sub>4</sub>/C Cycled with LiTFSI- and LiPF<sub>6</sub>-Based Electrolytes. *J. Mater. Chem.* **2009**, *19* (1), 82.
- (92) Stjerndahl, M. Stability Phenomena in Novel Electrode Materials for Lithium-Ion Batteries, Uppsala Universitet, 2007.
- (93) Arora, P.; Zhang, Z. Battery Separators. *Chem. Rev.* **2004**, *104* (10), 4419–

- 4462.
- (94) Armstrong, A. R.; Lyness, C.; Ménétrier, M.; Bruce, P. G. Structural Polymorphism in  $\text{Li}_2\text{CoSiO}_4$  Intercalation Electrodes: A Combined Diffraction and NMR Study. *Chem. Mater.* **2010**, *22* (8), 1892–1900.
- (95) Yamaguchi, B. Y. H.; Akatsuka, K.; Setoguchi, M.; Takaki, Y. Structure of Cobalt Dilithium Silicate  $\text{Fln-Li}_2\text{CoSiO}_4$ . *Acta Cryst.* **1979**, No. B 35, 2680–2682.
- (96) Li, Y.-X.; Gong, Z.-L.; Yang, Y. Synthesis and Characterization of  $\text{Li}_2\text{MnSiO}_4/\text{C}$  Nanocomposite Cathode Material for Lithium Ion Batteries. *J. Power Sources* **2007**, *174* (2), 528–532.
- (97) Sirisopanaporn, C.; Boulineau, A.; Hanzel, D.; Dominko, R.; Budic, B.; Armstrong, A. R.; Bruce, P. G.; Masquelier, C. Crystal Structure of a New Polymorph of  $\text{Li}_2\text{FeSiO}_4$ . *Inorg. Chem.* **2010**, *49* (16), 7446–7451.
- (98) Duncan, H.; Kondamreddy, A.; Mercier, P. H. J.; Le Page, Y.; Abu-Lebdeh, Y.; Couillard, M.; Whitfield, P. S.; Davidson, I. J. Novel Pn Polymorph for  $\text{Li}_2\text{MnSiO}_4$  and Its Electrochemical Activity As a Cathode Material in Li-Ion Batteries. *Chem. Mater.* **2011**, *23* (24), 5446–5456.
- (99) Arroyo-de Dompablo, M. E.; Armand, M.; Tarascon, J. M.; Amador, U. On-Demand Design of Polyoxianionic Cathode Materials Based on Electronegativity Correlations: An Exploration of the  $\text{Li}_2\text{MSiO}_4$  System (M = Fe, Mn, Co, Ni). *Electrochem. commun.* **2006**, *8* (8), 1292–1298.
- (100) Bui, K. M.; Dinh, V. A.; Ohno, T. Hybrid Functional Study on Diffusion of Silicate Cathode Material  $\text{Li}_2\text{NiSiO}_4$ . *J. Phys. Conf. Ser.* **2013**, *454* (1), 012061.
- (101) Wu, S. Q.; Zhu, Z. Z.; Yang, Y.; Hou, Z. F. Structural Stabilities, Electronic Structures and Lithium Deintercalation in  $\text{Li}_x\text{MSiO}_4$  (M = Mn, Fe, Co, Ni): A GGA and GGA + U Study. *Comput. Mater. Sci.* **2009**, *44* (4), 1243–1251.
- (102) Panda, M. R.; Cheruku, R.; Govindaraj, G.; Nagar, R. V. Investigations on Structural and Electrical Properties of  $\text{Li}_2\text{NiSiO}_4$ . In *Int.J. ChemTech Res.*; 2014; Vol. 6, pp 1962–1964.

- (103) Lyness, C.; Delobel, B.; Armstrong, A. R.; Bruce, P. G. The Lithium Intercalation Compound  $\text{Li}_2\text{CoSiO}_4$  and Its Behaviour as a Positive Electrode for Lithium Batteries. *Chem. Commun. (Camb)*. **2007**, No. c, 4890–4892.
- (104) Dominko, R.; Bele, M.; Kokalj, A.; Gaberscek, M.; Jamnik, J.  $\text{Li}_2\text{MnSiO}_4$  as a Potential Li-Battery Cathode Material. *J. Power Sources* **2007**, *174* (2), 457–461.
- (105) Politaev, V. V.; Petrenko, A. A.; Nalbandyan, V. B.; Medvedev, B. S.; Shvetsova, E. S. Crystal Structure, Phase Relations and Electrochemical Properties of Monoclinic  $\text{Li}_2\text{MnSiO}_4$ . *J. Solid State Chem.* **2007**, *180* (3), 1045–1050.
- (106) Nishimura, S. I.; Hayase, S.; Kanno, R.; Yashima, M.; Nakayama, N.; Yamada, A. Structure of  $\text{Li}_2\text{FeSiO}_4$ . *J. Am. Chem. Soc.* **2008**, *130* (40), 13212–13213.
- (107) Boulineau, A.; Sirisopanaporn, C.; Dominko, R.; Armstrong, A. R.; Bruce, P. G.; Masquelier, C. Polymorphism and Structural Defects in  $\text{Li}_2\text{FeSiO}_4$ . *Dalton Trans.* **2010**, *39* (27), 6310–6316.
- (108) Gummow, R. J.; Sharma, N.; Peterson, V. K.; He, Y. Crystal Chemistry of the Pmnb Polymorph of  $\text{Li}_2\text{MnSiO}_4$ . *J. Solid State Chem.* **2012**, *188*, 32–37.
- (109) Prosini, P.; Lisi, M.; Zane, D.; Pasquali, M. Determination of the Chemical Diffusion Coefficient of Lithium in  $\text{LiFePO}_4$ . *Solid State Ionics* **2002**, *148* (1-2), 45–51.
- (110) Bajars, G.; Kucinskis, G.; Smits, J.; Kleperis, J.; Lusiš, A. Characterization of  $\text{LiFePO}_4/\text{C}$  Composite Thin Films Using Electrochemical Impedance Spectroscopy. *IOP Conf. Ser. Mater. Sci. Eng.* **2012**, *38*, 012019.
- (111) Świętosławski, M.; Molenda, M.; Furczoń, K.; Dziembaj, R. Nanocomposite  $\text{C}/\text{Li}_2\text{MnSiO}_4$  Cathode Material for Lithium Ion Batteries. *J. Power Sources* **2013**, *244*, 510–514.
- (112) Hwang, C.; Kim, T.; Noh, Y.; Cha, W.; Shim, J.; Kwak, K.; Ok, K. M.; Lee, K.-K. Synthesis, Characterization, and Electrochemical Performance of V-Doped  $\text{Li}_2\text{MnSiO}_4/\text{C}$  Composites for Li-Ion Battery. *Mater. Lett.* **2015**.

- (113) Li, L. M.; Guo, H. J.; Li, X. H.; Wang, Z. X.; Peng, W. J.; Xiang, K. X.; Cao, X. Effects of Roasting Temperature and Modification on Properties of  $\text{Li}_2\text{FeSiO}_4/\text{C}$  Cathode. *J. Power Sources* **2009**, *189* (1), 45–50.
- (114) Zheng, Z.; Wang, Y.; Zhang, A.; Zhang, T.; Cheng, F.; Tao, Z.; Chen, J. Porous  $\text{Li}_2\text{FeSiO}_4/\text{C}$  Nanocomposite as the Cathode Material of Lithium-Ion Batteries. *J. Power Sources* **2012**, *198*, 229–235.
- (115) Zhang, S.; Deng, C.; Fu, B. L.; Yang, S. Y.; Ma, L. Effects of Cr Doping on the Electrochemical Properties of  $\text{Li}_2\text{FeSiO}_4$  Cathode Material for Lithium-Ion Batteries. *Electrochim. Acta* **2010**, *55* (28), 8482–8489.
- (116) Zhang, L.-L.; Duan, S.; Yang, X.-L.; Liang, G.; Huang, Y.-H.; Cao, X.-Z.; Yang, J.; Li, M.; Croft, M. C.; Lewis, C. Insight into Cobalt-Doping in  $\text{Li}_2\text{FeSiO}_4$  Cathode Material for Lithium-Ion Battery. *J. Power Sources* **2015**, *274*, 194–202.
- (117) Liivat, A. Structural Changes on Cycling  $\text{Li}_2\text{FeSiO}_4$  Polymorphs from DFT Calculations. *Solid State Ionics* **2012**, *228*, 19–24.
- (118) Masese, T.; Orikasa, Y.; Tassel, C.; Kim, J.; Minato, T.; Arai, H.; Mori, T.; Yamamoto, K.; Kobayashi, Y.; Kageyama, H.; Ogumi, Z.; Uchimoto, Y. Relationship between Phase Transition Involving Cationic Exchange and Charge-Discharge Rate in  $\text{Li}_2\text{FeSiO}_4$ . *Chem. Mater.* **2014**, *26* (3), 1380–1384.
- (119) Fisher, C. a J.; Kuganathan, N.; Islam, M. S. Defect Chemistry and Lithium-Ion Migration in Polymorphs of the Cathode Material  $\text{Li}_2\text{MnSiO}_4$ . *J. Mater. Chem. A* **2013**, *1* (13), 4207–4214.
- (120) Köhler, P.; Massa, W.; Reinen, D.; Hofmann, B.; Hoppe, R. Der Jahn-Teller-Effekt Des  $\text{Mn}^{3+}$ -Ions in Oktaedrischer Fluorkoordination. Ligandenfeldspektroskopische Und Magnetische Untersuchungen. *Zeitschrift für Anorg. und Allg. Chemie* **1978**, *446*, 131–158.
- (121) Ghose, S.; Kersten, M.; Langer, K.; Rossi, G.; Ungaretti, L. Crystal Field Spectra and Jahn Teller Effect of  $\text{Mn}^{3+}$  in Clinopyroxene and Clinoamphiboles from India. *Phys. Chem. Miner.* **1986**, *13*, 291–305.
- (122) Saracibar, A.; Wang, Z.; Carroll, K. J.; Meng, Y. S.; Dompablo, M. E. A. New

- Insights into the Electrochemical Performance of  $\text{Li}_2\text{MnSiO}_4$ : Effect of Cationic Substitutions. *J. Mater. Chem. A* **2015**, *3*, 6004–6011.
- (123) Wang, M.; Yang, M.; Ma, L.; Shen, X.; Zhang, X. Structural Evolution and Electrochemical Performance of  $\text{Li}_2\text{MnSiO}_4/\text{C}$  Nanocomposite as Cathode Material for Li-Ion Batteries. *J. Nanomater.* **2014**, *2014*, 1–6.
- (124) Sirisopanaporn, C.; Masquelier, C.; Bruce, P. G.; Armstrong, A. R.; Dominko, R. Dependence of  $\text{Li}_2\text{FeSiO}_4$  Electrochemistry on Structure. *J. Am. Chem. Soc.* **2011**, *133* (5), 1263–1265.
- (125) Nyttén, A.; Kamali, S.; Häggström, L.; Gustafsson, T.; Thomas, J. O. The Lithium Extraction/insertion Mechanism in  $\text{Li}_2\text{FeSiO}_4$ . *J. Mater. Chem.* **2006**, *16* (23), 2266.
- (126) Muraliganth, T.; Stroukoff, K. R.; Manthiram, A. Microwave-Solvothermal Synthesis of Nanostructured  $\text{Li}_2\text{MSiO}_4/\text{C}$  (M = Mn and Fe) Cathodes for Lithium-Ion Batteries. *Chem. Mater.* **2010**, *22* (20), 5754–5761.
- (127) Longo, R. C.; Xiong, K.; Cho, K. Multicomponent Silicate Cathode Materials for Rechargeable Li-Ion Batteries: An Ab Initio Study. *J. Electrochem. Soc.* **2013**, *160* (1), A60–A65.
- (128) Chen, R.; Heinzmann, R.; Mangold, S.; Chakravadhanula, V. S. K.; Hahn, H.; Indris, S. Structural Evolution of  $\text{Li}_2\text{Fe}_{1-y}\text{Mn}_y\text{SiO}_4$  ( $y = 0, 0.2, 0.5, 1$ ) Cathode Materials for Li-Ion Batteries upon Electrochemical Cycling. *J. Phys. Chem. C* **2013**, *117*, 884–893.
- (129) Kokalj, A.; Dominko, R.; Mali, G.; Meden, A.; Gaberscek, M.; Jamnik, J. Beyond One-Electron Reaction in Li Cathode Materials: Designing  $\text{Li}_2\text{Mn}_x\text{Fe}_{1-x}\text{SiO}_4$ . *Chem. Mater.* **2007**, *19* (15), 3633–3640.
- (130) Deng, C.; Zhang, S.; Yang, S. Y. Effect of Mn Substitution on the Structural, Morphological and Electrochemical Behaviors of  $\text{Li}_2\text{Fe}_{1-x}\text{Mn}_x\text{SiO}_4$  Synthesized via Citric Acid Assisted Sol-Gel Method. *J. Alloys Compd.* **2009**, *487* (1-2), 18–23.
- (131) Shao, B.; Abe, Y.; Taniguchi, I. Synthesis and Electrochemical Characterization of  $\text{Li}_2\text{Fe}_x\text{Mn}_{1-x}\text{SiO}_4/\text{C}$  ( $0 \leq x \leq 0.8$ ) Nanocomposite Cathode for



- Lithium-Ion Batteries. *Powder Technol.* **2013**, *235*, 1–8.
- (132) Guo, H.; Cao, X.; Li, X.; Li, L.; Li, X.; Wang, Z.; Peng, W.; Li, Q. Optimum Synthesis of  $\text{Li}_2\text{Fe}_{1-x}\text{Mn}_x\text{SiO}_4/\text{C}$  Cathode for Lithium Ion Batteries. *Electrochim. Acta* **2010**, *55* (27), 8036–8042.
- (133) Gummow, R. J.; Sharma, N.; Peterson, V. K.; He, Y. Synthesis, Structure, and Electrochemical Performance of Magnesium-Substituted Lithium Manganese Orthosilicate Cathode Materials for Lithium-Ion Batteries. *J. Power Sources* **2012**, *197*, 231–237.
- (134) Zhang, S.; Lin, Z.; Ji, L.; Li, Y.; Xu, G.; Xue, L.; Li, S.; Lu, Y.; Toprakci, O.; Zhang, X. Cr-Doped  $\text{Li}_2\text{MnSiO}_4$ /carbon Composite Nanofibers as High-Energy Cathodes for Li-Ion Batteries. *J. Mater. Chem.* **2012**, *22* (29), 14661.
- (135) Longo, R. C.; Xiong, K.; Kc, S.; Cho, K. Crystal Structure and Multicomponent Effects in Tetrahedral Silicate Cathode Materials for Rechargeable Li-Ion Batteries. *Electrochim. Acta* **2014**, *121*, 434–442.
- (136) West, K.; Zachau-Christiansen, B.; T., J. Thin-Film Vanadium Batteries Oxide Electrodes for Lithium Batteries. *J. Power Sources* **1993**, 127–134.
- (137) Li, Y.; Cheng, X.; Zhang, Y. Achieving High Capacity by Vanadium Substitution into  $\text{Li}_2\text{FeSiO}_4$ . *J. Electrochem. Soc.* **2012**, *159* (2), A69.
- (138) Shannon, R. D. Revised Effective Ionic Radii and Systematic Studies of Interatomic Distances in Halides and Chalcogenides. *Acta Crystallogr.* **1976**, *A32*, 751–767.
- (139) Liivat, A.; Thomas, J. O. A DFT Study of Polyanion Substitution into the Li-Ion Battery Cathode Material  $\text{Li}_2\text{FeSiO}_4$ . *Comput. Mater. Sci.* **2010**, *50* (1), 191–197.
- (140) Hong, Y.; Ying, Z.; Xuan, C. Effect of Vanadium Substitution on Structure of  $\text{Li}_2\text{FeSiO}_4/\text{C}$  Composites. *JOURNAL OF Electrochem.* **2013**, *19* (6), 565–570.
- (141) Zhang, L.-L.; Sun, H.-B.; Yang, X.-L.; Wen, Y.-W.; Huang, Y.-H.; Li, M.; Peng, G.; Tao, H.-C.; Ni, S.-B.; Liang, G. Study on Electrochemical Performance and Mechanism of V-Doped  $\text{Li}_2\text{FeSiO}_4$  Cathode Material for Li-

- Ion Batteries. *Electrochim. Acta* **2015**, *152*, 496–504.
- (142) Hao, H.; Wang, J.; Liu, J.; Huang, T.; Yu, A. Synthesis, Characterization and Electrochemical Performance of  $\text{Li}_2\text{FeSiO}_4/\text{C}$  Cathode Materials Doped by Vanadium at Fe/Si Sites for Lithium Ion Batteries. *J. Power Sources* **2012**, *210*, 397–401.
- (143) Deng, C.; Zhang, S.; Wu, Y. X.; Zhao, B. D. Partial Substitution of Mn/Si with V, Cr or Al in  $\text{Li}_2\text{MnSiO}_4$  Nanoparticle: Dependence of the Physical and Electrochemical Properties on the Substitution Strategy. *J. Electroanal. Chem.* **2014**, *719*, 150–157.
- (144) Jaén, J. a.; Jiménez, M.; Flores, E.; Muñoz, A.; Tabares, J. a.; Pérez Alcázar, G. a. Structural Study on Nickel Doped  $\text{Li}_2\text{FeSiO}_4$ . *Hyperfine Interact.* **2015**.
- (145) Molenda, M.; Świątosławski, M.; Rafalska-Łasocha, A.; Dziembaj, R. Synthesis And Properties Of  $\text{Li}_2\text{MnSiO}_4$  Composite Cathode Material For Safe Li-Ion Batteries. *Funct. Mater. Lett.* **2011**, *04* (02), 135–138.
- (146) Deng, C.; Sun, Y. H.; Zhang, S.; Lin, H. M.; Gao, Y.; Wu, B.; Ma, L.; Shang, Y.; Dong, G. Synthesis and Improved Properties of Nanostructured  $\text{Li}_2\text{MnSiO}_4/\text{C}$  via a Modified Sol-Gel Method. *Int. J. Electrochem. Sci.* **2012**, *7*, 4559–4566.
- (147) Molenda, M.; Świątosławski, M.; Wach, A.; Majda, D.; Kuśtrowski, P.; Dziembaj, R. Stability of  $\text{C}/\text{Li}_2\text{MnSiO}_4$  Composite Cathode Material for Li-Ion Batteries towards  $\text{LiPF}_6$  Based Electrolyte. *Solid State Ionics* **2014**, *262*, 98–101.
- (148) Deng, C.; Zhang, S.; Fu, B. L.; Yang, S. Y.; Ma, L. Characterization of  $\text{Li}_2\text{MnSiO}_4$  and  $\text{Li}_2\text{FeSiO}_4$  Cathode Materials Synthesized via a Citric Acid Assisted Sol-Gel Method. *Mater. Chem. Phys.* **2010**, *120* (1), 14–17.
- (149) Wang, F.; Chen, J.; Wang, C.; Yi, B. Fast Sol-Gel Synthesis of Mesoporous  $\text{Li}_2\text{MnSiO}_4/\text{C}$  Nanocomposite with Improved Electrochemical Performance for Lithium-Ion Batteries. *J. Electroanal. Chem.* **2013**, *688*, 123–129.
- (150) Zhou, H.; Einarsrud, M. A.; Vullum-Bruer, F. High Capacity Nanostructured  $\text{Li}_2\text{Fe}_x\text{SiO}_4/\text{C}$  with Fe Hyperstoichiometry for Li-Ion Batteries. *J. Power*

- Sources* **2013**, *235*, 234–242.
- (151) Bini, M.; Ferrari, S.; Ferrara, C.; Mozzati, M. C.; Capsoni, D.; Pell, A. J.; Pintacuda, G.; Canton, P.; Mustarelli, P. Polymorphism and Magnetic Properties of  $\text{Li}_2\text{MSiO}_4$  (M = Fe, Mn) Cathode Materials. *Sci. Rep.* **2013**, *3*, 3452.
- (152) Qu, L.; Fang, S.; Yang, L.; Hirano, S. Synthesis and Characterization of High Capacity  $\text{Li}_2\text{MnSiO}_4/\text{C}$  Cathode Material for Lithium-Ion Battery. *J. Power Sources* **2014**, *252*, 169–175.
- (153) Belharouak, I.; Abouimrane, A.; Amine, K. Structural and Electrochemical Characterization of  $\text{Li}_2\text{MnSiO}_4$  Cathode Material. *J. Phys. Chem. C* **2009**, *113*, 20733–20737.
- (154) Lv, D.; Wen, W.; Huang, X.; Bai, J.; Mi, J.; Wu, S.; Yang, Y. A Novel  $\text{Li}_2\text{FeSiO}_4/\text{C}$  Composite: Synthesis, Characterization and High Storage Capacity. *J. Mater. Chem.* **2011**, *21* (26), 9506.
- (155) Sun, D.; Wang, H.; Ding, P.; Zhou, N.; Huang, X.; Tan, S.; Tang, Y. In-Situ Synthesis of Carbon Coated  $\text{Li}_2\text{MnSiO}_4$  Nanoparticles with High Rate Performance. *J. Power Sources* **2013**, *242*, 865–871.
- (156) Bhaskar, a.; Deepa, M.; Rao, T. N.; Varadaraju, U. V. In Situ Carbon Coated  $\text{Li}_2\text{MnSiO}_4/\text{C}$  Composites as Cathodes for Enhanced Performance Li-Ion Batteries. *J. Electrochem. Soc.* **2012**, *159* (12), A1954–A1960.
- (157) Dahbi, M.; Urbonaitė, S.; Gustafsson, T. Combustion Synthesis and Electrochemical Performance of  $\text{Li}_2\text{FeSiO}_4/\text{C}$  Cathode Material for Lithium-Ion Batteries. *J. Power Sources* **2012**, *205*, 456–462.
- (158) Zhou, H.; Einarsrud, M.-A.; Vullum-Bruer, F. PVA-Assisted Combustion Synthesis and Characterization of Porous Nanocomposite  $\text{Li}_2\text{FeSiO}_4/\text{C}$ . *Solid State Ionics* **2012**, *225*, 585–589.
- (159) Kempaiah, D. M.; Rangappa, D.; Honma, I. Controlled Synthesis of Nanocrystalline  $\text{Li}_2\text{MnSiO}_4$  Particles for High Capacity Cathode Application in Lithium-Ion Batteries. *Chem. Commun.* **2012**, *48* (21), 2698.

- (160) Rangappa, D.; Murukanahally, K. D.; Tomai, T.; Unemoto, A.; Honma, I. Ultrathin Nanosheets of  $\text{Li}_2\text{MSiO}_4$  (M = Fe, Mn) as High-Capacity Li-Ion Battery Electrode. *Nano* **2012**, *4*.
- (161) Sato, M.; Ishigaki, T.; Uematsu, K.; Toda, K.; Okawa, H. Redetermination of the Low-Temperature Polymorph of  $\text{Li}_2\text{MnSiO}_4$  from Single-Crystal X-Ray Data. *Acta Crystallogr. Sect. E Struct. Reports Online* **2012**, *68* (9), i68–i69.
- (162) Mali, G.; Meden, A.; Dominko, R.  $^6\text{Li}$  MAS NMR Spectroscopy and First-Principles Calculations as a Combined Tool for the Investigation of  $\text{Li}_2\text{MnSiO}_4$  Polymorphs. *Chem. Commun. (Camb)*. **2010**, *46* (19), 3306–3308.
- (163) Liu, W.; Xu, Y.; Yang, R. Synthesis and Electrochemical Properties of  $\text{Li}_2\text{MnSiO}_4/\text{C}$  Nanoparticles via Polyol Process. *Rare Met.* **2010**, *29* (5), 511–514.
- (164) Shao, B.; Taniguchi, I. Synthesis of  $\text{Li}_2\text{MnSiO}_4/\text{C}$  Nanocomposites for Lithium Battery Cathode Employing Sucrose as Carbon Source. *Electrochim. Acta* **2013**, *128*, 156–162.
- (165) Shao, B.; Taniguchi, I. Synthesis of  $\text{Li}_2\text{FeSiO}_4/\text{C}$  Nanocomposite Cathodes for Lithium Batteries by a Novel Synthesis Route and Their Electrochemical Properties. *J. Power Sources* **2012**, *199*, 278–286.
- (166) Huang, X.; You, Y.; Ren, Y.; Wang, H.; Chen, Y.; Ding, X.; Liu, B.; Zhou, S.; Chu, F. Spray Drying-Assisted Synthesis of Hollow Spherical  $\text{Li}_2\text{FeSiO}_4/\text{C}$  Particles with High Performance for Li-Ion Batteries. *Solid State Ionics* **2015**, *278*, 203–208.
- (167) Zhang, L.; Ni, J.; Wang, W.; Guo, J.; Li, L. 3D Porous Hierarchical  $\text{Li}_2\text{FeSiO}_4/\text{C}$  for Rechargeable Lithium Batteries. *J. Mater. Chem. A* **2015**, *3* (22), 11782–11786.
- (168) Huang, X.; Li, X.; Wang, H.; Pan, Z.; Qu, M.; Yu, Z. Synthesis and Electrochemical Performance of  $\text{Li}_2\text{FeSiO}_4/\text{C}$  as Cathode Material for Lithium Batteries. *Solid State Ionics* **2010**, *181* (31–32), 1451–1455.
- (169) Kam, K. C.; Gustafsson, T.; Thomas, J. O. Synthesis and Electrochemical

- Properties of Nanostructured  $\text{Li}_2\text{FeSiO}_4/\text{C}$  Cathode Material for Li-Ion Batteries. *Solid State Ionics* **2011**, *192* (1), 356–359.
- (170) Gong, H.; Zhu, Y.; Wang, L.; Wei, D.; Liang, J.; Qian, Y. Solid-State Synthesis of Uniform  $\text{Li}_2\text{MnSiO}_4/\text{C}$ /graphene Composites and Their Performance in Lithium-Ion Batteries. *J. Power Sources* **2014**, *246*, 192–197.
- (171) Reddy, A. L. M.; Gowda, S. R.; Shaijumon, M. M.; Ajayan, P. M. Hybrid Nanostructures for Energy Storage Applications. *Adv. Mater.* **2012**, *24* (37), 5045–5064.
- (172) He, G.; Manthiram, A. Nanostructured  $\text{Li}_2\text{MnSiO}_4/\text{C}$  Cathodes with Hierarchical Macro-/Mesoporosity for Lithium-Ion Batteries. *Adv. Funct. Mater.* **2014**, *24*, 5277–5283.
- (173) Zhao, Y.; Wu, C.; Li, J.; Guan, L. Long Cycling Life of  $\text{Li}_2\text{MnSiO}_4$  Lithium Battery Cathodes under the Double Protection from Carbon Coating and Graphene Network. *J. Mater. Chem. A* **2013**, *1* (12), 3856.
- (174) Zhao, Y.; Li, J.; Wang, N.; Wu, C.; Ding, Y.; Guan, L. In Situ Generation of  $\text{Li}_2\text{FeSiO}_4$  Coating on MWNT as a High Rate Cathode Material for Lithium Ion Batteries. *J. Mater. Chem.* **2012**, *22* (36), 18797.
- (175) Xie, H.-M.; Wang, R.-S.; Ying, J.-R.; Zhang, L.-Y.; Jalbout, a. F.; Yu, H.-Y.; Yang, G.-L.; Pan, X.-M.; Su, Z.-M. Optimized  $\text{LiFePO}_4$ -Polyacene Cathode Material for Lithium-Ion Batteries. *Adv. Mater.* **2006**, *18* (19), 2609–2613.
- (176) Guo, H.; Xiang, K.; Cao, X.; Li, X.; Wang, Z.; Li, L. Preparation and Characteristics of  $\text{Li}_2\text{FeSiO}_4/\text{C}$  Composite for Cathode of Lithium Ion Batteries. *Trans. Nonferrous Met. Soc. China* **2009**, *19* (1), 166–169.
- (177) Zaghbi, K.; Ravet, N.; Gauthier, M.; Gendron, F.; Mauger, A.; Goodenough, J. B. B.; Julien, C. M. M. Optimized Electrochemical Performance of  $\text{LiFePO}_4$  at  $60^\circ\text{C}$  with Purity Controlled by SQUID Magnetometry. *J. Power Sources* **2006**, *163* (1), 560–566.
- (178) Aravindan, V.; Karthikeyan, K.; Kang, K. S.; Yoon, W. S.; Kim, W. S.; Lee, Y. S. Influence of Carbon towards Improved Lithium Storage Properties of  $\text{Li}_2\text{MnSiO}_4$  Cathodes. *J. Mater. Chem.* **2011**, *21* (8), 2470.

- (179) Brinker, C. J.; Scherer, G. W. *Sol-Gel Science: The Physics and Chemistry of Sol-Gel Processing*; Academic: New York, 1990.
- (180) Baes, C. F.; Mesmer, R. E. *The Hydrolysis of Cations*; Wiley, New York, 1976.
- (181) Cogan, H. D.; Setterstrom, C. A. Properties of Ethyl Silicate. *Chem. Eng. News* **1946**, *24*, 2499–2501.
- (182) Ring, T. A. *Fundamentals of Ceramic Powder Processing and Synthesis*; Academic Press, 1996.
- (183) Iler, R. K. *The Chemistry of eSilica: Solubility, Polymerization, Colloid and Surface Properties and Biochemistry of Silica*; Wiley, 1979.
- (184) Schaefer, D. W. Polymers, Fractals, and Ceramic Materials. *Science* **1989**, *243* (4894), 1023–1027.
- (185) Sacks, M. D.; Sheu, R.-S. Rheological Properties of Silica Sol-Gel Materials. *J. Non. Cryst. Solids* *92* (2-3), 383–396.
- (186) Ohtsuka, Y.; Watanabe, T.; Nishiyama, Y.; Matsuda, M.; Yokoi, H. Iron Dispersed Carbon Composites Formed from Iron-Polyvinylalcohol Complexes. *J. Mater. Sci.* **1994**, *29* (4), 877–882.
- (187) Bryaskova, R.; Pencheva, D.; Kale, G. M.; Lad, U.; Kantardjiev, T. Synthesis, Characterisation and Antibacterial Activity of PVA/TEOS/Ag-Np Hybrid Thin Films. *J. Colloid Interface Sci.* **2010**, *349* (1), 77–85.
- (188) Wekesa, M.; Sobhi, H. F. An Insight Into Mn ( II ) Chemistry: A Study of Reaction Kinetics Under Alkaline Conditions. *Acad. Sci.* **2011**, *2* (4), 34–37.
- (189) Ralston, K. D.; Chrisanti, S.; Young, T. L.; Buchheit, R. G. Corrosion Inhibition of Aluminum Alloy 2024-T3 by Aqueous Vanadium Species. *J. Electrochem. Soc.* **2008**, *155* (7), C350.
- (190) Poncelet, G.; Martens, J.; Delmon, B.; Grange, P.; Jacobs, P. A. *Preparation of Catalysts VI: Scientific Bases for the Preparation of Heterogeneous Catalysts*; Elsevier, 1995.
- (191) Ehde, P. M.; Petterson, L.; Glaser, J. Multicomponent Polyanions. 45. A

- Multinuclear NMR Study of Vanadat(V)-Oxalate Complexes in Aqueous Solution. *Acta Chemica Scandinavica*. 1991, pp 998–1005.
- (192) Pratsinis, S. E. Flame Aerosol Synthesis of Ceramic Powders. *Prog. Energy Combust. Sci.* **1998**, *24* (3), 197–219.
- (193) Athanassiou, E. K.; Grass, R. N.; Stark, W. J. Chemical Aerosol Engineering as a Novel Tool for Material Science: From Oxides to Salt and Metal Nanoparticles. *Aerosol Sci. Technol.* **2010**, *44* (2), 161–172.
- (194) Kammler, H. K.; Mädler, L.; Pratsinis, S. E. Flame Synthesis of Nanoparticles. *Chem. Eng. Technol.* **2001**, *24* (6), 583–596.
- (195) Dahl, P. I.; Thomassen, M. S.; Colmenares, L. C.; Barnett, A. O.; Lomas, S.; Vullum, P. E.; Hanetho, S. M.; Mokkelbost, T. Flame Spray Pyrolysis of Electrode Materials for Energy Applications. *Materials Res. Soc. Symp. Proc.* **2015**, *1747*.
- (196) Baranwal, R.; Villar, M. P.; Garcia, R.; Laine, R. M. Flame Spray Pyrolysis of Precursors as a Route to Nano-Mullite Powder: Powder Characterization and Sintering Behavior. *J. Am. Ceram. Soc.* **2001**, *61*, 951–961.
- (197) Ernst, F. O.; Kammler, H. K.; Roessler, A.; Pratsinis, S. E.; Stark, W. J.; Ufheil, J.; Novák, P. Electrochemically Active Flame-Made Nanosized Spinel:  $\text{LiMn}_2\text{O}_4$ ,  $\text{Li}_4\text{Ti}_5\text{O}_{12}$  and  $\text{LiFe}_5\text{O}_8$ . *Mater. Chem. Phys.* **2007**, *101* (2-3), 372–378.
- (198) Tsantilis, S.; Briesen, H.; Pratsinis, S. E. Sintering Time for Silica Particle Growth. *Aerosol Sci. Technol.* **2001**, *34* (3), 237–246.
- (199) Girish, H. N.; Shao, G.-Q. Advances in High-Capacity  $\text{Li}_2\text{MSiO}_4$  (M = Mn, Fe, Co, Ni...) Cathode Material for Lithium-Ion Batteries. *RSC Adv.* **2015**.
- (200) Ketteler, G.; Weiss, W.; Ranke, W.; Schlögl, R. Bulk and Surface Phases of Iron Oxides in an Oxygen and Water Atmosphere at Low Pressure. *Phys. Chem. Chem. Phys.* **2001**, *3* (6), 1114–1122.
- (201) Grundy, A. N.; Hallstedt, B.; Gauckler, L. J. Thermodynamic Assessment of the Mn-O System. *Metall. Trans. B* **2002**, *23* (6), 821–831.

- (202) Wriedt, H. A. The O-V ( Oxygen-Vanadium ) System. *Bull. Alloy phase Diagr.* **1989**, *10* (3), 271–277.
- (203) Yamaguchi, I.; Manabe, T.; Tsuchiya, T.; Nakajima, T.; Sohma, M.; Kumagai, T. Preparation and Characterization of Epitaxial VO<sub>2</sub> Films on Sapphire Using Postepitaxial Topotaxy Route via Epitaxial V<sub>2</sub>O<sub>3</sub> Films. *Jpn. J. Appl. Phys.* **2008**, *47* (2), 1022–1027.
- (204) Plumier, R.; Sougi, M. Observation of a First-Order Transition at  $T < T_c$  in MnV<sub>2</sub>O<sub>4</sub>. *Phys. B Condens. Matter* **1989**, *155*, 315–319.
- (205) Su, D. S. Electron Beam Induced Changes in Transition Metal Oxides. *Anal Bioanal Chem* **2002**, *374* (4), 732–735.
- (206) Su, D. S.; Wieske, M.; Beckmann, E.; Blume, A.; Mestl, G.; Schloegl, R. Reduction of V<sub>2</sub>O<sub>5</sub> in the Transmission Electron Microscope. *Catal. Letters* **2001**, *1* (2), 81–86.
- (207) Tan, H.; Verbeeck, J.; Abakumov, A.; Van Tendeloo, G. Oxidation State and Chemical Shift Investigation in Transition Metal Oxides by EELS. *Ultramicroscopy* **2012**, *116*, 24–33.
- (208) Rossell, M. D.; Agrawal, P.; Borgschulte, A.; Hébert, C.; Passerone, D.; Erni, R. Direct Evidence of Surface Reduction in Monoclinic BiVO<sub>4</sub>. *Chem. Mater.* **2015**, 150414110704005.
- (209) Bard, a. J.; Faulkner, L. R. *ELECTROCHEMICAL METHODS: Fundamentals and Applications*, 2nd Editio.; John Wiley and Sons, INC., 2001.
- (210) Meyers, J. P.; Doyle, M.; Darling, R. M.; Newman, J. The Impedance Response of a Porous Electrode Composed of Intercalation Particles. *J. Electrochem. Soc.* **2000**, *147* (8), 2930.
- (211) Prosen, E. J.; Gilmont, R.; Rossini, F. D. Heats of Combustion of Benzene, Toluene, Ethylbenzene, O-Xylene, M-Xylene, P-Xylene, N-Propylbenzene, and Styrene. *J. Res. Natl. Bur. Stand. (1934)*. **1945**, *34* (1), 65.
- (212) Domalski, E. S. Selected Values of Heats of Combustion and Heats of Formation of Organic Compounds Containing the Elements C, H, N, O, P, and



## Chapter 8 References

---

- S. J. Phys. Chem. Ref. Data.* 1972, pp 221–277.
- (213) Nyten, A.; Stjerndahl, M.; Rensmo, H.; Siegbahn, H.; Armand, M.; Gustafsson, T.; Edström, K.; Thomas, J. O. Surface Characterization and Stability Phenomena in  $\text{Li}_2\text{FeSiO}_4$  Studied by PES/XPS. *J. Mater. Chem.* **2006**, *16* (34), 3483.

## Scientific Papers



# Paper I

Reprinted with kind permission from Elsevier:

*Solid State Ionics*, **2015**, *276*, 26-32.

Effect of carbon content and annealing atmosphere on phase purity and morphology of  $\text{Li}_2\text{MnSiO}_4$  synthesized by a PVA assisted sol-gel method

Nils Wagner, Ann Mari Svensson, Fride Vullum-Bruer





## Effect of carbon content and annealing atmosphere on phase purity and morphology of $\text{Li}_2\text{MnSiO}_4$ synthesized by a PVA assisted sol–gel method



Nils Wagner, Ann-Mari Svensson, Fride Vullum-Bruer\*

Department of Materials Science and Engineering, Norwegian University of Science and Technology, 7401 Trondheim, Norway

### ARTICLE INFO

#### Article history:

Received 20 January 2015

Received in revised form 20 March 2015

Accepted 21 March 2015

Available online 10 April 2015

#### Keywords:

Li-ion battery

Sol-gel

$\text{LiMnSiO}_4$

Carbon coating

Annealing atmosphere

### ABSTRACT

Lithium transition metal orthosilicates of the general formula  $\text{Li}_2\text{MSiO}_4$  have gained great interest as potential positive electrode material for Li-ion batteries. This study reports the dependence of phase purity and morphology on heat treatment atmosphere and the amount of corn-starch as carbonization agent during a PVA assisted sol-gel synthesis of nano-sized porous  $\text{Li}_2\text{MnSiO}_4/\text{C}$  composites. All samples were indexed to the orthorhombic  $\text{Pmn}2_1$  polymorph, but samples with carbon contents less than 6% showed traces of the second orthorhombic polymorph  $\text{Pmnb}$ . Highest phase purities and a desired porous nano-sized morphology were obtained when heat treatments were carried out in 5%  $\text{H}_2$  and corn-starch amounts were  $\geq 25$  wt%. Powders with varying carbon amounts were produced and the electrochemical performance was determined by galvanostatic cycling at different current densities. Samples with a corn-starch amount of 25 wt% offered the highest initial discharge capacity of  $155 \text{ mAh g}^{-1}$  at a current density of  $3 \text{ mA g}^{-1}$ .

© 2015 Elsevier B.V. All rights reserved.

### 1. Introduction

Since the discovery of  $\text{LiFePO}_4$  as a cathode material for Li-ion batteries by Padhi et al. in 1997 [1] polyanion based materials gained great attention as potential Li-ion battery cathodes. Furthermore, polyanion based materials also reveal materials which in theory allow Li extraction/insertion beyond one Li ion per formula unit. Orthosilicates with the general formula  $\text{Li}_2\text{MSiO}_4$  ( $M = \text{Mn, Fe, Co}$ ) could in principle deliver two Li ions per formula unit, giving theoretical capacities up to  $333 \text{ mAh g}^{-1}$ . This is assuming that the transition metal possesses two redox couples within the potential window of a Li-ion battery and that the structure does not collapse [2,3]. Dominko et al. first reported on the synthesis of  $\text{Li}_2\text{MnSiO}_4$ , later called LMS as a promising candidate for Li-ion cathode materials [4]. LMS can in theory extract/insert beyond 1 Li per formula unit since manganese can undergo reversible redox reactions between +2 and +4. A challenge is the structural instability during cycling, which might be caused by a Jahn–Teller distortion of the tetrahedrally coordinated  $\text{Ar } 3d^4$  ion  $\text{Mn}^{3+}$  [5]. This might be eliminated by nano-structuring or implementing stabilizing dopants. However, in order to apply adequate doping strategies the synthesis of the mother compound LMS must be optimized with regard to a desired morphology and a minimum of parasitic secondary phases. Moreover, a general drawback of the orthosilicates is the rather low electronic and Li ionic conductivities. Electronic conductivity values reported in literature are about

$3 \times 10^{-14} \text{ S cm}^{-1}$  at  $60 \text{ }^\circ\text{C}$  [6]. This very poor conductivity value, which at room temperature is even about two orders of magnitude lower, needs to be overcome by applying a conductive coating (e.g. carbon). At the same time the particle size must be reduced to limit the mean diffusion length for Li ions [6,7].

The synthesis and properties of LMS was recently reported by different synthesis methods. Values in brackets give the initial discharge capacity reported and the according reference: A solution route ( $210 \text{ mAh g}^{-1}$  [8]), the Pechini method ( $185 \text{ mAh g}^{-1}$  [9],  $110 \text{ mAh g}^{-1}$  [10],  $147 \text{ mAh g}^{-1}$  [11]), sol-gel ( $181.6 \text{ mAh g}^{-1}$  [12],  $\sim 190 \text{ mAh g}^{-1}$  [13]), polyol method ( $132 \text{ mAh g}^{-1}$  [14]), solid state synthesis ( $160 \text{ mAh g}^{-1}$  [15]) and molten carbonate synthesis ( $156 \text{ mAh g}^{-1}$  [16]). Reported Pechini sol-gel syntheses are based on acetate precursors which react as buffer in a pH range of 4–5 which is unfavorable for the hydrolysis of TEOS. Furthermore, they take a long time, up to 8 days including an aging step and use technical polymers such as poly-N-vinylamide [9–11]. Also other technical substances such as lactones and phenolic resins are used as carbon sources [12,13].

Here we report on a simple wet chemical approach, namely an acidic PVA assisted sol-gel method using metal nitrates and TEOS as silicon precursor with subsequent carbothermal reduction using simple corn-starch and an  $\text{Ar}/\text{H}_2$  atmosphere as reducing agents. The rather quick synthesis yields nano-sized LMS particles with high phase purity, aggregated in a porous manner. Residues of PVA and the introduced corn-starch which was incorporated in amounts from 0 to 50 wt%, provide a carbon coating on the LMS particles (LMS/C composite) and thus enhance the electronic conductivity. In contrast to many other studies the secondary phases

\* Corresponding author.

E-mail address: fride.vullum-bruer@ntnu.no (F. Vullum-Bruer).

were not only indexed but quantified in order to gain information about the influence of atmosphere and carbonizing agent on the phase purity of LMS.

## 2. Experimental

### 2.1. Material synthesis

The acidic, PVA assisted  $\text{Li}_2\text{MnSiO}_4$  sol-gel synthesis described in this work is based on a  $\text{Li}_2\text{FeSiO}_4$  sol-gel process reported by Zhou et al. [17] with optimized parameters for LMS. 0.03 mole  $\text{Mn}(\text{NO}_3)_2 \cdot 4\text{H}_2\text{O}$  (Merck Ensure for analysis, >98%) and 0.06 mol dried  $\text{LiNO}_3$  (Alfa Aesar, 99%) was dissolved in 25 mL deionized  $\text{H}_2\text{O}$  and the pH was set to ~1.5 by adding  $\text{HNO}_3$  (Sigma Aldrich  $\geq 65\%$  pro Analyti). 0.03 mol tetraethyl orthosilicate (TEOS) (VWR 99%) was dissolved in 20 mL EtOH and added to the Li–Mn solution under vigorous stirring. The pale pink solution was stirred for 20 min at room temperature, before 1.14 g PVA (Sigma Aldrich Mowiol 10–98,  $M_w = 61,000$ ) dissolved in 20 mL was added. The pH of the solution was ~2.5. To ensure complexing of the metal cations, the solution was stirred for 1 h in a closed beaker at 60 °C, and then evaporated at 60 °C for 6 h until gelation occurred.

The formed gel was aged for 72 h in a closed Ar filled beaker before it was dried for 4 h at 130 °C. The dried gel was ground and calcined for 1 h at 450 °C in air or in 95% Ar 5%  $\text{H}_2$  later called H–Ar-mix-5 to combust the nitrates and parts of the organic residues. After the calcination the LMS precursor was mixed with different amounts of corn-starch (Carl Roth GmbH & Co. KG for laboratory use) (0–50 wt.%) as carbon source. An EtOH based suspension of the LMS precursor and corn-starch was intensively mortared till dryness. The final heat treatment for 10 h at 700 °C was performed in Ar or H–Ar-mix-5. A flow chart summarizing the synthesis with optimized parameters is shown in Fig. 1.

### 2.2. Characterization

Powder X-ray diffraction patterns were recorded on a Bruker D 8 Advance Da-Vinci with a LynxEye Xe detector working in Bragg–Brentano ( $\theta/2\theta$ ) geometry. Patterns were recorded using  $\text{CuK}\alpha$  and  $\text{MoK}\alpha$  radiation from  $2\theta = 15\text{--}75^\circ$  and  $5\text{--}75^\circ$ , respectively. Lattice parameter calculations, full pattern refinements and quantifications of secondary phases of powder X-ray diffraction patterns recorded using  $\text{MoK}\alpha$  radiation were done with the software Topas (Bruker AXS Version 4.2). The peak shape was refined using a Pseudo-Voigt approximation (PV2). The atomic positions not fixed by the geometry of the space-group  $\text{Pmn}2_1$  were allowed to converge, starting with the heaviest element. Refined parameters were used to quantify the phase fraction of powder diffraction patterns recorded using  $\text{CuK}\alpha$  radiation. Here, a fundamental parameter approach was used to fit the peak shape.

Surface area and porosity data were measured by nitrogen adsorption on a Micrometrics Tristar 3000. Powders were dried at 250 °C for 12 h in vacuum prior to analysis. A total of 94 points were measured for the adsorption/desorption isotherms.

The carbon content was determined with an Eltra CS 800 elementary analyzer. Morphology investigations were carried out by transmission electron microscopy. TEM analysis was done on a double  $\text{C}_s$  corrected cold field emission gun JEOL JEM-ARM200F operated at 200 kV, equipped with a large solid angle Centurio SDD (Silicon Drift Detector). For microscopy investigations, the powders were dispersed in isopropanol and sonicated for 20 min. A small droplet of the powder/alcohol suspension was placed on an amorphous carbon coated Cu TEM grid.

Assessment of electrochemical properties was done by galvanostatic charge–discharge measurements between 1.5 and 4.5 V and 1.5 and 4.8 V at 24 °C using a Maccor 4200. CR2016 coin cells were assembled in a glove box (dry Ar atmosphere) using LMS or LMS/C as cathode, Li-foil as anode and a Celgard 2400 film as electrode separator. The electrolyte consisted of 1 M  $\text{LiPF}_6$  (Aldrich  $\geq 99.99\%$ ) dissolved in a 3:7

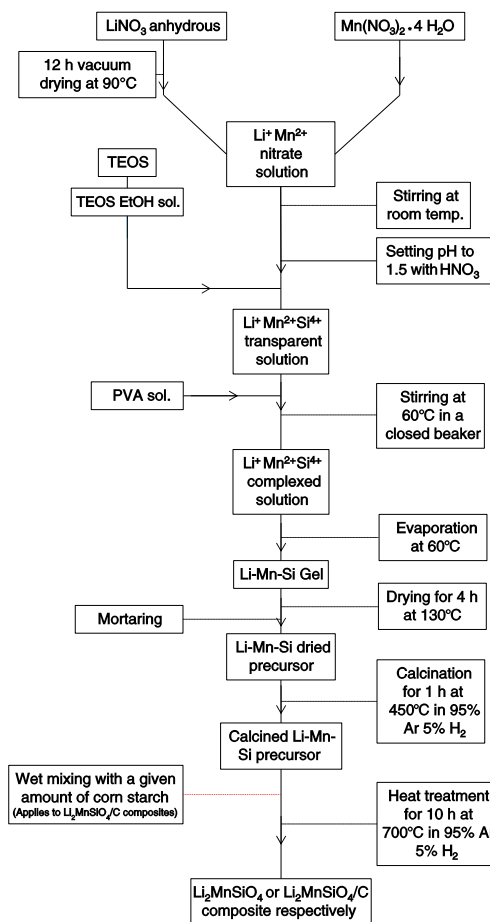


Fig. 1. Summarizing flow chart with optimized parameters for the LMS and LMS/C synthesis.

volume ratio of ethylene carbonate (Sigma 99%) and diethyl carbonate (Aldrich  $\geq 99\%$ ). For cathode fabrication, the active material, LMS or LMS/C respectively was mixed with 10 wt.% conductive carbon (Super P) and 5 wt.% PVDF (Kynar, reagent grade) as binder. N-methyl-2-pyrrolidone (NMP) (Sigma Aldrich >99%) was added as solvent and a slurry was formed by ball milling on a RETSCH mixer mill in a stainless steel container. The slurry was tape casted on Al foil as current collector and dried for 12 h at 90 °C in a vacuum oven. Cast thicknesses were about 15–20  $\mu\text{m}$ . Capacities are reported with respect to the mass of LMS or the LMS/C composite. The charge rate C was defined as a current density of  $330 \text{ mA g}^{-1} = 1\text{C}$ .

## 3. Results and discussion

### 3.1. Influences of the atmosphere and corn-starch amount on the phase purity

All obtained dried gels were amorphous but showed minor  $\text{LiNO}_3$  precipitates in the XRD patterns which are shown in the supporting

material. The weight loss during calcination in H–Ar–mix-5 and in air was measured to be approximately 37 wt.%. The phase purity of the resulting LMS/C showed a strong dependence on the  $p_{O_2}$  during the heat treatments which is dependent on the gas composition and the corn-starch content. Best results were achieved when both heat treatments were carried out in H–Ar–mix-5 and initial corn-starch contents were  $\geq 25$  wt.%. LMS adopts  $Li_3PO_4$  structures and is reported to exist in two orthorhombic and two monoclinic polymorphs, namely Pmn2<sub>1</sub>, Pmnb, P2<sub>1</sub>/n and Pn [4,18–20]. All samples were indexed to the orthorhombic Pmn2<sub>1</sub> polymorph of LMS. Secondary phases present for LMS and LMS/C with low carbon content were  $Li_2SiO_3$ ,  $Mn_2SiO_4$  and MnO, LMS/C samples produced with corn-starch amounts of  $\geq 25$  wt.% showed minor  $Li_2SiO_3$  and MnO impurities. The different heat treatment parameters and corn-starch content of a sample series A–D are given in Table 1.

Fig. 2a shows the phase composition of the corresponding samples. It can be seen in the next section that 30 wt.% corn-starch in powder A yields a similar carbon content in the final powder as 25 wt.% in powder D. Although the error of these quantifications might be as large as 5%, clear trends in increased phase purity are observed. Furthermore, quantified data of sample D using  $MoK_{\alpha}$  and  $CuK_{\alpha}$  radiation is in agreement, which indicates the accuracy of the values. Calcination in H–Ar–mix-5 is believed to hinder parasitic Mn oxidation and the formation of multivalent Mn oxides that need to be reduced during the final heat treatment. XRD patterns of the calcined precursors showed some crystallinity but were mainly amorphous and are shown in the supporting material. Fig. 2b shows the phase fraction with regard to the added corn-starch content from 0 to 50 wt.% for powder samples where both heat treatments were carried out in H–Ar–mix-5. It has to be mentioned that the shown phase fractions refer to the crystalline part of the samples and disregard the amorphous carbon content. Samples containing 10 and 20 wt.% corn-starch were not synthesized and the quantification of a sample containing 5 wt.% corn-starch was disregarded due to an unidentified secondary phase. The phase purity of all samples with added corn-starch amounts of 25 wt.% and more is higher than 95 wt.%. The difference in phase fraction of samples with added corn-starch amount  $\geq 25$  wt.% is well within the error range of Rietveld based quantifications. In addition, an increase in the amorphous carbon content caused by addition of more corn-starch in the synthesis will reduce the signal to noise ratio, thus it cannot be concluded if there is a significant difference in phase purity for corn-starch amounts of 25 wt.% or higher. Samples containing less corn starch showed lower phase purities and the appearance of a second orthorhombic LMS polymorph (Pmnb). This polymorph shows a  $2\theta$  diffraction peak at about  $30.6^\circ$  under  $CuK_{\alpha}$  radiation which is often disregarded or confused with a  $Mn_2SiO_4$  secondary phase which shows a peak at  $31.2^\circ$   $2\theta$ . As a result, significant amounts of Pmnb phases may be present in samples claimed to be indexed to Pmn2<sub>1</sub> [11,13,15]. Powder XRD patterns of samples calcined and reduced in H–Ar–mix-5 with varying corn-starch content are given in Fig. 3. The calculated carbon content is based on carbon content measurements shown in the following chapter. Part b shows a full pattern refinement using  $MoK_{\alpha}$  radiation, the corresponding lattice parameters for the orthorhombic Pmn2<sub>1</sub> unit cell were  $a = 6.3062$  Å,  $b = 5.3844$  Å and  $c = 4.9656$  Å and are in agreement with data from literature [4]. All further presented results are based on LMS and LMS/C powders were synthesized with optimized parameters where both heat treatments were carried out in H–Ar–mix-5.

**Table 1**  
Heat treatment atmospheres and carbon source amount of samples A–D.

Sample	Calcination atmosphere	Corn-starch [wt.%]	Heat treatment atmosphere
A	Air	30	Ar
B	Air	25	H–Ar–mix-5
C	H–Ar–mix-5	25	Ar
D	H–Ar–mix-5	25	H–Ar–mix-5

### 3.2. Morphology and carbon content

The PVA assisted sol–gel synthesis with additional gel aging was performed to obtain a strong gel network which does not collapse and yield porous nano-structured materials with high surface areas. Hydroxyl groups of the PVA can, in addition to bridging to polymerized silanol groups of the network, complex the metal cations and thus strengthen the network. It was shown for  $Li_2FeSiO_4$ , a very similar compound, that the addition of a complexing/bridging agent (PVA) during a sol gel method is essential to obtain a nano-porous structure [21]. The aging for 72 h under Ar atmosphere was performed in order to gain further structural strength by syneresis and further bond formation. The aged gel can withstand the capillary forces during drying and keep a porous structure [17]. Ar atmosphere was applied to hinder parasitic reactions between the expelling liquid and oxygen from the atmosphere.

The initial corn-starch content showed a strong influence on the resulting morphology of the powder. The residual carbon content of LMS/C composites with varying amounts of corn-starch (heat treated in H–Ar–mix-5) was measured with an elementary analyzer. Also three different LMS/C samples heat treated in Ar were measured. The results are shown in Fig. 4. An exponential growth fit for the samples heat treated in H–Ar–mix-5 is added as a guide for the eye.

Fig. 5a shows the surface area divided into micropore area and external area according to T-plot theory [22,23] for powders with the corresponding isotherms in the insert. The sum of micropore area and external area is equal to the BET surface area. In this case, the presentation of just the BET surface area without further differentiation would be inconvenient, since micropores are by definition smaller than 2 nm and thus inaccessible to complexed Li ions [17]. Here the external area is the surface area that is not attributed to micropores. By dividing the surface area in micropore area and external area the accessible surface area can be defined. This gives a more meaningful presentation of a porous electrode surface area. The powder morphology for corn-starch contents  $\geq 25$  wt.% consists out of porously agglomerated particles with a particle size of about 40–50 nm, while powders containing lower amounts of corn-starch showed a much lower surface area. It is believed that the carbon layer formed on the particle surface hinders particle growth to a certain extent. Since powders containing a relatively low amount of carbon are not covered by this film they might show a higher degree of particle growth and thus a reduced surface area. A high amount of meso/macro-porosity, which is accessible for complexed Li ions, is present. In addition, the powders show an increasing amount of micro-porosity with increasing corn-starch amount. This micro-porosity is believed to be attributed to the porous nature of the amorphous carbon layer on the particle surface. Fig. 5b shows the pore distribution based on desorption data according to BJH theory [24], of different corn-starch contents between 2 and 100 nm with a highlighted area between 3 and 6 nm. This area shows a peak in porosity increasing with increasing corn-starch amount, thus it can as well be attributed to the carbon layer. TEM analysis (Fig. 6.) revealed the porous nature of the agglomerated nano-particles. Furthermore, Fig. 6b and c shows the carbon coated particle surface of a sample containing 25 and 50 wt.% corn-starch, respectively. The porosity of this layer is clearly visible in Fig. 6c so it is concluded that the increasing micro-pore area and the abnormal porosity between 3 and 6 nm corresponds to the carbon layer. The electron diffraction pattern of LMS is shown in Fig. 6d. The main diffraction lines of polycrystalline Pmn2<sub>1</sub> LMS are visible. Comparing Fig. 6a and c also reveals the effect of the carbon source on the particle size. While crystallites in Fig. 6a, where 25 wt.% corn-starch was added to the synthesis, show particle sizes from approximately 50 to 100 nm, crystallites of the powder containing 50 wt.% corn-starch are in the range of 20–40 nm, which can be seen in Fig. 6c.

### 3.3. Electrochemical characterization

To investigate the importance of the carbon content and hence the electronic conductivity, CR2016 coin cells were fabricated with LMS



**Table 2**  
Irreversible capacity loss and corrected capacities during the first cycle of samples cycled at C/33 between 1.5 and 4.5 V.

Sample	Charge capacity 1st cycle [mAh g <sup>-1</sup> (LMS)]	Discharge capacity 1st cycle [mAh g <sup>-1</sup> (LMS)]	Irreversible capacity loss [%]
25 wt.% corn-starch	156.7	110.7	29.4
35 wt.% corn-starch	136.8	107.1	21.7
45 wt.% corn-starch	141.3	109.4	22.6
50 wt.% corn-starch	148.5	109.3	26.4

cathodes produced using 0, 5, 15, 25, 35, 45 and 50 wt.% added corn-starch. Furthermore, the cathode contained 10 wt.% Super P conductive carbon and 5 wt.% PVDF as binder. The counter electrode was in all cases Li foil. These coin cells were galvanostatically cycled between 1.5 and 4.5 V at charge rates corresponding to C/33 and C/4. Fig. 7 shows the first two cycles of the corresponding coin cells and the reversible discharge capacity for 15 cycles where the charge rate was C/33 in the first five cycles C/4 for the following 5 cycles and C/33 for the last five cycles.

All samples showed an irreversible capacity loss of 20–30% during the first cycle. The oxidation of the electrolyte is expected to contribute to a fraction of this loss, but cannot solely be responsible for the irreversible capacity loss. It is therefore likely that the extraction of Li ions is partly irreversible. Furthermore, Molenda et al. observed structural changes in the carbon coating by XPS which could also contribute to the irreversible capacity loss by a loss in electronic conductivity [12].

The need of a conductive coating is clearly seen. LMS cathodes with no carbon or only 5 wt.% addition of corn-starch showed very low reversible capacities of about 1.5–2 mAh g<sup>-1</sup> in the first cycle. 15 wt.% corn-starch which corresponds to 4 wt.% residual carbon is still not sufficient to obtain the necessary coating. The peak in performance was observed with an addition of 25 wt.% corn-starch, where the reversible discharge capacity in the first cycle was about 100 mAh g<sup>-1</sup>. That corresponds to the reversible extraction/insertion of 0.66 Li ions per formula unit assuming that the discharge capacity is solely due to Li insertion. Accordingly, it can be concluded that only the Mn<sup>3+</sup>/Mn<sup>2+</sup> redox couple

is active in the materials within the voltage range of 1.5–4.5 V. Higher corn-starch contents result in a slight capacity decrease. This can be attributed to the fact that less active material per weight of a cathode is present. Interestingly, the behavior changes at higher charge rate (in this case C/4), and cathodes containing 35, 45, and 50 wt.% corn-starch showed an increase in rate capability and thus higher capacities compared to the sample made with 25 wt.% corn-starch. Converting these values to reversible Li exchange values, the sample containing 25 wt.% corn-starch showed only a reversible exchange of 0.2 Li per formula unit, while a sample with 50 wt.% corn-starch showed a reversible exchange of 0.43 Li per formula unit. This indicates that the electronic conductivity which is even more important at higher rates is improved due to the increased residual carbon content. In addition, the decreased particle size of samples with higher residual carbon content could enhance the kinetics of Li-extraction/insertion. Samples containing 45 and 50 wt.% corn-starch show very similar external surface areas and rate capabilities as shown in Figs. 5a and 7b, respectively. Coin cells

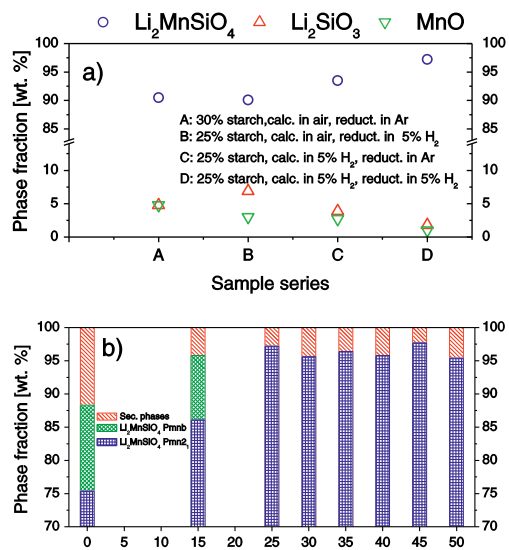


**Fig. 2.** a) Phase composition for different heat treatment atmospheres. b) Phase fraction for different starch contents at optimized synthesis parameters.

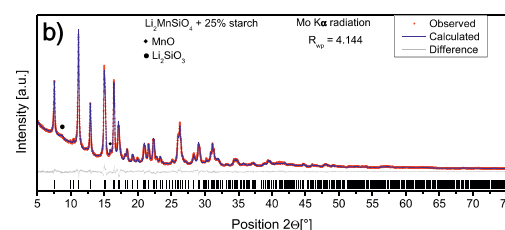
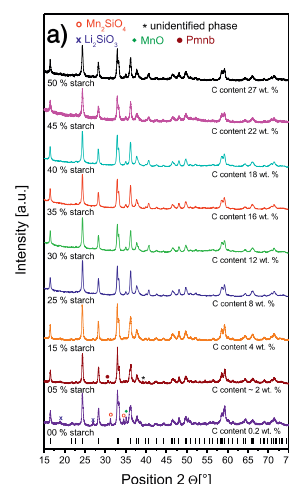


**Fig. 3.** a) Powder XRD pattern (CuK $\alpha$  radiation) of LMS/C synthesized with optimized parameters and different corn-starch contents. Residual carbon content is given. Asterisk marks the unidentified secondary phase in the 5% sample. b) Full pattern refinement (MoK $\alpha$  radiation) of a LMS/C sample.

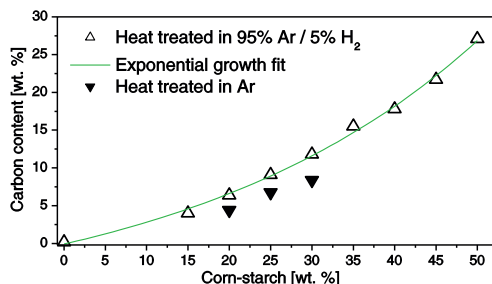


Fig. 4. Carbon content of LMS/C samples heat treated in H-Ar-mix-5 and in Ar respectively.

with cathodes containing 25 and 50 wt.% corn starch were also cycled up to 4.8 V. The charge and discharge was done with a charge rate of C/100 to investigate slow rate performance and at a charge rate of C/33 for 100 cycles for long-term performance investigations. Results are shown in Fig. 8. Here, the top abscissa in Fig. 8a and b shows the specific capacity per gram LMS (carbon content is subtracted from the mass of the composite to give active material mass) while the bottom abscissa shows the specific capacity per gram LMS/C composite. The slow cycling at a charge rate of C/100 resulted in a reversible capacity of  $155 \text{ mAh g}^{-1}$  and  $140 \text{ mAh g}^{-1}$  in the first cycle for cathodes containing 25 wt.% and 50 wt.% corn-starch, respectively. The corresponding irreversible capacity loss in the first cycle was 40 and 38.5%, indicating that more Li ions were extracted than inserted. Taking the carbon content of 9 and 27 wt.% into account and disregarding the minor impurities of both samples gives initial discharge capacities of  $170 \text{ mAh g}^{-1}$  and  $192 \text{ mAh g}^{-1}$ , respectively. The value of the sample containing 25 wt.% corn-starch corresponds well to the reversible extraction/insertion of one Li per formula and the 50 wt.% shows reversible Li exchange of 1.15 Li per formula unit under the same assumption as mentioned before. Furthermore, the sample containing 25 wt.% corn-starch shows an even more severe capacity fading already in the second cycle, where the discharge capacity already dropped by 11% down to  $138 \text{ mAh g}^{-1}$ , while the 50 wt.% sample only showed a 4% capacity drop. This might indicate that the amorphization of LMS shows a more prominent impact on the Li-extraction/insertion kinetics of larger particles present in the 25 wt.% corn-starch sample.

The same trend is visible in Fig. 8c. The sample containing 25 wt.% corn-starch shows more severe capacity fading on the first 20 cycles compared to the 50 wt.% one. The inset of Fig. 8b shows the coulombic

efficiency which exhibits values between 90 and 100% for both samples after the first few cycles.

If it is assumed that the majority of the first charge capacity is due to Li extraction, then the irreversible capacity loss in the first cycle gives a direct indication of a partly collapsed structure that does not allow full re-lithiation during the following discharge. This effect is supposed to be more prominent the more Li is extracted [25]. Table 2 shows corrected (mass of carbon is subtracted) charge and discharge capacities and the irreversible capacity loss in percent of cathodes synthesized using 25–50 wt.% corn-starch. Samples synthesized without or with a low amount of corn-starch addition are excluded because they showed very little or no electrochemical activity.

A trend of increasing irreversible capacity loss with increasing first charge capacity is visible indicating a higher degree of structural collapse when more Li is extracted. Furthermore, the charge plateau in the second cycle is in all cases shifted to lower potentials which would also indicate structural changes [26]. Recently, Devaraj et al. reported about LMS with a distinct charge and discharge plateau during the first ten cycles, indicating a preserved structure before degradation occurred [13]. This behavior was neither observed here, nor in other studies [4–6,8–12,14, 15]. Apart from the first charge, which shows a plateau at about 4.2 V no distinct charge plateaus were present. This also indicates structural degradation. The irreversible capacity is not solely due to structural collapse. In reality it is most probably a combination of irreversible electrolyte oxidation and structural degradation which becomes more prominent the more Li is extracted.

#### 4. Conclusions

The successful preparation of porous nano-sized LMS/C by a PVA assisted sol-gel method is reported. The addition of corn-starch was shown to be crucial for phase purity during the carbothermal reduction step as well as for the electrochemical performance by building up a conductive coating around the particles. In addition, it seems to hinder particle growth to a certain extent so that the resulting powder offers a high amount of porosity in the meso-/macro-range and a huge increase in accessible surface area. Also the effect of the atmosphere and thus  $p_{\text{O}_2}$  was shown to be of major importance for the synthesis of LMS. Highest phase purities of 95% or higher were achieved when heat treatments were carried out in 5%  $\text{H}_2$  (H-Ar-mix-5) and starch contents were  $\geq 25$  wt.%. Samples synthesized under these conditions were indexed to the orthorhombic space group  $\text{Pmn}2_1$  and showed only minor traces of secondary phases, namely  $\text{MnO}$  and  $\text{Li}_2\text{SiO}_3$ . If the applied corn-starch amount was 15 wt.% or lower, powders are consisted of a

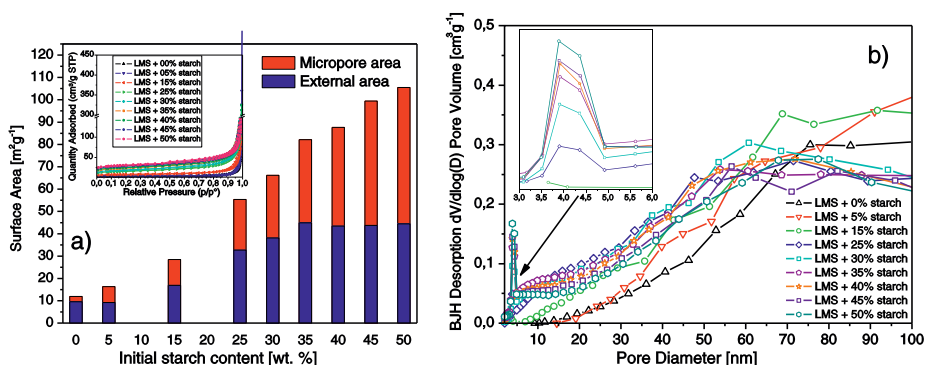


Fig. 5. a) BET surface area for powders with varying corn-starch content, including isotherms and micro-pore/external area separation. b) Pore size distribution for powders with varying corn-starch content.

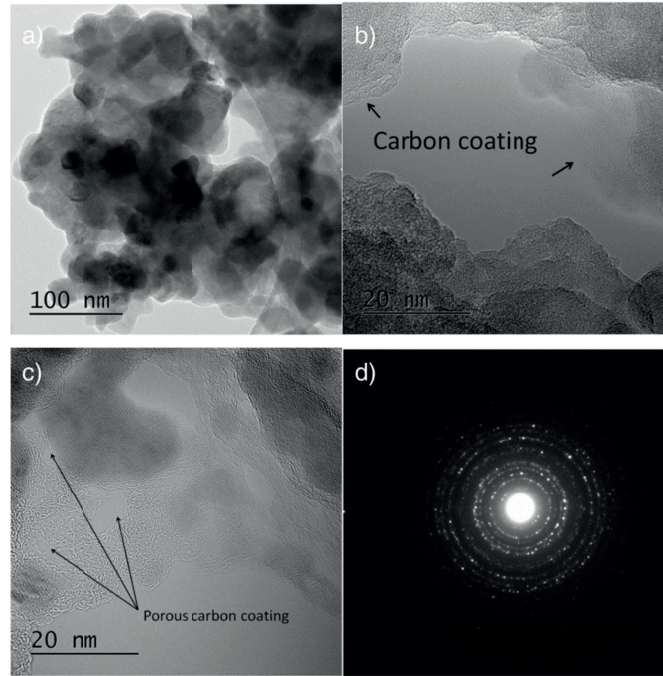


Fig. 6. TEM micrographs of a) the agglomerate structure of a sample containing 25 wt.% corn-starch, b) the carbon coating of a sample containing 25 wt.% corn-starch, c) the porosity of the carbon coating of a sample containing 50 wt.% corn-starch and d) the electron diffraction pattern.

mixture of orthorhombic Pmn2<sub>1</sub> and orthorhombic Pmnb polymorph of LMS in addition to an increased amount of secondary phases. The highest reversible capacity was observed using powder offering 25 wt.% corn-starch addition during synthesis. Coin-cells using this powder as cathode offered a discharge capacity of 155 mAh g<sup>-1</sup> cycled at C/100 and 124 mAh g<sup>-1</sup> cycled at C/33 in the first cycle. The first value corresponds approximately to the reversible extraction/insertion of one Li per formula unit taking the carbon content of the sample into consideration. Unfortunately all samples showed relatively low rate capabilities and irreversible

capacity fading during cycling, which is believed to be the result of a partly collapsed (amorphous) structure during cycling [25].

**Acknowledgments**

The authors gratefully acknowledge the Research Council of Norway for funding of the SilicatBatt project (grant number: 216469/E20), NORTEM seed and competence projects (grant number 11) and Dr. Per Erik Vullum are acknowledged for TEM analysis. Dr. Julian

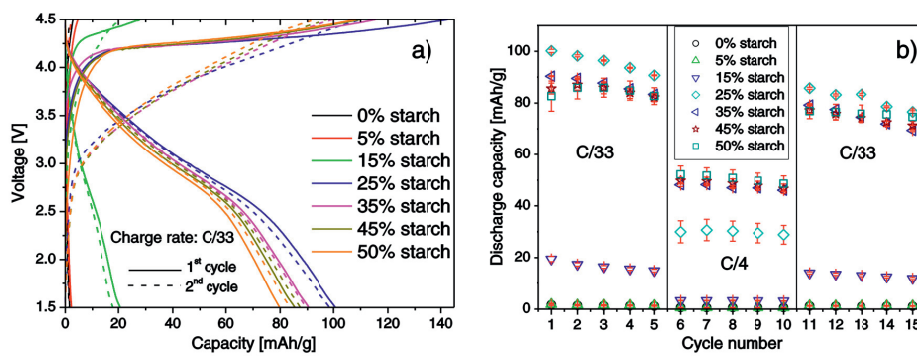


Fig. 7. Galvanostatic cycling of LMS cathodes offering a varying amount of corn-starch as carbon source. a) First two cycles at C/33. b) Reversible discharge capacity for 15 cycles at different charge rates.

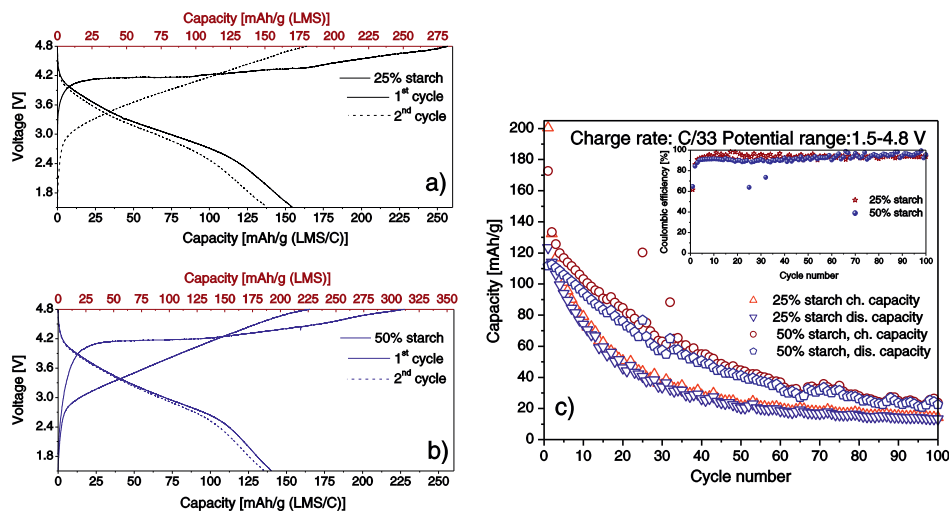


Fig. 8. First two galvanostatic cycles of LMS cathodes offering 25% a) and 50 wt.% b) corn-starch as carbon source up to 4.8 V at C/100. Bottom abscissa shows specific capacity per g LMS/C composite, top abscissa the specific capacity per g LMS. c) 100 cycles of cathodes offering 25% a) and 50 wt.% corn-starch at C/33.

Tolchard is acknowledged for his assistance with Rietveld analysis and Prof. Thomas Jüstel for allowing the use of the carbon determination facilities of Münster University of Applied Science Germany.

#### Appendix A. Supplementary data

Supplementary data to this article can be found online at <http://dx.doi.org/10.1016/j.ssi.2015.03.029>.

#### References

- [1] A.K. Padhi, K.S. Nanjundaswamy, J.B. Goodenough, *J. Electrochem. Soc.* 144 (1997) 1188–1194.
- [2] Islam M. Saiful, R. Dominko, C. Masquelier, C. Sirisopanorn, A.R. Armstrong, P.G. Bruce, *J. Mater. Chem.* 21 (2011) 9811–9818.
- [3] B.L. Ellis, K.T. Lee, L.F. Nazar, *Chem. Mater.* 22 (2010) 691–714.
- [4] R. Dominko, M. Bele, M. Gabersček, A. Meden, M. Remškar, J. Jamnik, *Electrochem. Commun.* 8 (2006) 217–222.
- [5] P. Larsson, R. Ahuja, A. Liivat, J.O. Thomas, *Comput. Mater. Sci.* 47 (2010) 678–684.
- [6] R. Dominko, *J. Power Sources* 184 (2) (2008) 462–468.
- [7] R.J. Gummow, Y. He, *J. Power Sources* 253 (2014) 315–331.
- [8] Y.X. Li, Z.L. Gong, Y. Yang, *J. Power Sources* 174 (2007) 528–532.
- [9] M. Świątosławski, M. Molenda, K. Furczo, R. Dziembaj, *J. Power Sources* 244 (2013) 510–514.
- [10] M. Świątosławski, M. Molenda, M. Grabowska, A. Wach, P. Kuśtrowski, R. Dziembaj, *Solid State Ionics* 263 (2014) 99–102.
- [11] M. Molenda, M. Świątosławski, A. Wach, D. Majda, P. Kuśtrowski, R. Dziembaj, *Solid State Ionics* 262 (2014) 98–101.
- [12] D. Sun, H. Wang, D. Ping, N. Zhou, X. Huang, S. Tan, Y. Tang, *J. Power Sources* 242 (2013) 865–871.
- [13] S. Devaraj, M. Kuezza, C.T. Ng, P. Balaya, *Electrochim. Acta* 102 (2013) 290–298.
- [14] W.G. Liu, Y.H. Xu, R. Yang, *Rare Metals* 29 (2010) 511–514.
- [15] V. Aravindan, K. Karthikeyan, K.S. Kang, W.S. Yoon, W.S. Kim, Y.S. Lee, *J. Mater. Chem.* 21 (2011) 2470–2475.
- [16] A. Kojima, T. Kojima, M. Tabuchi, T. Sakai, *J. Electrochem. Soc.* 159 (2012) A532–A537.
- [17] H. Zhou, M.-A. Einarsrud, F. Vullum-Bruer, *J. Power Sources* 235 (2013) 234–242.
- [18] V.V. Politaev, A.A. Petrenko, V.B. Nalbandyan, B.S. Medvedev, E.S. Shvetsova, *J. Solid State Chem.* 180 (3) (2007) 1045–1050.
- [19] R.J. Gummow, N. Sharma, V.K. Peterson, Y. He, *J. Solid State Chem.* 188 (2012) 32–37.
- [20] H. Duncan, A. Kondamreddy, P.H.J. Mercier, Y. Le Page, Y. Abu-Lebdeh, M. Couillard, P.S. Whitfield, I.J. Davidson, *Chem. Mater.* 23 (2011) 5446–5456.
- [21] H. Zhou, M.-A. Einarsrud, F. Vullum-Bruer, *Solid State Ionics* 225 (2012) 585–589.
- [22] S. Brunauer, P.H. Emmett, E. Teller, *J. Am. Chem. Soc.* 60 (1938) 309–319.
- [23] W.D. Harkins, G. Jura, *J. Am. Chem. Soc.* 66 (1944) 1366–1373.
- [24] E.P. Barrett, L.G. Joyner, P.P. Halenda, *J. Am. Chem. Soc.* 73 (1951) 373–380.
- [25] R. Dominko, M. Bele, A. Kokalj, M. Gabersček, J. Jamnik, *J. Power Sources* 174 (2) (2007) 457–461.
- [26] A. Nyttén, S. Kamali, L. Häggström, T. Gustafsson, J.O. Thomas, *J. Mater. Chem.* 16 (23) (2006) 2266–2272.



## Paper II

Reprinted with kind permission from the Electrochemical Society:

*ECS Transactions*, **2015**, *64* (22), 33-45.

Fe and V Substituted  $\text{Li}_2\text{MnSiO}_4/\text{C}$  as Potential Cathode Material for Li-ion Batteries

Nils Wagner, Antoine Dalod, Ann Mari Svensson, Fride Vullum-Bruer



## Fe and V Substituted $\text{Li}_2\text{MnSiO}_4/\text{C}$ as Potential Cathode Material for Li-ion Batteries

Nils Wagner<sup>a</sup>, Antoine Dalod<sup>a</sup>, Ann -Mari Svensson<sup>a</sup> and Fride Vullum-Bruer<sup>a</sup>

<sup>a</sup>Department of Materials Science and Engineering, Norwegian University of Science and Technology,  
7491 Trondheim, Norway

Lithium transition-metal silicate materials are promising candidates for next generation Li-ion batteries since they allow Li extraction/insertion beyond one Li ion per formula unit. They consist of cheap, non-toxic and abundant elements. Here we focus on the synthesis and electrochemical performance of Fe and V substituted  $\text{Li}_2\text{MnSiO}_4$ . Cations were substituted to overcome poor stability of the undoped compound and increase conductivity, thus expected to increase the electrochemical performance. Up to 20 mole % Fe and 5 mole % V were incorporated into orthorhombic  $\text{Pmn}2_1$   $\text{Li}_2\text{MnSiO}_4$  while keeping a high phase purity and the desired porous nano-sized structure. For materials with 20 mole % Fe substitution, the reversible Li intercalation capacity during slow cycling (C/33) was increased from 0.63 Li per formula unit for the undoped to 0.81 for the doped sample. A 5 mole % V substitution increased the reversible Li capacity from 0.65 Li per formula unit to 0.73.

### Introduction

Since Nyten *et al.* [1] reported  $\text{Li}_2\text{FeSiO}_4$  as a new Li-battery cathode material in 2005, transition metal ortho-silicates came into focus as potential cathode materials for next generation Li-ion batteries [1, 2, 3]. Transition metal ortho-silicates, where the transition metal is Fe or Mn are environmentally benign. In theory  $\text{Li}_2\text{MnSiO}_4$  allows the reversible exchange of up to two Li per formula unit, offering a theoretical capacity of  $333 \text{ mAhg}^{-1}$  [2, 3]. Dominko *et al.* reported on the synthesis of  $\text{Li}_2\text{FeSiO}_4$  (LFS) and  $\text{Li}_2\text{MnSiO}_4$  (LMS) and found the major drawback of the transition metal ortho-silicates to be the low electronic conductivity, which in the case of LMS is about  $3 * 10^{-14} \text{ Scm}^{-1}$  at  $60^\circ\text{C}$  [4, 5]. Furthermore, LMS suffers from severe capacity fading which is believed to be caused by a Jahn-Teller distortion of the tetrahedrally coordinated [Ar]  $3d^4$  ion  $\text{Mn}^{3+}$  during charging [6]. The Li diffusion coefficient in LMS is also reported to be rather poor,  $3.4 * 10^{-18} \text{ cm}^2\text{s}^{-1}$  [7]. Means to remedy this would be to reduce the mean diffusion length for the Li ions by nano-structuring combined with application of a conductive carbon coating [5, 8]. LMS has recently been synthesized by various wet chemical methods such as solution routes, sol-gel, Pechini and polyol methods. [7, 8, 9, 10, 11, 12, 13].

Here we try to manipulate the electrochemical performance and the stability of LMS by doping strategies. We report on an acidic, PVA assisted sol-gel method leading to



nano-sized LMS particles agglomerated in a porous manner. A carbon coating is applied by adding corn-starch prior to the final heat treatment. Up to 20 mole % Mn was substituted by Fe since LFS is reported to facilitate a stable exchange of up to 1 Li ion per formula unit [1, 5, 14]. Also, the redox couple Fe II/III is located at lower potentials and thus more easily accessible [5]. Previous research has often focused on the substitution of Fe by Mn in LFS [15, 16], but here we focus on the Mn-rich side in the LMS-LFS system.

Another interesting approach is the incorporation of V into lithium transition metal ortho-silicates. V offers various accessible oxidation states and is thus a promising ion in electrode materials for Li-ion batteries [17]. Recently, density functional theory calculations showed V substitution into LFS structurally stable up to 50 mole % [17]. Furthermore, an experimental study has reported a successful incorporation of 10 mole % V into LFS. The incorporation of V on either Fe or Si sites, with an increase in electrochemical performance when V is incorporated on a Si site compared to an undoped LFS sample were shown in the study [18]. A second study reported the successful incorporation of 5 mole % V into LFS but a decline in electrochemical properties, as well as phase separation at higher V substitution levels [19]. We demonstrate increased electrochemical response of LMS by incorporation of 5 mole % V. To our knowledge V substitution in LMS has never been demonstrated before.

## Experimental

### Synthesis

The materials synthesis was done according to a PVA assisted sol-gel method. A more detailed description of the synthesis is published elsewhere [13]. A 25 mL aqueous solution of 0.06 mole  $\text{LiNO}_3$  (Alfa Aesar, 99%) and 0.03 mole  $\text{Mn}(\text{NO}_3)_2 \cdot 4\text{H}_2\text{O}$  (Merck Emsure for analysis, > 98%) was set to pH 1.5 by the addition of  $\text{HNO}_3$  (Sigma-Aldrich,  $\geq 65\%$  pro Analysis), before it was mixed with 0.03 mole tetraethyl orthosilicate (TEOS) (VWR, 99%) dissolved in 20 mL EtOH (VWR Prolabo, 100%). The solution for Fe or V substituted samples was prepared in the same manner. In Fe substituted samples the Mn precursor was substituted in a range of 5-20 mole % by  $\text{Fe}(\text{NO}_3)_3 \cdot 9\text{H}_2\text{O}$  (Sigma-Aldrich, > 98%) while keeping the pH constant at 1.5.

5 mole % V was attempted on either Mn or Si site by partly substituting the Mn or Si precursor with 10 mL of an acidic  $\text{NH}_4\text{VO}_3$  (Sigma-Aldrich puriss p.a. > 99.5%) solution keeping the total solution volume and the pH value constant. The solution containing stoichiometric ratio of cations was then left for gelation at 60 °C for 6 h. The resulting gels were aged for 72 h before being dried at 120 °C and calcined at 450 °C in 95% Ar 5%  $\text{H}_2$  (Harmix) 5. Fe substituted samples and undoped LMS reference samples were then mixed with 25 wt. % corn-starch as carbon source and finally heat treated for 10 h at 625 °C in Harmix 5. V substituted samples and LMS reference samples were mixed with 40 wt. % corn-starch as carbon source and heat treated with the same temperature program. Finished carbon coated samples are denoted as undoped LMS/C and substituted LMS/C.

### Characterization

Powder X-ray diffraction analysis was performed on a Bruker D 8 Focus and a D 8 Advance Da-Vinci, both equipped with a linear PSD detector working in Bragg–Brentano ( $\Theta/2\Theta$ ) geometry. Scans were recorded from  $2\Theta = 15\text{--}70^\circ$  with a step size of  $0.013^\circ$  and an integration time of 1.5 s under  $\text{CuK}_\alpha$  radiation. Topas (Bruker AXS Version 4.2) was used for calculations of lattice parameters, full pattern refinements and quantification of secondary phases.

Porosity and surface area data were acquired by nitrogen adsorption on a Micrometrics TriStar 3000 gas adsorption analyzer at a temperature of  $-195.85^\circ\text{C}$  (liquid nitrogen). Samples were degassed for 24 h prior to analysis. 54 and 40 points were measured for the adsorption and desorption isotherms, respectively. T-plot theory based on BET theory was applied for micropore area and the external surface area differentiation [20, 21].

Further morphology analysis was carried out by field emission scanning electron microscopy on a Zeiss Supra 55 VP microscope. The working distance was 10 mm and the acceleration voltage was set to 10 kV.

Electrodes were fabricated by tape casting of a slurry containing 85 wt. % Fe or V substituted LMS/C samples or undoped LMS/C reference, 10 wt. % Super P Li and 5 wt. % PVDF binder. Electrodes were assembled in CR 2016 coin cells using 1 M  $\text{LiPF}_6$  (Sigma-Aldrich,  $\geq 99.99\%$ ) dissolved in a 3:7 volume ratio of ethylene carbonate (Sigma-Aldrich, 99%) and diethyl carbonate (Sigma-Aldrich,  $\geq 99\%$ ) as electrolyte. Li foil as negative electrode, separated by a Celgard 2400 film. Galvanostatic charge-discharge measurements were performed at  $24^\circ\text{C}$  in a potential window between 1.5 V and 4.8 V on a Maccor 4200. The charge rate 1C was defined as a current density of  $330\text{ mA g}^{-1}$  for simplicity.

## **Results and discussion**

### Phase analysis

The synthesis parameters of LMS/C were optimized in a previous study [13] and obtained compounds were indexed to the orthorhombic  $\text{Pmn}2_1$  polymorph of LMS. Minor traces of secondary phases, namely  $\text{Li}_2\text{SiO}_3$  and  $\text{MnO}$ , were present in all samples. Fig. 1 a) shows the phase fraction from Rietveld refinements of undoped LMS/C and 5, 10, 15 and 20 mole % Fe substituted LMS/C. Fe was in all cases incorporated into the structure and the amount of secondary phases decreases with increasing Fe content. The shown phase fractions refer to the crystalline content and thus disregard the amorphous carbon coating obtained from the corn-starch added during the synthesis. A previous study revealed that 25 wt. % corn-starch led to 9 wt. % carbon in the compound [13]. A full pattern refinement of a sample with 20 wt. % Fe substitution is given in fig 1 b). HKL reflections of the main phases and secondary phases are included. 20 mole % Fe substitution was the highest Fe concentration feasible with the synthesis parameters used in this study. Higher Fe substitution levels caused a too low pH value during the synthesis

and hindered a proper gelation of the sol. Fig. 1 b) also shows traces of elementary Fe in the sample.

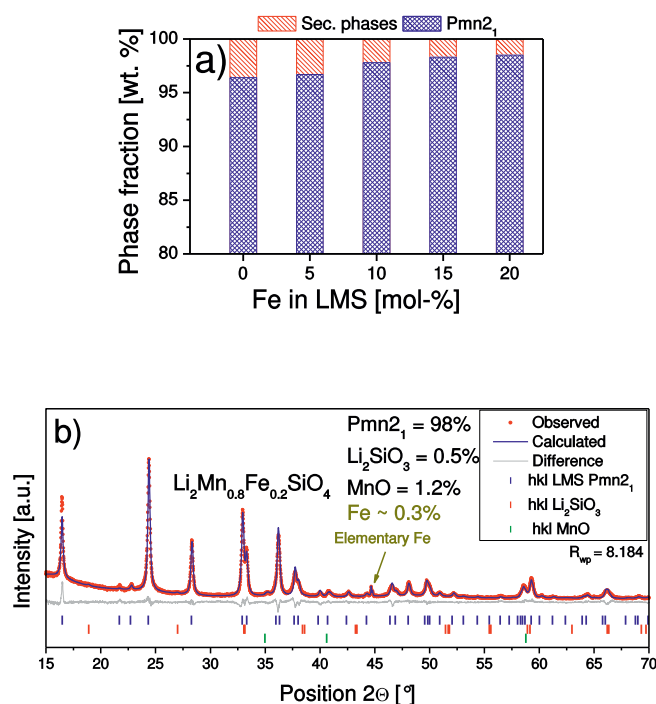


Fig. 1: a) Phase fraction for undoped and Fe substituted LMS/C samples. b) Powder XRD full pattern refinement of Li<sub>2</sub>Mn<sub>0.8</sub>Fe<sub>0.2</sub>SiO<sub>4</sub>

A further increase in the Fe concentration leads to an increased amount of elementary Fe in the compounds, since the Boudouard reaction resulting from the added carbon source and H<sub>2</sub> cause a severe reducing atmosphere during heat treatment. For higher Fe substitution levels the heat treatment atmosphere should be changed to Ar. Unit cell dimensions of LMS are in agreement with literature [4] and calculated to be  $a = 6.306 \text{ \AA}$ ,  $b = 5.384 \text{ \AA}$  and  $c = 4.966 \text{ \AA}$ . Increasing Fe substitution leads to decreasing lattice constants which can be attributed to the difference in ionic radii of tetrahedrally coordinated Mn<sup>2+</sup> and Fe<sup>2+</sup> [22].

Vanadium incorporation was attempted on either the Mn<sup>2+</sup> or the Si<sup>4+</sup> site of LMS using a V<sup>5+</sup> containing precursor. The addition of 25 or 30 wt. % corn-starch as carbon source was in both cases insufficient to form a carbon coating. Samples prepared showed a light grey body colour which is characteristic for samples with a low carbon content,

compared to black undoped and Fe substituted LMS/C samples. This might be caused by a consumption of the carbonizing agent during the reduction of V and/or reactions of ammonia with the carbonizing agent. Samples were finally successfully prepared using 40 wt. % corn-starch. Full pattern refinements of the nominal compositions  $\text{Li}_2\text{Mn}_{0.95}\text{V}_{0.05}\text{SiO}_4$  and  $\text{Li}_2\text{MnSi}_{0.95}\text{V}_{0.05}\text{O}_4$  are given in Fig. 2 a) and b) respectively. It should be mentioned that V can exist in multiple oxidation states from +II to +V where the existence of  $\text{V}^{3+}$  or  $\text{V}^{5+}$  would cause a deficiency of another cation in the compound for charge compensation.

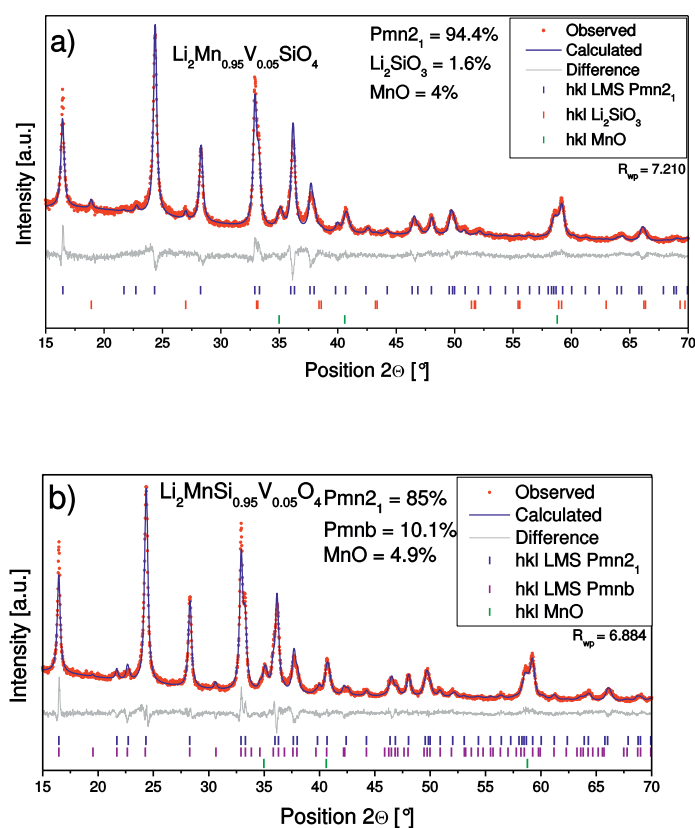


Fig. 2: Powder XRD full pattern refinements of the nominal compositions a)  $\text{Li}_2\text{Mn}_{0.95}\text{V}_{0.05}\text{SiO}_4$  and b)  $\text{Li}_2\text{MnSi}_{0.95}\text{V}_{0.05}\text{O}_4$

In both cases no V rich secondary phases appeared in the diffractograms. In the case of the intended composition  $\text{Li}_2\text{Mn}_{0.95}\text{V}_{0.05}\text{SiO}_4$  the amount of MnO secondary phase is about 2 wt.% higher than in an undoped LMS/C sample. But it cannot be concluded if

this is a significant difference, since standard deviations of Rietveld phase fractions might be as large as 5%. In the diffractogram of the nominal composition  $\text{Li}_2\text{MnSi}_{0.95}\text{V}_{0.05}\text{O}_4$  the amount of MnO is similar to  $\text{Li}_2\text{Mn}_{0.95}\text{V}_{0.05}\text{SiO}_4$  while no Li rich secondary phase is detectable. Furthermore, about 10 wt. % of the orthorhombic Pmnb polymorph of LMS is present. The incorporation of 5 mole % V showed only a minor influence on the unit cell dimensions. However, the sample with the nominal composition  $\text{Li}_2\text{MnSi}_{0.95}\text{V}_{0.05}\text{O}_4$  has a slight increase in the  $c$  lattice parameter from 4.967 to 4.973 Å. Rietveld refinements of numerous undoped LMS/C samples revealed that this increase is caused by the coexistence of LMS in Pmn2<sub>1</sub> and Pmnb space groups. Li *et al.* proposed a  $c$  parameter of 4.988 Å for LMS in Pmn2<sub>1</sub> [9]. However, the sample analyzed by Li *et al.* contained significant amounts of orthorhombic Pmnb in a Pmn2<sub>1</sub> matrix [9].

According to the Ellingham diagram of the V-O system the severe reducing atmosphere during heat treatment suggests that  $\text{V}^{5+}$  is reduced to  $\text{V}^{3+}$  [23]. The larger ionic radius of  $\text{V}^{3+}$  [22] would also cause V to occupy Mn sites rather than Si sites in LMS. The charge compensation could then be fulfilled by Mn deficiency according to the following defect equation:



Here,  $[\text{V}]$  is the concentration of vanadium, and  $[\text{Vac}]$  is the vacancy concentration.

V incorporation could also be compensated by Li deficiency and since Li is a very light element small changes in the Li content of LMS are not detectable by XRD. Finally, it needs to be mentioned that a definite answer to which site V occupies in LMS and in which oxidation state it occurs could not be determined. The V-O phase diagram is rather complex and shows a lot of different compounds with V in multivalent oxidation states between III and V [24].

The proposed defect equation is based on the XRD powder analysis, the increase in MnO secondary phase and abstinence of other secondary phases, and the severe reducing conditions during heat treatment.

### Morphology

All powders consisted of porously agglomerated particles in the range 50-100 nm, and from SEM and nitrogen adsorption it is visible that all powders offer high accessible surface areas that can be penetrated by a liquid electrolyte.

In order to overcome the poor ionic conductivity of LMS, nano-sized particles with a high surface area accessible to the electrolyte are required. Fig. 3 shows the surface area of the different samples, a) for the Fe substitution series and b) for the V substitution. The surface area plots are divided into external area and micropore area, the latter being defined as porosity smaller than 2 nm and thus not accessible to solvated Li ions in the electrolyte [25]. The sum of external area and micropore area equals the BET surface area measured by nitrogen adsorption. In Fig. 3 b)  $\text{Li}_2\text{Mn}_{0.95}\text{V}_{0.05}\text{SiO}_4$  is denoted as L(Mn95V5)S and  $\text{Li}_2\text{MnSi}_{0.95}\text{V}_{0.05}\text{O}_4$  as LM(Si95V5).

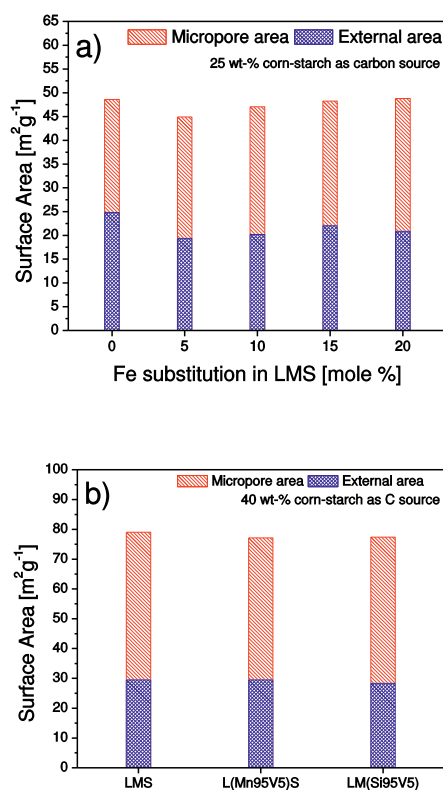


Fig. 3: BET surface area including micropore/external area separation: a) Fe substitution series b) V substitution

A previous study revealed that the microporosity can be attributed to the nature of the amorphous carbon coating [13]. Any amount of Fe substitution reduces the external surface area from approximately  $25 \text{ m}^2\text{g}^{-1}$  to  $20 \text{ m}^2\text{g}^{-1}$  while in the case of V substitution no difference was observed. External areas of the undoped and substituted samples were about  $30 \text{ m}^2\text{g}^{-1}$ . It needs to be mentioned that the corn-starch addition hinders particle growth and aggregation during heat treatment to a certain extent [13], hence undoped and substituted LMS/C samples shown in Fig. 3 b) offers an increased external surface area compared to those in Fig. 3 a). The increase in micropore area is caused by a higher carbon content due to the fact that 40 wt. % corn-starch was added with V substitution instead of 25 wt. with Fe substitution. SEM micrographs of a 10 mole % Fe substituted sample are given in Fig. 4.

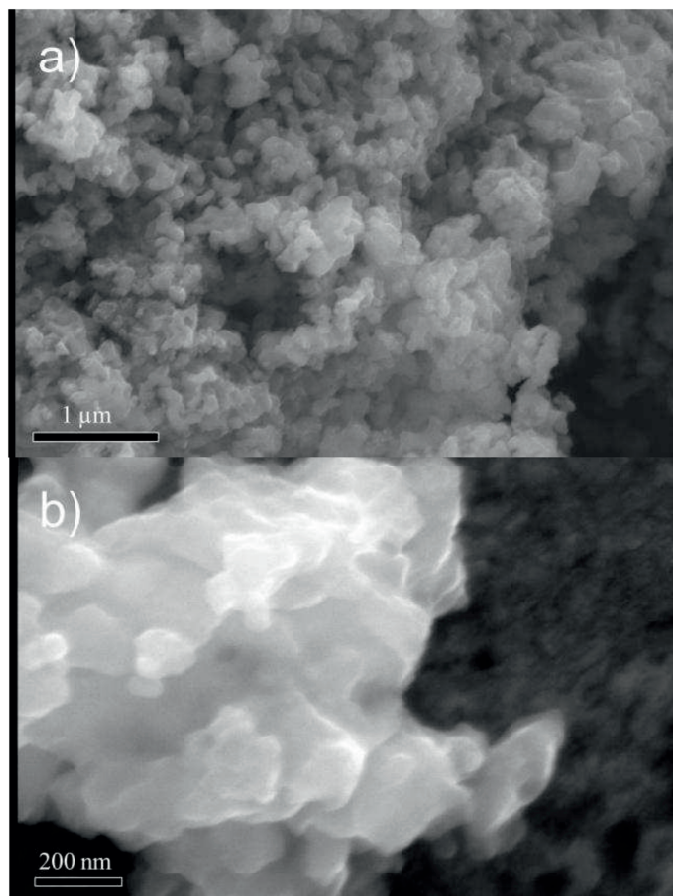


Fig. 4: SEM micrographs of a 10 mole % Fe substituted LMS/C sample: a) 20 k magnification b) 74 k magnification

#### Galvanostatic cycling

In order to investigate the effect of cation substitution in LMS/C, CR-2016 coin cells were fabricated with substituted LMS/C positive electrodes and the corresponding undoped LMS/C samples. Fig. 5 shows the galvanostatic cycling curves for Fe substituted samples. The first cycle of 10, 15 and 20 mole % Fe substituted samples against the undoped LMS/C at a current density of  $10 \text{ mA g}^{-1}$  ( $C/33$ ) is given in Fig. 5 a). Fig. 5 b) shows the charge and discharge capacity of Fe substituted LMS/C samples for 12 cycles where the charge rate was  $C/33$  in the initial three cycles, before it was increased to  $C/10$  and then to  $C/4$  for the three cycles at each charge rate and finally decreased again to  $C/33$  for the last three cycles.

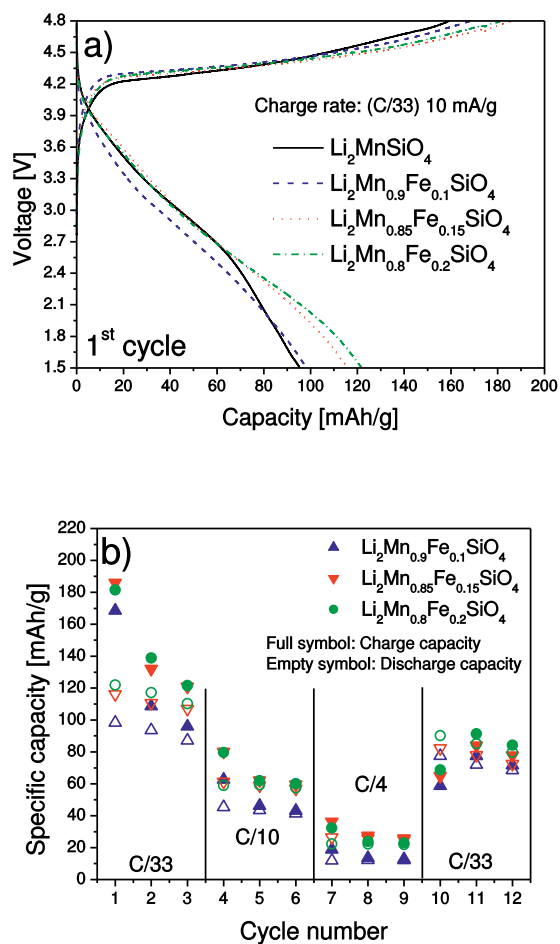


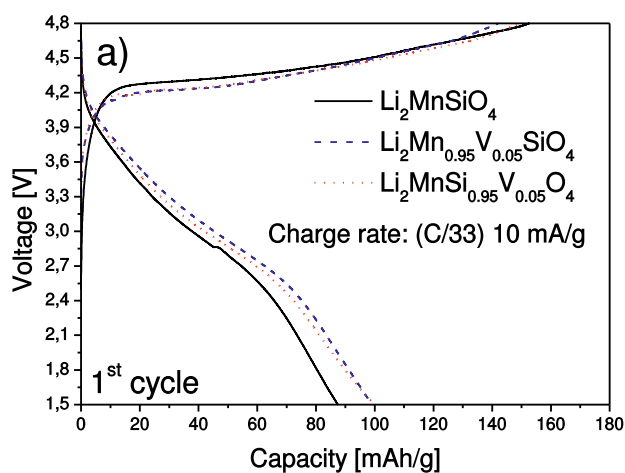
Fig. 5: Galvanostatic cycling of Fe substituted LMS/C (25 wt. % corn-starch as carbon source): a) First cycle of 10, 15 and 20 mole % Fe substituted LMS/C and an undoped LMS/C reference at C/33. b) Charge and discharge capacities of 10, 15 and 20 mole % Fe substituted LMS/C for 12 cycles at different charge rates

A clear increase in the first discharge capacity with increasing Fe content is visible in Fig. 5 a). The discharge capacity is increased from  $95 \text{ mAhg}^{-1}$  for undoped LMS/C to  $122 \text{ mAhg}^{-1}$  for the 20 mole % Fe substituted sample. Neglecting the carbon content (9 wt. %) these values correspond to approximately 0.63 and 0.81 Li per formula unit, respectively. This improvement could be attributed to a combination of improved structural stability



and higher Li diffusion and/or electronic conductivity. In addition, the irreversible capacity loss during the first cycle is reduced from 40 to 33%, which indicates that Fe substitution affects structural stability. Previously, an increase in rate capability with increasing carbon content in the samples have been demonstrated [13], hence poor rate capability shown in Fig. 5 b) is likely caused by low electronic conductivity of the samples. Despite this, an increase in performance even at higher rates is observed for higher Fe substitution levels, possibly due to improved Li diffusion rates, higher electronic conductivity, the at lower voltages situated Fe II/III redox couple or any combination of these factors. Overall capacity decay within the 12 cycles is still visible so the structural instability of LMS during cycling is still dominant even at 20 mole % Fe substitution.

Samples with 5 mole % V substitution were cycled in the same manner and results are illustrated in Fig 6. Fig. 6 a) shows the first cycle of both V substituted samples and an undoped LMS/C reference, also containing 40 wt. % corn-starch as carbon source to keep the approximate carbon content constant.



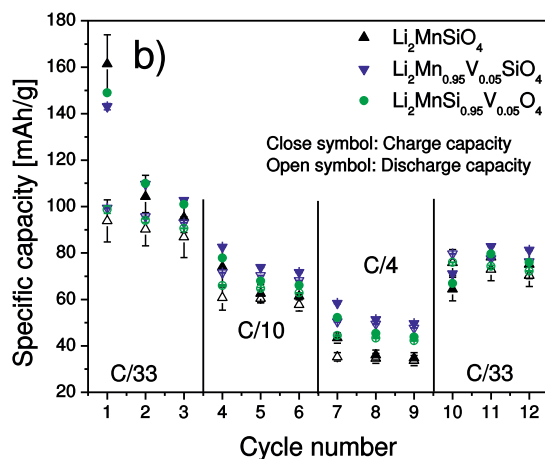


Fig. 6: Galvanostatic cycling of V substituted LMS/C (40 wt. % corn-starch as carbon source): a) First cycle of nominal compositions  $\text{Li}_2\text{Mn}_{0.95}\text{V}_{0.05}\text{SiO}_4/\text{C}$  and  $\text{Li}_2\text{MnSi}_{0.95}\text{V}_{0.05}\text{O}_4/\text{C}$  and an undoped LMS/C reference at C/33. b) Charge and discharge capacities for 12 cycles at different charge rates

Both V substituted samples behaved similarly, which suggests that V in both cases was incorporated on the same crystallographic site and exists in the same oxidation state. The first discharge capacity was in both cases, with values of 99 and 100  $\text{mAhg}^{-1}$ , about 10% higher compared to the undoped sample with a discharge capacity of 88  $\text{mAhg}^{-1}$ . This corresponds to an increase of the reversible Li exchange from 0.65 to 0.73 Li per formula unit. Furthermore, V substituted samples actually offered a lower charge capacity in the first cycle compared to the undoped material, and thus a reduction in the irreversible capacity loss of about 10%. The deintercalation potential is shifted to slightly lower potentials against  $\text{Li}/\text{Li}^+$  and the intercalation potential is increased in potential against  $\text{Li}/\text{Li}^+$ . This is most probably caused by vacant sites in the structure which could influence the Li ion mobility. Whether or not V undergoes redox reactions in the structure and hence is electrochemically active cannot yet be concluded. Fig. 6 b) reveals that this increase in electrochemical performance is observed also at higher charge rates. V substituted samples showed discharge capacities of 45-50  $\text{mAhg}^{-1}$  at C/4 while undoped LMS/C only showed about 35  $\text{mAhg}^{-1}$ , but the initial capacity could not be retained within 12 cycles.

## Conclusions

Nano-sized LMS/C was successfully doped with up to 20 mole % Fe. Fe substituted LMS/C shows increased electrochemical performance. The reversible intercalation of Li in the first cycle was increased from about 0.63 Li per formula unit for an undoped LMS/C sample to 0.81 Li per formula unit for a 20 mole % Fe substituted sample during

cycling at  $10 \text{ mA g}^{-1}$ . Still, Fe substituted samples showed a poor rate capability and high capacity decay. Higher substitution levels are probably needed to overcome this behaviour. We also demonstrated the incorporation of 5 mole % V into LMS. It was intended to incorporate V either on a Mn site or on a Si site in LMS. Powder XRD data and the fact that the heat treatment is carried out under severe reducing conditions would indicate that V is present in the oxidation state III and would hence prefer a Mn site. V substitution enhanced the electrochemical performance and increased the reversible intercalation of Li from 0.65 to 0.73 Li per formula unit at  $10 \text{ mA g}^{-1}$ . Values of the intercalation and deintercalation potentials were also shifted, but it cannot be concluded if this is caused by the incorporation of vacant sites in the lattice or by redox activity of V.

### Acknowledgements

The authors gratefully acknowledge the Research Council of Norway for funding of the SilicatBatt project (grant number: 216469/E20).

### References

- [1] Nyten A., Abouimrane A., Armand M., Gustafsson T., Thomas J. O., *Electrochemistry Communications*, **7**, 156 (2005).
- [2] Saiful Islam M., Dominko R., Masquelier C., Sirisopanaporn C., Armstrong A. R., Bruce P. G., *J. Mater. Chem.*, **21**, 9811 (2011).
- [3] B. L. Ellis, K. T. Lee, L. F. Nazar, *Chem. Mater.*, **22**, 691 (2010).
- [4] Dominko R., Bele M., Gaberšček M., Meden A., Remškar M., Jamnik J., *Electrochemistry Communications*, **8**, 217 (2006).
- [5] Dominko R., *J. Power Sources*, **184**(2), 462 (2008).
- [6] Muraliganth T., Stroukoff K. R., Manthiram A., *Chem. Mater.*, **22**, 5754 (2010).
- [7] Świętosławski M., Molenda M., Furczo K., Dziembaj R., *J. Power Sources*, **244**, 510 (2013).
- [8] Gummow R. J., He Y., *J. Power Sources*, **253**, 315 (2014).
- [9] Li Y. X., Gong Z. L., Yang Y., *J. Power Sources*, **174**, 528 (2007).
- [10] Sun, D., Wang H., Ping D., Zhou N., Huang X., Tan S., Tang Y., *J. Power Sources*, **242**, 865 (2013).
- [11] Devaraj S., Kuezmá M., Ng C.T., Balaya P., *Electrochimica Acta*, **102**, 290 (2013).
- [12] Liu W. G., Xu Y. H., Yang R., *Rare Metals*, **29**, 511 (2010).
- [13] Wagner N., Svensson A-M., Vullum-Bruer F., Effect of carbon content and annealing atmosphere on phase purity and morphology of  $\text{Li}_2\text{MnSiO}_4$  synthesized by a PVA assisted Sol-Gel method, *in preparation*.
- [14] Nadhera M., Dominko R., Hanzel D., Reiter J., Gaberšček M., *J. Electrochem. Soc.*, **156**, A619, (2009).
- [15] C. Deng C., Zhang S., Yang S. Y., *J. Alloys and Compounds*, **487**, L18 (2009).
- [16] Guo H., Cao X., Li X., Li L., Li X., Wang Z., Peng W., Li Q., *Electrochimica Acta*, **55**, 8036 (2010).
- [17] Li Y., Cheng X., Zhang Y., *J. Electrochem. Soc.*, **159**(2), A69 (2012).
- [18] Hao H., Wang J., Liu J., Huang T., Yu A., *J. Power Sources*, **210**, 397 (2012).
- [19] Yang H., Zhang Y., Cheng X., *J. Electrochemistry*, **19**(6), 565 (2013).

- [20] Brunauer S., Emmett P. H., Teller E., *J. American Chemical Society*, **60**, 309 (1938).
- [21] Harkins W. D., Jura G., *J. American Chemical Society*, **66**, 1366 (1944).
- [22] Shannon R. D., *Acta Crystallographica*, **A 32**, 751 (1976).
- [23] Yamaguchi I., Manabe T., *Thin Solid Films*, **366**, 294 (2000).
- [24] Wriedt H. A., *Bulletin of Alloy Phase Diagrams*, **10**(3), 271 (1989).
- [25] Zhou H., Einarsrud M-A., Vullum-Bruer F., *J Power Sources*, **235**, 234 (2013).



# Paper III



# On Vanadium Substitution in $\text{Li}_2\text{MnSiO}_4/\text{C}$ as Positive Electrode for Li-ion Batteries

Nils P. Wagner<sup>a</sup>, Per Erik Vullum<sup>b,c</sup>, Magnus Kristofer Nord<sup>c</sup>, Ann Mari Svensson<sup>a</sup> and Fride Vullum-Bruer<sup>a</sup>

<sup>a</sup>*Department of Materials Science and Engineering, Norwegian University of Science and Technology,*

*7491 Trondheim, Norway*

<sup>b</sup>*SINTEF Materials and Chemistry, 7491 Trondheim, Norway*

<sup>c</sup>*Department of Physics, Norwegian University of Science and Technology,*

*7491 Trondheim, Norway*

## Abstract

Vanadium substitution is an interesting approach to manipulate the properties of the poor electronic and ionic conducting lithium transition metal orthosilicates. Especially, if incorporated on the Si-site it could alter the highly insulating character of the  $\text{SiO}_4$  framework. This study addresses the feasibility and limitations of V substitution in  $\text{Li}_2\text{MnSiO}_4$ . Nominal compositions of  $\text{Li}_2\text{Mn}_{1-x}\text{V}_x\text{SiO}_4$  ( $0 \leq x \leq 0.2$ ) and  $\text{Li}_2\text{MnSi}_{1-x}\text{V}_x\text{O}_4$  ( $0 \leq x \leq 0.3$ ) were synthesised by a sol-gel method, and the structural evolution was analysed by X-ray diffraction and transmission electron microscopy (TEM) coupled with electron energy loss spectroscopy (EELS). While the solid solubility of V on tetrahedral Mn-sites was shown to be limited, substantial amounts of V entered the structure when intended to substitute Si. Elemental mapping by TEM showed that V was highly inhomogeneously distributed and high energy resolution EELS demonstrated that the majority of V was present in a tetravalent state. The nominal compositions  $\text{Li}_2\text{MnSi}_{1-x}\text{V}_x\text{O}_4$  ( $0 \leq x \leq 0.3$ ) showed superior electrochemical performance, with reduced charge transfer resistance and an increased Li-ion diffusion coefficient. Furthermore, cyclic voltammetry revealed increased redox activity which can be attributed to V within the concentration series. The best performance was achieved with 25 mol % V substitution. V substitution beyond 25 mol % caused deterioration of the properties.



## Introduction

Environmentally benign lithium transition metal orthosilicates of the general formula  $\text{Li}_2\text{MSiO}_4$  ( $\text{M} = \text{Mn, Fe}$ ) have gained interest since Nyttén *et al.* reported  $\text{Li}_2\text{FeSiO}_4$  as cathode material for Li-ion batteries.<sup>1</sup> These polyanion compounds consist of abundant elements and allow in theory the reversible exchange of 2 Li ions per formula unit.<sup>2-4</sup>  $\text{Li}_2\text{MnSiO}_4$  is an interesting candidate, since Mn can exist in different oxidation states (II, III, IV) within the potential window of a commercial Li-ion battery, thus gives rise to a high theoretical capacity of  $333 \text{ mAhg}^{-1}$  for the exchange of 2 Li per formula unit.<sup>5</sup>  $\text{Li}_2\text{MnSiO}_4$  adopts  $\beta$  and  $\gamma$   $\text{Li}_3\text{PO}_4$  structures where all cations are tetrahedrally coordinated. So far two orthorhombic ( $Pmn2_1$ ,  $Pmnb$ ) and two monoclinic ( $P2_1n$ ,  $Pn$ ) polymorphs are known. Most syntheses include an annealing step at elevated temperatures between 600 and 800 °C and result in orthorhombic  $Pmn2_1$  or a mixture of  $Pmn2_1$  and  $Pmnb$ .<sup>2,6-9</sup> A major drawback of  $\text{Li}_2\text{MnSiO}_4$  is the structural instability upon cycling which is believed to be caused by cooperative Jahn-Teller distortions during oxidation, causing a change in the Mn coordination, and the amorphisation of the structure.<sup>10,11</sup> Furthermore, the rather insulating character and the low ionic conductivity of  $\text{Li}_2\text{MnSiO}_4$  need to be addressed. Dominko *et al.* reported a low electronic conductivity of  $3 \cdot 10^{-14} \text{ Scm}^{-1}$  at 60 °C.<sup>2</sup> The reported Li ion diffusion coefficient ranges between  $10^{-14}$  and  $10^{-18} \text{ cm}^2\text{s}^{-1}$ .<sup>12,13</sup> The reported values are some orders of magnitude lower than diffusion coefficients reported for  $\text{Li}_2\text{FeSiO}_4$  and  $\text{LiFePO}_4$ .<sup>14,15</sup> DFT calculations by Kuganathan *et al.* further revealed a high activation energy barrier for Li ion migration of 0.95 eV in orthorhombic  $Pmn2_1$   $\text{Li}_2\text{MnSiO}_4$ .<sup>5</sup> Means of remedying the conductivity issues have so far been to coat  $\text{Li}_2\text{MnSiO}_4$  with a thin layer of conductive carbon. The aim of this coating is to enhance the electronic conductivity while keeping the particle size in the nanoregime in order to minimise the mean diffusion length of Li ions.<sup>2,9,16,17</sup> In addition, doping strategies on either the Mn-site or the Si-site are an interesting approach to manipulate the conductivity issues. It was pointed out that doping of trivalent Al on the Si-site is energetically favourable and would lead to charge compensation by interstitial Li ions.<sup>5</sup> Another approach is to synthesise lithium transition metal orthosilicates of the general formula  $\text{Li}_2\text{Mn}_{1-x}\text{Fe}_x\text{SiO}_4$ , with the aim to keep a high theoretical capacity by exploiting the 2 redox couples of Mn combined with the stability of  $\text{Li}_2\text{FeSiO}_4$ .<sup>17-24</sup>  $\text{Li}_2\text{FeSiO}_4$  and  $\text{Li}_2\text{MnSiO}_4$  crystallise both in  $\beta$  and  $\gamma$   $\text{Li}_3\text{PO}_4$  structures<sup>4</sup> and since Mn and Fe are direct neighbours in the periodic table, similarities can be expected. Another interesting candidate for partial substitution of the transition metal or silicon in  $\text{Li}_2\text{MSiO}_4$  compounds is vanadium. V is known as cathode material in the form of  $\text{V}_2\text{O}_5$ ,<sup>25-27</sup> and according to recent DFT calculations up to 50 mol % V substitution on the Fe-site of  $\text{Li}_2\text{FeSiO}_4$  is supposed to be stable and give rise to three additional redox couples.<sup>28</sup> Calculations by Liivat and Thomas suggest the possibility of

a partial substitution of  $\text{SiO}_4^{4-}$  units by  $\text{VO}_4^{3-}$ , charge compensated by Li vacancies.<sup>29</sup> They also found the tetrahedral structure to stabilise  $\text{VO}_4^{4-}$ . Up to date, experimental studies of V doping in  $\text{Li}_2\text{MSiO}_4$  compounds show inconsistencies and are not very thorough. A study by Yang *et al.* shows phase separation into V and Fe containing spinel phases at higher doping levels of V in  $\text{Li}_2\text{FeSiO}_4$ , and a general decay of the electrochemical properties.<sup>30</sup> Zhang *et al.* substituted up to 7 mol % V on the Fe-site of  $\text{Li}_2\text{FeSiO}_4$  and found a strong increase of electrochemical properties for 5 mol % V substitution.<sup>31</sup> At the same time their XRD data shows that almost all major  $\text{Li}_2\text{FeSiO}_4$  diffraction peaks diminish at increased V concentrations. The evolution of a spinel phase, with the main peak at about  $35^\circ 2\theta$  is ignored, and refinements based on the quality of their diffraction data are questionable. Hao *et al.* reported an increase in electrochemical performance when 10 mol % V are substituted on the Si-site of  $\text{Li}_2\text{FeSiO}_4$ , while substitution on the Fe site causes deterioration of the electrochemical properties.<sup>14</sup> This group also ignores the appearance of spinel peaks when part of the Fe is replaced by V. Both groups further confirmed trivalent V in their samples, when substitution was attempted on Fe-sites, by X-ray photoelectron spectroscopy (XPS). However, the measured signal could also be attributed to trivalent V from the ignored V containing spinel phases, since XPS does not allow for high spatial resolution. To the authors' knowledge there are so far no computational studies concerning V substitution in  $\text{Li}_2\text{MnSiO}_4$ . A broader doping study including up to 10 mol % V on either the Mn or the Si-site of  $\text{Li}_2\text{MnSiO}_4$  by Deng *et al.* demonstrated an increased discharge capacity for 5 mol % V on both sites, but deterioration for 10 mol % V.<sup>32</sup> We also previously reported improved electrochemical properties by the incorporation of 5 mol % V into the Mn or Si-site of  $\text{Li}_2\text{MnSiO}_4$ .<sup>24</sup> Another recent study by Hwang *et al.* reports up to 10 mol %  $\text{V}^{3+}$  substitution in  $\text{Li}_2\text{MnSiO}_4$ , and claims no redox contribution of V, but a positive effect on the Li diffusion coefficient.<sup>13</sup> Here, we report a more systematic study of the feasibility and limits of V substitution in  $\text{Li}_2\text{MnSiO}_4$ . Samples with the nominal compositions  $\text{Li}_2\text{Mn}_{1-x}\text{V}_x\text{SiO}_4$  ( $0 \leq x \leq 0.2$ ) and  $\text{Li}_2\text{Mn}_{1-y}\text{Si}_{1-x}\text{V}_x\text{O}_4$  ( $0 < x \leq 0.3$ ) were prepared and characterised, with focus on the phase evolution as a function of V concentration. A combination of scanning TEM (STEM) and high energy resolution EELS was performed to determine the oxidation states and to map the distribution of V with high spatial resolution. Finally, the electrochemical properties as a function of the V content were examined.

## Experimental

### *Sample preparation*

The  $\text{Li}_2\text{MnSiO}_4$  reference sample was synthesised by an acidic PVA assisted sol-gel method using metal nitrates and TEOS as precursors. 0.03 mol  $\text{Mn}(\text{NO}_3)_2 \cdot 4\text{H}_2\text{O}$  (Merck Ensure for analysis, > 98%) was dissolved in 25 mL deionised  $\text{H}_2\text{O}$  and 0.06 mol dried  $\text{LiNO}_3$  (Alfa Aesar, 99 %) was added to the solution. The pH of the solution was set to  $\sim 1.5$  by adding  $\text{HNO}_3$  (Sigma Aldrich  $\geq 65$  % pro Analysis) in order to stabilise  $\text{Mn}^{2+}$  and control the gelation properties. A second solution consisting of 0.03 mol tetraethyl orthosilicate (TEOS) (VWR 99 %) and 20 mL EtOH was added drop wise to the metal cation solution under vigorous stirring. After 20 min 1.14 g PVA (Sigma Aldrich Mowiol 10-98, Mw =61,000) dissolved in 20 mL  $\text{H}_2\text{O}$  was added and the sol was left for gelation at 70 °C under slow stirring. The resulting gel was aged for 72 h at room temperature prior to drying at 120 °C in air and calcination at 450 °C for 1 h in flowing 5 %  $\text{H}_2$  95 % Ar atmosphere. After calcination the precursor was wet mortared with 25 wt. % corn-starch as carbon source and EtOH as dispersant. The compound was finally heat treated for 10 h at 650 °C in flowing 5 %  $\text{H}_2$  95 % Ar atmosphere to obtain the main phase and carbon coat the material in a single step. Further process details are published elsewhere.<sup>33</sup> Nominal compositions of  $\text{Li}_2\text{Mn}_{1-x}\text{V}_x\text{SiO}_4$  ( $0 \leq x \leq 0.2$ ) and  $\text{Li}_2\text{MnSi}_{1-x}\text{V}_x\text{O}_4$  ( $0 \leq x \leq 0.3$ ) were synthesised in the same manner, where either the Mn or Si precursor was partially substituted by equivalent molar concentration of V. The V precursor  $\text{NH}_4\text{VO}_3$  (Sigma-Aldrich puriss p.a. > 99.5%) was dissolved under addition of 1.5 times the molar equivalent of oxalic acid (Sigma Aldrich puriss. p.a., anhydrous,  $\geq 99.0$  %) in 15 mL deionised  $\text{H}_2\text{O}$ . The solution was left to react for 1 h before it was mixed with a 15 mL  $\text{H}_2\text{O}$  solution containing  $\text{LiNO}_3$  and  $\text{Mn}(\text{NO}_3)_2 \cdot 4\text{H}_2\text{O}$ . TEOS and PVA solutions were added in the same manner as for the reference sample, and the sol was left to gel as described above. Gel ageing, drying, calcination and reduction parameters were the same as for the reference.

### *Characterisation*

Structural analysis was performed by powder X-ray diffraction using a Bruker D 8 Advance Da-Vinci working in Bragg-Brentano ( $\Theta/2\Theta$ ) geometry. Powder XRD patterns were recorded from  $2\Theta = 15-75^\circ$  under  $\text{CuK}\alpha$  radiation, with a step-size of  $0.013^\circ$  and an integration time of 0.75 s, using a variable slit setup. The structure of  $\text{Li}_2\text{MnSiO}_4$  was fitted to the space group  $Pmn2_1$  using Topas (Bruker AXS Version 4.2). The starting model was proposed by Li *et al.*<sup>34</sup>. The nominal compositions

$\text{Li}_2\text{MnSi}_{1-x}\text{V}_x\text{O}_4$  ( $0 \leq x \leq 0.3$ ) were fitted to this model, disregarding the substituted V in the model. Surface area and porosity data were acquired, by nitrogen adsorption according to BET, T-plot and BJH theory, on a Micrometrics Tristar 3000. The powder was vacuum dried for 24 h at 250 °C prior to analysis. Further morphological and structural analysis was carried out by (scanning) transmission electron microscopy ((S)TEM). The powder samples were dispersed in ethanol, and a droplet was transferred to a holey carbon coated Cu TEM grid. Prior to TEM characterisations, the samples were gently plasma cleaned 2-10 s inside a shielding port by a Fischione plasma cleaner to remove possible contaminations. TEM was performed with a double Cs corrected, coldFEG JEOL ARM200CF, operated at 200 kV and equipped with a Gatan Quantum ER for electron energy loss spectroscopy (EELS) and a large solid angle (98 srad) Centurio detector for X-ray energy dispersive spectroscopy (EDS). Spectroscopy (both EDS and EELS) was performed with a 27 mrad convergence semi-angle and a 384 pA probe current. Sub-pixel scanning was always applied to have an effective exposure time of less than 200  $\mu\text{s}$  in every location of the map to avoid possible beam damage. Elemental mapping by EELS was performed with an energy dispersion of 1 eV/channel and a collection semi-angle of 66 mrad. High energy resolution EELS was performed with an energy dispersion of 0.1 eV/channel, a collection semi-angle of 33 mrad, and an energy resolution of 0.6 eV. Dual EELS (two EEL spectra were acquired in every pixel of the maps) was used for the fine structure analysis of the V and Mn  $L_{2,3}$  EEL white lines. The low loss spectrum, including the zero loss peak, was used to calibrate the energy scale and to allow for the low loss plasmon signal to be convolved with the core loss Mn and V  $L_{2,3}$  peaks to account for multiple scattering. The EELS maps were in general processed with a model based approach<sup>35</sup> using the open source software HyperSpy.<sup>36</sup> Two Hartree-Slater edges were used to model the  $L_2$  and  $L_3$  ionisation edges for both V and Mn.<sup>37</sup>

### *Electrochemical characterisation*

For electrochemical characterisations cathodes were produced by tape casting an N-Methyl-2-pyrrolidone (NMP Sigma Aldrich > 99 %) based slurry on Al foil as current collector. The slurry contained 85 wt. % active material, 10 wt. % conductive carbon (Super P Li, Timcal) and 5 wt. % Polyvinylidene fluoride (PVDF) (Kynar, reagent grade) as binder. Cast thicknesses were 15-20  $\mu\text{m}$  and the solid load was about 2  $\text{mg cm}^{-2}$ . CR2016 coin cells were assembled in a glove box (dry Ar atmosphere) using a 16 mm circular cathode, a Celgard 2400 separator and a circular Li metal disc as anode. The electrolyte consisted of 1 M  $\text{LiPF}_6$  dissolved in a 1:1 volume ratio of Ethylene carbonate / Diethyl carbonate solution (Aldrich Battery grade). Furthermore, three electrode set-ups were assembled using ECC-Ref 3 electrode test cells from EL-cell. For the three electrode set-up Li was used as counter and reference electrode.

The separator was a 1.55 mm thick glass fibre disc. To protect the cathode from the sharp fibers a Celgard separator was placed between the cathode and the glass fibre. Galvanostatic cycling was performed on a LANHE CT 2001A in the potential window of 1.5 – 4.7 vs. Li/Li<sup>+</sup> at room temperature. Specific capacities are reported with respect to the mass of the corresponding carbon coated composites. To have a more comparable charge rate, only the one electron reaction of Mn<sup>2+</sup>/Mn<sup>3+</sup> was taken into account, and for mathematical simplicity the charge rate was defined as a current density of 160 mA g<sup>-1</sup> = 1C. Cyclic voltammograms (CV) and AC impedance spectroscopy data were measured on a Princeton Applied Research Parstat 4000 potentiostat at room temperature. CV sweep rate was 0.1 mVs<sup>-1</sup> in a potential window of 1.5 – 4.7 vs. Li/Li<sup>+</sup>. Impedance data were collected at open circuit potential (OCP). The amplitude of the alternating current (AC) signal was set to 10 mV in an AC frequency range of 10 KHz to 10 mHz. Furthermore, *in situ* XRD experiments to examine the structural changes upon cycling were conducted during the first two galvanostatic cycles of Li<sub>2</sub>MnSiO<sub>4</sub> and Li<sub>2</sub>MnSi<sub>0.75</sub>V<sub>0.25</sub>O<sub>4</sub>. Pouch cells were assembled using the same electrodes, separator and electrolyte as previously described. Cycling was performed on a Princeton Applied Research Parstat 4000 at C/16 in a potential window of 1.5 – 4.7 vs. Li/Li<sup>+</sup>. The XRD patterns were recorded continuously on a Bruker D 8 Advance Da-Vinci with a LynxEye Xe detector working in Bragg–Brentano ( $\Theta/2\Theta$ ) geometry using Mo K $_{\alpha}$  radiation in transmission mode. The additional layers of Al, PE, PP and Li that the beam had to penetrate in transmission mode, limited the observable  $2\Theta$  region without interference from the cell components. Scans were recorded from 11.7 to 15.8 °  $2\Theta$  (step-size of 0.015 °, integration time 3 s).

## Results and discussion

### *Phase evolution and powder morphology dependency on the V concentration*

The applied V precursor initially contains pentavalent V. Oxalic acid was added to ensure an acidic media in order to suppress the formation of V polyions and the oxidation of divalent Mn. The reducing character of oxalic acid further caused a partial reduction of V to a tetravalent oxyion, visible through a colour change from yellow to a deep bluish green solution. Upon gelation under atmospheric conditions V is reoxidised, visible by another colour change back to yellow. All dried gels were mainly amorphous. However, some gels showed minor LiNO<sub>3</sub> precipitations. Figure 1 shows XRD patterns of the thermal history of the carbon coated Li<sub>2</sub>MnSiO<sub>4</sub> sample, which was used as reference. During calcination the crystallisation of Li<sub>2</sub>SiO<sub>3</sub> and spinel phases occurs. After the calcined sample is mixed with corn-starch as carbon former and heat treated at 650 °C, mainly Li<sub>2</sub>MnSiO<sub>4</sub> in the space-group *Pmn2*<sub>1</sub> is present.

Additionally, minor traces of MnO and  $\text{Li}_2\text{SiO}_3$  were detected. The appearance of minor secondary phases is often reported for  $\text{Li}_2\text{MnSiO}_4$ .<sup>9</sup> It is most probably due to an uncompleted phase formation, which can be explained by sluggish kinetics in this complicated quaternary oxide.

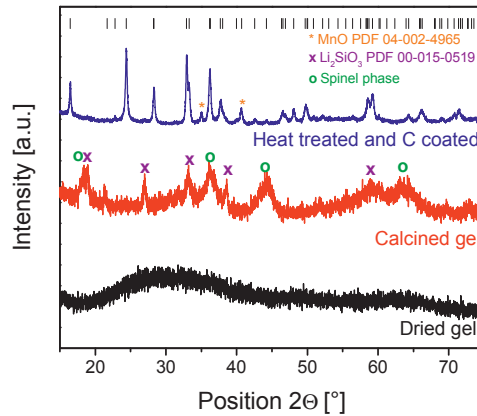
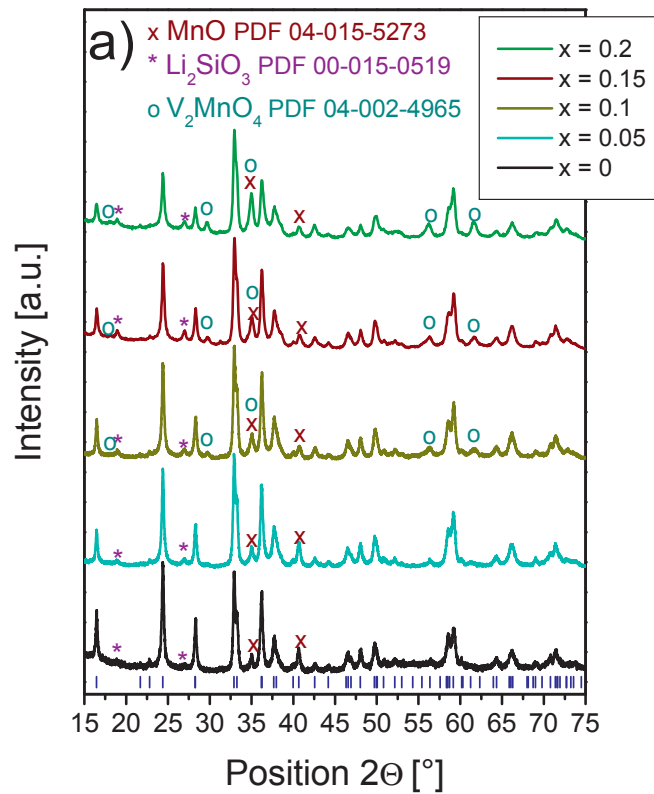


Figure 1: Powder XRD patterns of the  $\text{Li}_2\text{MnSiO}_4$  reference sample after gel drying, after calcination, and after final heat treatment and C coating. Phases are denoted and  $\text{Li}_2\text{MnSiO}_4$   $Pmn2_1$  bragg reflections are included.

The powder XRD patterns of the nominal compositions  $\text{Li}_2\text{Mn}_{1-x}\text{V}_x\text{SiO}_4$  ( $0 \leq x \leq 0.2$ ), magnified areas 26 to 30.5 and 54 to 65 °  $2\theta$  and the crystal structure including the  $010$ ,  $011$  and  $002$  lattice planes are given in Figure 2. The V concentration was progressively increased in 5 mol % steps until 20 mol %. A clear increasing trend in secondary phases is visible. Next to the previously mentioned  $\text{Li}_2\text{SiO}_3$  and MnO, an increasing amount of a V rich spinel phase was detected, indicating the limited solubility of V on the Mn-site of  $\text{Li}_2\text{MnSiO}_4$ . The magnified areas 26 to 30.5 and 54 to 65 °  $2\theta$  show an increase in the intensity of the spinel and  $\text{Li}_2\text{SiO}_3$  peaks, while the  $200$  diffraction line of  $\text{Li}_2\text{MnSiO}_4$ , although steady in position, is strongly decreasing in intensity and at the same time broadening. Reduced intensities were also detected for the  $010$ ,  $011$  and  $002$  reflections at 16.4, 24.4 and 36.2 °  $2\theta$ , respectively. Both the  $010$  and  $011$  lattice planes offer a high electron density mainly due to Mn, which is the heaviest atom of the structure and hence exhibits the highest electron density. The same is valid for the  $200$  plane, but for clarity of the figure, the illustration of the  $200$  plane was ignored. The observations of decreasing peak intensities from

Bragg scattering by planes with a high electron density governed by Mn, while the amount of a V and Mn containing spinel phase is increasing, leads to the conclusion that the V solid solubility on the Mn-site is very limited. Elevated concentrations of V, which is octahedrally coordinated and trivalent in the spinel phase,<sup>38</sup> do not populate the tetrahedral Mn-sites but rather cause phase separation. In fact, the apparent decrease of the 002 intensity at higher V concentrations, suggests a highly defective  $\text{Li}_2\text{Mn}_{1-x}\text{SiO}_4$  structure. Similar observations were made by Yang *et al.* for V substitution on the Fe-site of  $\text{Li}_2\text{FeSiO}_4$ .<sup>30</sup> As previously mentioned, other authors ignored the presence of spinel diffraction lines in their diffractograms when they claimed V substitution on the transition metal-site of both  $\text{Li}_2\text{FeSiO}_4$  and  $\text{Li}_2\text{MnSiO}_4$ .<sup>14,31,32</sup> The increased amount of  $\text{Li}_2\text{SiO}_3$  is correspondingly inevitable, since the transition metal concentration necessary to form the main phase is decreased.



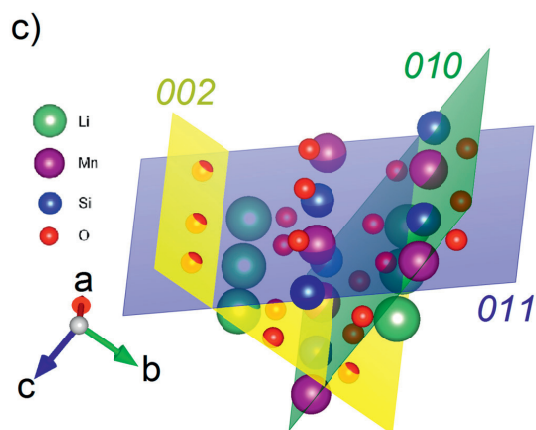
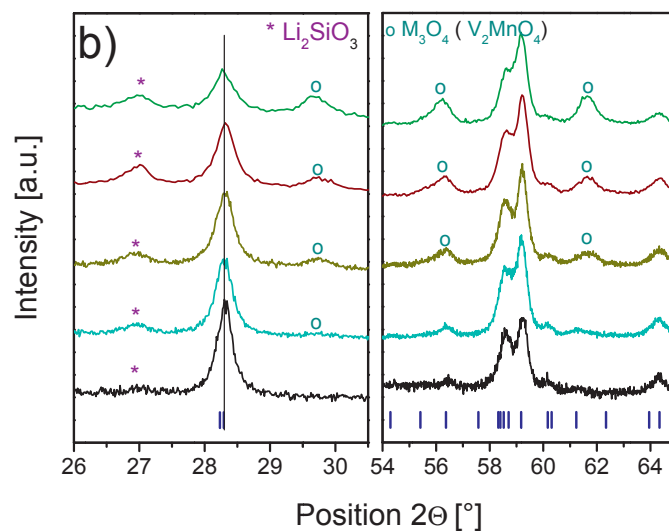


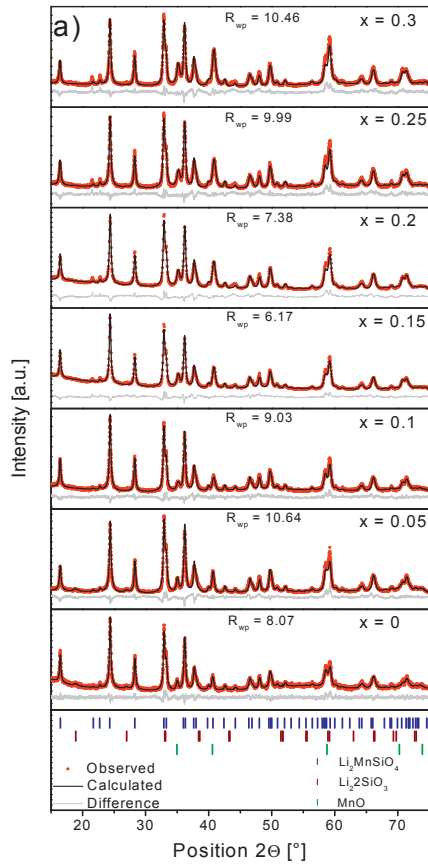
Figure 2: a) Powder XRD patterns of the nominal compositions  $\text{Li}_2\text{Mn}_{1-x}\text{V}_x\text{SiO}_4$  ( $0 \leq x \leq 0.2$ ) including denotation of secondary phases and  $\text{Li}_2\text{MnSiO}_4$   $Pmn2_1$  bragg reflections. b) Magnification of the corresponding powder XRD patterns in the range of 16-30.5 and 54-65  $2\theta$  with a clear increase in a V and Mn containing spinel phase and  $\text{Li}_2\text{SiO}_3$ . c) Lattice planes of the  $\text{Li}_2\text{MnSiO}_4$   $Pmn2_1$  structure corresponding to the peaks that show a reduced intensity with increasing V concentration.



Contrary to the observations made for  $\text{Li}_2\text{Mn}_{1-x}\text{V}_x\text{SiO}_4$ , the nominal compositions  $\text{Li}_2\text{MnSi}_{1-x}\text{V}_x\text{O}_4$  ( $0 \leq x \leq 0.3$ ) show no evidence of V rich spinel phases. The patterns were fitted to a  $\text{Li}_2\text{MnSiO}_4$  model. The nanocrystalline character in combination with a substantial amount of carbon cause broad peaks and a low signal to noise ratio, which make a reasonable fit challenging. The incorporation of V into the elaborated model, in order to find the site occupancy, did not deliver meaningful insights and hence is omitted. Figure 3 shows the corresponding fitted powder XRD patterns and a magnified region from 16 to 23.4 ° 2 $\Theta$ . The intensities of the diffraction lines corresponding to a cubic, rock-salt structured MnO related phase are increasing, and the peak shapes are broadening at higher V concentrations. Further observations were irregular changes in peak intensities and substantial increased intensities of the  $Pmn2_1$   $110$  and  $101$  diffraction lines. Moreover, the position of the former changed within the concentration series. If it is assumed that V occupies Si-sites, Bragg scattering from Si-rich planes should increase in intensity, since V has a higher scattering power than Si due to the higher atomic number. Significant changes in the  $110$  and  $101$  diffraction lines which correspond mainly to Li, hence indicate increasing disorder in the crystal structure, as well as local deviations and distortion of the unit cell which could lead to a lowered symmetry. The increased intensity of the two diffraction lines could indicate a partial Li-V or Li-Mn site reversal with increasing V concentration. Cation site-reversal is observed in  $\text{Li}_2\text{FeSiO}_4$ . The material undergoes a transition to an inversed  $\beta_{\text{II}}$  structure, which is similar to the structure of  $\text{Li}_2\text{MnSiO}_4$ , but Fe occupies half the Li-sites. The reversal causes increased intensities of the  $110$  and  $101$  diffraction lines.<sup>39</sup>  $Pmn2_1$  lattice parameters, the calculated crystallite size, and the carbon content from TGA analysis are given in Table 1. The lattice parameters of the concentration series show a minor inconsistent trend to an increased cell volume. This observation was unexpected, since even pentavalent V has a bigger ionic radius than Si, and should influence the lattice parameters more pronounced if V solely occupies one crystallographic site. Crystallite sizes were calculated to range between 36-56 nm from the full width at half maximum of the  $011$  peak. The calculations accounted for peak shape broadening due to strain. The calculated crystallite sizes are comparable. One exception is the 15% sample, which shows the biggest crystallites with 56 nm. The carbon contents are comparable. The same was valid for the nominal compositions  $\text{Li}_2\text{Mn}_{1-x}\text{V}_x\text{SiO}_4$  ( $0 \leq x \leq 0.2$ ) where the estimated carbon contents from TGA data also ranged between 4 and 5 wt. %.

**Table 1: Lattice constants and XRD crystallite sizes of the nominal compositions  $\text{Li}_2\text{MnSi}_{1-x}\text{V}_x\text{O}_4$  ( $0 \leq x \leq 0.3$ ).**

x	a [Å]	b [Å]	c [Å]	Cell volume [Å <sup>3</sup> ]	Crystallite size [nm]	Carbon content [wt. %]
0	6.30499(85)	5.38475(78)	4.96513(66)	168.570(40)	41.1	6
0.05	6.3041(12)	5.38533(91)	4.96266(88)	168.481(52)	37.9	5
0.1	6.30693(95)	5.38441(82)	4.96386(73)	168.568(44)	38.5	5
0.15	6.3038(12)	5.3859(11)	4.9640(11)	168.538(61)	55.8	4
0.2	6.3043(14)	5.3844(14)	4.9622(13)	168.442(73)	42.5	4
0.25	6.30972(96)	5.38682(84)	4.96421(75)	168.730(45)	36.2	5
0.3	6.3094(12)	5.3889(10)	4.96461(93)	168.801(55)	36.6	5



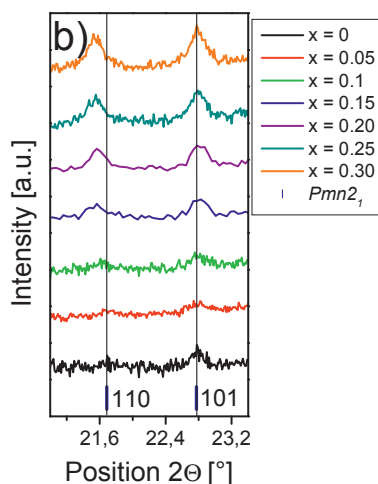


**Figure 3:** a) Fitted powder XRD patterns of the nominal compositions  $\text{Li}_2\text{MnSi}_{1-x}\text{V}_x\text{O}_4$  ( $0 \leq x \leq 0.3$ ) including  $\text{Li}_2\text{MnSiO}_4$   $Pmn2_1$ ,  $\text{Li}_2\text{SiO}_3$  and  $\text{MnO}$  Bragg reflections. b) Highlighted area from 21 to 23.4 °  $2\theta$  including the  $110$   $101$   $Pmn2_1$   $hkl$  positions and a vertical line as a guide for the eye.

Since the XRD patterns of the nominal compositions  $\text{Li}_2\text{MnSi}_{1-x}\text{V}_x\text{O}_4$  ( $0 \leq x \leq 0.3$ ) suggest incorporation of V into the structure, further physio-chemical characterisation was focused on these samples. To gain a deeper understanding of how V is incorporated into the structure STEM EELS spectral maps of the nominal compositions  $\text{Li}_2\text{MnSiO}_4$ ,  $\text{Li}_2\text{MnSi}_{0.9}\text{V}_{0.1}\text{O}_4$  and  $\text{Li}_2\text{MnSi}_{0.75}\text{V}_{0.25}\text{O}_4$  were acquired. The set-up described in the experimental section was carefully chosen to hinder beam damage during acquisition, since V is prone to reduction if exposed to the high energy electron beam for prolonged times.<sup>40,41</sup> The elemental distribution of Li, Mn, Si and O was homogenous in all cases, and except for the carbon coating no amorphous areas were detected. Figures 4 a) and b) show high angle annular dark field (HAADF) STEM images of agglomerates with the nominal compositions  $\text{Li}_2\text{MnSi}_{0.9}\text{V}_{0.1}\text{O}_4$  and  $\text{Li}_2\text{MnSi}_{0.75}\text{V}_{0.25}\text{O}_4$ , respectively. Red dotted lines indicate the areas where EELS maps were acquired. The corresponding V maps, made from the V  $L_{2,3}$  peaks, are shown in c) and d).

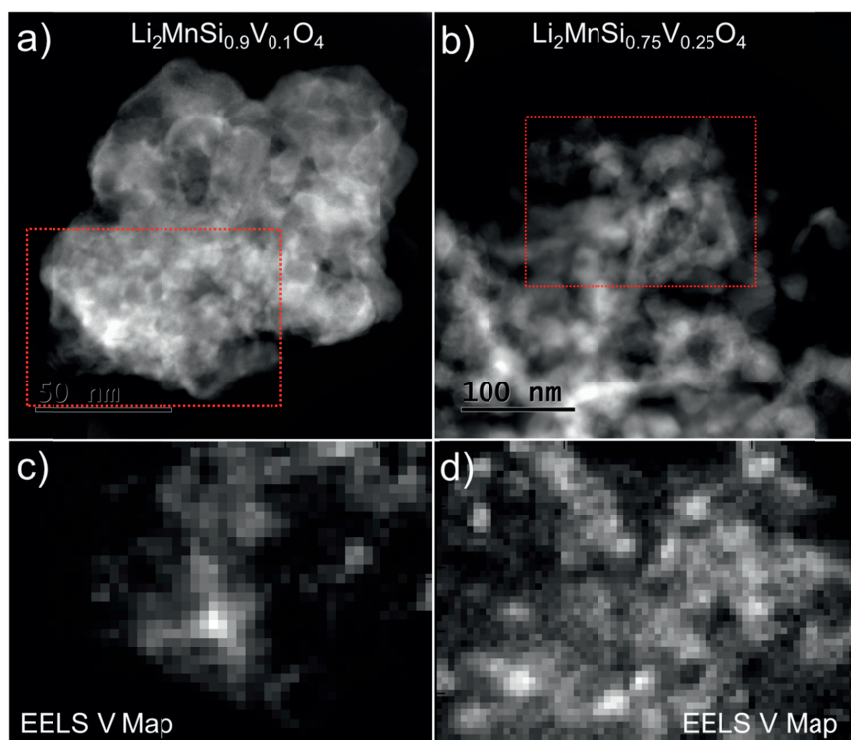


Figure 4: HAADF STEM micrographs of the nominal compositions a)  $\text{Li}_2\text{MnSi}_{0.9}\text{V}_{0.1}\text{O}_4$  and b)  $\text{Li}_2\text{MnSi}_{0.75}\text{V}_{0.25}\text{O}_4$ . The regions for EELS spectrum imaging are highlighted. V maps of c)  $\text{Li}_2\text{MnSi}_{0.9}\text{V}_{0.1}\text{O}_4$  and d)  $\text{Li}_2\text{MnSi}_{0.75}\text{V}_{0.25}\text{O}_4$ .

The results indicate that V is incorporated into the structure, but in both cases the distribution of V in the samples is highly inhomogeneous, where distinct areas show much higher V concentrations. These V inhomogeneities will have a major influence on the local compositions of the materials and probably cause numerous defects like stacking faults and local breaches of symmetry, which could explain the increase in misfit of the XRD pattern with increasing V concentration. In fact, if strain effects were disregarded during crystallite size calculations, the calculated values of V substituted samples ranged from 27 to 25 nm. The primary oxidation state of V was in both samples the same, but the 10 mol % and the 25 mol % samples showed some differences with respect to the second oxidation state that was observed. Figures 5 a) and b) show the V  $L_{2,3}$  edges from the 10 mol % and the 25 mol % samples with cor-

responding Mn L<sub>2,3</sub> edges from the same pixels in the spectrum images as the main V signal. The most representative V spectrum, i.e. the most commonly observed oxidation state in the acquired spectrum images, is shown as a solid black line. The second, but less common V oxidation state, present in each of the samples, is shown by dashed blue lines.

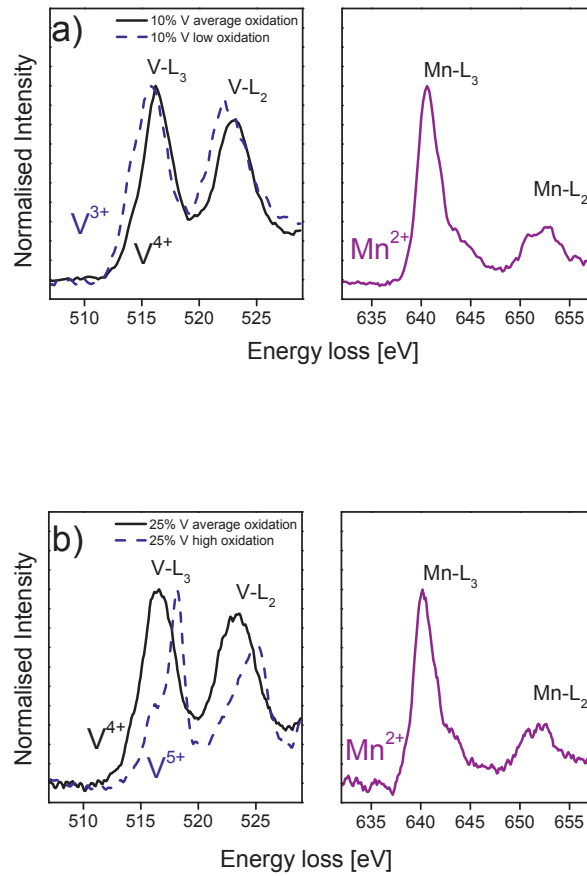


Figure 5: Most representative V L<sub>2,3</sub> (solid black line) and the corresponding Mn L<sub>2,3</sub> peaks acquired from the same pixel of the spectrum images of the nominal compositions a)  $\text{Li}_2\text{MnSi}_{0.9}\text{V}_{0.1}\text{O}_4$  and b)  $\text{Li}_2\text{MnSi}_{0.75}\text{V}_{0.25}\text{O}_4$ . The minor V L<sub>2,3</sub> peaks (dashed blue line) are recorded from different pixels.

Careful analysis of the energy loss at the peak onset, the shape of the fine structure, and comparison to data from other well established microscopy research groups<sup>42,43</sup> strongly suggest the majority of V to be present in a tetravalent state. In fact, Liivat and Thomas suggested the tetrahedral structure offering a stabilising effect on  $\text{VO}_4^{4-}$  units.<sup>29</sup> Differences were detected in the second, but less common V oxidation states that were seen in each of the samples. In the case of  $\text{Li}_2\text{MnSi}_{0.9}\text{V}_{0.1}\text{O}_4$  the minority oxidation state was characterized by a  $L_{2,3}$  peak that was shifted towards a lower energy loss, and the difference in onset was  $\sim 0.8$  eV. In  $\text{Li}_2\text{MnSi}_{0.75}\text{V}_{0.25}\text{O}_4$  the opposite trend was observed. A second oxidation state characterised by a  $L_{2,3}$  peak that was shifted about 1.2 eV in onset towards higher energy, was present. These chemical shifts correlate excellently with reported values,<sup>42</sup> and can be attributed to small amounts of trivalent V present in  $\text{Li}_2\text{MnSi}_{0.9}\text{V}_{0.1}\text{O}_4$  and pentavalent V in  $\text{Li}_2\text{MnSi}_{0.75}\text{V}_{0.25}\text{O}_4$ . The fine structure of Mn in close neighbourhood to the measured V signal, can be clearly attributed to divalent Mn.<sup>42</sup> However, also minor fractions of trivalent Mn were detected in all the samples. Tetravalent V would not require any charge compensation if located on vacant Si-sites. However, the inhomogeneous distribution and the changes in the XRD patterns indicate considerable disorder. The V signals corresponding to a different valence require charge compensation. A lower valence could be compensated by partly oxidation of Mn to a trivalent state. Pentavalent V on the other hand would require the formation of vacancies in the Li or Mn sub-lattice. We recently reported the possibility of  $\text{Li}_2\text{MnSiO}_4$  being stable in a slightly Mn deficient state.<sup>44</sup> Furthermore, EDS mapping of Mn and O rich particles, which can be attributed to the MnO related phase, also showed considerable amounts of V. This suggests that the secondary phase detected by XRD should be more correctly addressed as rock-salt structured  $\text{Mn}_{1-x}\text{V}_y\text{O}$  ( $1-x+y < 1$ ). MnO phases are well known to exist as cation sub-stoichiometric oxides, and could very possibly accommodate limited V amounts. If the increase in the secondary phase is due to a thermodynamic limit of V substitution or the thermal and atmospheric history of the samples cannot be concluded. The highly reducing atmosphere during heat treatment could cause partial reduction of the initially pentavalent V to a trivalent state, and our findings suggest only limited solubility for the trivalent ion. A non-stoichiometric situation may occur if parts of the reduced V cannot be incorporated into the structure. This resulting non-stoichiometry would then cause segregation of the excess Mn and Li. Combining the findings of a non-homogeneous V distribution as well as minor amounts of V in a different valence state leads to the conclusion of varying local compositions which could explain the fact that it was not possible to elaborate a meaningful Rietveld model with increasing V concentration. It could also explain why no substantial increase in cell volume was detected. The X-ray diffractograms give most probably a highly strained average of locally very different compositions, which can still fairly well be described by the  $Pmn2_1$  space group. The inhomogeneous character, the different oxidation states of V, and the increasing amount of the  $\text{Mn}_{1-x}\text{V}_y\text{O}$

( $1-x+y < 1$ ) will cause significant amounts of point defects and defects of a higher order in the structure. Hence it might alter the electronic structure of the material and possibly also affect the Li diffusion.

TEM bright field micrographs of the nominal compositions  $\text{Li}_2\text{MnSiO}_4$  and  $\text{Li}_2\text{MnSi}_{0.75}\text{V}_{0.25}\text{O}_4$ , and vertically aligned electron diffraction patterns of the samples are shown in Figure 6. Electron diffraction patterns were taken from large agglomerates (regions 1.5  $\mu\text{m}$  in diameter containing several hundred single crystals) to visualise an average which allows for comparison. The powders consist of loosely agglomerated nanoparticles with an overall similar morphology. Primary particles range in both cases from 25 to 40 nm validating the crystallite sizes calculated from XRD data. The particles are surrounded by a thin layer of amorphous carbon, which was intended in order to increase the electronic conductivity of the materials. The electron diffraction pattern of the reference and the 25 mol % V sample are comparable and no extra diffraction rings could be detected. They hence strengthen the assumption of a system that can be overall still described by the orthorhombic  $Pmn2_1$  structure.

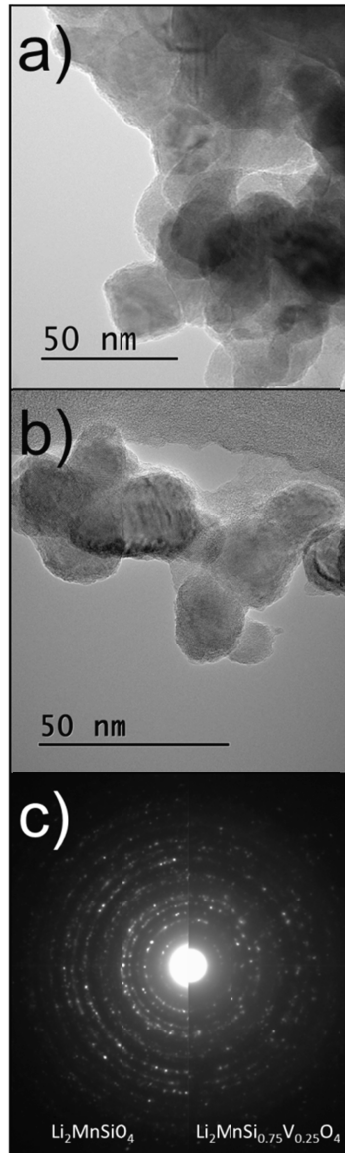


Figure 6: TEM bright field micrographs of the nominal compositions a)  $\text{Li}_2\text{MnSiO}_4$  and b)  $\text{Li}_2\text{MnSi}_{0.75}\text{V}_{0.25}\text{O}_4$ . c) show a vertically aligned electron diffraction pattern taken from bigger agglomerates of  $\text{Li}_2\text{MnSiO}_4$  and  $\text{Li}_2\text{MnSi}_{0.75}\text{V}_{0.25}\text{O}_4$ .



The surface area was measured according to T-plot theory which allows to divide the data into micropore area (pores < 2nm) and external surface area. Furthermore, the pore-size distribution was calculated from the BJH desorption data of the  $\text{Li}_2\text{Mn}_{1-x}\text{V}_x\text{SiO}_4$  concentration series. The results are summarised in Figure 7.

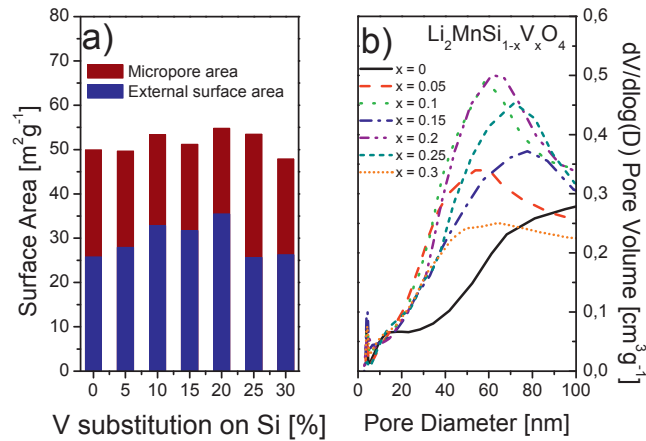


Figure 7: a) BET surface area divided into micropore area and external surface area of the  $\text{Li}_2\text{Mn}_{1-x}\text{V}_x\text{SiO}_4$  samples. b) Pore-size distribution of the  $\text{Li}_2\text{Mn}_{1-x}\text{V}_x\text{SiO}_4$  samples.

The external surface area shows an increase up to 20% V substitution, for higher substitution levels it decreases again to the value of the reference sample. The micropore area shows an opposing trend so that the overall surface area of the samples stays similar with values around  $50\text{ m}^2\text{g}^{-1}$ . The inaccuracy of the method has a proportional trend with the surface area values, and TEM suggested rather comparable morphologies. The pore size distribution data shows slight changes towards a smaller mean pore diameter. The morphology of V substituted samples appears to be rather similar and hence cannot be used to explain any major differences in the electrochemical properties.

### *Electrochemical analysis*

The performance of  $\text{Li}_2\text{Mn}_{1-x}\text{V}_x\text{SiO}_4$  ( $0 \leq x \leq 0.15$ ) and  $\text{Li}_2\text{MnSi}_{1-x}\text{V}_x\text{O}_4$  ( $0 \leq x \leq 0.3$ ) were assessed by galvanostatic cycling. Analysis of the nominal composition  $\text{Li}_2\text{Mn}_{0.8}\text{V}_{0.2}\text{SiO}_4$  was omitted since phase separation was already predominant. The first charge and discharge curves of the samples are shown in Figure 8 a) and b). While c) shows the rate performance of  $\text{Li}_2\text{MnSi}_{0.75}\text{V}_{0.25}\text{O}_4$ . All experiments were carried out at room temperature.

Substitution of V on the Mn-site did not show significant changes in the charge/discharge behaviour. The charge capacity was in all cases about  $160 \text{ mAhg}^{-1}$ , and the corresponding discharge showed capacities ranging between 100 and  $110 \text{ mAhg}^{-1}$ . This corresponds to an irreversible loss of about 35%. Interestingly, the capacity is not decreasing with increasing phase separation. This could be caused by the highly defective structure showing higher Li diffusion. Also, it is not excluded that small amounts of V could be offering additional redox activity in the structure. However, V substitution on the Si-site showed a major impact on the electrochemical response of the system. The first charge and discharge capacity increased within the concentration series and peaked at 25 mol % V. Only the 15 mol % sample was an exception and showed a slightly decreased capacity compared to the 10 mol % sample. XRD data suggested the crystallite size of this sample to be significantly larger, which could have a negative influence on the charge discharge characteristics of this sample. The charge capacity of the 25 mol % sample was 25% higher, and the discharge capacity about 60% higher compared to the values of the reference sample. The irreversible capacity loss hence is decreased to a value of 20%. However, the sloping discharge profile suggests the known structural collapse of  $\text{Li}_2\text{MnSiO}_4$  to occur also in V substituted samples. The lowered irreversible loss could be caused by larger  $\text{VO}_4$  units keeping the structure more open and hence allow more relithiation. 30 mol % V substitution caused the discharge capacity to decrease again to about  $115 \text{ mAhg}^{-1}$ . It should be kept in mind that the amount of the dense rock-salt structured  $\text{Mn}_{1-x}\text{V}_y\text{O}$  phase is increasing within the series, and will at some point influence the amount of electrochemically active material available. An interesting feature of the discharge curve of the V substituted samples is the less pronounced kink occurring at about 2.5 V.

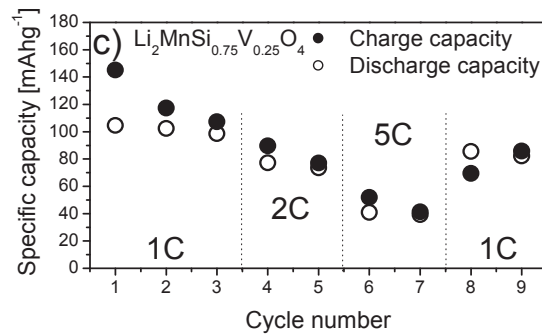
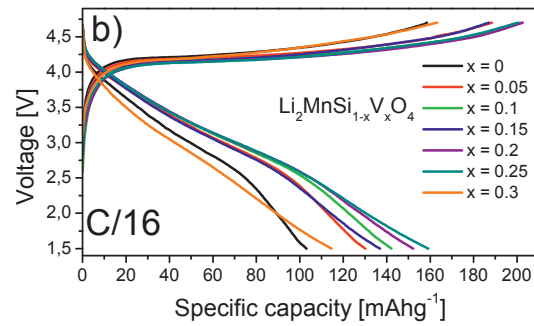
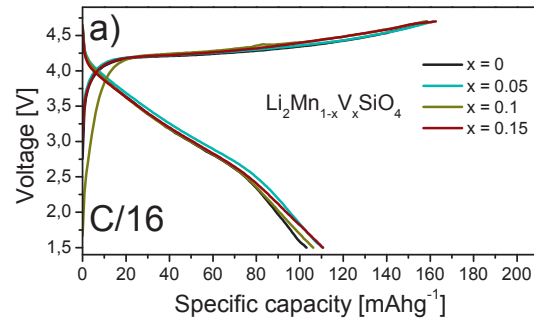


Figure 8: First galvanostatic cycle at C/16 and room temperature of a)  $\text{Li}_2\text{Mn}_{1-x}\text{V}_x\text{SiO}_4$  ( $0 \leq x \leq 0.15$ ) and b)  $\text{Li}_2\text{MnSi}_{1-x}\text{V}_x\text{O}_4$  ( $0 \leq x \leq 0.3$ ). c)  $\text{Li}_2\text{MnSi}_{0.75}\text{V}_{0.25}\text{O}_4$  cycled at different rates.

Figure 8 c) shows the rate capability of  $\text{Li}_2\text{MnSi}_{0.75}\text{V}_{0.25}\text{O}_4$  at 1C, 2C and 5C. The sample delivers a comparable capacity at 1C as the reference sample at C16. The rate performance of  $\text{Li}_2\text{MnSiO}_4$  is rather poor, as previously reported.<sup>33</sup> To understand the structural changes upon charging, *in situ* XRD patterns were recorded of  $\text{Li}_2\text{MnSiO}_4$  and  $\text{Li}_2\text{MnSi}_{0.75}\text{V}_{0.25}\text{O}_4$  upon galvanostatic cycling. *In situ* cycling was carried out in pouch cells consisting of polyethylene coated aluminium. The observed capacities in this set-up were slightly lower than the capacities measured in CR 2016 coin cells. The difference is most probably due to an inhomogeneous pressure distribution and contacting in the in house made pouch cells. The limited interference free  $2\theta$  region allowed the observation of the  $Pmn2_1$   $111/200$  and  $210/020$  double peaks. To keep an adequate time resolution, the scan time was limited to about 22 min per scan, while the cells were cycled at a slow rate of C/16. To increase the readability, the results are presented as level plots in Figures 9 a) and b).

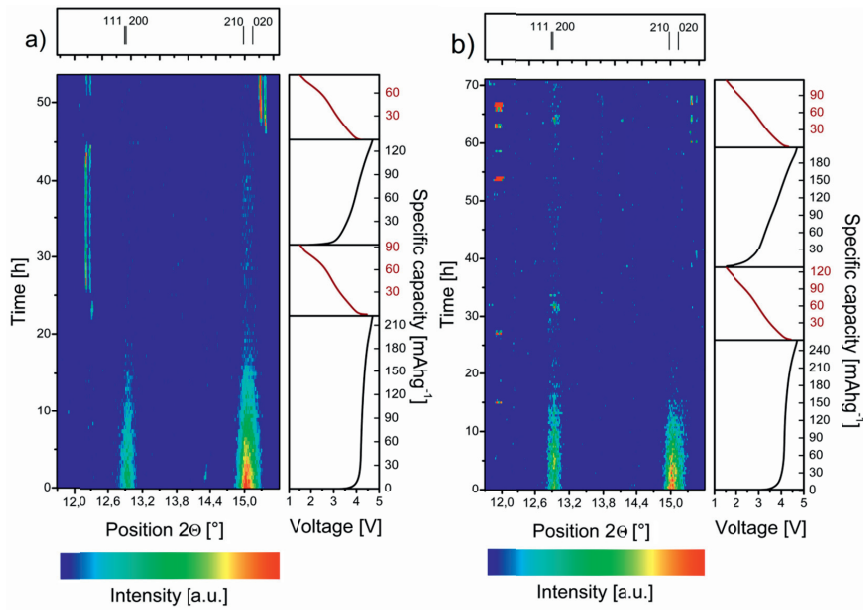


Figure 9: *In situ* XRD upon the first two galvanostatic cycles at C/16 for a)  $\text{Li}_2\text{MnSiO}_4$  and b)  $\text{Li}_2\text{MnSi}_{0.75}\text{V}_{0.25}\text{O}_4$ .

The *in situ* analysis revealed that the peak intensity of both the reference sample and the 25 mol % V substituted sample is decreasing upon the first oxidation. In both cases the diffraction lines corresponding to the  $Pmn2_1$  structure diminish into the background noise at capacities close to the value of the one electron reaction. According to crystal field theory, trivalent Mn is highly destabilised in a tetrahedral field. Distortions or changes in coordination would stabilise the Mn centre but could lead to a loss of long range order. The amorphisation was shown to be irreversible since none of the corresponding peaks reappears upon reduction or the subsequent cycle. In both cases some other peaks appear and disappear. The limited measurement window did not allow indexing of these diffraction lines. Furthermore, it cannot be concluded that these peaks appear on the cathode side since the scan was performed in transition mode. The multiple layers that had to be penetrated also limit the resolution of the *in situ* measurement. To confirm that the observed disappearance of the two double peaks is representative, the cells were disassembled and Cu K $\alpha$  XRD scans were recorded of the cathodes. In both cases only very minor peaks corresponding to the  $Pmn2_1$  structure could still be detected in a highly amorphous matrix, confirming the nearly complete loss of long-range order after the initial charge. This confirms that V does not contribute to any stabilisation of the structure upon cycling. To address the question if V shows electrochemical activity in  $\text{Li}_2\text{MnSi}_{1-x}\text{V}_x\text{O}_4$ , or if the increased activity is caused by increased conductivity of the materials, cyclic voltammograms were recorded. Figure 10 shows the voltammograms of the first and second cycle of  $\text{Li}_2\text{MnSi}_{1-x}\text{V}_x\text{O}_4$  ( $0 \leq x \leq 0.3$ ). Further shown are galvanostatic long-term cycling data of  $\text{Li}_2\text{MnSiO}_4$  and  $\text{Li}_2\text{MnSi}_{0.75}\text{V}_{0.25}\text{O}_4$  and differential capacity plots of various cycles.

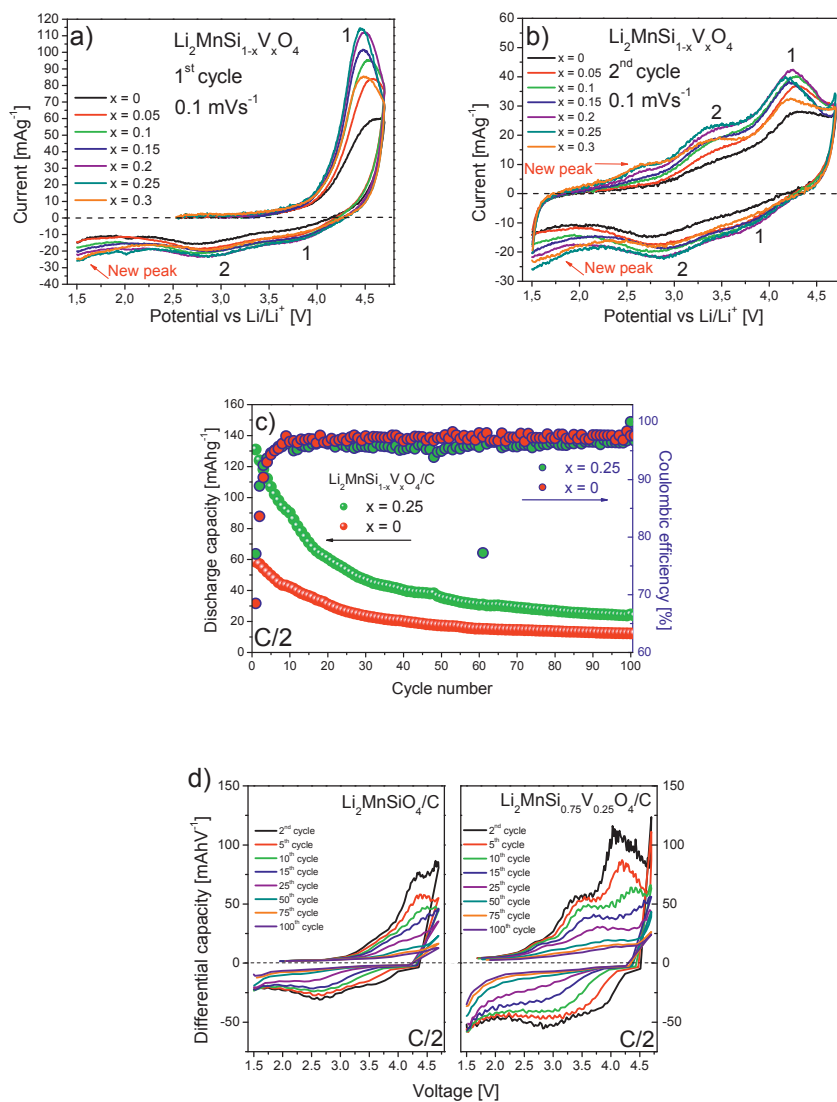
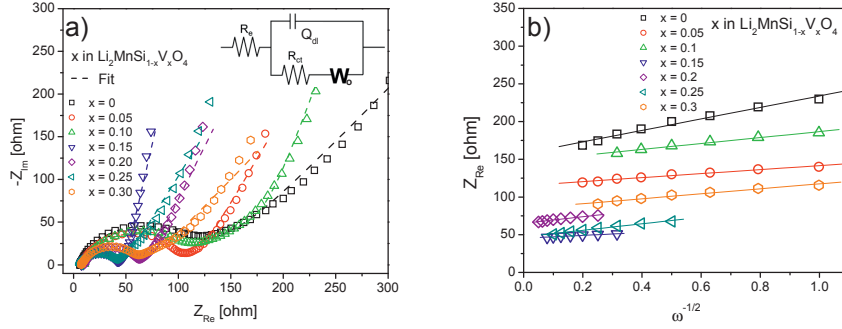


Figure 10: Cyclic voltammograms of  $\text{Li}_2\text{MnSi}_{1-x}\text{V}_x\text{O}_4$  ( $0 \leq x \leq 0.3$ ) a) first cycle and b) second cycle. Scan rate was set to  $0.1 \text{ mVs}^{-1}$ . c) Long-term cycling at  $C/2$  of  $\text{Li}_2\text{MnSiO}_4$  and  $\text{Li}_2\text{MnSi}_{0.75}\text{V}_{0.25}\text{O}_4$ . d) Differential capacity profile of  $\text{Li}_2\text{MnSiO}_4$  and  $\text{Li}_2\text{MnSi}_{0.75}\text{V}_{0.25}\text{O}_4$  of the 2<sup>nd</sup>, 5<sup>th</sup>, 10<sup>th</sup>, 15<sup>th</sup>, 25<sup>th</sup>, 50<sup>th</sup>, 75<sup>th</sup> and 100<sup>th</sup> cycle of the long-term cycling from c).

The onset of oxidation and the centre of the anodic peak are shifted to slightly lower potentials with increasing V concentration. Furthermore, the anodic peak area is increasing in the concentration series and peaking at 25 mol % V substitution. The signal for 30 mol % V substitution is reduced again, and the data is in agreement with the galvanostatic load curves. No additional signal can be detected on first oxidation. In the cathodic direction, two broad peaks are observed where the first minor peak is located at about 3.8 V and the second major peak at about 2.7 V. The splitting into two extremely broad peaks can be directly linked to the structural degradation, since the redox potential of a given cation is dependent on its chemical environment. In this case the first minor peak is believed to correspond to Mn still in its initial coordination, while the second major peak at lower potential displays Mn in an altered environment and possibly in a different coordination. For V substituted samples both peaks are shifted to slightly higher potentials, which could be caused by a decreased overpotential. Interestingly, an additional peak appears at potentials close to the cut off potential. Upon the second anodic polarisation, the reference sample shows two broad anodic peaks, one obvious and the other one barely visible. The same peaks are observable for the V substituted samples, with the same increasing behaviour as described for the first cycle. In addition, also a new anodic peak, of increasing intensity within the concentration series, at about 2.7 V is observed. The subsequent cathodic polarisation reassembles the first cycle qualitatively, where V substituted samples show an increased response, and the additional peak at relatively low potentials. Liivat and Thomas calculated the redox potential of  $V^{4+}/V^{5+}$  vs.  $Li/Li^+$  to be 2.1 V in a hypothetical  $Li_2FeVO_4$  structure.<sup>29</sup> This value would fit to the observed additional anodic peak at 2.7 V and the cathode peak below 2 V, but cannot explain why no additional anodic peak was observed upon the first oxidation. The long-term cycling of the reference and the 25 mol % V substituted sample showed a strong decay in discharge capacity upon cycling for both samples, while the coulombic efficiency reaches values between 95 and 100% after the first few cycles. After 20 cycles the reference sample and the 25 mol % V substituted sample showed capacity retentions of 50% and 46%, respectively. During later cycles the sloping profile is less pronounced, but still present. The experiment was terminated after 100 cycles. The remaining discharge capacity was 12 and 25  $mAhg^{-1}$  for the reference and the 25 mol % V substituted samples, respectively. Differential capacity profiles of selected cycles for both samples were derived. The first plot shows the 2<sup>nd</sup> cycle. It qualitatively reassembles the CV curves. Also here, the additional anodic and cathodic peaks of the V substituted sample, located at about 2.7 V and close to cut-off, respectively, are visible. But it is obvious that in both cases all peaks are decreasing upon cycling, and almost all visible Mn redox activity disappears after prolonged cycling. In order to understand how V substitution influences the charge transfer resistance and the Li diffusion of  $Li_2MnSiO_4$ , the materials were further analysed by AC impedance spectroscopy. The Nyquist representation with the suggested equivalent circuit model in

the inset is given in Figure 10 a). Figure 10 b) shows the dependence of  $Z_{Re}$  on  $\omega^{-1/2}$  in the range where  $Z_{Re}$  and  $Z_{Im}$  are parallel. The AC impedance spectra consisted in all cases of a depressed semi-circle in the high frequency region followed by a line profile. The data can be described by a modified Randles circuit. The first resistor,  $R_e$ , accounts for the electrolyte resistance. The next components in parallel are a resistor, accounting for the charge transfer resistance  $R_{ct}$ , and a constant phase element (CPE), related to the double layer capacitance  $Q_{dl}$ . The CPE in parallel to the resistor (Cole element) was chosen to describe the depressed profile of the semi-circle, which is caused by an inhomogeneous current density distribution due to the porous structure. The low frequency part of the impedance spectra was fitted by an open circuit terminus Generalised Finite Warburg element  $W_o$ .



**Figure 11: AC impedance data of  $\text{Li}_2\text{MnSi}_{1-x}\text{V}_x\text{O}_4$  ( $0 \leq x \leq 0.3$ ). a) Nyquist representation including the fitted line and the equivalent circuit. b)  $Z_{Re}$  vs.  $\omega^{-1/2}$ .**

The values of  $R_e$ ,  $R_{ct}$  and Li diffusion coefficient ( $D_{Li}$ ) are given in Table 2. The diffusion coefficient was calculated according to a Warburg model with a linear over-voltage-current relationship<sup>45,46</sup> using the following equation:<sup>47,48</sup>

$$D = \frac{R^2 T^2}{2A^2 n^4 F^4 C_{Li}^2 \sigma^2} \quad (1)$$

Where  $R$  and  $T$  are the universal gas constant and the absolute temperature, respectively,  $A$  is the surface area of the electrode,  $n$  the number of electrons in the electrochemical reaction (1 for Li),  $F$  is the Faraday constant, and  $C_{Li}$  is the Li ion concen-



tration in the material.  $C_{\text{Li}}$  can be described as the quotient of density and molar mass, multiplied by a factor 2 to account for 2 Li per formula unit. In this case it was assumed that the substituted materials are identical with the desired nominal compositions. The lattice parameters given in Table 1 were applied to calculate the crystal density of each sample. The parameter  $\sigma$  is the slope of  $Z_{\text{Re}}$  vs.  $\omega^{-1/2}$  in the range where  $Z_{\text{Re}}$  and  $Z_{\text{Im}}$  have similar slopes.

**Table 2: Electrolyte and charge transfer resistance and calculated Li diffusion coefficients.**

x in $\text{Li}_2\text{MnSi}_{1-x}\text{V}_x\text{O}_4$	$^1R_e$ [Ohm]	$^1R_{\text{ct}}$ [Ohm]	$^2D_{\text{Li}}$ [ $\text{cm}^2\text{s}^{-1}$ ]
<b>0</b>	6.312 (1.11%)	84.31 (3.42%)	9.7E-16
<b>0.05</b>	8.08 (0.76%)	86.43 (0.89%)	8.1E-15
<b>0.1</b>	8.86 (0.85%)	95.41 (1.31%)	3.6E-15
<b>0.15</b>	7.61 (1.20%)	31.88 (1.36%)	1.6E-14
<b>0.2</b>	9.51 (0.82%)	49.29 (1.16%)	3.1E-15
<b>0.25</b>	6.78 (0.84%)	24.76 (1.78%)	3.0E-15
<b>0.3</b>	7.71 (1.12%)	43.49 (1.18%)	5.2E-15

<sup>1</sup> Uncertainty given in brackets. <sup>2</sup> Assumptions are described in the main text.

Table 2 shows that V substitution influences the charge transfer resistance and the Li diffusion coefficient. The results are in agreement with the galvanostatic cycling experiments and CV measurements. A decreased charge transfer resistance is observable for V substitution levels  $\geq 15$  mol %. The lowered charge transfer is probably caused by  $\text{VO}_4$  units interrupting the strongly insulating  $\text{SiO}_4$  framework. The STEM EELS analysis revealed the strongly inhomogeneous distribution of V, which most probably makes every sample unique and hence could explain inconsistencies in the  $R_{\text{ct}}$  values. Discussed strain, stacking faults and defects in the structure seem to also positively influence the diffusion coefficient for Li ions, which for all V substituted samples is increased by one order of magnitude and is in the range of E-15  $\text{cm}^2\text{s}^{-1}$ . The exact values have to be taken with caution due to the assumptions made. But the reported range seems reasonable, and galvanostatic cycling at elevated rates also strongly suggests increased Li diffusion for V substituted samples.

## Conclusions

In-depth investigations concerning the feasibility of substituting V for Mn or Si in  $\text{Li}_2\text{MnSiO}_4$  were performed. A sol-gel method was employed and samples with the nominal compositions  $\text{Li}_2\text{Mn}_{1-x}\text{V}_x\text{SiO}_4$  ( $0 \leq x \leq 0.2$ ) and  $\text{Li}_2\text{MnSi}_{1-x}\text{V}_x\text{O}_4$  ( $0 \leq x \leq 0.3$ ) were synthesised. The  $\text{Li}_2\text{MnSiO}_4$  reference was indexed and fitted to a  $\beta_{\text{II}}$   $Pmn2_1$  model. V substitution on the Mn-site was shown to cause phase separation and V exclusion at V concentrations  $\geq 10$  mol %. An increasing amount of a V containing spinel phase and  $\text{Li}_2\text{SiO}_3$  was detected. The substitution onto the Si-site caused increased misfits in the patterns suggesting disorder. But, overall the system could still be identified by the space group  $Pmn2_1$ . STEM EELS revealed inhomogeneous distributions of V, which was mainly present in a tetravalent state. Dependent on the concentration, some lower valence V at lower concentrations and higher valence V at higher concentrations were detected. These findings suggest varying local compositions. Furthermore, XRD and STEM EELS revealed a secondary MnO phase to be more correctly addressed as  $\text{Mn}_{1-x}\text{V}_y\text{O}$  ( $1-x+y < 1$ ). This phase is believed to be caused either by a limited solid solubility of the system, or induced by the thermal history of the sample. The  $\text{Li}_2\text{MnSi}_{1-x}\text{V}_x\text{O}_4$  ( $0 \leq x \leq 0.3$ ) structures were shown to offer superior electrochemical properties compared to the reference and to the  $\text{Li}_2\text{Mn}_{1-x}\text{V}_x\text{SiO}_4$  ( $0 \leq x \leq 0.2$ ) samples. The discharge capacity was highest for the nominal composition  $\text{Li}_2\text{MnSi}_{0.75}\text{V}_{0.25}\text{O}_4$ , which reached  $160 \text{ mAhg}^{-1}$  in the initial cycle. This value corresponds roughly to the 1 Li per formula unit reaction and was 40% higher than the reference sample. Additional redox activity which could be attributed to the  $\text{V}^{4+}/\text{V}^{5+}$  redox couple was revealed by CV measurements. EIS spectra showed decreased charge transfer resistance and increased values for Li diffusion. Unfortunately, no effect on the structural instability upon cycling was detected and *in situ* XRD analysis showed amorphisation for both the substituted and the reference sample.

## Acknowledgements

The research council of Norway is gratefully acknowledged for funding the SilicatBatt project (grant number: 216469/E20). TEM characterization was supported by the project NORTEM (Grant 197405) within the programme INFRASTRUCTURE of the Research Council of Norway (RCN). NORTEM was co-funded by the RCN and the project partners NTNU, UiO and SINTEF.

## References

- (1) Nytén, A.; Abouimrane, A.; Armand, M.; Gustafsson, T.; Thomas, J. O. Electrochemical Performance of  $\text{Li}_2\text{FeSiO}_4$  as a New Li-Battery Cathode Material. *Electrochem. commun.* **2005**, *7* (2), 156–160.
- (2) Dominko, R.; Bele, M.; Gaberšček, M.; Meden, A.; Remškar, M.; Jamnik, J. Structure and Electrochemical Performance of  $\text{Li}_2\text{MnSiO}_4$  and  $\text{Li}_2\text{FeSiO}_4$  as Potential Li-Battery Cathode Materials. *Electrochem. commun.* **2006**, *8* (2), 217–222.
- (3) Ellis, B. L.; Lee, K. T.; Nazar, L. F. Positive Electrode Materials for Li-Ion and Li-Batteries. *Chem. Mater.* **2010**, *22* (3), 691–714.
- (4) Islam, M. S.; Dominko, R.; Masquelier, C.; Sirisopanaporn, C.; Armstrong, A. R.; Bruce, P. G. Silicate Cathodes for Lithium Batteries: Alternatives to Phosphates? *J. Mater. Chem.* **2011**, *21*, 9811–9818.
- (5) Kuganathan, N.; Islam, M. S.  $\text{Li}_2\text{MnSiO}_4$  Lithium Battery Material: Atomic-Scale Study of Defects, Lithium Mobility, and Trivalent Dopants. *Chem. Mater.* **2009**, *21* (21), 5196–5202.
- (6) Politaev, V. V.; Petrenko, A. A.; Nalbandyan, V. B.; Medvedev, B. S.; Shvetsova, E. S. Crystal Structure, Phase Relations and Electrochemical Properties of Monoclinic  $\text{Li}_2\text{MnSiO}_4$ . *J. Solid State Chem.* **2007**, *180* (3), 1045–1050.
- (7) Duncan, H.; Kondamreddy, A.; Mercier, P. H. J.; Le Page, Y.; Abu-Lebdeh, Y.; Couillard, M.; Whitfield, P. S.; Davidson, I. J. Novel Pn Polymorph for

- $\text{Li}_2\text{MnSiO}_4$  and Its Electrochemical Activity As a Cathode Material in Li-Ion Batteries. *Chem. Mater.* **2011**, *23* (24), 5446–5456.
- (8) Gummow, R. J.; Sharma, N.; Peterson, V. K.; He, Y. Crystal Chemistry of the Pmnb Polymorph of  $\text{Li}_2\text{MnSiO}_4$ . *J. Solid State Chem.* **2012**, *188*, 32–37.
- (9) Gummow, R. J.; He, Y. Recent Progress in the Development of  $\text{Li}_2\text{MnSiO}_4$  Cathode Materials. *J. Power Sources* **2014**, *253*, 315–331.
- (10) Larsson, P.; Ahuja, R.; Liivat, A.; Thomas, J. O. Structural and Electrochemical Aspects of Mn Substitution into  $\text{Li}_2\text{FeSiO}_4$  from DFT Calculations. *Comput. Mater. Sci.* **2010**, *47* (3), 678–684.
- (11) Saracibar, A.; Wang, Z.; Carroll, K. J.; Meng, Y. S.; Dompablo, M. E. A. New Insights into the Electrochemical Performance of  $\text{Li}_2\text{MnSiO}_4$ : Effect of Cationic Substitutions. *J. Mater. Chem. A* **2015**, *3*, 6004–6011.
- (12) Świątosławski, M.; Molenda, M.; Furczoń, K.; Dziembaj, R. Nanocomposite C/ $\text{Li}_2\text{MnSiO}_4$  Cathode Material for Lithium Ion Batteries. *J. Power Sources* **2013**, *244*, 510–514.
- (13) Hwang, C.; Kim, T.; Noh, Y.; Cha, W.; Shim, J.; Kwak, K.; Ok, K. M.; Lee, K.-K. Synthesis, Characterization, and Electrochemical Performance of V-Doped  $\text{Li}_2\text{MnSiO}_4/\text{C}$  Composites for Li-Ion Battery. *Mater. Lett.* **2015**.
- (14) Hao, H.; Wang, J.; Liu, J.; Huang, T.; Yu, A. Synthesis, Characterization and Electrochemical Performance of  $\text{Li}_2\text{FeSiO}_4/\text{C}$  Cathode Materials Doped by Vanadium at Fe/Si Sites for Lithium Ion Batteries. *J. Power Sources* **2012**, *210*, 397–401.
- (15) Bajars, G.; Kucinskis, G.; Smits, J.; Kleperis, J.; Lūsis, A. Characterization of  $\text{LiFePO}_4/\text{C}$  Composite Thin Films Using Electrochemical Impedance Spectroscopy. *IOP Conf. Ser. Mater. Sci. Eng.* **2012**, *38*, 012019.
- (16) Moskon, J.; Dominko, R.; Cerc-Korošec, R.; Gabersček, M.; Jamnik, J. Morphology and Electrical Properties of Conductive Carbon Coatings for Cathode Materials. *J. Power Sources* **2007**, *174* (2), 683–688.
- (17) Dominko, R.  $\text{Li}_2\text{MSiO}_4$  (M = Fe And/or Mn) Cathode Materials. *J. Power*

*Sources* **2008**, *184* (2), 462–468.

- (18) Chen, R.; Heinzmann, R.; Mangold, S.; Chakravadhanula, V. S. K.; Hahn, H.; Indris, S. Structural Evolution of  $\text{Li}_2\text{Fe}_{1-y}\text{Mn}_y\text{SiO}_4$  ( $y = 0, 0.2, 0.5, 1$ ) Cathode Materials for Li-Ion Batteries upon Electrochemical Cycling. *J. Phys. Chem. C* **2013**, *117*, 884–893.
- (19) Deng, C.; Zhang, S.; Yang, S. Y. Effect of Mn Substitution on the Structural, Morphological and Electrochemical Behaviors of  $\text{Li}_2\text{Fe}_{1-x}\text{Mn}_x\text{SiO}_4$  Synthesized via Citric Acid Assisted Sol-Gel Method. *J. Alloys Compd.* **2009**, *487* (1-2), 18–23.
- (20) Guo, H.; Cao, X.; Li, X.; Li, L.; Li, X.; Wang, Z.; Peng, W.; Li, Q. Optimum Synthesis of  $\text{Li}_2\text{Fe}_{1-x}\text{Mn}_x\text{SiO}_4/\text{C}$  Cathode for Lithium Ion Batteries. *Electrochim. Acta* **2010**, *55* (27), 8036–8042.
- (21) Kokalj, A.; Dominko, R.; Mali, G.; Meden, A.; Gaberscek, M.; Jamnik, J. Beyond One-Electron Reaction in Li Cathode Materials: Designing  $\text{Li}_2\text{Mn}_x\text{Fe}_{1-x}\text{SiO}_4$ . *Chem. Mater.* **2007**, *19* (15), 3633–3640.
- (22) Rangappa, D.; Murukanahally, K. D.; Tomai, T.; Unemoto, A.; Honma, I. Ultrathin Nanosheets of  $\text{Li}_2\text{MSiO}_4$  ( $M = \text{Fe}, \text{Mn}$ ) as High-Capacity Li-Ion Battery Electrode. *Nano* **2012**, *4*.
- (23) Shao, B.; Abe, Y.; Taniguchi, I. Synthesis and Electrochemical Characterization of  $\text{Li}_2\text{Fe}_x\text{Mn}_{1-x}\text{SiO}_4/\text{C}$  ( $0 \leq x \leq 0.8$ ) Nanocomposite Cathode for Lithium-Ion Batteries. *Powder Technol.* **2013**, *235*, 1–8.
- (24) Wagner, N.; Dalod, A.; Svensson, A.; Vullum-Bruer, F. Fe and V Substituted  $\text{Li}_2\text{MnSiO}_4/\text{C}$  as Potential Cathode Material for Li-Ion Batteries. *ECS Trans.* **2015**, *64* (22), 33–45.
- (25) West, K.; Zachau-Christiansen, B.; T., J. Thin-Film Vanadium Batteries Oxide Electrodes for Lithium Batteries. *J. Power Sources* **1993**, 127–134.
- (26) Dong, W.; Rolison, D. R.; Dunn, B. Electrochemical Properties of High Surface Area Vanadium Oxide Aerogels. *Electrochem. Solid State Lett.* **2001**, *3*, 457–459.

- (27) Tarascon, J. M.; Armand, M. Issues and Challenges Facing Rechargeable Lithium Batteries. *Nature* **2001**, *414* (6861), 359–367.
- (28) Li, Y.; Cheng, X.; Zhang, Y. Achieving High Capacity by Vanadium Substitution into  $\text{Li}_2\text{FeSiO}_4$ . *J. Electrochem. Soc.* **2012**, *159* (2), A69.
- (29) Liivat, A.; Thomas, J. O. A DFT Study of Polyanion Substitution into the Li-Ion Battery Cathode Material  $\text{Li}_2\text{FeSiO}_4$ . *Comput. Mater. Sci.* **2010**, *50* (1), 191–197.
- (30) Hong, Y.; Ying, Z.; Xuan, C. Effect of Vanadium Substitution on Structure of  $\text{Li}_2\text{FeSiO}_4$  /C Composites. *JOURNAL OF Electrochem.* **2013**, *19* (6), 565–570.
- (31) Zhang, L.-L.; Sun, H.-B.; Yang, X.-L.; Wen, Y.-W.; Huang, Y.-H.; Li, M.; Peng, G.; Tao, H.-C.; Ni, S.-B.; Liang, G. Study on Electrochemical Performance and Mechanism of V-Doped  $\text{Li}_2\text{FeSiO}_4$  Cathode Material for Li-Ion Batteries. *Electrochim. Acta* **2015**, *152*, 496–504.
- (32) Deng, C.; Zhang, S.; Wu, Y. X.; Zhao, B. D. Partial Substitution of Mn/Si with V, Cr or Al in  $\text{Li}_2\text{MnSiO}_4$  Nanoparticle: Dependence of the Physical and Electrochemical Properties on the Substitution Strategy. *J. Electroanal. Chem.* **2014**, *719*, 150–157.
- (33) Wagner, N.; Svensson, A.-M.; Vullum-Bruer, F. Effect of Carbon Content and Annealing Atmosphere on Phase Purity and Morphology of  $\text{Li}_2\text{MnSiO}_4$  Synthesized by a PVA Assisted Sol-gel Method. *Solid State Ionics* **2015**, *276*, 26–32.
- (34) Li, Y.-X.; Gong, Z.-L.; Yang, Y. Synthesis and Characterization of  $\text{Li}_2\text{MnSiO}_4$ /C Nanocomposite Cathode Material for Lithium Ion Batteries. *J. Power Sources* **2007**, *174* (2), 528–532.
- (35) Manoubi, T.; Tencé, M.; Walls, M. G.; Colliex, C.; Solides, P.; Cedex, O. Curve Fitting Methods for Quantitative Energy Loss Spectroscopy Analysis in Electron. *Microsc. Microanal. Microstruct.* **1990**, *1* (1), 23–39.
- (36) de la Pea, F.; Burdet, P.; Ostasevicius, T.; Sarahan, M.; Nord, M.; Fauske, V. T.; Taillon, J.; Eljarrat, A.; Mazzucco, S.; Donval, G.; Zagonel, L. F.; Walls, M.; Iyengar, I. HyperSpy.

- (37) Ahn, C. C.; Rez, P. Inner Shell Edge Profiles in Electron Energy Loss Spectroscopy. *Ultramicroscopy* **1985**, *17*, 105–115.
- (38) Plumier, R.; Sougi, M. Observation of a First-Order Transition at  $T < T_c$  in  $MnV_2O_4$ . *Phys. B Condens. Matter* **1989**, *155*, 315–319.
- (39) Armstrong, A. R.; Kuganathan, N.; Islam, M. S.; Bruce, P. G. Structure and Lithium Transport Pathways in  $Li_2FeSiO_4$  Cathodes for Lithium Batteries. *J. Am. Chem. Soc.* **2011**, *133*, 13031–13035.
- (40) Su, D. S. Electron Beam Induced Changes in Transition Metal Oxides. *Anal Bioanal Chem* **2002**, *374* (4), 732–735.
- (41) Su, D. S.; Wieske, M.; Beckmann, E.; Blume, A.; Mestl, G.; Schloegl, R. Reduction of  $V_2O_5$  in the Transmission Electron Microscope. *Catal. Letters* **2001**, *1* (2), 81–86.
- (42) Tan, H.; Verbeeck, J.; Abakumov, A.; Van Tendeloo, G. Oxidation State and Chemical Shift Investigation in Transition Metal Oxides by EELS. *Ultramicroscopy* **2012**, *116*, 24–33.
- (43) Rossell, M. D.; Agrawal, P.; Borgschulte, A.; Hébert, C.; Passerone, D.; Erni, R. Direct Evidence of Surface Reduction in Monoclinic  $BiVO_4$ . *Chem. Mater.* **2015**, 150414110704005.
- (44) Wagner, N.; Svensson, A.-M.; Vullum-Bruer, F. Liquid Feed Flame Spray Pyrolysis as Alternative Synthesis for Electrochemically Active Nanosized  $Li_2MnSiO_4$ . *Prep.* **2015**.
- (45) Bard, a. J.; Faulkner, L. R. *ELECTROCHEMICAL METHODS: Fundamentals and Applications*, 2nd Editio.; John Wiley and Sons, INC., 2001.
- (46) Meyers, J. P.; Doyle, M.; Darling, R. M.; Newman, J. The Impedance Response of a Porous Electrode Composed of Intercalation Particles. *J. Electrochem. Soc.* **2000**, *147* (8), 2930.
- (47) Zhang, L.-L.; Duan, S.; Yang, X.-L.; Peng, G.; Liang, G.; Huang, Y.-H.; Jiang, Y.; Ni, S.-B.; Li, M. Reduced Graphene Oxide Modified  $Li_2FeSiO_4/C$  Composite with Enhanced Electrochemical Performance as Cathode Material

for Lithium Ion Batteries. *ACS Appl. Mater. Interfaces* **2013**, *5*, 12304–12309.

- (48) Wang, X.; Hao, H.; Liu, J.; Huang, T.; Yu, A. A Novel Method for Preparation of Macroporous Lithium Nickel Manganese Oxygen as Cathode Material for Lithium Ion Batteries. *Electrochim. Acta* **2011**, *56* (11), 4065–4069.





# Paper IV



# Liquid-Feed Flame Spray Pyrolysis as Alternative Synthesis for Electrochemically Active Nanosized $\text{Li}_2\text{MnSiO}_4$

Nils Wagner<sup>a</sup>, Ann Mari Svensson<sup>a</sup> and Fride Vullum-Bruer<sup>a</sup>

<sup>a</sup>*Department of Materials Science and Engineering, Norwegian University of Science  
and Technology, 7491 Trondheim, Norway*

## Abstract

A novel liquid-feed flame spray pyrolysis synthesis with reducing post heat treatment yielding highly phase pure nanosized and carbon coated  $\text{Li}_2\text{MnSiO}_4$  is reported. In contrast to most  $\text{Li}_2\text{MnSiO}_4$  synthesis routes reported, aerosol combustion methods are excellently scalable and not as time consuming as most wet chemical syntheses. Flame spray pyrolysis was performed using solutions with varying ratios of  $\text{H}_2\text{O}$ , EtOH and p-Xylene. The importance of solution combustibility to form loosely agglomerated nanoparticles is highlighted. Particles from the p-Xylene aided flame spray pyrolysis showed a mean particle size of 20 nm and  $Pmn2_1$  structure after annealing and carbon coating. The electrochemical performance as cathode material was assessed by galvanostatic cycling and *in situ* XRD in half cells. The highest discharge capacity observed was  $190 \text{ mAhg}^{-1}$  at room temperature and a rate of C/50.

## Introduction

At present, rechargeable Li-ion batteries outperform all other battery concepts with respect to volumetric and gravimetric energy density. Nonetheless extensive research is on-going to optimise the cells. Especially the positive electrode materials show a great mismatch in specific capacity compared to graphite which is used as negative electrode in commercially available Li-ion batteries<sup>1</sup>. Moreover, the most common cathode material in Li-ion batteries, LiCoO<sub>2</sub>, accounts for about 50% of the materials cost of the battery<sup>2</sup>. Lately, polyanion materials like phosphates and silicates based on the abundant elements Fe and Mn as redox active ions gained attention and represent with Li<sub>2</sub>MnSiO<sub>4</sub> (LMS) a material which in theory can deliver 2 Li ions per formula unit and thus in theory offer capacities exceeding 300 mAhg<sup>-1</sup><sup>3-6</sup>. In fact, according to a recent study by Andre *et al.* from the BMW group, LMS would theoretically meet the required energy density and capacity values for the next generation Li-ion battery cathodes in all-electric vehicles<sup>7</sup>. Dominko *et al.* first reported LMS as potential cathode for Li-ion batteries in 2006 and indexed it to the tetrahedral structures with the orthorhombic space-group  $Pmn2_1$ <sup>5,8</sup>. Afterwards another orthorhombic and two monoclinic polymorphs, namely  $Pmnb$ ,  $P2_1n$  and  $Pn$ , all adopting Li<sub>3</sub>PO<sub>4</sub> structures were reported<sup>9-11</sup>. Just like the Fe analogue, Li<sub>2</sub>FeSiO<sub>4</sub>, LMS is a poor electronic and ionic conductor and thus requires nanoscale particles and a conductive coating to overcome these shortcomings<sup>5,12,13</sup>. However, it is believed that changes in the Mn coordination during oxidation cause amorphisation of the structure which leads to irreversible capacity fading<sup>14-17</sup>. Ab initio calculations by Saracibar *et al.* predict that Ni substitution could be beneficial to stabilise the crystal structure upon delithiation (oxidation)<sup>15</sup>. The vast majority of reported syntheses of LMS are wet chemical methods. Solvothermal syntheses deliver the highest reported capacities of over 200 mAh g<sup>-1</sup> in the first discharge<sup>18-21</sup>. Other authors report success by sol-gel related methods, polyol methods or molten carbonate syntheses<sup>22-26</sup>. However, these wet-chemical routes can be very time consuming. Sol-gel syntheses with a process time of up to 8 days are reported<sup>22</sup>. Another major drawback of wet chemical syntheses is the limited scalability. If a new cathode material shall ever be commercialised, scalability and time efficiency are very important factors. Flame assisted aerosol processes like flame hydrolysis and flame spray pyrolysis combine scalability and time efficiency while allowing good control of particle sizes in the nanoregime. Nanosized fumed silica, titania and carbon blacks are in fact commercially produced in large quantities by aerosol flame processes<sup>27</sup>. Here we report production of LMS by an alternative novel synthesis route, namely liquid-feed flame spray pyrolysis later called FSP, combined with a reducing heat treatment and carbon coating as an excellent scalable and time efficient route to obtain nanosized LMS. We especially highlight the importance of solution combustibility towards the morphology and thus the elec-

trochemical performance of the final product. In addition, influences on XRD phase purity dependent on Mn stoichiometry are discussed and the structural degradation is investigated by *in situ* XRD during galvanostatic cycling.

## Experimental

### *Sample preparation*

Two different kinds of precursor solutions for FSP were investigated. The first approach was a solution based on a water to ethanol ratio of 1:5 by volume. 0.06 mole dried  $\text{LiNO}_3$  (Alfa Aesar, 99%) and 0.03 mole  $\text{Mn}(\text{NO}_3)_2 \cdot 4\text{H}_2\text{O}$  (Merck Ensure for analysis, >98%) were dissolved in 20 mL deionised  $\text{H}_2\text{O}$  and added to a solution of 0.03 mole tetraethyl orthosilicate (TEOS) (VWR 99%) in 80 mL EtOH under vigorous stirring. In the second approach the solution was based on a p-xylene to ethanol ratio of 1:5 by volume. The same Li, Mn and Si precursors were dissolved in 100 mL EtOH at 50 °C under vigorous stirring and prior to pyrolysis 25 mL p-Xylene was added as fuel enhancer. Following this route, also samples with 6 and 9 mole % Mn sub-stoichiometry were produced. FSP was performed on a NPS10, Tethis S.p.A. The solutions were sprayed into a  $\text{CH}_4/\text{O}_2$  (flow rate: 1.5/3 L/min) flame at a constant liquid and dispersion gas ( $\text{O}_2$ ) flow rate of 5 mL/min. The pressure drop (dispersion gas at the nozzle tip) was set to  $\sim 2.0$  bar and the powders were collected on a glass microfiber filter (Whatman GF6). After FSP the as-pyrolysed precursors were mixed with 25 wt. % corn-starch (Carl Roth GmbH & Co. KG for laboratory use) and wet ball milled for 10 h using YSZ grinding balls ( $\varnothing$  5 mm) and EtOH as a dispersant in a 125 mL polyethylene bottle. As a final step the precursor mixtures were heat treated in a reducing atmosphere (5%  $\text{H}_2$  in Ar: flow rate 25 L/h) at three different temperatures, 550, 600 and 650 °C and different dwell times. The heating and cooling rate was in all cases 200 °C  $\text{h}^{-1}$ . The final heat treatment parameters were 650 °C for 10 h in all cases. For clarity reasons a sample index comprising the differences of the synthesised samples is given in Table 1.

**Table 1: Sample index of the 4 different samples synthesised in this study.**

Sample index	Nominal composition	Flame pyrolysis solution
LMS @ EtOH	$\text{Li}_2\text{MnSiO}_4$	80 mL EtOH 20 mL $\text{H}_2\text{O}$
LMS @ Xylene	$\text{Li}_2\text{MnSiO}_4$	100 mL EtOH 25 mL p-Xylene
LM0.94S @ Xylene	$\text{Li}_2\text{Mn}_{0.94}\text{SiO}_4$	100 mL EtOH 25 mL p-Xylene
LM0.91S @ Xylene	$\text{Li}_2\text{Mn}_{0.91}\text{SiO}_4$	100 mL EtOH 25 mL p-Xylene

For cathode preparation a slurry containing 75 wt. % active material, 15 wt. % conductive carbon (Super P Timcal) and 10 wt. % Polyvinylidene fluoride (PVDF) (Kynar, reagent grade) as binder dispersed in N-Methyl-2-pyrrolidone (NMP) (Sigma Aldrich > 99 %) was prepared and tape casted on Al foil as current collector and dried for 12 h at 90 °C in a vacuum oven. The solid load was about 1 mg cm<sup>-2</sup>.

### *Characterisation*

Phase formation and structural analysis of the samples was performed by X-ray powder diffraction. XRD patterns were recorded on a Bruker D 8 Advance Da-Vinci, equipped with a linear PSD detector working in Bragg-Brentano ( $\Theta/2\Theta$ ) geometry. All powder patterns were recorded using Cu K $\alpha$  radiation (1.54060 Å). Patterns for phase formation analysis were recorded from 15 to 75° 2 $\Theta$  with a step-size of 0.013 ° and an integration time of 0.75 s. For structural analysis, patterns were recorded from 15 to 140° 2 $\Theta$  with a step-size of 0.013 ° and an integration time of 1 s. Structural refinements were performed with Topas (Bruker AXS Version 4.2). A Pearson approximation (PVII) was applied to refine the peak shapes. All atomic positions not fixed by *Pmn2<sub>1</sub>* geometry were allowed to converge, starting with the heaviest element. Refinements were also used to quantify the phase fraction of powder diffraction patterns. Details about *in situ* XRD measurements are given in the next paragraph. The surface area and pore distribution of the materials was measured by Nitrogen adsorption on a Micrometrics Tristar 3000, according to BET, BJH and T-plot theory. All samples were vacuum dried at 250°C for 24 h prior to analysis. Thermogravimetric analysis (TGA) was performed to measure the carbon content of the samples using a Netzsch STA 449C Jupiter thermo analyser. The materials were heated to 850 °C in synthetic air (30mL min<sup>-1</sup>) at a heating rate of 10 °C min<sup>-1</sup>. The morphology of the samples was further studied by electron microscopy. 3D information was gathered on a Zeiss Supra 55 VP field emission electron microscope. Furthermore, high magnification micrographs were recorded using a double Cs corrected cold field emission gun JEOL JEM-ARM200F (scanning) transmission electron microscope ((S)TEM). Samples for microscopy investigations were dispersed in EtOH and sonicated for 20 min. A small droplet of the powder/alcohol suspension was placed on a FE-SEM sample holder or an amorphous carbon coated Cu TEM grid, respectively.

### *Electrochemical characterisation*

The electrochemical properties of the prepared LMS cathode materials were assessed by galvanostatic charge-discharge measurements on a Maccor 4200. All measurements were performed at room temperature. The applied potential window and C- rate are

given in the corresponding sections. For comparability reasons of the C-rate, only the one electron reaction of  $\text{Mn}^{2+}/\text{Mn}^{3+}$  was considered and for simplicity 1C was defined as a current density of  $160 \text{ mAh g}^{-1}$ . CR2016 coin cells were assembled in a glove box (dry Ar atmosphere) using a 16 mm circular LMS cathode, a circular Li disc as anode and a Celgard 2400 film as electrode separator. Commercial 1 M  $\text{LiPF}_6$  dissolved in a 1:1 volume ratio of Ethylene carbonate / Diethyl carbonate solution (Aldrich Battery grade) was used as electrolyte. Additionally, the structural changes of LMS were investigated by *in situ* XRD experiments during the first two galvanostatic cycles. A conventional pouch cell was assembled for *in situ* experiments. The electrodes, separator and electrolyte were the same as previously described. An image of the experimental setup and a description of the *in situ* pouch cells are shown in the supplementary information. The cell was galvanostatically cycled on a Princeton Applied Research Parstat 4000 at C/16 rate starting from OCP. The potential window was 1.5 – 4.7 V and the cell was cycled twice. The *in situ* XRD patterns were recorded continuously on a Bruker D 8 Advance Da-Vinci with a LynxEye Xe detector working in Bragg–Brentano ( $\Theta/2\Theta$ ) geometry using Mo  $\text{K}_\alpha$  radiation in transmission mode. Scans were recorded from  $11.7$  to  $15.8^\circ 2\Theta$  (step-size of  $0.015^\circ$ , integration time 3 s). The *in situ* measurement is presented as a level plot. Due to the additional layers of Al, PE and Li that the beam had to penetrate in transmission mode, the observable  $2\Theta$  region without interference from the cell components was limited to the above mentioned  $2\Theta$  values. Furthermore, pre and post *ex situ* analysis scans of the cathode were recorded from  $15$  to  $75^\circ 2\Theta$  (step-size of  $0.013^\circ$ , integration time 1 s) using Cu  $\text{K}_\alpha$  radiation.

## Results and discussion

### *Structural evolution*

All as-pyrolysed powders consisted of a mixture of crystalline  $\text{Li}_2\text{CO}_3$  and Li-Mn oxides. Si containing oxides could not be detected by XRD and were probably present in an amorphous state. Lack of LMS phase formation during pyrolysis was expected due to the extremely short residence time of the particles in the temperature zone. Further, the oxidising conditions of the  $\text{CH}_4/\text{O}_2$  flame cause Mn oxidation and thus hinder phase formation. An XRD pattern of the as-pyrolysed powder is given in the supplementary information. The as-pyrolysed samples were then mixed with 25 wt. % corn-starch as carbon source. Amongst other studies, we previously demonstrated that uncoated LMS has a very low electrochemical activity and thus any characterisation of uncoated LMS samples was omitted in this study<sup>23</sup>. The powder corn-starch mixture was then heat treated at 550, 600 and 650 °C with a dwell time of 10



h in flowing 5% H<sub>2</sub> 95 % Ar. Figure 1 shows the corresponding XRD patterns of LMS @ EtOH and LMS @ Xylene.

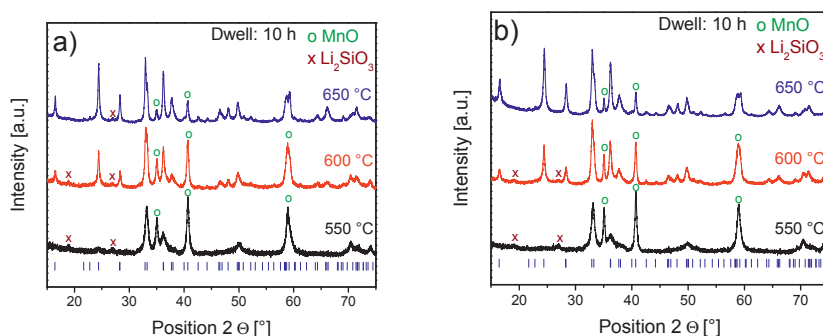


**Figure 1: Powder XRD pattern of a) LMS @ EtOH heat treated at 550, 600 and 650 °C and b) LMS @ Xylene heat treated at 550, 600 and 650 °C, including denotation of secondary phases and LMS  $Pmn2_1$  Bragg reflections.**

The onset of phase formation was in both cases detected for samples heat treated at 600 °C and the main phase was in both cases dominant at 650 °C. In the case of LMS @ EtOH traces of MnO and Li<sub>2</sub>SiO<sub>3</sub> were detectable, while for LMS @ Xylene only traces of MnO were detected. But in both cases the main pattern could be clearly attributed to orthorhombic  $Pmn2_1$  LMS<sup>5</sup>. Reported higher heat treatment temperatures (700-800 °C) often result in a mixture of  $Pmn2_1$  and  $Pmnb$  LMS. This is clearly recognisable by the appearance of a peak at about 30.6 ° under Cu K<sub>α</sub> radiation, which is sometimes disregarded or misinterpreted as a secondary phase<sup>26,28,29</sup>. To prevent this polymorph mixture we limited the heat treatment temperature to 650 °C. In addition, the influence of the dwell time was investigated for the LMS @ Xylene sample. Shorter dwell times resulted in incomplete phase formation, saturation was observed at about 8-10 h thus all further samples were prepared using these heat treatment parameters. The corresponding figure is shown in the supplementary information. Morphological investigations presented in the next chapter show LMS @ Xylene to be more promising, thus further improvements and characterisation were carried out. As shown in Figure 1 b) there are still traces of MnO present next to the main phase. According to preliminary refinements about 3 wt. % of the phase fraction can be attributed to MnO. This could imply that the synthesised LMS @ Xylene is present in a Mn deficient form. It was hence attempted to produce nominal sub stoichiometric LMS @ Xylene, namely LM0.94S @ Xylene and LM0.91S @ Xylene by

subsequently reducing the  $\text{Mn}(\text{NO}_3)_2 \cdot 4\text{H}_2\text{O}$  precursor by 6 and 9 mole %. Figure 2 a) shows the resulting evolution of the MnO secondary phase. Figure 2 b) shows a full pattern refinement of LM0.94S @ Xylene which gave the highest phase purity. The refinement model matches the observed pattern fairly well. The increased background at low  $2\Theta$  angles is caused by the fixed slit set up. Crystalline phase fractions and the calculated crystallite size of all samples are summarised in Table 2.

**Table 2: Phase fractions of LMS @ Xylene, LM0.94S @ Xylene and LM0.91S @ Xylene according to Rietveld refinements.**

Sample Index	$\text{Li}_2\text{MnSiO}_4$ [wt. %]	MnO [wt. %]	$\text{Li}_2\text{SiO}_3$ [wt. %]	Crystallite size from XRD [nm]
LMS @ Xylene	97	3	-	23.5
LM0.94S @ Xylene	99	1	-	24
LM0.91S @ Xylene	96.5	1.5	2	25

The lattice parameters of the refined orthorhombic  $\text{Pmn}2_1$  structure of LM0.94S @ Xylene are  $a = 6.313 \text{ \AA}$ ,  $b = 5.383 \text{ \AA}$  and  $c = 4.970 \text{ \AA}$ . The lattice parameters of the other 2 compositions synthesised by Xylene assisted FSP are very similar and they all agree with data from literature <sup>5</sup>. Figure 2 a) and Table 2 show that the MnO secondary phase is reduced but does not disappear even at 9 mole % Mn sub-stoichiometry. For the stoichiometric and 6 mole % Mn sub-stoichiometric samples MnO was the only detectable secondary phase, but when the Mn concentration is further reduced,  $\text{Li}_2\text{SiO}_3$  emerges and no further reduction of the MnO phase is observed. This could be caused by only a small difference in energy of formation of MnO and LMS and the tolerance of LMS for Mn deficiency resulting in a low driving force for phase combination at the given temperature. In fact, the appearance of MnO as the only visible secondary phase even for samples with a reduced Mn content indicates that LMS samples synthesised in this study are Mn deficient. This could be charge compensated either by vacancies in the oxygen sub lattice or by a partial oxidation of  $\text{Mn}^{2+}$  to  $\text{Mn}^{3+}$  to maintain electro neutrality.

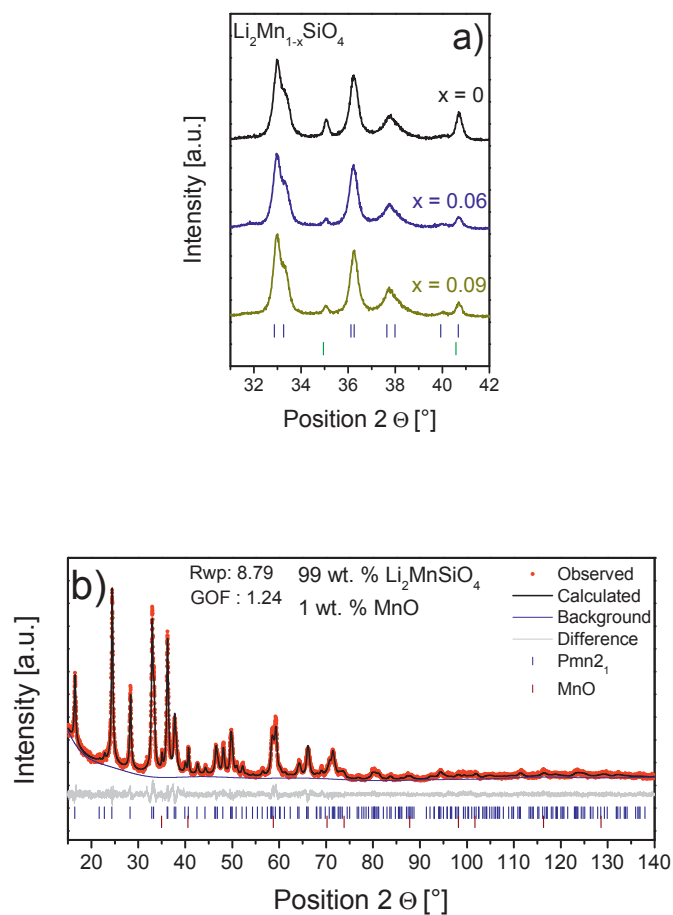


Figure 2: a) XRD patterns of LMS @ Xylene, LM0.94S @ Xylene and LM0.91S @ Xylene showing the phase evolution of the MnO secondary phase. b) Full pattern refinement of LM0.94S @ Xylene.

It is noteworthy that all refinements underestimate the Mn 2a occupancy to values about 0.7-0.75 without showing high values of Li/Mn site reversal.  $\text{Mn}^{2+}$  on a Li-site would cause changes in the diffraction pattern due to the much higher electron density. On the other hand it could hardly be distinguished if a Mn site is actually vacant or occupied by Li due to the very low electron density of  $\text{Li}^+$ . Dominko *et al.* ex-

plained this phenomena by disorder <sup>5</sup>. A part of the Mn atoms could occupy states in the interstitial octahedral voids. This would explain the remaining mismatch between the observed and the calculated XRD patterns and the underestimated Mn occupancy. Further details of all refinements are shown in the supplementary information.

*Influence of precursor solution combustibility and final heat treatment on the powder morphology*

The precursor solution or in other words the fuel for the FSP process had a major impact on the morphology of the final powders. Since LMS shows rather poor electronic and ionic conductivities the particle size is very important for the electrochemical properties. Furthermore, porosity in the meso and macro range is beneficial to maximise the contact area of the cathode material and the electrolyte and thus enhance the electrochemical kinetics. Table 3 shows the surface area values divided into micropore area and external surface area and the residual carbon content of the sample measured by TGA. We define the external area by the part of the total BET surface area that is not attributed to microporosity, which is by definition smaller than 2 nm in diameter. We have previously shown that to a great extent the micropore area can be attributed to porosity in the amorphous carbon coating <sup>23</sup>.

**Table 3: Surface area and carbon content of synthesised LMS samples.**

Sample index	BET surface area [m <sup>2</sup> g <sup>-1</sup> ]	External surface area [m <sup>2</sup> g <sup>-1</sup> ]	Micropore area [m <sup>2</sup> g <sup>-1</sup> ]	Carbon content [wt. %]
LMS @ EtOH	72.2	49.2	23.0	6
LMS @ Xylene	97.3	67.8	29.5	6
LM0.94S @ Xylene	93.5	64	29.5	6
LM0.91S @ Xylene	88.7	61.4	27.3	6

All LMS samples showed a very similar carbon content of about 6 wt. %. Further, all Xylene assisted FSP samples showed 20-30% elevated external surface areas compared to the LMS @ EtOH sample. SEM analysis revealed major morphological differences between samples produced with and without Xylene addition. Figure 3 shows SEM micrographs of LMS @ EtOH and LMS @ Xylene, where a) and c) show the corresponding powders as received from FSP and b) and d) the final powders of LMS @ EtOH and LMS @ Xylene respectively. The resulting morphology of FSP remains almost completely preserved after the powders were heat treated and carbon coated.

Both powders consist of loosely agglomerated nanograins but the as-pyrolysed and final powder of LMS @ EtOH exhibited a large amount of dense spherical particles in the sub- $\mu\text{m}$  and  $\mu\text{m}$  regime. These particles were also present in the LMS @ Xylene sample but in a much lower quantity. The appearance of spherical dense particles during conventional spray pyrolysis is well known and caused by volume precipitation during pyrolysis<sup>30</sup>. The increased density of these spherical sub- $\mu\text{m}$  particles can be directly linked to the combustibility of the precursor solution, which in case of the EtOH / p-Xylene solution is enhanced compared to the EtOH / H<sub>2</sub>O solution. A similar phenomenon was observed by Dahl *et al.* during the comparison of different solvents used for FSP of binary oxides<sup>31</sup>.

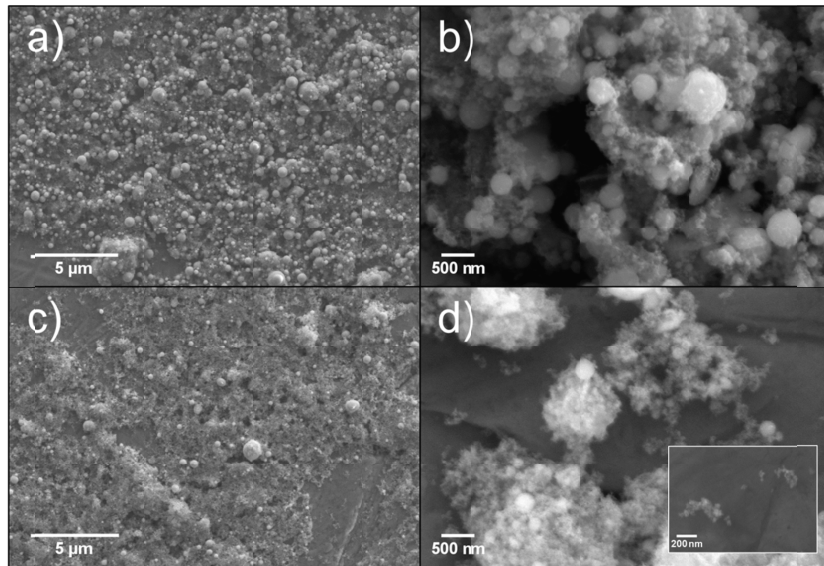


**Figure 3:** SEM micrographs of different LMS powders, magnifications are given in brackets. a) LMS @ EtOH as-pyrolysed (5k), b) LMS @ EtOH (20k), c) LMS @ Xylene as-pyrolysed (5k), d) LMS @ Xylene (20k) the inset show the same powder at a higher magnification (40k).

TEM/STEM analysis further revealed that the LMS @ Xylene sample consists of nanoparticles with a mean particle size of about 20 nm ranging from 10 to 40 nm. For this analysis the remaining few spherical sub- $\mu\text{m}$  particles were omitted. This fits well with the calculated crystallite size from XRD data. Bright-field TEM and STEM images are given in Figure 4. In the STEM micrograph also the amorphous carbon layer surrounding the grains and the crystal orientation are indicated.

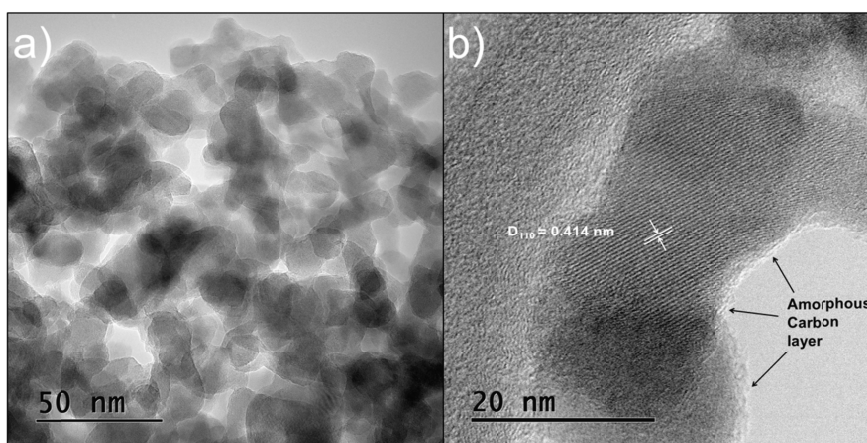


**Figure 4:** a) TEM micrograph showing weakly agglomerated LMS grains. b) STEM micrograph of LMS grains surrounded by a thin layer of amorphous Carbon.

#### *The impact of precursor combustibility on the electrochemical performance*

As mentioned in the previous section the precursor solution combustibility resulted in quite noticeable morphological changes. Large micron sized particles or dense agglomerates in the same range are undesirable for materials offering low ionic and electronic conductivity values like LMS. To verify the influence of the morphology, cathodes were fabricated of all synthesised LMS powders and galvanostatically cycled in a potential window of 1.5 – 4.7 V at room temperature and C/16 rate. Figure 5 shows the corresponding first and second cycle.

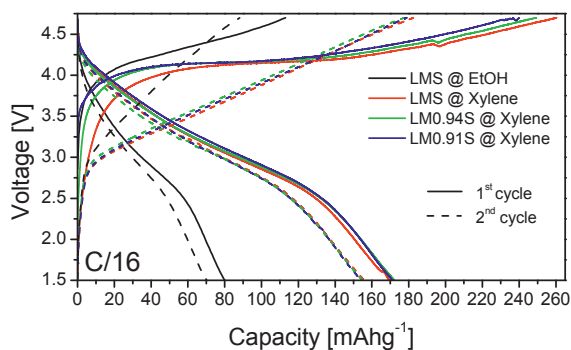


**Figure 5: First and second galvanostatic cycle of LMS @ EtOH, LMS @ Xylene, LM0.94S @ Xylene and LM0.91S @ Xylene.**

All samples suffered from an irreversible capacity loss (ICL) of about 30% in the first cycle. This loss can partly be attributed to parasitic oxidation reactions of the electrolyte and interphase formation but also the structural degradation must be considered. The structure may already completely collapse during the first oxidation and does not allow full relithiation upon reduction. Despite the ICL which is present in all cases, a tremendous increase in discharge capacity of over 100% from 80 to about 170  $\text{mAh g}^{-1}$  is visible when comparing LMS @ EtOH with the Xylene assisted samples. In the Mn sub-stoichiometry series almost no difference in discharge capacity was detectable which is most probably due to comparable phase purity and the fact that all synthesised samples showed a Mn stoichiometry  $< 1$  according to XRD data. The second charge profile looks completely different from the first one, which indicates structural changes. This behaviour is well known and understood for  $\text{Li}_2\text{FeSiO}_4$ , where the delithiation is shifted to lower potentials caused by structural rearrangements<sup>32-35</sup>. In contrast to this, not only the onset of oxidation is lowered to potentials at about 3 V but also the slope of the charge curve is much steeper without any plateau like regions which could be explained by the loss of crystallinity and thus order. The discharge profile in the second cycle remains the same but a loss in discharge capacity of about 10-15  $\text{mAh g}^{-1}$  is present. The capacity fading makes it challenging to investigate the rate capability since the discharge capacity is influenced by both, the number of cycles the battery was tested and the charge rate.

Figure 6 a) shows the first discharge capacity of LM0.94S @ Xylene at four different rates ranging from C/50 to C/2. The coulombic efficiency is in all cases about 70%. The inset shows the first 20 cycles of the same materials at C rates from C/2 to 5C. Furthermore, the capacity fade with respect to the potential window and thus the amount of Li extracted/inserted for 150 cycles is shown in figure 6 b).

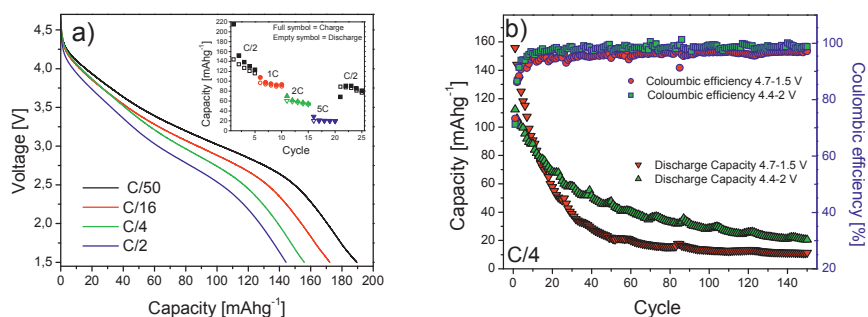


**Figure 6:** a) First discharge of LM0.94S @ Xylene at different rates, 20 cycles at higher rates are shown in the figure inset. b) Discharge capacity of LM0.94S @ Xylene during 150 cycles in two different potential windows 4.7-1.5 and 4.4 to 2.0 V. The right ordinate shows the coulombic efficiency in %.

Figure 6 a) shows the first discharge capacity rating from 145 to 190 mAh g<sup>-1</sup> depending on the C-rate. The values at C/50 and C/16 are 190 and 170 mAh g<sup>-1</sup>, respectively. Additionally, it has to be considered that capacities reported here are with respect to the LMS/C where the amorphous carbon coating acts as conductivity enhancer. To obtain the specific capacity of the bare silicate the weight of the carbon coating (6 wt. %) needs to be subtracted which leads to values of ~180 and 200 mAh g<sup>-1</sup> at C/16 and C/50, respectively. Both values cannot be solely attributed to the Mn<sup>3+</sup>/Mn<sup>2+</sup> redox couple, especially considering that the charge capacity is 30 % higher. It is believed that the second Li is mobilised to a certain amount at slow C-rates by the Mn<sup>4+</sup>/Mn<sup>3+</sup> redox couple. Figure 6 b) shows that the known capacity decay of LMS is directly related to the potential window of operation and thus to the amount of Li being extracted from the structure during each charge. LM0.94S @ Xylene was cycled in two different potential windows, 1.5-4.7 and 2-4.4 V at C/4. The sample cycled in the large potential window showed an initial discharge capacity of 156 mAh g<sup>-1</sup>. After 20 cycles the capacity dropped to 58 mAh g<sup>-1</sup>, which corresponds to a capacity retention of only 37%. On the other hand, the sample cycled in the



smaller potential window retained 62% of its initial value of  $112 \text{ mAh g}^{-1}$ . It can be concluded that the capacity decay is directly linked to the amount of Li removed from the structure and thus the oxidation state of Mn. To further confirm that the ICL in the first cycle cannot be solely attributed to unwanted oxidation reactions it was attempted to completely mobilise the first Li at lower potentials. This was accomplished by inserting a potentiostatic step in the galvanostatic cycling program. LM0.91S @ Xylene was charged at C/16 to a moderate potential of 4.2 V and kept at this potential until the current density dropped to a value of 0.005 C. Afterwards it was discharged at C/16 to 1.5 V and subsequently cycled again without the potentiostatic step. The result of the experiment is shown in Figure 7.

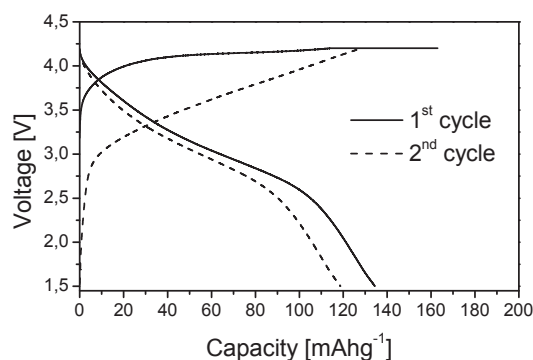


**Figure 7: First to cycles of LM0.91S @ Xylene at C/16 in a potential window of 1.5 – 4.2 V including a potentiostatic step at 4.2 V until the current density declined to a value of 0.005 C at the end of the first charge.**

The charge capacity of  $163 \text{ mAh g}^{-1}$  fits well with the theoretical capacity of the one electron reaction, especially considering the carbon coating and the fact that the studied LMS samples show slight Mn sub-stoichiometry. The corresponding discharge capacity was only  $134 \text{ mAh g}^{-1}$ , hence still showing a prominent ICL of 18% even at potentials well within the kinetically controlled stability range of the electrolyte<sup>36</sup>. In order to further confirm that the capacity decay is caused by irreversible amorphisation, the structural evolution of LM0.94S @ Xylene was monitored during the first two galvanostatic cycles in a pouch cell by *in situ* X-ray diffraction using Mo K<sub>α</sub> radiation in transmission mode. The corresponding *in situ* level plot is shown in Figure 8. The  $2\Theta$  range was limited to 11.7 to 15.8 °. In this range the *111 200* and *210 020* double peaks were monitored. The intensity of these two double peaks during the

first scan was set as maximum intensity in the level plot representation. This short scan range was chosen to omit strong peaks from the polyethylene and Al from the pouch material and current collector. To keep a good time resolution the scan, time was chosen to be as short as possible ( $\sim 22$  min) while the cell was charged at a low rate of C/16. The charge-discharge behaviour in the pouch cell was somewhat different to the experiments on coin-cells showing an increased charge and a decreased discharge capacity which could be caused by an inhomogeneous pressure distribution in our *in situ* cells<sup>37</sup>.

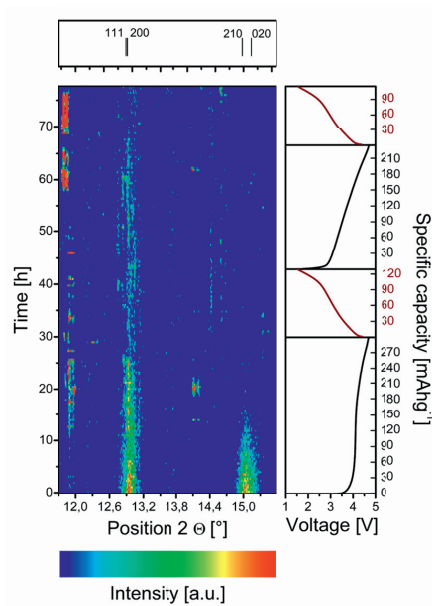


Figure 8: *In situ* XRD level plot during the first two galvanostatic cycles at C/16 of an LM0.94S @ Xylene pouch cell using Mo  $K_{\alpha}$  radiation in transmission mode. At the top the 2 observed double peaks are shown and on the right hand the cycling profile.

The *in situ* XRD level plot shows clearly the loss of crystallinity of the LM0.94S @ Xylene cathode during the first charge. The (210) (020) double peak disappears at potentials slightly higher than 4 V and a state of charge of about  $120 \text{ mAhg}^{-1}$  which corresponds to 0.72 Li per formula unit if side reactions are excluded. The (111) (200) double peak diminishes into the background noise at higher potentials of about 4.6 V. During discharge and in the subsequent cycle none of the  $Pmn2_1$  peaks reappear, we

thus conclude the amorphisation is irreversible. Interestingly, other peaks appear in the *in situ* measurement. As shown in the level plot one sharp double peak or two very close peaks appear at about 11.8-11.9° 2 $\Theta$  and they seem to be slightly shifted to lower 2 $\Theta$  angles in the second cycle. Another peak appears in both the first and second charge at potentials of around 4.25 V at 2 $\Theta$  of about 14.1° but disappears again as the potential is increased. Unfortunately, due to the short scan range and the quality of data none of these peaks could be indexed. Also one has to consider that any crystallisation occurring in the cell would be monitored since the experiment was performed in transmission mode. To further investigate changes on the cathode and to gain a better signal to noise ratio, the *in situ* cell was disassembled and the cathode was washed multiple times with DEC to remove LiPF<sub>6</sub>. A diffractogram was recorded from 15 to 75° 2 $\Theta$  using Cu K $\alpha$  radiation. The results are compared to a fresh electrode and shown in Figure 9.

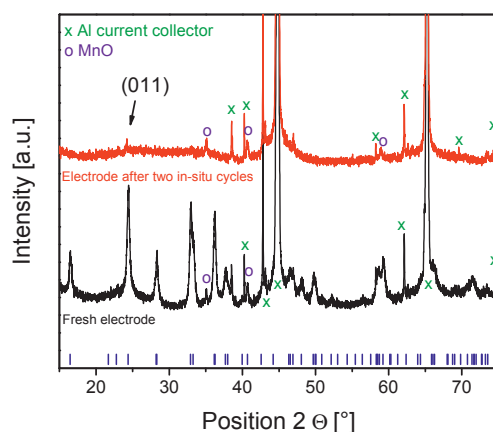


Figure 9: XRD patterns of an LM0.94S @ Xylene fresh electrode and after two *in situ* cycles. LMS  $Pmn2_1$  Bragg reflections are added and the peaks originating from the MnO impurity and the Al current collector are denoted. Additional Al peaks are instrument caused by parasitic Cu K $\beta$  and W L radiation.

None of the observed unknown peaks during the *in situ* measurement were observed on the cycled electrode, making it impossible to conclude the chemical composition of the observed crystallisation and the exact place where it occurs. Alongside the peaks of the Al current collector and the MnO secondary phase, only a weak signal which

could be attributed to the  $011$  main peak of  $Pmn2_1$  LMS is still visible while all other peaks of the main structure completely disappeared, confirming the irreversible amorphisation of LMS upon cycling.

## Conclusions

With liquid-feed flame spray pyrolysis, an alternative method which enables preparation of nanoscaled LMS/C in large quantities is reported. It was shown that the combustibility of the precursor solution had a major impact on the particle morphology and the resulting electrochemical performance. All prepared samples based on the 5:1 EtOH / P-Xylene solution are believed to exhibit slight Mn sub-stoichiometry. For the nominal and the 6 mole % Mn sub-stoichiometric samples traces of MnO was the only detectable secondary phase. Further reduction of the Mn concentration caused formation of  $\text{Li}_2\text{SiO}_3$ . The highest capacity achieved in this study was  $190 \text{ mAhg}^{-1}$  during the first discharge at a charge rate of C/50. At a higher C rate of C/2 the first discharge capacity still exceeded  $140 \text{ mAhg}^{-1}$ . Values over  $166 \text{ mAhg}^{-1}$  cannot solely be caused by the  $\text{Mn}^{2+/3+}$  redox couple. Also, the high charge capacities suggest activity of the second redox couple ( $\text{Mn}^{3+/4+}$ ) at slow C-rates, but the structural collapse does not allow full delithiation during the discharge. The theoretical capacity was not reached even during the charge at low rates and it can thus be concluded that to mobilise the second Li ion not only the structural instability must be overcome but also electrolytes with a larger potential window are required. All samples in this study showed a prominent irreversible capacity loss between the first charge and discharge and capacity fade caused by the structural instability of LMS. *In situ* XRD experiments showed that a complete loss of crystallinity already occurs during the first charge. This loss was shown to be irreversible and no XRD peaks corresponding to LMS reoccurred during the discharge and the subsequent cycle. It is concluded that LMS has major shortcomings to be solved before it could potentially become interesting for battery applications, since the ability of delivering two Li per formula unit is not possible in the given potential range without the stabilisation of the structure. Nonetheless, it is noteworthy that in principle the reported synthesis should also be applicable for  $\text{Li}_2\text{FeSiO}_4$  which shows more potential as a stable low cost cathode material for Li-ion batteries, as well as other transition metal oxides suitable for battery applications.

## Acknowledgements

The research council of Norway is gratefully acknowledged for funding the SilicatBatt project (grant number: 216469/E20). NORTEM seed and competence projects (grant number 11) and Dr. Per Erik Vullum are acknowledged for TEM analysis.

## References

- (1) Tarascon, J. M.; Armand, M. Issues and Challenges Facing Rechargeable Lithium Batteries. *Nature* **2001**, *414* (6861), 359–367.
- (2) Gaines, L.; Cuenca, R. *Costs of Lithium-Ion Batteries for Vehicles*; 2000; Vol. 48.
- (3) Padhi, A. K.; Nanjundaswamy, K. S.; Goodenough, J. B. Phospho-Olivines as Positive-Electrode Materials for Rechargeable Lithium Batteries. *J. Electrochem. Soc.*, **1997**, *144* (4), 1188.
- (4) Nytén, A.; Abouimrane, A.; Armand, M.; Gustafsson, T.; Thomas, J. O. Electrochemical Performance of  $\text{Li}_2\text{FeSiO}_4$  as a New Li-Battery Cathode Material. *Electrochem. commun.* **2005**, *7* (2), 156–160.
- (5) Dominko, R.; Bele, M.; Gaberšček, M.; Meden, A.; Remškar, M.; Jamnik, J. Structure and Electrochemical Performance of  $\text{Li}_2\text{MnSiO}_4$  and  $\text{Li}_2\text{FeSiO}_4$  as Potential Li-Battery Cathode Materials. *Electrochem. commun.* **2006**, *8* (2), 217–222.
- (6) Kuganathan, N.; Islam, M. S.  $\text{Li}_2\text{MnSiO}_4$  Lithium Battery Material: Atomic-Scale Study of Defects, Lithium Mobility, and Trivalent Dopants. *Chem. Mater.* **2009**, *21* (21), 5196–5202.
- (7) Andre, D.; Kim, S.-J.; Lamp, P.; Lux, S. F.; Maglia, F.; Paschos, O.; Stiaszny, B. Future Generations of Cathode Materials: An Automotive Industry Perspective. *J. Mater. Chem. A* **2015**, *3*, 6709–6732.
- (8) Dominko, R.  $\text{Li}_2\text{MSiO}_4$  (M = Fe And/or Mn) Cathode Materials. *J. Power Sources* **2008**, *184* (2), 462–468.

- (9) Politaev, V. V.; Petrenko, A. A.; Nalbandyan, V. B.; Medvedev, B. S.; Shvetsova, E. S. Crystal Structure, Phase Relations and Electrochemical Properties of Monoclinic  $\text{Li}_2\text{MnSiO}_4$ . *J. Solid State Chem.* **2007**, *180* (3), 1045–1050.
- (10) Duncan, H.; Kondamreddy, A.; Mercier, P. H. J.; Le Page, Y.; Abu-Lebdeh, Y.; Couillard, M.; Whitfield, P. S.; Davidson, I. J. Novel Pn Polymorph for  $\text{Li}_2\text{MnSiO}_4$  and Its Electrochemical Activity As a Cathode Material in Li-Ion Batteries. *Chem. Mater.* **2011**, *23* (24), 5446–5456.
- (11) Gummow, R. J.; Sharma, N.; Peterson, V. K.; He, Y. Crystal Chemistry of the Pmnb Polymorph of  $\text{Li}_2\text{MnSiO}_4$ . *J. Solid State Chem.* **2012**, *188*, 32–37.
- (12) Islam, M. S.; Dominko, R.; Masquelier, C.; Sirisopanaporn, C.; Armstrong, A. R.; Bruce, P. G. Silicate Cathodes for Lithium Batteries: Alternatives to Phosphates? *J. Mater. Chem.* **2011**, *21*, 9811–9818.
- (13) Gummow, R. J.; He, Y. Recent Progress in the Development of  $\text{Li}_2\text{MnSiO}_4$  Cathode Materials. *J. Power Sources* **2014**, *253*, 315–331.
- (14) Larsson, P.; Ahuja, R.; Liivat, A.; Thomas, J. O. Structural and Electrochemical Aspects of Mn Substitution into  $\text{Li}_2\text{FeSiO}_4$  from DFT Calculations. *Comput. Mater. Sci.* **2010**, *47* (3), 678–684.
- (15) Saracibar, A.; Wang, Z.; Carroll, K. J.; Meng, Y. S.; Dompablo, M. E. A. New Insights into the Electrochemical Performance of  $\text{Li}_2\text{MnSiO}_4$ : Effect of Cationic Substitutions. *J. Mater. Chem. A* **2015**, *3*, 6004–6011.
- (16) Dominko, R.; Bele, M.; Kokalj, A.; Gaberscek, M.; Jamnik, J.  $\text{Li}_2\text{MnSiO}_4$  as a Potential Li-Battery Cathode Material. *J. Power Sources* **2007**, *174* (2), 457–461.
- (17) Dominko, R.; Arčon, I.; Kodre, A.; Hanžel, D.; Gaberšček, M. In-Situ XAS Study on  $\text{Li}_2\text{MnSiO}_4$  and  $\text{Li}_2\text{FeSiO}_4$  Cathode Materials. *J. Power Sources* **2009**, *189* (1), 51–58.
- (18) Qu, L.; Fang, S.; Yang, L.; Hirano, S. Synthesis and Characterization of High Capacity  $\text{Li}_2\text{MnSiO}_4/\text{C}$  Cathode Material for Lithium-Ion Battery. *J. Power Sources* **2014**, *252*, 169–175.

- (19) Rangappa, D.; Murukanahally, K. D.; Tomai, T.; Unemoto, A.; Honma, I. Ultrathin Nanosheets of  $\text{Li}_2\text{MSiO}_4$  (M = Fe, Mn) as High-Capacity Li-Ion Battery Electrode. *Nano* **2012**, *4*.
- (20) Muraliganth, T.; Stroukoff, K. R.; Manthiram, A. Microwave-Solvothermal Synthesis of Nanostructured  $\text{Li}_2\text{MSiO}_4/\text{C}$  (M = Mn and Fe) Cathodes for Lithium-Ion Batteries. *Chem. Mater.* **2010**, *22* (20), 5754–5761.
- (21) Kempaiah, D. M.; Rangappa, D.; Honma, I. Controlled Synthesis of Nanocrystalline  $\text{Li}_2\text{MnSiO}_4$  Particles for High Capacity Cathode Application in Lithium-Ion Batteries. *Chem. Commun.* **2012**, *48* (21), 2698.
- (22) Świątosławski, M.; Molenda, M.; Furczoń, K.; Dziembaj, R. Nanocomposite  $\text{C}/\text{Li}_2\text{MnSiO}_4$  Cathode Material for Lithium Ion Batteries. *J. Power Sources* **2013**, *244*, 510–514.
- (23) Wagner, N.; Svensson, A.-M.; Vullum-Bruer, F. Effect of Carbon Content and Annealing Atmosphere on Phase Purity and Morphology of  $\text{Li}_2\text{MnSiO}_4$  Synthesized by a PVA Assisted Sol-gel Method. *Solid State Ionics* **2015**, *276*, 26–32.
- (24) Sun, D.; Wang, H.; Ding, P.; Zhou, N.; Huang, X.; Tan, S.; Tang, Y. In-Situ Synthesis of Carbon Coated  $\text{Li}_2\text{MnSiO}_4$  Nanoparticles with High Rate Performance. *J. Power Sources* **2013**, *242*, 865–871.
- (25) Liu, W.; Xu, Y.; Yang, R. Synthesis and Electrochemical Properties of  $\text{Li}_2\text{MnSiO}_4/\text{C}$  Nanoparticles via Polyol Process. *Rare Met.* **2010**, *29* (5), 511–514.
- (26) Aravindan, V.; Karthikeyan, K.; Kang, K. S.; Yoon, W. S.; Kim, W. S.; Lee, Y. S. Influence of Carbon towards Improved Lithium Storage Properties of  $\text{Li}_2\text{MnSiO}_4$  Cathodes. *J. Mater. Chem.* **2011**, *21* (8), 2470.
- (27) Pratsinis, S. E. Flame Aerosol Synthesis of Ceramic Powders. *Prog. Energy Combust. Sci.* **1998**, *24* (3), 197–219.
- (28) Devaraj, S.; Kuezza, M.; Ng, C. T.; Balaya, P. Sol-Gel Derived Nanostructured  $\text{Li}_2\text{MnSiO}_4/\text{C}$  Cathode with High Storage Capacity. *Electrochim. Acta* **2013**, *102*, 290–298.

- (29) Shao, B.; Taniguchi, I. Synthesis of  $\text{Li}_2\text{MnSiO}_4/\text{C}$  Nanocomposites for Lithium Battery Cathode Employing Sucrose as Carbon Source. *Electrochim. Acta* **2013**, *128*, 156–162.
- (30) Messing, G. L.; Zhang, S.-C.; Jayanthi, G. V. Ceramic Powder Synthesis by Spray Pyrolysis. *J. Am. Ceram. Soc.* **1993**, *76* (11), 2707–2726.
- (31) Dahl, P. I.; Thomassen, M. S.; Colmenares, L. C.; Barnett, A. O.; Lomas, S.; Vullum, P. E.; Hanetho, S. M.; Mokkelbost, T. Flame Spray Pyrolysis of Electrode Materials for Energy Applications. *Materials Res. Soc. Symp. Proc.* **2015**, *1747*.
- (32) Nyttén, A.; Kamali, S.; Häggström, L.; Gustafsson, T.; Thomas, J. O. The Lithium Extraction/insertion Mechanism in  $\text{Li}_2\text{FeSiO}_4$ . *J. Mater. Chem.* **2006**, *16* (23), 2266.
- (33) Sirisopanaporn, C.; Masquelier, C.; Bruce, P. G.; Armstrong, A. R.; Dominko, R. Dependence of  $\text{Li}_2\text{FeSiO}_4$  Electrochemistry on Structure. *J. Am. Chem. Soc.* **2011**, *133* (5), 1263–1265.
- (34) Liivat, A. Structural Changes on Cycling  $\text{Li}_2\text{FeSiO}_4$  Polymorphs from DFT Calculations. *Solid State Ionics* **2012**, *228*, 19–24.
- (35) Zhou, H.; Einarsrud, M. A.; Vullum-Bruer, F. In Situ X-Ray Diffraction and Electrochemical Impedance Spectroscopy of a Nanoporous  $\text{Li}_2\text{FeSiO}_4/\text{C}$  Cathode during the Initial Charge/discharge Cycle of a Li-Ion Battery. *J. Power Sources* **2013**, *238*, 478–484.
- (36) Scrosati, B.; Garche, J. Lithium Batteries: Status, Prospects and Future. *J. Power Sources* **2010**, *195* (9), 2419–2430.
- (37) Villevieille, C.; Sasaki, T.; Novák, P. Novel Electrochemical Cell Designed for Operando Techniques and Impedance Studies. *RSC Adv.* **2014**, *4* (13), 6782.





# Paper V



# Flame-made Lithium Transition Metal Orthosilicates

Nils Wagner<sup>a</sup>, Ann Mari Svensson<sup>a</sup> and Fride Vullum-Bruer<sup>a</sup>

<sup>a</sup>*Department of Materials Science and Engineering, Norwegian University of Science and Technology, 7491 Trondheim, Norway*

## Abstract

$\text{Li}_2\text{MSiO}_4$  ( $\text{M} = \text{Fe}, \text{Mn}, \text{Co}$ ) compounds have since their discovery gained increased attention as alternative, inexpensive and inherently safe positive electrodes for Li-ion batteries. To meet the required performance for an electrode, sophisticated, complex and time-consuming synthesis measures are required at present. Here, we present a time-efficient and scalable aerosol combustion method with subsequent annealing, leading to nanoscale and carbon-coated  $\text{Li}_2\text{FeSiO}_4$  and  $\text{Li}_2\text{Fe}_{0.5}\text{Mn}_{0.5}\text{SiO}_4$ . Using liquid-feed flame spray pyrolysis, we demonstrate synthesis of highly phase pure materials in a relatively short time. The importance of the precursor concentration, in order to obtain loosely agglomerated nanoparticles, is discussed and the long-term performance is investigated. In the case of  $\text{Li}_2\text{FeSiO}_4$ , the optimised precursor concentration yielded particles of about 30 nm, which delivered an initial discharge capacity of up to  $150 \text{ mAhg}^{-1}$  at  $60 \text{ }^\circ\text{C}$  and  $C/20$ . Furthermore, over 50% of the capacity is retained at a high rate of  $5C$ , and long-term cycling showed outstanding capacity retention of over 90% after 300 cycles at a moderate rate of  $C/2$ .  $\text{Li}_2\text{Fe}_{0.5}\text{Mn}_{0.5}\text{SiO}_4$  on the other hand, was shown to suffer from a severe capacity fade, and upon prolonged cycling the redox activity can be attributed solely to Fe.

## Introduction

As  $\text{LiFePO}_4$  is a well-established cathode material for Li-ion batteries, other polyanion materials, like  $\text{Li}_2\text{MSiO}_4$ , where  $\text{M} = \text{Fe}$  and  $\text{Mn}$ , have recently gained much interest as alternative cathode materials. They are interesting since they consist of cheap, abundant and environmentally benign elements. Strong Si-O bonds in the framework result in a good thermal stability and the transition metal to Li ratio of 1:2 could, in theory, allow the exchange of two Li per formula unit, giving rise to high theoretical capacities exceeding  $300 \text{ mAh g}^{-1}$ .<sup>1-3</sup>  $\text{Li}_2\text{MSiO}_4$  compounds adopt  $\beta$  and  $\gamma$   $\text{Li}_3\text{PO}_4$  structures depending on the synthesis conditions and the transition metal cation.<sup>4,5</sup> One major shortcoming of the orthosilicates is the low conductivity values both with respect to electronic and ionic conductivity. These shortcomings can be overcome by the application of a conductive carbon coating and the synthesis of nanostructured materials to limit the mean diffusion length for Li ions.<sup>6,7</sup> A high porosity in the meso and macro range, and thus a high contact area for the electrolyte, was also shown to be significant.<sup>8-11</sup> The majority of reported syntheses are wet chemical methods, such as solvothermal,<sup>12-14</sup> solution and sol-gel related processes,<sup>10,15-17</sup> and combustion syntheses.<sup>11,18</sup> Unfortunately, most of these syntheses are not scalable, or are hard to control during up-scaling, and hence are not applicable for the preparation of large quantities of electrochemically active orthosilicates. We previously demonstrated liquid-feed flame spray pyrolysis (LF-FSP) as a novel alternative method to synthesise nanoscaled  $\text{Li}_2\text{MnSiO}_4$ , offering a high discharge capacity of up to  $190 \text{ mAh g}^{-1}$ , and excellent rate capability.<sup>19</sup>  $\text{Li}_2\text{MnSiO}_4$ , however, suffers from severe capacity decay and amorphisation of the structure, caused by distortions and changes in the Mn coordination upon oxidation.<sup>19-22</sup> Contrarily,  $\text{Li}_2\text{FeSiO}_4$  was shown to be stable in the one electron reaction range and is thus an interesting candidate as low cost alternative cathode.<sup>7,23</sup> Mn substitution in  $\text{Li}_2\text{FeSiO}_4$  would be attractive, if the structure does not collapse, since Mn can give rise to two additional redox couples. Also, the  $\text{Mn}^{2+}/\text{Mn}^{3+}$  redox reaction occurs at higher potentials vs.  $\text{Li}/\text{Li}^+$  compared to the  $\text{Fe}^{2+}/\text{Fe}^{3+}$  redox reaction.<sup>24,25</sup> The combination could result in a higher specific energy, due to an increased capacity and higher voltage. Here, we communicate LF-FSP of an EtOH/p-Xylene based metal nitrate and tetraethyl orthosilicate solution, combined with a reducing heat-treatment and carbon coating, as a time-efficient and scalable method to synthesise  $\text{Li}_2\text{FeSiO}_4$  and  $\text{Li}_2\text{Fe}_{0.5}\text{Mn}_{0.5}\text{SiO}_4$  as a cathode material for Li-ion batteries.

## Experimental

### *Sample preparation*

In this study, samples of the composition  $\text{Li}_2\text{FeSiO}_4$  (LFS) and  $\text{Li}_2\text{Fe}_{0.5}\text{Mn}_{0.5}\text{SiO}_4$  (LFMS) were synthesised. The solutions for LF-FSP consisted of EtOH and p-Xylene in a volume ratio of 5:1 and a total volume of 125 mL. In the case of LFS, two different Fe precursor concentrations,  $0.24 \text{ mol L}^{-1}$  and  $0.12 \text{ mol L}^{-1}$ , were investigated. For the higher concentration,  $0.03 \text{ mol Fe}(\text{NO}_3)_3 \cdot 9\text{H}_2\text{O}$  (Sigma-Aldrich, > 98%) was dissolved in the above mentioned amount of solvent under vigorous stirring at  $50 \text{ }^\circ\text{C}$ . Subsequently,  $0.06 \text{ mol LiNO}_3$  (Alfa Aesar, 99%) and  $0.03 \text{ mol}$  tetraethyl orthosilicate (TEOS) (VWR 99%) were added. The lower concentration solution was made with exactly half the amount of precursors. The samples are subsequently denoted as LFS 0.24 and LFS 0.12. One solution of LFMS at high concentration was prepared. The LFMS 0.24 solution was prepared in the same manner as the higher concentrated LFS solution, and  $0.015 \text{ mol Fe}(\text{NO}_3)_3 \cdot 9 \text{H}_2\text{O}$  was substituted by  $\text{Mn}(\text{NO}_3)_2 \cdot 4\text{H}_2\text{O}$  (Merck Ensure for analysis, >98%). The LF-FSP process was performed on a NPS10 Tethis S.p.A., at a constant liquid and dispersion gas ( $\text{O}_2$ ) flow rate of  $5 \text{ mL min}^{-1}$ . The solutions were sprayed into a  $\text{CH}_4/\text{O}_2$  (flow rate:  $1.5/3 \text{ L min}^{-1}$ ) flame with a pressure drop (dispersion gas at the nozzle tip) of  $\sim 2 \text{ bar}$ . After the LF-FSP process, the powders were collected on a glass microfiber filter (Whatman GF6). As the carbon source, 30 wt. % corn-starch (Carl Roth GmbH & Co. KG for laboratory use) was mixed with the collected powders by wet ball milling for 10 h, using an equivalent volume of YSZ grinding media ( $\text{Ø} 5 \text{ mm}$ ) and EtOH as a dispersant. Heat treatments were carried out in a reducing atmosphere (2%  $\text{H}_2$  in Ar: flow rate  $10 \text{ L/h}$ ), at  $650 \text{ }^\circ\text{C}$  and 10 h dwell, to allow phase formation and carbon coating in a single step. The heating and cooling rates were  $200 \text{ }^\circ\text{C h}^{-1}$ .

### *Physiochemical characterisation*

The phase formation and phase purity was monitored by X-ray diffraction. All X-ray powder diffraction patterns were recorded on a Bruker D8 Advance Da-Vinci equipped with a LynxEye Xe detector, working in Bragg-Brentano ( $\Theta/2\Theta$ ) geometry. Patterns were recorded using  $\text{CuK}_\alpha$  ( $1.54060 \text{ \AA}$ ) radiation. The scan range for the as pyrolysed powders was  $15$  to  $75 \text{ }^\circ 2\Theta$  with a step-size of  $0.013 \text{ }^\circ$  and an integration time of  $0.75 \text{ s}$ . The final samples were recorded from  $15$  to  $140 \text{ }^\circ 2\Theta$  with a step-size of  $0.013 \text{ }^\circ$  and an integration time of  $1 \text{ s}$ . Lattice parameter calculations and full pattern refinements for the quantification of secondary phases was performed with Topas (Bruker AXS Version 4.2). Fundamental parameters were applied to refine the peak

shapes. The refinement of LFS in the space group  $P2_1n$  was started with a model by Dahbi *et al.*<sup>18</sup>. The lattice parameters and the angle  $\beta$  were allowed to relax and subsequently the atomic positions were allowed to relax, starting with the heaviest atom. The refinements of the LFMS sample were done by combining this model with a previously reported model for  $\beta_{II}$   $\text{Li}_2\text{MnSiO}_4$ .<sup>16,26</sup> The carbon content was estimated by thermogravimetric analysis (TGA) in synthetic air ( $30 \text{ mL min}^{-1}$ ) on a Netzsch STA 449C Jupiter thermo analyser. Samples were heated to  $850 \text{ }^\circ\text{C}$  at a heating rate of  $10 \text{ }^\circ\text{C min}^{-1}$ . Surface area and pore size distribution data was acquired by nitrogen adsorption on a Micrometrics Tristar 3000, for which the samples were vacuum dried at  $110 \text{ }^\circ\text{C}$  for 24 h. Further morphological investigations were carried out by field emission scanning electron microscopy (FE-SEM) on a Zeiss Supra 55 VP. The samples were prepared by ultra-sonication of a powder EtOH suspension for 20 min prior to analysis.

#### *Electrochemical characterisation*

The electrochemical properties were assessed by galvanostatic cycling experiments on a Maccor 4200. Applied voltage windows were 1.5 - 4.4 V for LFS samples and 1.5 - 4.7 V for LFMS samples. All samples were characterised at room temperature. Additionally, cells made with LFS 0.12 were characterised at  $60 \text{ }^\circ\text{C}$ . The corresponding electrodes were prepared by a tape casting method. A slurry containing 75 wt. % active material, 15 wt. % conductive carbon (Super P Timcal) and 10 wt. % polyvinylidene fluoride (PVDF) (Kynar, reagent grade) as binder dispersed in N-Methyl-2-pyrrolidone (NMP) (Sigma Aldrich > 99 %) was prepared using a shaker mill (20 min). This slurry was tape casted on Al foil as current collector and dried for 12 h at  $90 \text{ }^\circ\text{C}$  in vacuum. Circular cathodes ( $\text{\O} 16 \text{ mm}$ ) with a solid load of about  $1.5 \text{ mg cm}^{-2}$  were cut from the casts. Using these cathodes, CR2016 coin cells were assembled in a glove box (dry Ar atmosphere). Circular Li discs acted as counter electrodes, separated by a Celgard 2400 PP film. The applied electrolyte was 1 M  $\text{LiPF}_6$  dissolved in a 1:1 volume ratio of ethylene carbonate / diethyl carbonate solution (Aldrich Battery grade). The measured capacities are reported with respect to the mass of the carbon coated composite. The charge rate, C, was defined as a current density of  $160 \text{ mA g}^{-1} = 1\text{C}$ . After galvanostatic cycling experiments, selected batteries were disassembled in a glove box, and XRD scans of the cathode were recorded to investigate the structural integrity. Scans were recorded from  $15$  to  $65 \text{ }^\circ 2\Theta$  (step-size of  $0.013 \text{ }^\circ$ , integration time 2 s) using  $\text{Cu K}_\alpha$  radiation and compared to the patterns of the corresponding powders.

## Results and discussion

XRD patterns of the three as-pyrolysed powders are shown in Fig. 1. All powders were shown to be highly amorphous. Crystalline parts were indexed to  $\text{Li}_2\text{CO}_3$  and one or more spinel phases. The exact chemical composition of the spinel phase could not be resolved due to low crystallinity and peak broadening effects.

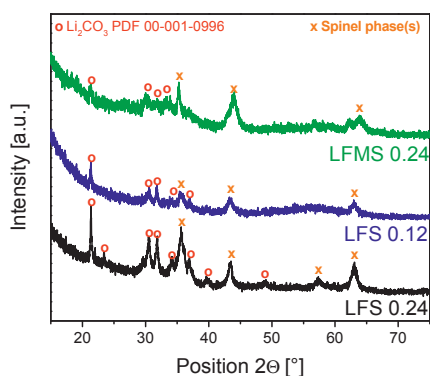
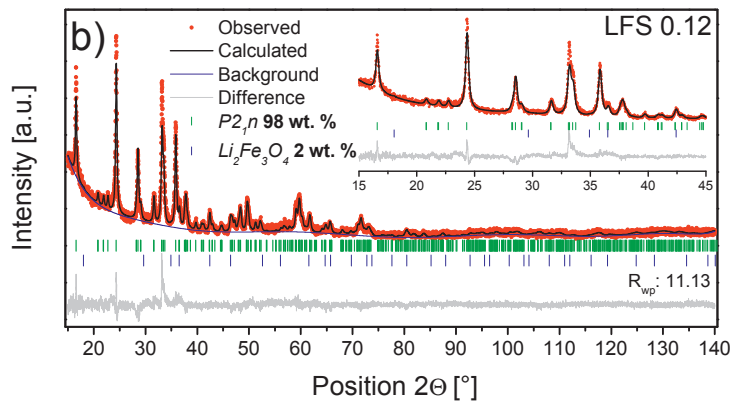
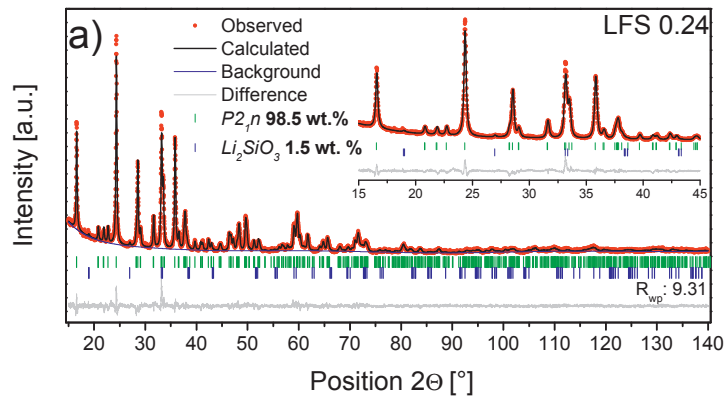


**Figure 1:** Powder XRD patterns of as-pyrolysed LFS 0.24 (black), LFS 0.12 (blue) and LFMS 0.24 (green).

It was expected that phase formation would not occur during the pyrolysis. The combination of extremely high temperatures, a short residence time, and the oxidising nature of the flame during the LF-FSP process, does not allow the phase formation of such a complex system. The Rietveld profiles of the samples are shown in Fig. 2. Both LFS samples were present in the  $\gamma_s$  polymorph ( $P2_1n$ ), and the LFMS 0.24 consisted of a mixture of  $\gamma_s$  and  $\beta_{II}$  ( $Pmn2_1$ ) polymorphs, which is commonly reported for  $\text{Li}_2\text{MnSiO}_4$ .<sup>6,27</sup> LFS 0.24 showed a higher crystallinity and a better signal to noise ratio compared to LFS 0.12 and LFMS 0.24. Accordingly, the structural model was refined with LFS 0.24. In the case of LFS 0.12 only the unit cell dimensions and the angle  $\beta$  were refined. Since LFMS 0.24 consisted of a polymorph mixture, the model for LFS 0.24 was combined with a previously reported model for  $\text{Li}_2\text{MnSiO}_4$ .<sup>16,19</sup> The phase fraction was calculated to consist of 61 wt. % monoclinic  $P2_1n$ , and 37 wt. % orthorhombic  $Pmn2_1$ . Unfortunately, the quality of our data did not allow a meaningful refinement of the cation occupancy in each polymorph of the



LFMS 0.24 sample. The crystalline fraction of LFS 0.24 and LFMS 0.24 showed minor traces of  $\text{Li}_2\text{SiO}_3$ , calculated to be 1.5 wt. % and 2 wt. %, respectively. In the case of LFS 0.12,  $\text{Li}_2\text{SiO}_3$  could not be detected but 2 wt. % of a cubic  $\text{Li}_2\text{Fe}_3\text{O}_4$  phase was present. Calculated phase fractions can have error margins of up to 5 % but the fits obtained in this study seem reasonable and the secondary phase peaks are hardly distinguishable from the background. The corresponding cell parameters and calculated crystallite sizes, from the full width at half maximum of the  $111$  peak ( $011$  for orthorhombic  $Pmn2_1$ ), are given in Table 1.



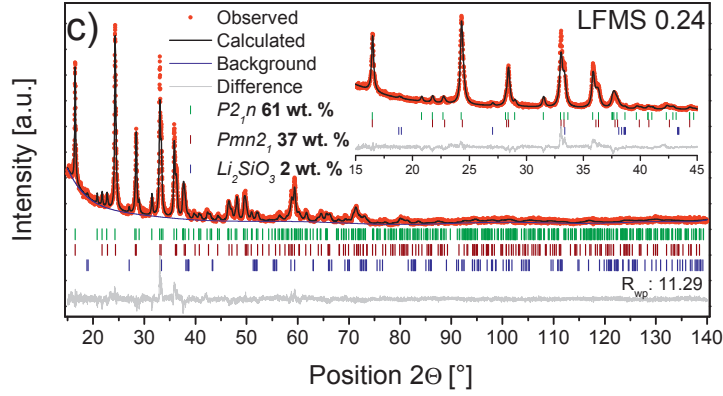


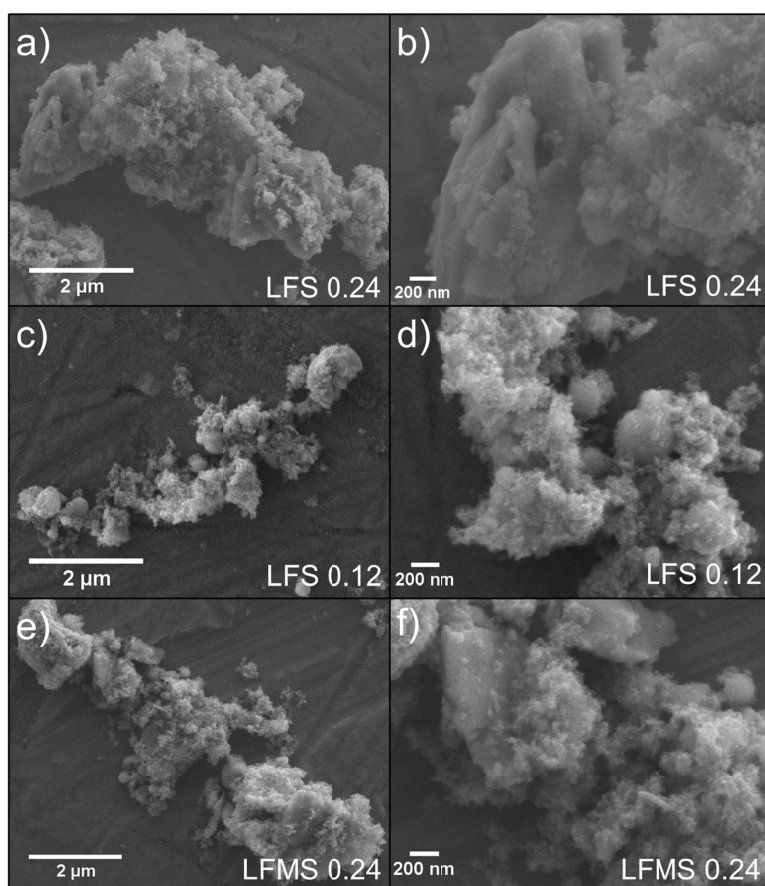
Figure 2: Rietveld profiles of a) LFS 0.24, b) LFS 0.12 and c) LFMS 0.24. Including a magnified region 15-45 ° 2 $\Theta$ , the corresponding  $hkl$  values and the calculated phase fraction.

Table 1: Unit cell parameters and calculated crystallite size of LFS 0.24, LFS 0.12 and LFMS 0.24.

Sample	a [Å]	b [Å]	c [Å]	$\beta$ [°]	Unit cell volume [Å <sup>3</sup> ]	Crystallite size from 111 [nm]
LFS 0.24 ( <i>P</i> <sub>2</sub> 1 <i>n</i> )	8.21987(37)	5.01401(15)	8.24400(37)	98.9590(21)	335.628(24)	42
LFS 0.12 ( <i>P</i> <sub>2</sub> 1 <i>n</i> )	8.2164(10)	5.01225(39)	8.2424(11)	98.9363(54)	335.326(66)	28
LFMS 0.24 ( <i>P</i> <sub>2</sub> 1 <i>n</i> )	8.2688(23)	5.00961(39)	8.2689(26)	98.8757(78)	338.43(15)	40
LFMS 0.24 ( <i>P</i> mn2 <sub>1</sub> )	6.2772(17)	5.3745(14)	4.96277(80)	-	167.428(68)	34

The unit cell dimensions of the two LFS samples are very similar to each other and in agreement with data from the literature.<sup>10,18</sup> The 50 % Mn substituted sample LFMS 0.24 offers increased *P*<sub>2</sub>1*n* unit cell dimensions along the a and the c-axis while the b-axis is slightly shortened, leading to an overall increased cell volume. At the same time the *P*mn2<sub>1</sub> unit cell has a slightly smaller volume than previously reported data for Li<sub>2</sub>MnSiO<sub>4</sub>.<sup>19</sup> This can be explained by the difference in ionic radius of tetrahedrally coordinated Mn<sup>2+</sup> and Fe<sup>2+</sup>, where the former has an ionic radius of 0.80

Å, and the latter 0.77 Å.<sup>28</sup> Further, the decreased precursor concentration of LFS 0.12 led to a reduced crystallite size. The difference in the calculated crystallite sizes and the increased degree of crystallinity of LFS 0.24 compared to LFS 0.12 suggests morphological differences. For LFMS 0.24, a discrepancy of the calculated crystallite size between the two polymorphs is visible. While the  $P2_1n$  crystallite size is in the same range as for LFS 0.24, the  $Pmn2_1$  crystallite size is notably smaller. For this sample in particular, strain between both polymorphs could influence the calculated values. Fig. 3 shows FE-SEM micrographs of all powders.



**Figure 3: FE-SEM micrographs of LFS 0.24 (a and b), LFS 0.12 (c and d) and LFMS 0.24 (e and f).**

All powders consist primarily of loosely agglomerated nanoscale particles, but differences, are clearly visible, in particular for the two LFS samples. The higher magnification reveals that parts of the LFS 0.24 sample consist of large irregularly shaped, dense agglomerates. However, the LFS 0.12 sample offers mainly loosely agglomerated nanoparticles and some spherical sub- $\mu\text{m}$  ( $> 200$  nm) size dense agglomerates. The authors observed a similar morphology for LF-FSP synthesised  $\text{Li}_2\text{MnSiO}_4$ ,<sup>19</sup> although without the concentration effect observed here. This gives a clear indication that the concentration of the  $\text{Fe}(\text{NO}_3)_3 \cdot 9\text{H}_2\text{O}$  precursor has a pronounced effect on particle growth and agglomeration. It cannot be concluded if the ferric ion itself or the increased amount of nitrate anions and crystal water is causing this effect. LFMS 0.24 also shows some dense agglomerated areas, clearly visible in the upper left corner of Fig. 3 f), but the amount of these agglomerates is reduced compared to the LFS 0.24 sample. The addition of corn-starch prior to the annealing not only ensures the generation of a carbon coating but also hinders further particle growth. This is supported by the BET data, illustrated in Table 2, comparing the as-pyrolysed powders and the carbon coated powders.

**Table 2: Surface area data, divided into micropore area (pore  $< 2$  nm) and external surface area for as-pyrolysed and coated samples. As-pyrolysed samples are denoted by AP.**

Sample	BET surface area [ $\text{m}^2\text{g}^{-1}$ ]	External surface area [ $\text{m}^2\text{g}^{-1}$ ]	Micropore area [ $\text{m}^2\text{g}^{-1}$ ]
LFS 0.24 AP	48.04	39.38	8.66
LFS 0.24	70.11	36.81	33.30
LFS 0.12 AP	94.02	87.16	6.86
LFS 0.12	94.97	71.81	23.16
LFMS 0.24 AP	60.11	50.11	10.00
LFMS 0.24	79.60	56.76	22.84

Furthermore, the surface area in Table 2 is divided into micropore area and external surface area, where the latter reflects the active surface area of the material since micropores are by definition smaller than 2 nm and cannot be penetrated by the solvated ions<sup>10</sup> It was previously shown that the micropores can, to a high extent, be attributed to porosity of the amorphous carbon coating. This is likely the case here as well, since the amount of microporosity is, in all three cases, increased after the annealing step. The lowered Fe precursor concentration led to a strong increase in the external surface area, and hence indicates smaller particles, which is in agreement with the FE-SEM observations. The surface area of the Mn substituted sample

LFMS 0.24 lies between the two LFS samples. This is also in agreement with the FE-SEM observations, where we pointed out that the amount of dense agglomerates is reduced. The noticeably increased micropore area in all cases gives a first indication of a substantial amount of carbon in the samples. Fig. 4 shows the pore size distributions and the TGA curves used to estimate the carbon content of the three samples.

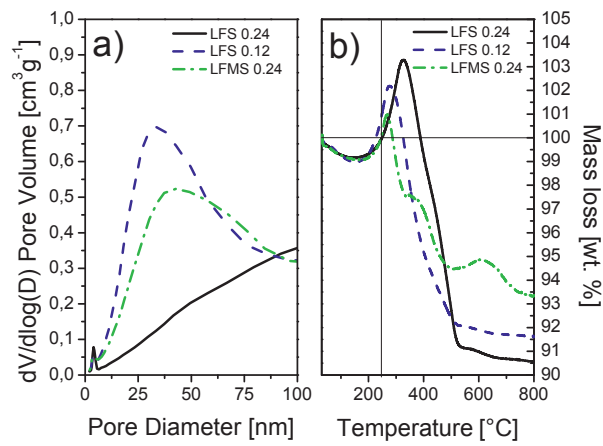


Figure 4: a) Pore size distribution, b) TGA profile in synthetic air of LFS 0.24, LFS 0.12 and LFMS 0.24.

The pore volume in the meso-range of LFS 0.12 and LFMS 0.24 is larger than for LFS 0.24, which is also supported by the FE-SEM data. The combination of these observations strengthen the hypothesis that high  $\text{Fe}(\text{NO}_3)_3 \cdot 9\text{H}_2\text{O}$  precursor concentrations lead to particle growth and the formation of dense agglomerates. Both LFS 0.24 and LFS 0.12 show an onset of mass gain at about 200 °C which can be attributed to the oxidation of  $\text{Fe}^{2+}$ , resulting in the formation of  $\text{Li}_2\text{SiO}_3$  and  $\text{Fe}_2\text{O}_3$ .<sup>18</sup> This mass gain is followed by a mass loss, at temperatures < 500 °C, caused by the oxidation of the carbon coating, causing evolution of CO and CO<sub>2</sub>. The carbon content estimated from the mass loss is in the case of LFS 0.24 about 12 wt. %, and in the case of LFS 0.12 about 10 wt. %. The curve of the LFMS 0.24 sample is quite similar but shows some mass regain and loss at temperatures > 500 °C. The additional Mn cation complicates the TGA profile since it can form different oxides dependent on the temperature and the oxygen partial pressure.<sup>29</sup> If it is assumed that the mass loss between 270 °C and 500 °C is caused by the decomposition of the car-

bon coating, the initial carbon content of the sample is about 6-7 %. Electrodes were fabricated from all samples, and the electrochemical properties were assessed by galvanostatic cycling at room temperature. The upper cut-off voltage for both LFS samples was set to 4.4 V, whilst LFMS 0.24 was charged up to 4.7 V, to allow the oxidation of Mn. Fig. 5 a), b) and c) show the first, second and fifth galvanostatic cycles of the corresponding samples at a charge rate of C/20. Fig. 5 d) and e) show the resulting differential capacity plots of LFS 0.12 and LFMS 0.24.

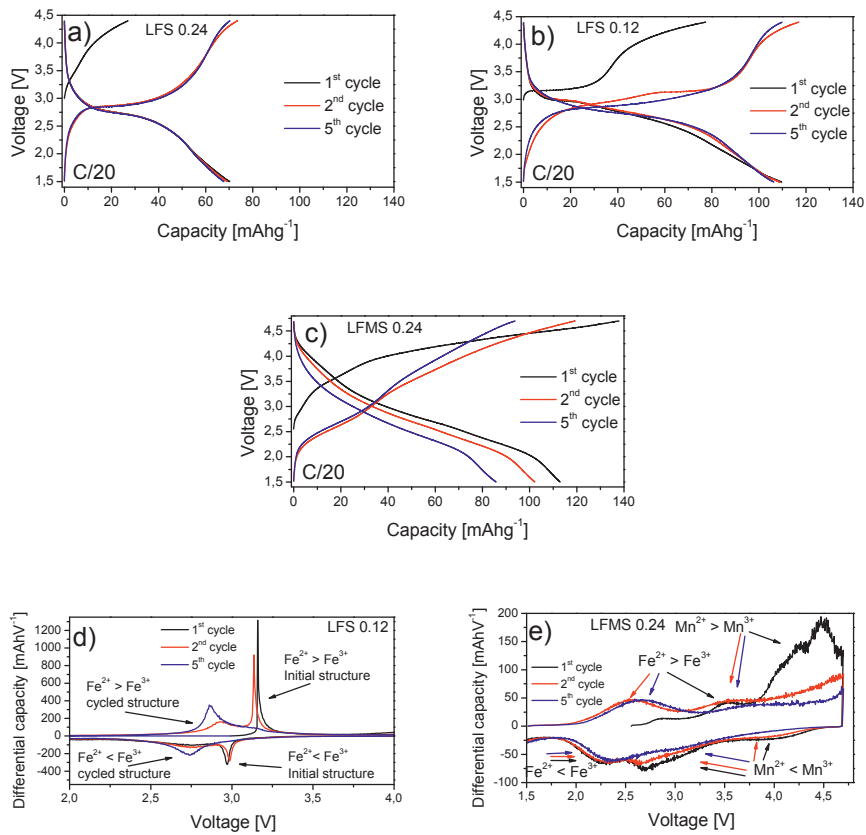
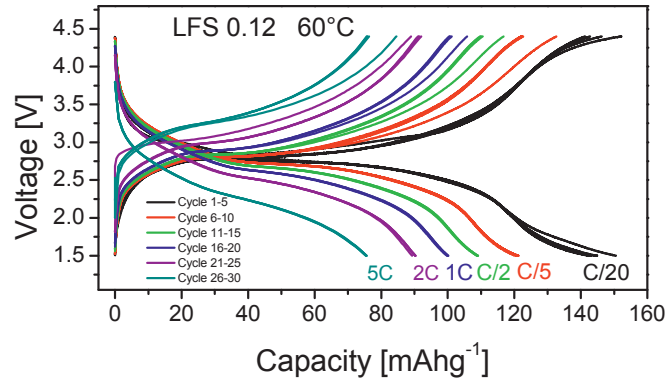


Figure 5: First, second and fifth galvanostatic cycle of a) LFS 0.24, b) LFS 0.12 and c) LFMS 0.24. The corresponding differential capacity plots of LFS 0.12 and LFMS 0.24 are shown in d) and e) respectively.

Both LFS samples showed a reduced capacity during the first charge, which can be attributed to the partial oxidation of Fe during prolonged storage in air.<sup>30</sup> However, the mixed metal sample LFMS 0.24 does not show this effect in a pronounced manner, and also our previous studies on  $\text{Li}_2\text{MnSiO}_4$  have not shown a reduced charge capacity on the first cycle.<sup>16,31</sup> This suggests that divalent Mn is not as prone to oxidation in contact with air as divalent Fe. The discharge capacity of LFS 0.12 is  $110 \text{ mAhg}^{-1}$ , more than 50 % higher than of LFS 0.24. The enhanced electrochemical activity can be attributed to the smaller particle size and higher surface area of the material. LFMS 0.24 shows a very similar first discharge capacity but a substantial, irreversible capacity loss during the first cycle and a capacity retention of only 76 % after five cycles.

LFS has been shown to undergo structural rearrangements upon cycling. The as-prepared monoclinic  $\gamma_s$  polymorph converts to an inverted orthorhombic  $\beta_{\text{II}}$  structure.<sup>4,32</sup> As this occurs, the connectivity of the  $\text{FeO}_4$  units changes, and hence so do the intercalation/deintercalation potentials. This can be seen in the galvanostatic cycling plots but it is even more visible in the differential capacity plot in Fig. 5 d). In the initial cycle, the deintercalation potential is located at 3.15 V and the corresponding intercalation potential at 2.99 V. Upon cycling, these peaks disappear while new anodic and cathodic peaks appear at 2.87 V and 2.75 V, respectively. The differential capacity plot of LFMS 0.24 (Fig. 5 e)) is more complicated. As already seen in Fig. 5 c), the voltage profile of LFMS changes upon cycling. During the first and second discharge, three distinct slopes can be distinguished, whereas in the fifth cycle the first slope at high potentials disappeared. The strongly sloping curves and the capacity fade already indicate a progressing structural degradation. The sloping profile leads to wide peaks in the differential capacity plot. The redox reaction of Mn and Fe are indicated by arrows in the colour corresponding to the cycle. During the first oxidation, only minor activity can be detected below 4 V. The broad minor peak at about 3.5 V can be attributed to the oxidation of  $\text{Fe}^{2+}$  to  $\text{Fe}^{3+}$ . Indeed,  $\text{Fe}^{2+}$  in LFMS 0.24 could also have been partly oxidised upon storage. At potentials over 4 V a huge peak occurs which is attributed to the oxidation of  $\text{Mn}^{2+}$  to  $\text{Mn}^{3+}$ . During the following discharge, three distinct broad cathodic peaks occur. The first and second broad peaks are located at about 4 and 2.7 V, respectively. Several authors have shown by cyclic voltammetry that  $\text{Li}_2\text{MnSiO}_4$  exhibits two peaks upon initial discharge independent of whether their reported capacities indicated a one or two electron reaction.<sup>33–35</sup> If one considers the structural collapse of  $\text{Li}_2\text{MnSiO}_4$ , the minor first cathodic peak, at around 4 V, can be attributed to  $\text{Mn}^{2+}/\text{Mn}^{3+}$  still in its initial chemical environment, while the second, more pronounced peak would correspond to  $\text{Mn}^{2+}/\text{Mn}^{3+}$  in an altered chemical environment. This is also the case for LFMS 0.24. The third cathodic peak at 2.3 V corresponds to the  $\text{Fe}^{2+}/\text{Fe}^{3+}$  reduction, and the

subsequent oxidation shows the according anodic peak at about 2.5 V. The anodic  $\text{Mn}^{2+}/\text{Mn}^{3+}$  peak during the second oxidation is also shifted to lower potentials and becomes extremely broad. Finally, in the fifth cycle only the peaks corresponding to the  $\text{Fe}^{2+}/\text{Fe}^{3+}$  redox couple are still visible while any Mn activity is visually absent. This could be caused by Mn dissolution in combination with a structural collapse. These findings are in agreement with other reports communicating severe capacity fade upon cycling for Mn substituted  $\text{Li}_2\text{FeSiO}_4$ ,<sup>36,37</sup> as well as theoretical predictions.<sup>20</sup> Since LFS 0.12 showed a superior performance compared to LFS 0.24, further characterisation of LFS 0.24 was omitted. The initial capacity of  $110 \text{ mAhg}^{-1}$  is still lower than the theoretical capacity of  $166 \text{ mAhg}^{-1}$  for the one electron reaction. However, it has to be considered that 10 wt. % of LFS 0.12 consists of amorphous carbon and does not take part in the electrochemical reaction at these potentials. To give a more realistic number of how many Li ions per transition metal are extracted/inserted, the carbon coating needs to be subtracted from the active material mass. This leads to a discharge capacity of  $122 \text{ mAhg}^{-1}$  for the pure active material, which corresponds to the insertion of about 0.74 Li per transition metal ion. To push this number closer to 1, the kinetics were enhanced by cycling LFS 0.12 at an elevated temperature of  $60^\circ\text{C}$ . The corresponding galvanostatic cycling profile of LFS 0.12 at different C rates is shown in Fig. 6. The cell was cycled at C/20, C/5, C/2, 1C, 2C and 5C for five consecutive cycles. As previously mentioned the first charge profile looks different from the rest, and was excluded for clarity of the figure.



**Figure 6:** Galvanostatic cycles of LFS 0.12 at  $60^\circ\text{C}$ . The cell was cycled five times at each C rate, ranging from C/20 to 5C. The first charge is excluded.



Despite the previously described behaviour during the first charge, no discrepancy between charge and discharge capacity was detected, demonstrating the reversibility of the reaction also at elevated temperatures. The initial discharge capacity was  $150 \text{ mAhg}^{-1}$ . This value corresponds well to the complete one electron reaction ( $\text{Li}_2\text{FeSiO}_4 \leftrightarrow \text{LiFeSiO}_4$ ) if the carbon content ( $\sim 10 \text{ wt. } \%$ ) is subtracted from the active mass of the cathode. Within the first five cycles, the capacity stabilises at values of about  $140 \text{ mAhg}^{-1}$ . At a rate of  $1\text{C}$  and  $5\text{C}$ ,  $2/3$  and  $1/2$  of the initial capacity is retained, respectively. This displays an acceptable rate performance. Fig. 7 shows the rate performance, ranging from  $\text{C}/20$  to  $5\text{C}$ , of LFMS 0.24 and LFS 0.12 at room temperature. Parts b) and c) show the long-term performance of both samples at  $\text{C}/2$  rate including the coulombic efficiency and differential capacity plots of different cycles in the insets.

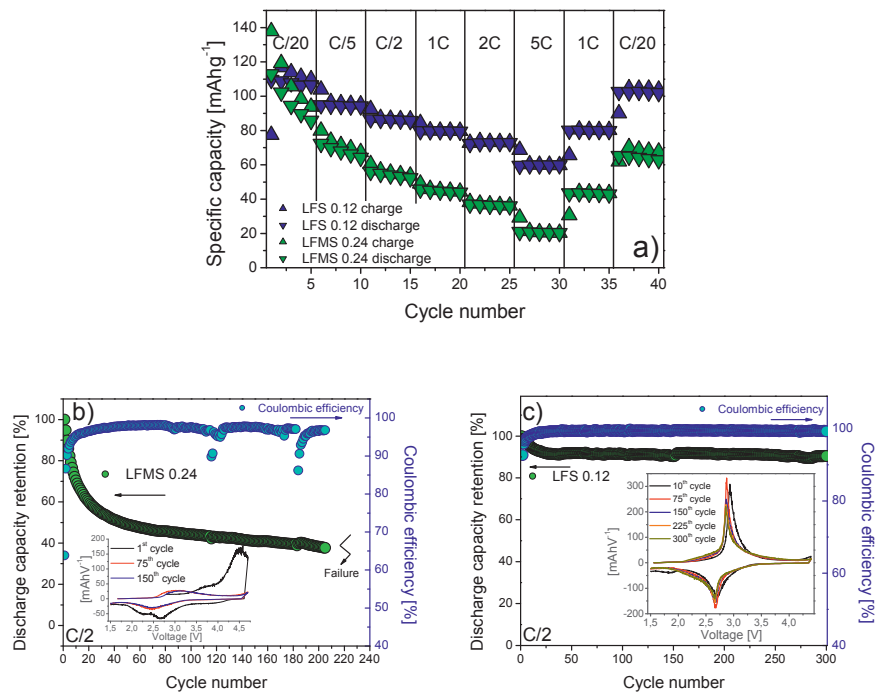
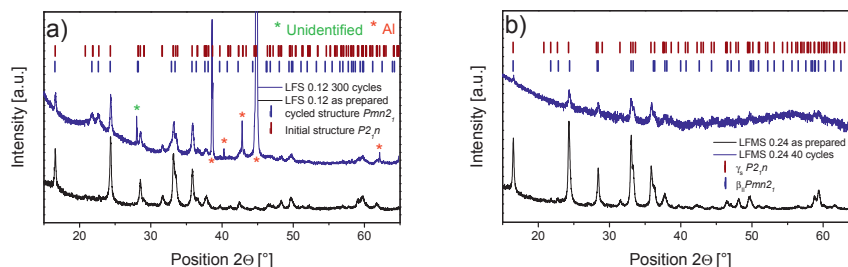


Figure 7: a) Rate capability of LFMS 0.24 and LFS 0.12 at room temperature. b) Long-term cycling of LFMS 0.24 at  $\text{C}/2$ . Inset shows the differential capacity of the 1<sup>st</sup>, 75<sup>th</sup> and 150<sup>th</sup> cycle. c) Long-term cycling of LFS 0.12 at  $\text{C}/2$ . Inset shows the differential capacity of the 10<sup>th</sup>, 75<sup>th</sup>, 150<sup>th</sup>, 225<sup>th</sup> and 300<sup>th</sup> cycle.

LFS 0.12 shows an overall stable cycling behaviour at 60 °C and room temperature. Also, at room temperature, over half of the initial capacity is retained at a high current density of 800 mA $g^{-1}$  (5C), hence proving the temperature independence of the rate capability in the given temperature region. After 40 cycles, the LFS 0.12 sample shows a capacity retention of 94%. However, LFMS 0.24 shows a severe capacity fade during the initial cycles at C/20 rate. Hence, it is not straight forward to define the rate capability, since the lower capacity at higher rates is influenced by the loss already occurred in the initial cycles. Further, the capacity fade of LFMS 0.24 is much less pronounced at higher rates. We link this behaviour to Li<sub>2</sub>MnSiO<sub>4</sub>, where the capacity decay is directly linked to the amount of Li exchanged and hence the capacity.<sup>19,33</sup> Fig. 7 b) shows the capacity retention during long time cycling of LFMS 0.24 at C/2 rate. The capacity retention after 40 cycles is only 50 %. Afterwards, only a slow decay is observable. The cell broke down after 205 cycles, possibly caused by side reactions due to the high potential window. The inset shows the differential capacity of the 1<sup>st</sup>, 75<sup>th</sup> and 150<sup>th</sup> cycle. The first cycle resembles the differential capacity plot discussed in Fig. 5 e), and as previously mentioned any Mn activity disappears from the differential capacity plot after prolonged cycling. The differential capacity during the 75<sup>th</sup> and 150<sup>th</sup> cycle show 1 anodic and 1 cathodic peak corresponding to the Fe<sup>2+</sup>/Fe<sup>3+</sup> redox reaction. These two peaks are slightly shifted in potential and raise the question if structural rearrangements happen upon prolonged cycling. In comparison, LFS 0.12 shows a stable cycling profile with a capacity retention > 90% after 300 cycles. The coulombic efficiency approaches 100 % after the first few cycles. The inset shows the differential capacity of the 10<sup>th</sup>, 75<sup>th</sup>, 150<sup>th</sup>, 225<sup>th</sup> and 300<sup>th</sup> cycles demonstrating the excellent stability of the system. The stability was confirmed by post-mortem XRD in a fully discharged state. Disassembly of the LFS 0.12 cell after 300 cycles was carried out in an Ar filled glove box. The electrode was thoroughly washed with DEC. The LFMS 0.24 cell, shown in Fig. 7 a) was also disassembled for post-mortem XRD. In contrast to the LFS 0.12 cell, the LFMS 0.24 showed poor dimensional stability. Fig. 8 shows the corresponding XRD patterns, including XRD scans of the fresh electrode materials for comparison. Note that LFS 0.12 was measured on the Al current collector. Al peaks and an unidentified peak are denoted by asterisks.



**Figure 8:** a) XRD pattern of LFS 0.12 after 300 cycles, at a fully discharged state, including a pattern of the as prepared sample and  $hkl$  positions of the initial  $P2_1n$  structure and a inverted  $Pmn2_1$  structure according to Armstrong *et al.*<sup>4</sup>. b) XRD pattern of LFMS 0.24 after 40 cycles, at a fully discharged state, including a pattern of the as prepared sample and  $hkl$  positions of the initial  $P2_1n$  and  $Pmn2_1$  structures.

Both post-cycling scans show a rather poor signal-to-noise ratio, caused by the small sample amount in addition to a high amorphous fraction resulting from the carbon coating and additives (Super P and PVDF). Topas suggests the cycled LFS 0.12 sample shown in Fig. 8a), to consist of 80 wt. % inverted  $\beta_{II}$  ( $Pmn2_1$ ) and 20 wt. % as synthesised  $\gamma_s$  ( $P2_1n$ ). These numbers have to be handled with caution but clear evidence for the structural changes can be observed in the region 20 to 25 ° 2 $\theta$ . Pronounced  $Pmn2_1$  110 and 101 peaks are visible at 21.7 and 22.6 ° 2 $\theta$ , respectively. These two peaks would be of a very minor intensity for a non-inversed  $Pmn2_1$  structure, since the corresponding lattice planes offer very limited electron density. Due to the Fe/Li site reversal however, the electron density and hence the intensity of these peaks is strongly increased. Further, the peaks at about 33 ° 2 $\theta$  show broadening, which can be explained by the 210 peak of the inversed structure which is located at slightly lower angles than the 10-3 30-1 double peak of the initial structure. The remains of a partly non-inversed structure could be explained by the fact that during cycling only about 0.5-0.6 Li per formula unit were extracted and reinserted. In the case of LFMS 0.24, small peaks resembling the initial XRD pattern are still present. This is in contrast to  $Li_2MnSiO_4$ , where irreversible amorphisation occurs already upon the first charge.<sup>15,19</sup> However, the pattern of the cycled LFMS 0.24 suggests a high amorphous content. Further the poor quality does not allow any conclusions to whether the remaining crystalline fraction still consists of  $Li_2Fe_{0.5}Mn_{0.5}SiO_4$ , or a Mn deficient phase.

## Conclusions

A novel scalable synthesis method is reported. Liquid-feed flame spray pyrolysis with a subsequent heat treatment in reducing atmosphere is capable of producing large amounts of electrochemically active, nanosized  $\text{Li}_2\text{FeSiO}_4$  and  $\text{Li}_2\text{Fe}_{0.5}\text{Mn}_{0.5}\text{SiO}_4$  with high phase purities. The concentration of the Fe precursor was shown to have a major impact on particle growth, and  $\text{Li}_2\text{FeSiO}_4$  synthesised from a less concentrated solution showed increased surface area and enhanced electrochemical properties.  $\text{Li}_2\text{FeSiO}_4$  synthesised in this study was indexed to the monoclinic  $\gamma_s$  polymorph, while  $\text{Li}_2\text{Fe}_{0.5}\text{Mn}_{0.5}\text{SiO}_4$  was present in a mixture of monoclinic  $\gamma_s$  and orthorhombic  $\beta_{II}$ . The latter reached a discharge capacity of  $115 \text{ mAhg}^{-1}$  at a rate of C/20. Hence, large amounts of both cations undergo a one electron redox reaction. Severe capacity fading upon cycling was observed, similar to the well-known behaviour of  $\text{Li}_2\text{MnSiO}_4$ . Only 40 % of the initial capacity was retained after prolonged cycling. Differential capacity plots suggest that the redox activity in later cycles is caused solely by the  $\text{Fe}^{2+}/\text{Fe}^{3+}$  redox couple. Mn is believed to either form an electrochemically inert amorphous phase or dissolve into the electrolyte. Contrary to  $\text{Li}_2\text{MnSiO}_4$ , where an irreversible amorphisation occurs during the first charge, the solid solution  $\text{Li}_2\text{Fe}_{0.5}\text{Mn}_{0.5}\text{SiO}_4$  was shown to be at least partly crystalline after prolonged cycling. This indicates a slightly more stable structure compared to the pure Mn compound.  $\text{Li}_2\text{FeSiO}_4$  on the other hand, was shown to be stable upon prolonged cycling. In this study,  $\text{Li}_2\text{FeSiO}_4$  was cycled up to 300 times with more than 90 % capacity retention, and differential capacity in combination with post cycling XRD suggests a stable system.  $\text{Li}_2\text{FeSiO}_4$  offered an adequate rate performance with a capacity retention of over 50% at 5C. At elevated temperatures and a slow rate, the reversible exchange of up to one Li per Fe was shown. It should be kept in mind that this is the first time  $\text{Li}_2\text{FeSiO}_4$  was synthesised by LF-FSP, and the authors believe that optimisation of the precursors would allow better control of the morphology. That could lead to the full utilisation of one Li per transition metal at moderate current densities, giving rise to a quick and scalable synthesis for nanoscale  $\text{Li}_2\text{FeSiO}_4$  as cathode for Li-ion batteries.

## Acknowledgements

The research council of Norway is gratefully acknowledged for funding of the Silicat-Batt project (grant number: 216469/E20).

## References

- (1) Tarascon, J. M.; Armand, M. Issues and Challenges Facing Rechargeable Lithium Batteries. *Nature* **2001**, *414* (6861), 359–367.
- (2) Ellis, B. L.; Lee, K. T.; Nazar, L. F. Positive Electrode Materials for Li-Ion and Li-Batteries. *Chem. Mater.* **2010**, *22* (3), 691–714.
- (3) Nytén, A.; Abouimrane, A.; Armand, M.; Gustafsson, T.; Thomas, J. O. Electrochemical Performance of  $\text{Li}_2\text{FeSiO}_4$  as a New Li-Battery Cathode Material. *Electrochem. commun.* **2005**, *7* (2), 156–160.
- (4) Armstrong, A. R.; Kuganathan, N.; Islam, M. S.; Bruce, P. G. Structure and Lithium Transport Pathways in  $\text{Li}_2\text{FeSiO}_4$  Cathodes for Lithium Batteries. *J. Am. Chem. Soc.* **2011**, *133*, 13031–13035.
- (5) Gummow, R. J.; He, Y. Recent Progress in the Development of  $\text{Li}_2\text{MnSiO}_4$  Cathode Materials. *J. Power Sources* **2014**, *253*, 315–331.
- (6) Dominko, R.; Bele, M.; Gaberšček, M.; Meden, A.; Remškar, M.; Jamnik, J. Structure and Electrochemical Performance of  $\text{Li}_2\text{MnSiO}_4$  and  $\text{Li}_2\text{FeSiO}_4$  as Potential Li-Battery Cathode Materials. *Electrochem. commun.* **2006**, *8* (2), 217–222.
- (7) Islam, M. S.; Dominko, R.; Masquelier, C.; Sirisopanaporn, C.; Armstrong, A. R.; Bruce, P. G. Silicate Cathodes for Lithium Batteries: Alternatives to Phosphates? *J. Mater. Chem.* **2011**, *21*, 9811–9818.
- (8) Zheng, Z.; Wang, Y.; Zhang, A.; Zhang, T.; Cheng, F.; Tao, Z.; Chen, J. Porous  $\text{Li}_2\text{FeSiO}_4/\text{C}$  Nanocomposite as the Cathode Material of Lithium-Ion Batteries. *J. Power Sources* **2012**, *198*, 229–235.
- (9) Zhang, P.; Zheng, Y.; Wu, S. Q.; Zhu, Z. Z.; Yang, Y. Hybrid Density Functional Investigations of  $\text{Li}_2\text{MSiO}_4$  (M=Mn, Fe and Co) Cathode Materials. *Comput. Mater. Sci.* **2014**, *83*, 45–50.
- (10) Zhou, H.; Einarsrud, M. A.; Vullum-Bruer, F. High Capacity Nanostructured  $\text{Li}_2\text{Fe}_x\text{SiO}_4/\text{C}$  with Fe Hyperstoichiometry for Li-Ion Batteries. *J. Power*

*Sources* **2013**, *235*, 234–242.

- (11) Zhou, H.; Einarsrud, M.-A.; Vullum-Bruer, F. PVA-Assisted Combustion Synthesis and Characterization of Porous Nanocomposite  $\text{Li}_2\text{FeSiO}_4/\text{C}$ . *Solid State Ionics* **2012**, *225*, 585–589.
- (12) Zhang, L.; Ni, J.; Wang, W.; Guo, J.; Li, L. 3D Porous Hierarchical  $\text{Li}_2\text{FeSiO}_4/\text{C}$  for Rechargeable Lithium Batteries. *J. Mater. Chem. A* **2015**, *3* (22), 11782–11786.
- (13) Yang, J.; Kang, X.; He, D.; Peng, T.; Hu, L.; Mu, S. Hierarchical Shuttle-like  $\text{Li}_2\text{FeSiO}_4$  as a Highly Efficient Cathode Material for Lithium-Ion Batteries. *J. Power Sources* **2013**, *242*, 171–178.
- (14) Muraliganth, T.; Stroukoff, K. R.; Manthiram, A. Microwave-Solvothermal Synthesis of Nanostructured  $\text{Li}_2\text{MSiO}_4/\text{C}$  (M = Mn and Fe) Cathodes for Lithium-Ion Batteries. *Chem. Mater.* **2010**, *22* (20), 5754–5761.
- (15) Dominko, R.  $\text{Li}_2\text{MSiO}_4$  (M = Fe And/or Mn) Cathode Materials. *J. Power Sources* **2008**, *184* (2), 462–468.
- (16) Wagner, N.; Svensson, A.-M.; Vullum-Bruer, F. Effect of Carbon Content and Annealing Atmosphere on Phase Purity and Morphology of  $\text{Li}_2\text{MnSiO}_4$  Synthesized by a PVA Assisted Sol-gel Method. *Solid State Ionics* **2015**, *276*, 26–32.
- (17) Zhang, L.-L.; Duan, S.; Yang, X.-L.; Liang, G.; Huang, Y.-H.; Cao, X.-Z.; Yang, J.; Li, M.; Croft, M. C.; Lewis, C. Insight into Cobalt-Doping in  $\text{Li}_2\text{FeSiO}_4$  Cathode Material for Lithium-Ion Battery. *J. Power Sources* **2015**, *274*, 194–202.
- (18) Dahbi, M.; Urbonaitė, S.; Gustafsson, T. Combustion Synthesis and Electrochemical Performance of  $\text{Li}_2\text{FeSiO}_4/\text{C}$  Cathode Material for Lithium-Ion Batteries. *J. Power Sources* **2012**, *205*, 456–462.
- (19) Wagner, N.; Svensson, A.-M.; Vullum-Bruer, F. Liquid Feed Flame Spray Pyrolysis as Alternative Synthesis for Electrochemically Active Nanosized  $\text{Li}_2\text{MnSiO}_4$ . *Prep.* **2015**.

- (20) Larsson, P.; Ahuja, R.; Liivat, A.; Thomas, J. O. Structural and Electrochemical Aspects of Mn Substitution into  $\text{Li}_2\text{FeSiO}_4$  from DFT Calculations. *Comput. Mater. Sci.* **2010**, *47* (3), 678–684.
- (21) Saracibar, A.; Wang, Z.; Carroll, K. J.; Meng, Y. S.; Dompablo, M. E. A. New Insights into the Electrochemical Performance of  $\text{Li}_2\text{MnSiO}_4$ : Effect of Cationic Substitutions. *J. Mater. Chem. A* **2015**, *3*, 6004–6011.
- (22) Kokalj, A.; Dominko, R.; Mali, G.; Meden, A.; Gaberscek, M.; Jamnik, J. Beyond One-Electron Reaction in Li Cathode Materials: Designing  $\text{Li}_2\text{Mn}_x\text{Fe}_{1-x}\text{SiO}_4$ . *Chem. Mater.* **2007**, *19* (15), 3633–3640.
- (23) Girish, H. N.; Shao, G.-Q. Advances in High-Capacity  $\text{Li}_2\text{MSiO}_4$  (M = Mn, Fe, Co, Ni...) Cathode Material for Lithium-Ion Batteries. *RSC Adv.* **2015**.
- (24) Arroyo-de Dompablo, M. E.; Armand, M.; Tarascon, J. M.; Amador, U. On-Demand Design of Polyoxianionic Cathode Materials Based on Electronegativity Correlations: An Exploration of the  $\text{Li}_2\text{MSiO}_4$  System (M = Fe, Mn, Co, Ni). *Electrochem. commun.* **2006**, *8* (8), 1292–1298.
- (25) Wu, S. Q.; Zhu, Z. Z.; Yang, Y.; Hou, Z. F. Structural Stabilities, Electronic Structures and Lithium Deintercalation in  $\text{Li}_x\text{MSiO}_4$  (M = Mn, Fe, Co, Ni): A GGA and GGA + U Study. *Comput. Mater. Sci.* **2009**, *44* (4), 1243–1251.
- (26) Li, Y.-X.; Gong, Z.-L.; Yang, Y. Synthesis and Characterization of  $\text{Li}_2\text{MnSiO}_4/\text{C}$  Nanocomposite Cathode Material for Lithium Ion Batteries. *J. Power Sources* **2007**, *174* (2), 528–532.
- (27) Sato, M.; Ishigaki, T.; Uematsu, K.; Toda, K.; Okawa, H. Redetermination of the Low-Temperature Polymorph of  $\text{Li}_2\text{MnSiO}_4$  from Single-Crystal X-Ray Data. *Acta Crystallogr. Sect. E Struct. Reports Online* **2012**, *68* (9), i68–i69.
- (28) Shannon, R. D. Revised Effective Ionic Radii and Systematic Studies of Interatomic Distances in Halides and Chalcogenides. *Acta Crystallogr.* **1976**, *A32*, 751–767.
- (29) Terayama, K.; Ikeda, M. Study on Thermal Decomposition of  $\text{MnO}_2$  and  $\text{Mn}_3\text{O}_4$  by Thermal Analysis. *Trans. Japan Inst. Met.* **1983**, *24* (11), 754–758.

- (30) Nyten, A.; Stjerndahl, M.; Rensmo, H.; Siegbahn, H.; Armand, M.; Gustafsson, T.; Edström, K.; Thomas, J. O. Surface Characterization and Stability Phenomena in  $\text{Li}_2\text{FeSiO}_4$  Studied by PES/XPS. *J. Mater. Chem.* **2006**, *16* (34), 3483.
- (31) Wagner, N.; Dalod, A.; Svensson, A.; Vullum-Bruer, F. Fe and V Substituted  $\text{Li}_2\text{MnSiO}_4/\text{C}$  as Potential Cathode Material for Li-Ion Batteries. *ECS Trans.* **2015**, *64* (22), 33–45.
- (32) Liivat, A. Structural Changes on Cycling  $\text{Li}_2\text{FeSiO}_4$  Polymorphs from DFT Calculations. *Solid State Ionics* **2012**, *228*, 19–24.
- (33) Wang, M.; Yang, M.; Ma, L.; Shen, X.; Zhang, X. Structural Evolution and Electrochemical Performance of  $\text{Li}_2\text{MnSiO}_4/\text{C}$  Nanocomposite as Cathode Material for Li-Ion Batteries. *J. Nanomater.* **2014**, *2014*, 1–6.
- (34) Sun, D.; Wang, H.; Ding, P.; Zhou, N.; Huang, X.; Tan, S.; Tang, Y. In-Situ Synthesis of Carbon Coated  $\text{Li}_2\text{MnSiO}_4$  Nanoparticles with High Rate Performance. *J. Power Sources* **2013**, *242*, 865–871.
- (35) Wang, F.; Chen, J.; Wang, C.; Yi, B. Fast Sol-Gel Synthesis of Mesoporous  $\text{Li}_2\text{MnSiO}_4/\text{C}$  Nanocomposite with Improved Electrochemical Performance for Lithium-Ion Batteries. *J. Electroanal. Chem.* **2013**, *688*, 123–129.
- (36) Shao, B.; Abe, Y.; Taniguchi, I. Synthesis and Electrochemical Characterization of  $\text{Li}_2\text{Fe}_x\text{Mn}_{1-x}\text{SiO}_4/\text{C}$  ( $0 \leq x \leq 0.8$ ) Nanocomposite Cathode for Lithium-Ion Batteries. *Powder Technol.* **2013**, *235*, 1–8.
- (37) Deng, C.; Zhang, S.; Yang, S. Y. Effect of Mn Substitution on the Structural, Morphological and Electrochemical Behaviors of  $\text{Li}_2\text{Fe}_{1-x}\text{Mn}_x\text{SiO}_4$  Synthesized via Citric Acid Assisted Sol-Gel Method. *J. Alloys Compd.* **2009**, *487* (1-2), 18–23.





# Appendix



# Appendix A

## Supporting Material Paper I

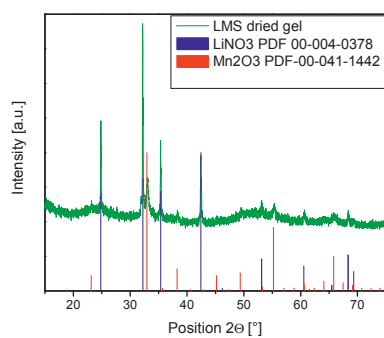


Figure A.1: Powder XRD pattern of dried gel aged for 72 h.

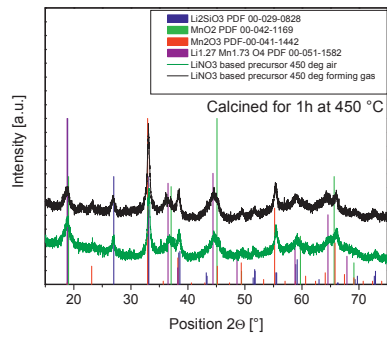


Figure A.2: Powder XRD pattern of calcined LMS precursor.

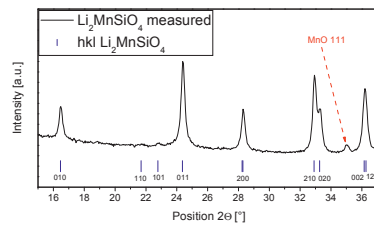


Figure A.3: *HKL* planes of  $Pmn2_1$   $\text{Li}_2\text{MnSiO}_4$ .

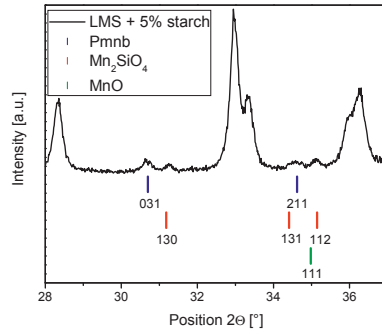


Figure A.4: *Pmnb* polymorph, Mn<sub>2</sub>SiO<sub>4</sub> and MnO secondary phases in LMS containing 5 wt-% corn-starch.

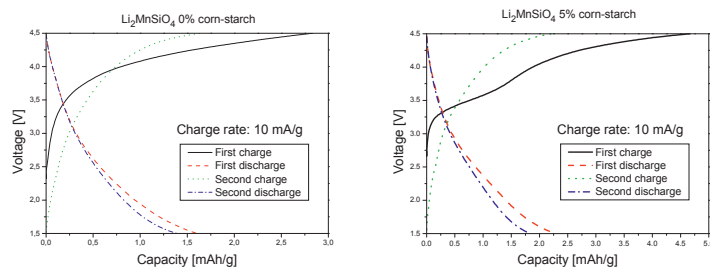


Figure A.5: Galvanostatic cycling of LMS cathodes a) without corn-starch as carbon source b) with 5 wt. % corn-starch as carbon source.



# Appendix B

## Supporting Material Paper IV

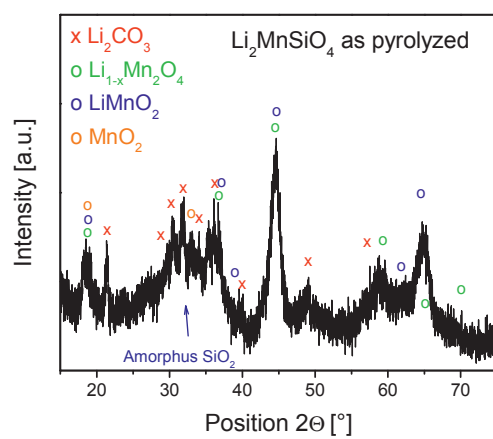


Figure B.1: XRD pattern of a LMS sample after flame spray pyrolysis without any further annealing.



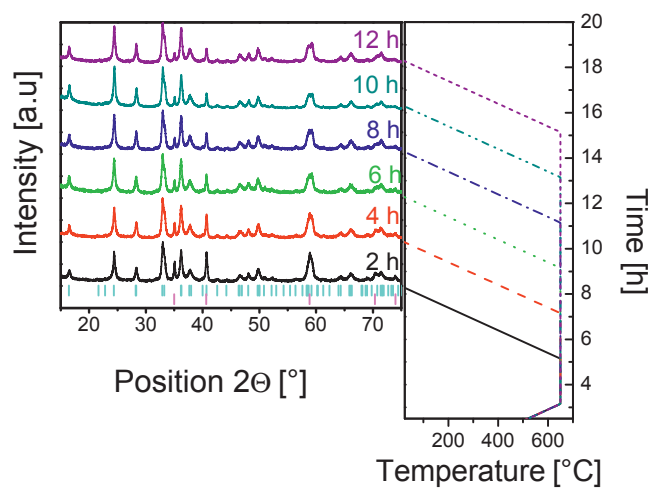
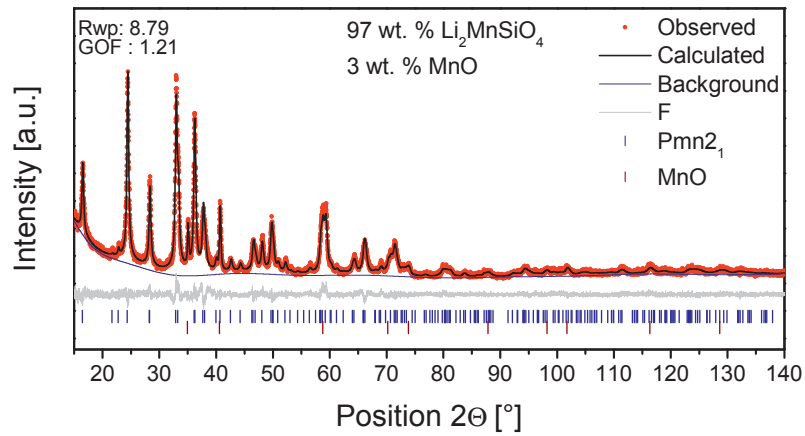


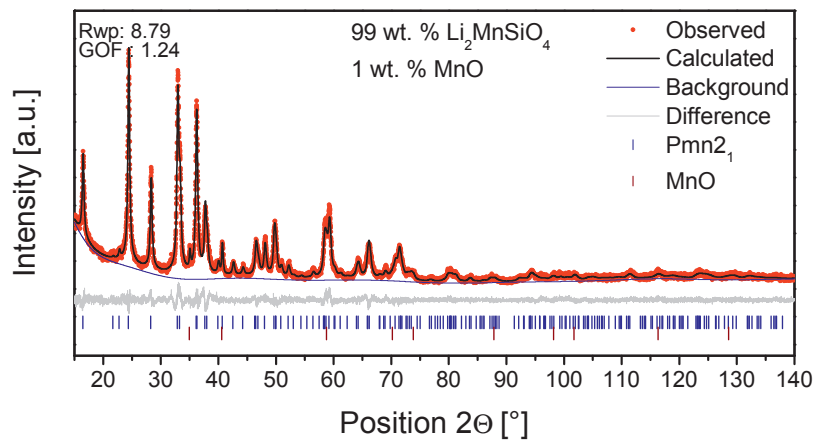
Figure B.2: XRD patterns of LMS @ Xylene heat treated at 650 °C with different dwell time. Pmn<sub>21</sub> and MnO bragg reflections are indicated by the cyan and pink bars respectively.

Dataset B.1: Rietveld refinements, lattice parameters and atomic positions including Mn occupancy of orthorhombic  $Pmn2_1$  LMS @ Xylene, LM0.94S @ Xylene and LM0.91S @ Xylene.

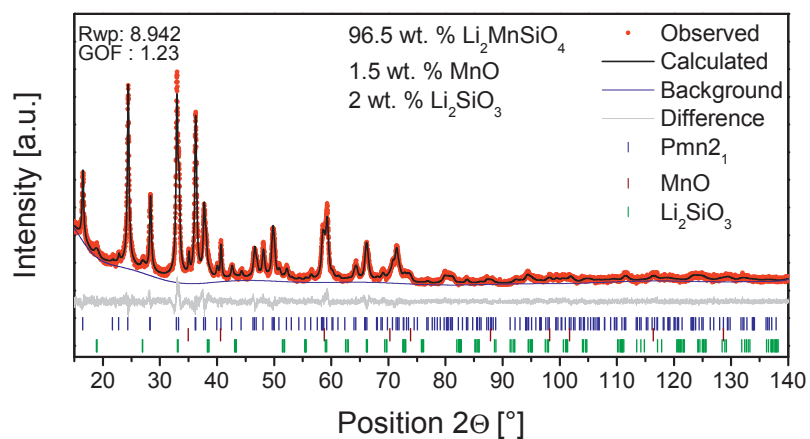
### LMS @ Xylene



### LM0.94S @ Xylene



### LM0.91S @ Xylene



Lattice parameters and atomic coordinates of the xylene assisted LMS samples.

Sample	A[Å]	B[Å]	C[Å]
LMS @ Xylene	6.3111	5.3834	4.9692
LM0.94S @ Xylene	6.3127	5.3830	4.9698
LMS0.91 @ Xylene	6.3094	5.3849	4.9654

Lattice parameters of the three xylene assisted LMS samples

Site	x	y	z	Atom	Occ.
Li	0.2382	0.3398	0.8540	Li <sup>+</sup>	0.9863
Mn on Li	0.2382	0.3398	0.8540	Mn <sup>2+</sup>	0.0137
Mn	0.5000	0.8329	0.8939	Mn <sup>2+</sup>	0.7053 <sup>1</sup> 0.7447 <sup>3</sup>
Si	0.0000	0.8198	-0.0835	Si <sup>4+</sup>	1
O1	0.2177	0.6688	0.8042	O <sup>2-</sup>	1
O2	0.0000	0.1260	0.8422	O <sup>2-</sup>	1
O3	0.5000	0.1699	0.7545	O <sup>2-</sup>	1

Atomic coordinates and occupancies of LMS

<sup>1</sup>Refined Mn occ. of LMS @ Xylene

<sup>2</sup>Refined Mn occ. of LMS 0.94 @ Xylene

<sup>3</sup>Refined Mn occ. of LMS 0.91 @ Xylene

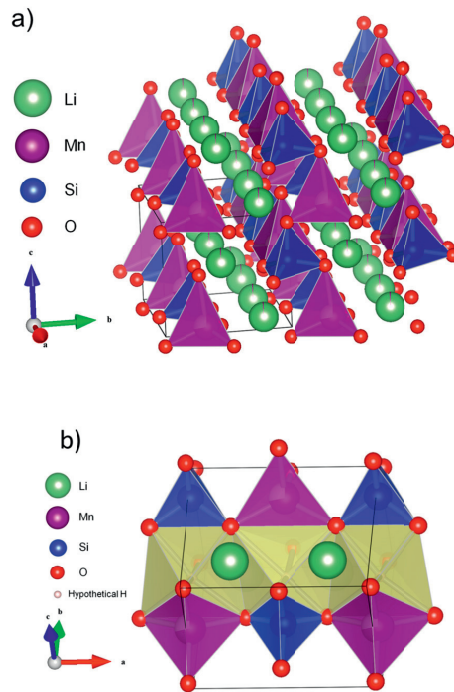


Figure B.3: Crystal structure of LMS based on the refined data of LM0.94S @ Xylene roughly along the a direction b) Illustration of the octahedral interstitial positions which could be partly occupied by Mn and cause fitting mismatches by artificial hydrogen atoms.

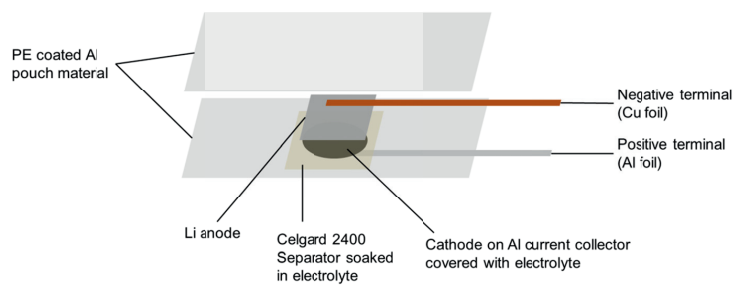


Figure B.4: Scheme of the *in situ* XRD pouch cell.

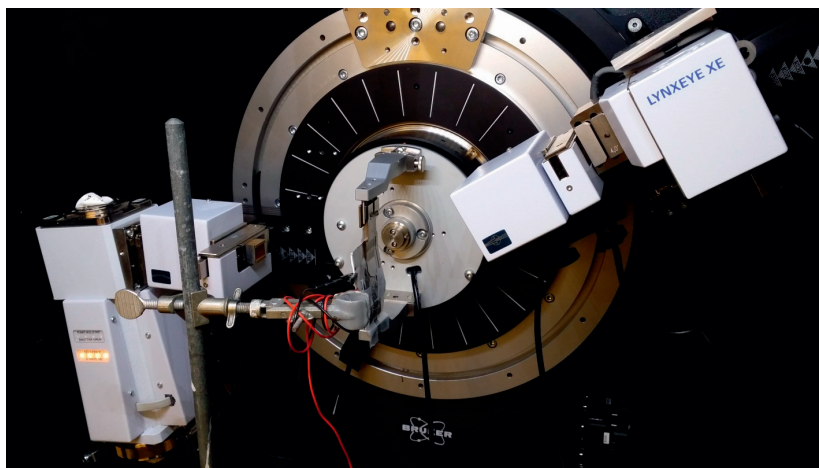


Figure B.5: Photograph of the *in situ* XRD set up.